Politecnico di Milano
Department of Mathematics
Doctoral Program In Mathematical Models and Methods in Engineering

---

Numerical methods for simulation and optimization of wave energy converter arrays

Doctoral Dissertation of
Marco Gambarini

Supervisor
Prof. Edie Miglio

Co-supervisor
Prof. Gabriele Ciaramella

Tutor
Prof. Gabriele Grillo

The Chair of the Doctoral Program
Prof. Michele Correggi

2024 – 37th cycle

Abstract

The mitigation of climate change requires the increasing adoption of renewable energy sources. Since their production is influenced by weather events and can thus be only partially scheduled, it is essential to diversify their mix. In this context, marine renewable energies are a significant opportunity, as indicated by their inclusion in the energy strategies of the European Union. This thesis focuses on wave energy extraction devices, known as WECs (Wave Energy Converters). The existing devices have small nominal power output compared to alternative technologies, such as wind turbines. For this reason, installation in large parks is required. The devices in a park interact with each other through diffraction and radiation processes, whose result is known as the park effect. This can lead to a reduction of the extracted power, if not properly taken into account at the design stage. In this thesis, we propose mathematical models and numerical methods for the simulation and optimization of WEC parks, which can be useful tools for analysis and preliminary design. Our first contribution concerns park simulation. For the numerical solution of the linear potential model equations, discretized with the BEM (Boundary Element Method), we introduce a novel preconditioner. It is based on the block-Jacobi method combined with a coarse correction, and it is effective in reducing the computational time. Regarding optimization, the optimal design problem of a WEC park, with the objective of maximizing power subject to the operative constraints, has been gradually tackled. First, we focused on the optimization of the control parameters at fixed layout, developing an optimization framework that is robust with respect to the operating uncertainties. We have considered in particular the uncertainty with respect to the direction of incident waves, treated through suitable stochastic optimization algorithms. After that, we have examined the problem of layout optimization, with fixed controls. While the most common approaches in the literature are based on metaheuristic algorithms, we have developed a gradient-based method. The possibility of computing the gradient exists thanks to a suitable choice of the hydrodynamic model. The resulting optimization method has been applied to a park of water turbine OWC (Oscillating Water Column) devices. For this kind of device, a lumped parameter model has also been developed. Finally, the combined problem of optimizing positions and control parameters has been tackled by adopting a gradient-flow approach, introducing a solution methodology based on adaptive Runge-Kutta methods.

Sommario

La mitigazione dei cambiamenti climatici richiede l'adozione crescente di fonti rinnovabili di energia. Al fine di soddisfare in modo affidabile la domanda è necessario diversificare le fonti in uso, dato che la loro produzione è influenzata dagli eventi meteorologici e difficilmente programmabile. In questo contesto, le energie rinnovabili marine costituiscono un'opportunità rilevante, testimoniata dal loro inserimento nelle strategie energetiche dell'Unione Europea. Questa tesi si concentra sui dispositivi di estrazione di energia dal moto ondoso, noti come WEC (*Wave Energy Converter*). I generatori esistenti presentano potenze nominali molto minori rispetto ad altre tecnologie, quali le turbine eoliche: è pertanto necessario costruire parchi di grandi dimensioni. I dispositivi di un parco interagiscono tra loro tramite processi di diffrazione e radiazione, il cui insieme è noto come effetto parco e può portare a una riduzione della potenza estratta se non gestito opportunamente in fase di progetto. In questa tesi vengono proposti modelli matematici e metodi numerici per la simulazione e l'ottimizzazione di parchi di WEC, utili come strumenti di analisi e progetto preliminare. Il primo contributo riguarda la simulazione. Per la soluzione numerica delle equazioni del modello idrodinamico a potenziale lineare, discretizzate con il metodo BEM (*Boundary Element Method*), viene introdotto un nuovo precondizionatore, basato sul metodo di Jacobi a blocchi combinato con una correzione coarse. Il suo utilizzo consente una riduzione significativa dei tempi di calcolo. Dal punto di vista dell'ottimizzazione, il problema di progetto ottimo di un parco di WEC, con l'obiettivo di massimizzare la potenza rispettando i vincoli operativi, è stato affrontato gradualmente. Inizialmente, l'attenzione è stata posta sull'ottimizzazione dei parametri di controllo a disposizione fissata, sviluppando una strategia robusta rispetto alle incertezze operative. È stata considerata in particolare l'incertezza rispetto alla direzione delle onde incidenti, trattata con opportuni algoritmi di ottimizzazione stocastica. In seguito, è stato esaminato il problema complementare di ottimizzazione della disposizione dei generatori, a controlli fissati. A differenza degli approcci più comuni nella letteratura, basati su metodi metaeuristici, è stato sviluppato un metodo basato sul gradiente. La possibilità di calcolare tale gradiente esiste grazie a una scelta adeguata del modello idrodinamico. Il metodo di ottimizzazione risultante è stato applicato a un parco di dispositivi a colonna d'acqua oscillante (OWC, *Oscillating Water Column*) con turbina in acqua; per tali dispositivi è stato preliminarmente introdotto un modello dinamico a parametri concentrati. Infine, il problema combinato di ottimizzazione di posizioni e parametri di controllo è stato affrontato con un approccio di tipo gradient flow, introducendo una metodologia di soluzione basata su metodi di Runge-Kutta adattivi.

Ringraziamenti

Questo dottorato è durato tre anni, un tempo sufficiente per incontrare e confrontarsi con un grande numero di persone. Guardando indietro, c'è sempre il rischio di perdersi qualcuno: mi scuso quindi in anticipo per eventuali dimenticanze.

Il primo ringraziamento va ai miei relatori, Edie Miglio e Gabriele Ciaramella, che mi hanno dato l'opportunità di lavorare su questi argomenti, indirizzandomi e aiutandomi anche in momenti in cui non era semplice farlo.

Ringrazio poi i miei tutor in RSE, Stefano Maran, Giordano Agate e Antonella Frigerio, per la disponibilità a trovare un punto di incontro tra questo lavoro di ricerca e le sue possibili applicazioni industriali. Grazie a Matthieu Ancellin per le discussioni e la collaborazione sul codice Capytaine. Grazie a Giuseppe Passoni per avermi introdotto alla fisica delle onde, a Tommaso Vanzan per la collaborazione nel lavoro di ottimizzazione stocastica, ad Andrea Mola per l'aiuto nel comprendere i metodi numerici per onde non lineari e la pazienza, e a Julien Salomon per le discussioni scientifiche e per l'invito alla conferenza a Roscoff, che mi ha aiutato a entrare nell'argomento delle energie rinnovabili marine. Ringrazio Jacopo Gallizioli e Giorgio Travaglini, i due tesisti che ho avuto modo di seguire, per avermi aiutato a chiarire alcuni punti del lavoro.

Grazie a tutti i colleghi del dipartimento che ho conosciuto, e in particolare quelli del Tender, per i momenti belli dentro e fuori dalla Nave e per l'accoglienza. Ringrazio in particolare Enrico per il proficuo lavoro di peer-review interna. Ringrazio inoltre il mio tutor Gabriele Grillo per il supporto e la disponibilità. Grazie alla mia famiglia, a Sara e ai miei amici, per essere stati con me durante questo percorso.

Contents

1 Introduction **1**

I Simulation of wave-body interactions **7**

2 Mathematical modeling of surface wave propagation **9**
2.1 The general nonlinear case 9
2.2 Stokes expansions 17
2.3 Airy wave theory 20
2.3.1 Model formulation 21
2.3.2 Reciprocity and Haskind relation 26
2.4 Wave climates 27

3 Numerical methods **31**
3.1 Boundary element method 31
3.2 Interaction theory 36
3.3 Spectrum discretization 41

4 A preconditioner for linear free-surface BEM **45**
4.1 The coarse-corrected block-Jacobi algorithm 46
4.2 Implementation with $\mathcal{H}$-matrices 49
4.3 Numerical experiments 51

II Optimization of wave energy converter arrays **55**

5 Review of control and optimization strategies **57**
5.1 State of the art 57
5.2 Treatment of constraints 59

6 Robust optimal reactive control of arrays **63**
6.1 Optimization problem 64
6.1.1 Problem statement 64
6.1.2 Well-posedness of the optimization problem 66
6.2 Numerical optimization strategy 70
6.2.1 Penalty method 70

6.2.2 Gradient computation and first-order optimality condition . 71
6.2.3 Sample average approximation 72
6.2.4 Robust stochastic approximation 74
6.2.5 Treatment of stochasticity 75
6.2.6 Implementation and comparison between SAA and robust SA 78
6.3 Numerical results 80
6.3.1 Single-body optimization 80
6.3.2 Two-body optimization 81
6.3.3 Multi-body optimization: devices on two concentric arcs . . 82
6.3.4 Multi-body optimization: 4×4 square arrangement 85
6.3.5 Extension to multiple random parameters 86
6.4 Discussion and developments 90

7 Optimal layout design of arrays 91
7.1 Optimization problem statement 92
7.2 Isolated device 92
7.2.1 Mathematical model 92
7.2.2 Simulation and optimization 103
7.3 Arrays of devices 109
7.3.1 Mathematical model 109
7.3.2 Simulation and optimization 110
7.4 Discussion and developments 120

8 Combined optimization of layout and control parameters 123
8.1 Optimization algorithm 124
8.1.1 Gradient flow 124
8.1.2 Scaling and preconditioning 125
8.1.3 Adaptive time stepping 126
8.2 Modeling of the WEC optimal design problem 130
8.2.1 Cost function and decision variables 130
8.2.2 State problem: dynamic and hydrodynamic equations . . . 131
8.2.3 Inequality constraints 131
8.2.4 Algebraic setting and differentials 134
8.3 Numerical experiments 137
8.4 Discussion and developments 140

9 Conclusions and developments 143

A Power matrices and related results 145

B Results about the domain constraint 149

Bibliography 153

Chapter 1

Introduction

Electricity and heat generation produce the most significant fraction of greenhouse gas (GHG) emissions among human activities: in 2020, they accounted for about 31% of total GHG emissions, and about 42% of CO_2 emissions worldwide [143]. Such emissions contribute to the worsening of climate change, which is causing extreme weather events to become more intense and frequent. In turn, the energy sector is suffering from the effects of these events. On the one hand, climate events disrupt the power grid operation and are directly related to long (more than 8 hours) power outages [43]. On the other hand, energy production itself, notably from renewable sources, is affected. In 2023, a reduction in hydroelectric energy production occurred in different parts of the world, due to droughts and early snowmelt [84]. Wind and solar production may also be affected by climate change [88], with their combined shortage events, called 'dunkelflaute' (literally "dark period without wind"), being especially disruptive and receiving special attention [101]. Since reliance on renewable energy sources is increasing worldwide thanks to the application of emission reduction policies, understanding and mitigating the effects of climate change on them is crucial. A diversification of energy sources is one of the main possible strategies for guaranteeing a reliable supply.

In this context, wave energy is an attractive solution. Waves are mainly generated by the wind, but they can travel very long distances after their generation: hence, waves in a location can provide significant power even when the wind is calm. Indeed, wave energy has been indicated as complementary to wind energy, in that combined installations can provide a more reliable power output, with a reduction in the annual hours of zero production compared to using a single source [87]. Such a combination could also be generally beneficial in terms of structural loads, since wave energy converters may shield wind turbine supports from waves. Aero-hydro-servo studies of small parks of wave energy converters (WEC) combined with wind turbines have recently been performed [29, 183], indicating that the presence of WECs has a small effect on the power output of the wind turbine and a beneficial effect in terms of alleviation of dynamic loads and pitch motion amplitude. However, a possible unfavorable effect in terms of heave motion amplitude is also predicted. A possible advantage of wave energy over wind energy is its density: the wave power flow areal density from locally, wind-generated waves may be as much as five times larger than the power flow

density of the wind above [52]. In other words, wave power is concentrated in a much thinner layer, potentially requiring smaller devices, with reduced environmental and landscape impact [38]. The worldwide wave energy potential has been estimated as about 2 TW, which corresponds to about 17000 TWh/year. About 5% of it has been estimated to be realistically utilizable [74]. The areas with the largest potential are located at latitudes of 40°–60° in both hemispheres, notably on the western coasts of Europe and North America, while enclosed basins, such as the Mediterranean Sea, are less energetic [145]. For comparison, the worldwide electricity consumption in 2022 was about 27000 TWh [84]. Hence, wave energy has the potential of becoming a rather small, but still significant contributor to renewable energy strategies.

Despite its potential, wave energy conversion is still having a very limited use, even though it has been studied for a very long time. The first patent dates back to 1799, and early experiments were carried out throughout the 19th century [133, Chapter 2]. The first part of the 20th century saw the development of the first, small working generators, such as wave-powered navigation buoys [111][1]. Interest grew with the oil crisis in the 1970s, and with the inclusion of wave energy in the renewable energy research and development plan of the European Commission in 1991 [51]. A large amount of theoretical research has been carried out in the last decades, and many prototypes have been tested, with mixed success. This has been due to high experimentation costs and failures caused by severe sea conditions [38]. In recent years, however, interest has been surging, and installations are expected to increase. Indeed, some WEC device concepts have reached a mature stage of development, and institutions have set specific goals for the reduction of the levelized cost of energy from waves [160]. Proposals of the European Commission [2] regard as "realistic and achievable" a target of 1 GW installed capacity by 2030 and of 40 GW by 2050 for ocean energy.[2] Remote islands and offshore plants are considered a natural area of application for wave energy [1]. In addition, many ports are implementing strategies to reduce their carbon footprint by switching to renewable power sources, and wave and tidal energy are being considered among the possible choices [22, 131].

In terms of energy cost, a comparison between fossil fuels, marine energy, and other renewable sources is shown in Figure 1.1. While many sources, such as hydropower and wind, have become competitive with fossil fuel generation in terms of cost, and others, such as solar, have quickly evolved, the cost of marine energy is still significantly greater. One of the reasons for this greater cost is that there is presently no dominating wave energy technology, as opposed to what has happened in the wind energy field, which has mainly settled on horizontal axis turbines. A categorization of wave energy converters is presented in Figure 1.2. In terms of working principle, we distinguish between oscillating water column (OWC) devices, overtopping devices (OTD), and wave-activated bodies (WAB). In an OWC, water oscillates inside a chamber, forced by the external wave motion. Typically, the chamber is connected to the atmosphere through a duct, in which

[1] `https://www.ryokuseisha.com/eng/common-eng/PDF/LargeTypeLightedBuoys.pdf`

[2] This includes, in addition to wave energy, tidal energy, ocean thermal energy conversion, and salinity gradient power generation [3], which are out of the scope of this work. For comparison, the installed wind energy capacity in Europe was 236 GW as of 2021 [4].

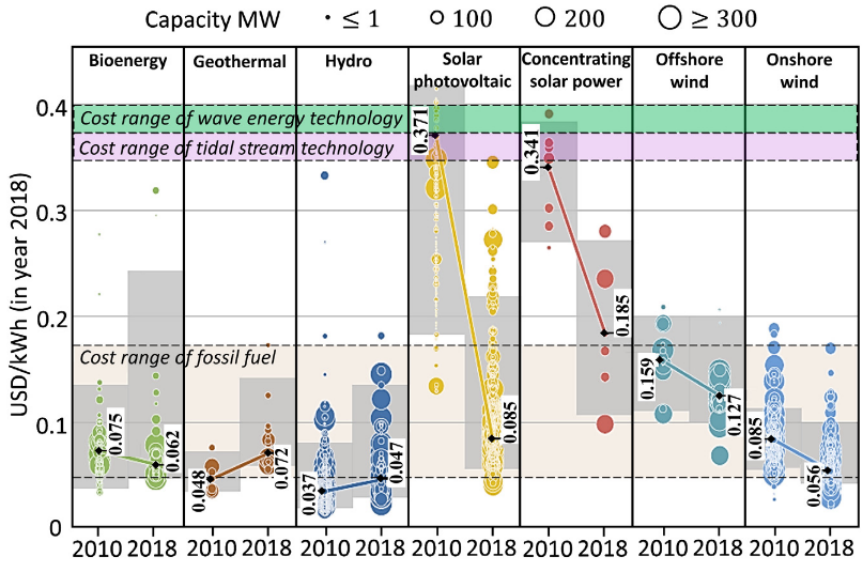

Figure 1.1: *LCOE evolution of different renewable energy sources, compared to fossil fuel and marine energy (adapted from [85]).*

a symmetric air turbine is mounted. The airflow caused by the water column oscillations provides energy to the turbine. In alternative, it is possible to install a water turbine. In an OTD, wave motion causes water to overtop the device's walls and fall into an elevated reservoir. Then, water is released back into the sea through a low-head (e.g., Kaplan) turbine [133, Chapter 8]. Finally, a WAB is a floating body, or a multi-body system, which oscillates under wave forces. This motion drives an electrical generator. The specific implementation details of each technology largely depend on the installation location. In this regard, there is a distinction between onshore devices, that may be mounted on a pier or breakwater, nearshore devices, and offshore devices, the difference between the latter two being mainly due to water depth.

Another explanation for the high cost of wave energy is that single WECs have relatively small production capabilities, and a limited possibility of scaling up compared to other technologies such as wind turbines [15]. For this reason, it is crucial from the economical point of view to install them in arrays. For the sea area to be efficiently utilized, arrays should be quite dense. Hence, devices may need to be installed close together. This implies the appearance of mutual hydrodynamic interactions, which may be unfavorable in terms of power. The result of these interactions is known as the park effect, and it has received considerable interest in the wave energy literature [13].

The necessity of designing large parks of devices requires the adoption of hydrodynamic models which can accurately predict wave loads in different scenarios and capture the park effect, and the development of efficient numerical methods and solvers. The maximization of the power of an array, or the minimization of the cost of energy, can partially be tackled with classical optimization methods, but also require devising strategies for the treatment of complex geometric and

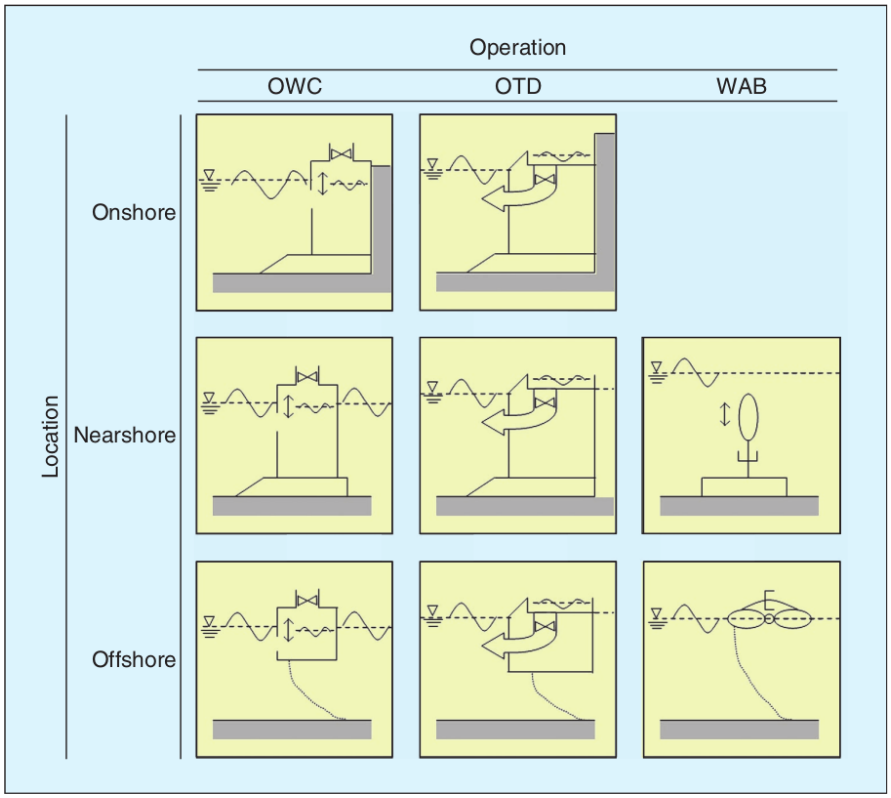

Figure 1.2: *Classification of wave energy converters (from [38]) based on the operating principle and on the installation location.*

operative constraints, such as non-convex admissible domains and constraints on state variables. This thesis aims to provide some novel contributions in the two mentioned fields of numerical methods for hydrodynamic problems and park optimization, and it is accordingly divided into two parts. In Part I, we concentrate on mathematical models and numerical methods. More specifically, in Chapter 2 we review models, and in particular potential wave theory, which is the most commonly used one. In Chapter 3, two numerical methods for the solution of the hydrodynamic problem are reviewed: the boundary element method (BEM) and interaction theory, together with the treatment of irregular waves. In Chapter 4, we present a novel preconditioner for the solution of the wave problem for a large array of floating bodies using the boundary element method. In Part II, we deal with array optimization and control. First, a review of the literature on this topic is provided in Chapter 5. Then, in Chapter 6 we introduce a new numerical framework for the robust optimization of control parameters for an array of WEC of the WAG type, assuming the layout to be fixed. In Chapter 7, we present a work on the complementary problem of optimizing the layout of a park of devices whose control strategy has been fixed. In particular, we consider a park of devices of the water turbine OWC type, which are preliminarily characterized. This activity has been carried out during a curricular internship at the company Ricerca sul Sistema Energetico - RSE S.p.A.[3] Finally, in Chapter 8, we propose a numerical framework for the solution of the combined optimal design problem of park layout and control. Perspectives and ideas for future work on the topic are discussed in Chapter 9.

The original work presented in this thesis has appeared in a conference proceeding, two published articles, and a submitted preprint, listed in the following:

1. G. Ciaramella, M. Gambarini, and E. Miglio. A preconditioner for free-surface hydrodynamics BEM. In *Domain Decomposition Methods in Science and Engineering XXVII*, pages 125–132. Springer Nature Switzerland, 2024. doi:10.1007/978-3-031-50769-4_14;

2. M. Gambarini, G. Ciaramella, E. Miglio, and T. Vanzan. Robust optimization of control parameters for WEC arrays using stochastic methods. *Journal of Computational Physics*, 493:112478, nov 2023. doi:10.1016/j.jcp.2023.112478;

3. M. Gambarini, G. Agate, G. Ciaramella, E. Miglio, and S. Maran. Modeling and optimization for arrays of water turbine OWC devices. *Ocean Engineering*, 312:119132, 2024. doi:https://doi.org/10.1016/j.oceaneng.2024.119132;

4. M. Gambarini, G. Ciaramella, and E. Miglio. A gradient flow approach for combined layout-control design of wave energy parks. 2024. Submitted; arXiv preprint available. doi:10.48550/ARXIV.2409.10200.

[3] https://www.rse-web.it/

Part I

Simulation of wave-body interactions

Chapter 2

Mathematical modeling of surface wave propagation

A complete description of the fluid dynamics of surface wave propagation around an array of wave energy converters would require solving the full Navier-Stokes equations on a time-varying domain. The domain changes in time because of the free surface motion, which is itself unknown. It thus needs to be determined by solving an additional equation, coupled to the Navier-Stokes system, and considering the effect of the atmosphere (i.e., in the simplest possible case, imposing the pressure to be equal to the atmospheric pressure, assumed uniform). The numerical solution of the coupled problem described here would be prohibitive in terms of time and computational resources. For this reason, simpler models, still able to capture the essential physics but much less computationally demanding, have been considered in the literature. The most common model is linear potential flow theory [77], and this is the choice that has been made in this thesis. We mention that some work exists about coupling the Navier-Stokes equations (possibly in their Reynolds-averaged form) with linear potential flow theory for the description of free surface flow [91, 173].

This chapter provides a review of potential wave theory, starting from discussing its assumptions in the nonlinear case, and going through the main steps of its linearization. First, in Section 2.1 the general, nonlinear potential flow model for free surface flow is introduced and its assumptions are discussed, both in the presence and in the absence of interacting objects. Then, in Sec. 2.2, the Stokes expansions for small amplitude waves are introduced. The first order case, known as Airy wave theory, is further detailed in Sec. 2.3, for the case of monochromatic waves. Finally, the general case of irregular, i.e., not monochromatic, waves, is treated in Sec. 2.4, together with a comparison of real wave climates against the limits of validity of the presented models.

2.1 The general nonlinear case

The potential flow model is based on the assumptions of incompressible and irrotational flow, the latter being closely related to the negligibility of viscous effects. It is also possible to derive a linear surface wave theory without the assumption

of irrotational, inviscid flow; this has been presented in [121], and will not be discussed further.

An incompressible flow is one in which density ρ is constant along path lines, i.e., $D\rho/Dt = 0$, where D/Dt is the material (or convective) derivative [95]. Denoting as $\boldsymbol{v}$ the flow velocity, the mass balance law for a generic, compressible flow is

$$\frac{\partial \rho}{\partial t} + \nabla \cdot (\rho \boldsymbol{v}) = 0 \Leftrightarrow \nabla \cdot \boldsymbol{v} = -\frac{1}{\rho}\frac{D\rho}{Dt}. \tag{2.1}$$

A complete dimensional analysis of the contributions to (2.1) is presented in [162, p. 138]. It is found that the right hand side is negligible whenever the following conditions hold:

$$\mathrm{Ma}^2 \ll 1, \quad \frac{gL}{c^2} \ll 1, \quad \frac{L}{cT} \ll 1, \quad \mathrm{Re} \gg 1. \tag{2.2}$$

Here, $\mathrm{Ma} := V/c$ is the Mach number, V is a characteristic velocity, c is the sound speed, g is the gravity field, L is a characteristic length, T a characteristic time, and $\mathrm{Re} := VL/\nu$ is the Reynolds number, ν being the kinematic viscosity. For water in standard conditions, $c \approx 1500$ m/s and $\nu \approx 10^{-6}$ m^2/s [163]. The surface wave propagation and wave-device interaction problems of our interest have various length scales: a single device may have dimensions of the order of a few meters, while entire arrays may range to hundreds of meters, and typical wave heights are of the order of $H \approx 1$–3 m. As a time scale, we consider the wave period, typically in the range $T \approx 5$–10 s. The velocity scale may be chosen as $V = H/T$ (in fact, the maximum velocity amplitude in a linear, monochromatic wave is $\pi H/T$, see [30, Sec. 3.5.1]), so that $V \approx 1$ m/s at most. Hence, $\mathrm{Ma} \sim 10^{-3}$, $gL/(c^2) \sim 10^{-5}$–10^{-3}, $L/(cT) \sim 10^{-4}$–10^{-2}, $\mathrm{Re} \sim 10^6$–10^8. These estimates confirm that the conditions (2.2) hold, and thus (2.1) reduces within good approximation to $\nabla \cdot \boldsymbol{v} = 0$, that is, the velocity field can be considered solenoidal. It should be mentioned that this does not imply that density is uniform: indeed, a common model for free-surface hydrodynamics is the Boussinesq approximation, in which the flow field is considered solenoidal, and yet density differences are taken into account to include buoyancy effects. The reverse implication, that uniform density implies solenoidal flow, is instead true because of (2.1).

Our next assumption is irrotationality. An irrotational flow is one in which vorticity $\boldsymbol{\omega} = \nabla \times \boldsymbol{v}$ is zero. Let us start from the case with no immersed or floating structures and consider Kelvin's theorem, which is valid for incompressible flow with conservative body forces [163, Eq. 14.14]. It describes the convective derivative of the circulation Γ, that is the integral of vorticity over a surface S:

$$\frac{D\Gamma}{Dt} = \int_{\partial S} \left[-\frac{1}{\rho}\nabla p + \nu \Delta \boldsymbol{v} \right] \cdot d\boldsymbol{x}, \quad \Gamma := \int_S \boldsymbol{\omega} \cdot \boldsymbol{n} dS = \int_{\partial S} \boldsymbol{v} \cdot d\boldsymbol{x}, \tag{2.3}$$

where p is the pressure. If the flow is barotropic, i.e., if p is a function of ρ alone (and this happens, among other cases, if ρ is constant, or if the flow is isoentropic), and if viscous effects are negligible, then an element of fluid with zero initial vorticity will always have zero vorticity. The vorticity of a fluid parcel may thus

change if the parcel either traverses a region where viscous effects are important, such as a boundary layer, or is subjected to baroclinic (non-barotropic) effects. Irrotationality is then justified by observing that if wave motion can be considered inviscid and if it is started from rest conditions, the flow shall remain irrotational thereafter, see e.g. [98,163,174]. Wave motion is typically started by the action of the wind, through a resonance mechanism between the air pressure distribution and the free surface oscillations. This process can indeed be explained under the assumption of inviscid, irrotational flow [137]. However, the wind will also exert a shear stress over the free surface, generating a boundary layer, and thus a vortical region, where viscous effects are important. The assumption of irrotational flow can hence be considered valid if waves have propagated far enough from the region in which they were generated by wind effects that viscous phenomena have already decayed, or if boundary layers are negligibly thin; and in both cases, the flow may also be considered inviscid.

The last mentioned requirement, that boundary layers (and also, possibly, shear layers and wakes) be thin, would make the assumption of irrotational, inviscid flow reasonable also in the presence of immersed objects, provided that the incident flow is irrotational. However, this is true only for a few specific cases, such as streamlined objects at low angle of attack and high Reynolds number[1]. Wave energy converters are not streamlined objects in general. For this reason, justifying the irrotationality assumption and, more generally, the adoption of the potential flow model, is more delicate in this case. Chakrabarti [30, Chap. 6] proposed relying on two dimensionless numbers for model choice: the Keulegan-Carpenter number $KC = VT/D$ and the diffraction parameter $\pi D/\lambda$. Here, D is the characteristic dimension of the device (e.g., the diameter for a cylinder), while λ is the wavelength. As already remarked above, we may take $V = \pi H/T$, and thus $KC = \pi H/D$. The Keulegan-Carpenter number measures the ratio of drag forces to inertia (added mass) forces. Drag forces are largely due to viscous effects, with a direct link to vorticity, and thus cannot be computed satisfactorily using potential theory. Inertia forces are instead related to non-dissipative processes, and can be computed under potential flow assumptions (see, e.g., the introductory presentation in [94]). The potential model is thus adequate if KC is small. The diffraction parameter measures the interaction of the immersed object with waves. A small value of $\pi D/\lambda$ means that the object is small compared to the wavelength, so that it produces a negligible perturbation to the wave field. As a consequence, wave forces acting on it can be computed by integration of the undisturbed wave potential, obtaining the so-called Froude-Krylov force. Conversely, when the diffraction parameter is large, the object significantly perturbs the wave field, and diffraction computations considering the presence of the object need to be performed, possibly using a potential flow model. These observations are schematized in Figure 2.1, and in particular the potential flow model is applicable with reasonable accuracy in regions I, II, III, and IV.

Having discussed its assumptions, the potential flow model in the presence of a set of N_b wave energy conversion devices is now derived. Since the curl

[1]Moreover, in such a case, only the lift component of force would be accurately obtained from a potential flow solution.

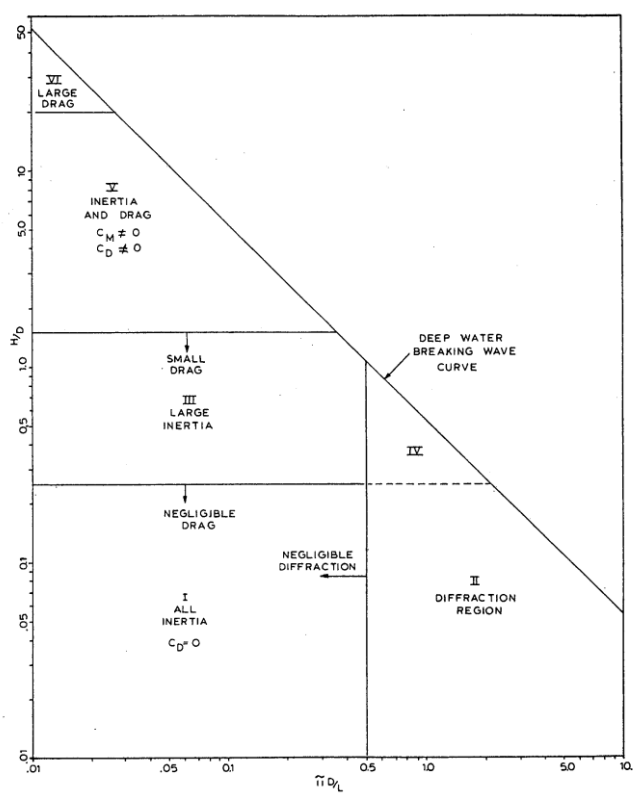

Figure 2.1: *Dominant force contributions for a vertical cylinder [30, Fig. 7.46].*

of the gradient of any regular scalar field is zero, thanks to the assumption of irrotationality one can define a potential ϕ such that the velocity is $\boldsymbol{v} = \nabla\phi$. The assumption of incompressible flow then leads to

$$\nabla \cdot (\nabla\phi) = \Delta\phi = 0, \tag{2.4}$$

which must hold inside the fluid domain Ω (see Fig. 2.2). This is a purely kinematic equation, and indeed, if the domain is fixed and appropriate boundary conditions are imposed, then the flow field can be completely determined without considering the momentum equation. However, in the case of free surface flow, the position of the free surface is not known a priori, and a dynamic equation is needed to close the problem. Moreover, dynamic considerations are required to compute the pressure, whose integration yields the forces on the immersed objects, which in turn determine their motion. We neglect viscous effects, consistently with the discussion reported above about the interplay between viscosity and vorticity. The momentum balance equation is then Euler's equation with volume forces given by the gravity field:

$$\frac{\partial \boldsymbol{v}}{\partial t} + (\boldsymbol{v} \cdot \nabla)\boldsymbol{v} + \frac{1}{\rho}\nabla p = -g\hat{\boldsymbol{z}}, \tag{2.5}$$

where $\hat{\boldsymbol{z}}$ is the unit vector in the positive (upwards) z direction. We now use the vector identity

$$((\nabla \times \boldsymbol{v}) \times \boldsymbol{v}) = (\boldsymbol{v} \cdot \nabla)\boldsymbol{v} - \frac{1}{2}\nabla\|\boldsymbol{v}\|^2, \tag{2.6}$$

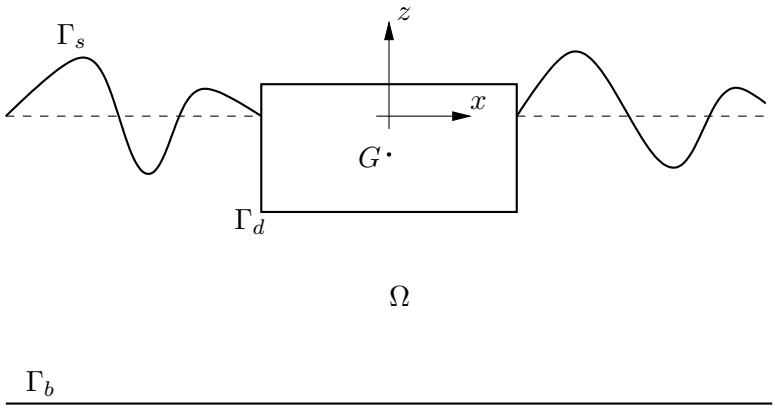

Figure 2.2: *Domain of the hydrodynamic problem. A single device is drawn for clarity.*

whose left hand side is zero in our case because of the assumption of irrotational flow, and the definition of the velocity potential, to write

$$\frac{\partial}{\partial t}\nabla\phi + \frac{1}{2}\nabla\|\nabla\phi\|^2 - \frac{1}{\rho}\nabla p = -\nabla(gz). \tag{2.7}$$

Now, assuming that the potential is a smooth function of space and time, the gradient and the time derivative can be exchanged. Assuming, further, that the density is uniform, we have

$$\nabla\left(\frac{\partial\phi}{\partial t} + \frac{1}{2}\|\nabla\phi\|^2 + \frac{p}{\rho} + gz\right) = 0, \tag{2.8}$$

which means that the quantity inside parentheses is constant in space, and thus equal to a function of time alone:

$$\frac{\partial\phi}{\partial t} + \frac{1}{2}\|\nabla\phi\|^2 + \frac{p}{\rho} + gz = C(t). \tag{2.9}$$

This is the unsteady Bernoulli equation. Constant $C(t)$ may be absorbed into $\partial_t\phi$ or p/ρ since the potential is defined up to an arbitrary constant [163, p. 839], and, in incompressible flow, the same holds for the pressure. The final expression of the unsteady Bernoulli equation is then

$$\frac{\partial\phi}{\partial t} + \frac{1}{2}\|\nabla\phi\|^2 + \frac{p}{\rho} + gz = 0. \tag{2.10}$$

Boundary conditions for the Laplace equation (2.4) are described in the following. Impermeability conditions can be enforced at the wall and free surface boundaries. The bottom is treated as a fixed wall, so that the normal velocity must be zero: $\partial_n\phi = 0$ on Γ_b.

The wetted surfaces of devices, $\Gamma_{d,\ell}$, $\ell = 1, \ldots, N_b$, are instead moving. Here, we consider an impermeable floating device model, limited to rigid heaving motion (vertical translation). This model describes a device of the wave-activated body type. In Sec. 7.2.1 the model of an oscillating water column device will additionally be introduced. Let us call ζ_ℓ the vertical coordinate of the center of mass of the ℓ-th

device with respect to its hydrostatic equilibrium elevation. Then the boundary condition reads $\partial_n \phi = \dot{\zeta}_\ell n_z$ on $\Gamma_{d,\ell}$, where n_z is the vertical component of the normal vector directed outwards from the device and into the domain, and $\Gamma_{d,\ell}$ is a moving boundary. $\zeta_\ell(t)$ is the solution of the dynamic equation for a device, which, taking into account pressure forces, weight force and a control force $F_u(t)$, is

$$m_\ell \ddot{\zeta}_\ell = -\int_{\Gamma_{d,\ell}} p n_z d\Gamma - m_\ell g + F_u(t). \tag{2.11}$$

Here, m_ℓ is the mass of the ℓ-th device. Various possible control strategies, leading to different expressions for $F_u(t)$, will be explored in Chapter 5. In the remainder of this chapter, we consider the so-called reactive control approach [108], corresponding to $F_u(t) = -c_\ell \dot{\zeta}_\ell(t) - \kappa_\ell \zeta_\ell(t)$, where c_ℓ and κ_ℓ are the equivalent damping and stiffness coefficients of ℓ-th device's power take-off mechanism. With this specification, each device behaves as a damped harmonic oscillator:

$$m_\ell \ddot{\zeta}_\ell + c_\ell \dot{\zeta}_\ell + \kappa_\ell \zeta_\ell = -\int_{\Gamma_{d,\ell}} p n_z d\Gamma - m_\ell g. \tag{2.12}$$

This mass-spring-damper model is quite general, in that, in addition to the reactive control force, it also allows to include linearized mooring and viscous loads as additional contributions to the damping and stiffness coefficients.

We now move to the free surface, which is defined by $z = \eta(x, y, t)$, i.e., it is the zero level set of function $F(x, y, z, t) := z - \eta(x, y, t)$. For impermeability to hold, the normal component of the flow velocity at the free surface, $\partial_n \phi$, must coincide with the normal velocity of the surface itself, $\boldsymbol{v}_{fs} \cdot \boldsymbol{n}$. We first observe that at fixed t, due to the orthogonality between the gradient and any level set, the normal vector is $\boldsymbol{n} = \nabla F / \|\nabla F\|$. Let us now consider a point $\boldsymbol{x} = (x, y, z)$ of the free surface: then $F(\boldsymbol{x}, t) = 0$ and, for any infinitesimal interval dt, we must still have $F(\boldsymbol{x} + \boldsymbol{v}_{fs} dt, t + dt) = 0$ [118, Sec. 1.1.2]. Expanding the last expression, we obtain

$$\underbrace{F(\boldsymbol{x}, t)}_{=0} + \nabla F \cdot \boldsymbol{v}_{fs} dt + \frac{\partial F}{\partial t} dt = 0 \quad \forall dt, \tag{2.13}$$

and in particular, substituting the expression of the normal vector,

$$\boldsymbol{v}_{fs} \cdot \boldsymbol{n} = -\frac{1}{\|\nabla F\|} \frac{\partial F}{\partial t}. \tag{2.14}$$

On the other hand,

$$\frac{\partial \phi}{\partial n} = \boldsymbol{n} \cdot \nabla \phi = \frac{\nabla F}{\|\nabla F\|} \cdot \nabla \phi, \tag{2.15}$$

so that, comparing (2.14) with (2.15), we have

$$\nabla F \cdot \nabla \phi = -\frac{\partial F}{\partial t}. \tag{2.16}$$

This is equivalent to $DF/Dt = 0$, which states that a material point on the surface must remain on the surface during its motion. This is physically reasonable,

with the exception of areas where surface currents converge or diverge, leading to downwelling (water descending below the surface) and upwelling (water emerging), respectively.[2] Replacing the definition of F, we finally obtain

$$\frac{\partial \eta}{\partial t} = \frac{\partial \phi}{\partial z} - \frac{\partial \eta}{\partial x}\frac{\partial \phi}{\partial x} - \frac{\partial \eta}{\partial y}\frac{\partial \phi}{\partial y}. \tag{2.17}$$

We will call this equation the kinematic free surface boundary condition.

As mentioned, kinematic considerations are not sufficient for determining the motion of the free surface. An additional condition is obtained by imposing that the pressure at the free surface is equal to the atmospheric pressure, to which we assign the reference value zero.[3] Substituting this requirement in (2.10), we have

$$\frac{\partial \phi}{\partial t} + \frac{1}{2}\|\nabla \phi\|^2 + g\eta = 0. \tag{2.18}$$

Finally, for the problem to be well-posed, an additional condition must be imposed for the behavior of the potential at infinity in the horizontal directions. Some choices will be discussed in the following sections; see also [174, Sect. 12].

The above considerations lead to the system

$$\begin{cases} \Delta \phi = 0 & \text{in } \Omega \\ \dfrac{\partial \phi}{\partial n} = 0 & \text{on } \Gamma_b \\ \dfrac{\partial \phi}{\partial n} = \dot{\zeta}_\ell n_z & \text{on } \Gamma_{d,\ell},\ \ell = 1, \dots, N_b \\ \dfrac{\partial \eta}{\partial t} = \dfrac{\partial \phi}{\partial z} - \dfrac{\partial \eta}{\partial x}\dfrac{\partial \phi}{\partial x} - \dfrac{\partial \eta}{\partial y}\dfrac{\partial \phi}{\partial y} & \text{on } \Gamma_s \\ \dfrac{\partial \phi}{\partial t} + \dfrac{1}{2}\|\nabla \phi\|^2 + g\eta = 0 & \text{on } \Gamma_s \\ \phi \to \phi_\infty & \text{for } x^2 + y^2 \to \infty \\ p = -\rho \dfrac{\partial \phi}{\partial t} - \dfrac{1}{2}\rho \|\nabla \phi\|^2 - \rho g z & \\ m_\ell \ddot{\zeta}_\ell + c_\ell \dot{\zeta}_\ell + \kappa_\ell \zeta_\ell = -\displaystyle\int_{\Gamma_{d,\ell}} p n_z d\Gamma - m_\ell g & \ell = 1, \dots, N_b. \end{cases} \tag{2.19}$$

Energy of a wave field

Since we are interested in wave energy applications, it is important to be able to quantify the energy of a wave field. This can be done through two different quantities: the energy density per unit area E and the energy flux per unit width J. The former is obtained by vertical integration from the bottom to the free

[2] In such cases, either the surface is not represented by a differentiable function, or the velocity field is discontinuous.

[3] This is convenient because, thanks to this choice, forces on partially immersed objects can be computed by integrating only over their wetted surface.

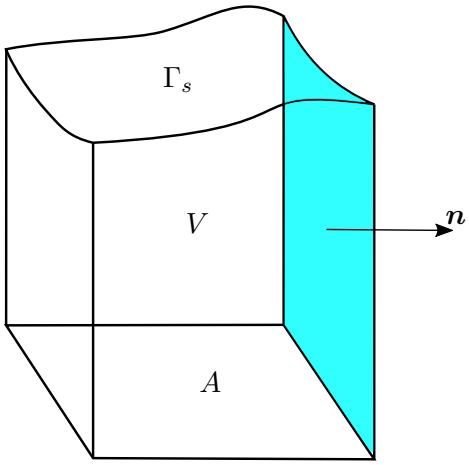

Figure 2.3: *The control volume V used for the computation of the wave energy flux J in the direction $\boldsymbol{n}$, that coincides with the normal to the light blue vertical boundary.*

surface of the total mechanical energy per unit volume, that is the sum of kinetic and potential contributions:

$$E = \rho \int_{-h}^{\eta} \left(\frac{1}{2} \|\nabla\phi\|^2 + gz \right) dz. \tag{2.20}$$

We will instead compute the flux J in the direction of a vector $\boldsymbol{n}$ from a balance of E over a control volume. Let us call V the control volume, bounded by the sea bottom, by fixed vertical immaterial boundaries, and by the moving free surface Γ_s (see Fig. 2.3). The total energy stored in V can be written as an integral on area A, that is its projection on the horizontal plane:

$$\mathcal{E} = \int_A E(x,y) dA. \tag{2.21}$$

The time derivative of (2.21) can be evaluated by means of the Reynolds transport theorem [126, Sec. 6.8]:

$$\begin{aligned} \frac{d\mathcal{E}}{dt} &= \rho \frac{d}{dt} \int_V \left(\frac{1}{2} \|\nabla\phi\|^2 + gz \right) dV \\ &= \rho \int_V \frac{\partial}{\partial t} \left(\frac{1}{2} \|\nabla\phi\|^2 + gz \right) dV + \rho \int_{\partial V} \left(\frac{1}{2} \|\nabla\phi\|^2 + gz \right) \boldsymbol{v}_b \cdot \boldsymbol{n} d\Gamma, \end{aligned} \tag{2.22}$$

where $\boldsymbol{v}_b$ is the velocity of the boundary. In particular, $\boldsymbol{v}_b = 0$ for the bottom and lateral, vertical boundaries, thanks to the definition of the control volume. Hence, the last integral has a non-zero contribution only from the free surface boundary Γ_s. Now, the time derivative of z is zero, and the velocity term can be manipulated as follows:

$$\frac{\partial}{\partial t} \frac{1}{2} \|\nabla\phi\|^2 = \frac{1}{2} \frac{\partial}{\partial t} \left(\frac{\partial\phi}{\partial x_i} \frac{\partial\phi}{\partial x_i} \right) = \frac{\partial}{\partial x_i} \left(\frac{\partial\phi}{\partial t} \frac{\partial\phi}{\partial x_i} \right) - \frac{\partial\phi}{\partial t} \frac{\partial^2\phi}{\partial x_i^2}, \tag{2.23}$$

where the last term is zero since ϕ satisfies the Laplace equation. (2.22) then reduces to

$$\frac{d\mathcal{E}}{dt} = \rho \int_{\partial V} \frac{\partial \phi}{\partial t} \frac{\partial \phi}{\partial n} d\Gamma + \rho \int_{\Gamma_s} \left(\frac{1}{2} \|\nabla \phi\|^2 + gz \right) \boldsymbol{v}_b \cdot \boldsymbol{n} d\Gamma. \tag{2.24}$$

We are interested in the energy flux in the direction $\boldsymbol{n}$, which is the normal to one the lateral walls of V. Per unit width, we thus have

$$J = \int_{-h}^{\eta} \rho \frac{\partial \phi}{\partial t} \frac{\partial \phi}{\partial n} dz. \tag{2.25}$$

The results of this section will be specialized to the case of a linear monochromatic wave in Sec. 2.3.

2.2 Stokes expansions

System (2.19) provides a complete description of the hydrodynamic problem and of the devices' motions. However, both its analytical and numerical solutions present significant difficulties in the most general case, such as the fact that the domain is time-varying. For this reason, a perturbation approach known as Stokes expansions is now presented (see [30, 41, 139, 174]). Its main advantage is the reduction to a sequence of linear problems posed on a time-invariant domain.

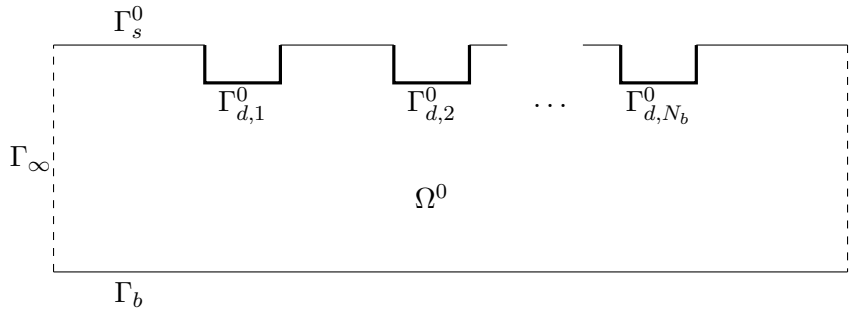

Figure 2.4: *Reference domain of the hydrodynamic problem (slice).*

The derivation starts by shifting boundary conditions on moving boundaries $\Gamma_{d,\ell}$, Γ_s to fixed, reference boundaries $\Gamma_{d,\ell}^0$, Γ_s^0 (see Fig. 2.4) by Taylor series: for a generic function f,

$$\begin{aligned} f(x,y,\eta(x,y,t),t) =& f(x,y,0,t) + \frac{\partial f}{\partial z}(x,y,0,t)\eta(x,y,t) \\ &+ \frac{1}{2}\frac{\partial^2 f}{\partial z^2}(x,y,0,t)\eta^2(x,y,t) + \ldots, \end{aligned} \tag{2.26}$$

and analogously for $\Gamma_{d,\ell}$, with ζ in place of η. The pressure integral on the wetted device surface $\Gamma_{d,\ell}$ must also be computed taking into account that it is a time-varying surface. In particular, considering Fig. 2.5, the pressure integral over $\Gamma_{d,\ell}$

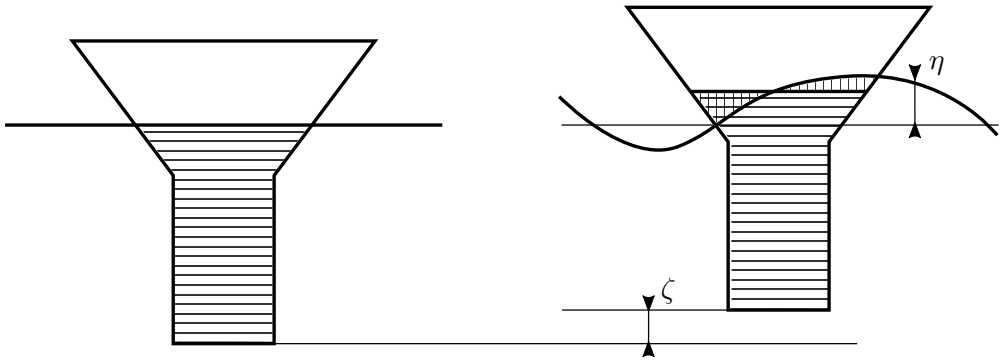

Figure 2.5: *Front view of a device. Left: reference configuration; hatched region:* Γ_d^0. *Right: deformed configuration at time* t*; horizontally hatched region:* $\Gamma_d^0 + \zeta(t)\hat{\boldsymbol{z}}$*, vertically hatched region: domain of integral* $I^*(t)$.

at time t can be decomposed as [64]

$$\int_{\Gamma_{d,\ell}} pn_z d\Gamma = \int_{\Gamma^0_{d,\ell}} p(\boldsymbol{x} + \zeta\hat{\boldsymbol{z}})n_z d\Gamma + \underbrace{\int_{\gamma_w^0} d\gamma \int_{\zeta(t)}^{\eta(x,y,t)} pn_z \frac{dz}{\sqrt{1-n_z^2}}}_{I^*(t)}, \tag{2.27}$$

where γ_w^0 is the equilibrium waterplane area perimeter and $d\gamma dz/\sqrt{1-n_z^2}$ is the area element.[4] The integration bounds in z for $I^*(t)$ reflect the fact that the corresponding area must be added to $\Gamma^0_{d,\ell}$ where $\eta > \zeta$, and removed from $\Gamma^0_{d,\ell}$ otherwise.

The solution is approximated as a power series expansion in a small parameter ϵ, which can be interpreted as the nondimensional wave amplitude scale $\epsilon = kH/2$, where k is the wavenumber. The expansion is performed around a reference equilibrium state characterized by $\phi = 0$, $\ddot{\zeta} = \dot{\zeta} = 0$, $\eta = 0$, and nonzero pressure.

$$\phi = \sum_{n=1}^{\infty} \epsilon^n \phi_n, \quad \zeta = \zeta_0 + \sum_{n=1}^{\infty} \epsilon^n \zeta_n, \quad \eta = \sum_{n=1}^{\infty} \epsilon^n \eta_n, \quad p = \sum_{n=0}^{\infty} \epsilon^n p_n. \tag{2.28}$$

Expansions for potential and free surface elevation start from $n = 1$, because of the definition of the reference state mentioned above. The procedure is then to first shift all boundary conditions to reference surfaces in (2.19), then introduce the expansions (2.28), and finally collect the coefficients of different powers of ϵ. We will consider expansions up to first order, which will be used in the remainder of the thesis, and then provide some short remarks about higher order results and alternative models.

Applying the procedure described above is quite straightforward, but the computation of integrals requires some attention and leads to the definition of a few important quantities, and for that reason it is here reported in detail. First, we report the expansion of the pressure, shifted to the current device surface:

$$p(\boldsymbol{x} + \zeta(t)\hat{\boldsymbol{z}}, t) = -\epsilon\rho \frac{\partial \phi_1}{\partial t}(\boldsymbol{x}, t) - \rho g(z + \epsilon\zeta_1(t)) + o(\epsilon), \tag{2.29}$$

[4]The area element is written without its determinator in [41, 139], which corresponds to assuming that the device's walls are vertical at the waterplane. The denominator is instead considered in [64].

from which we recognize that p_0 is the hydrostatic pressure, $p_0 = -\rho g z$. The first term of the right hand side of (2.27) is then

$$\int_{\Gamma^0_{d,\ell}} p(\boldsymbol{x} + \zeta \hat{\boldsymbol{z}}) n_z d\Gamma = -\epsilon \int_{\Gamma^0_{d,\ell}} \rho \frac{\partial \phi_1}{\partial t} n_z d\Gamma - \rho g \int_{\Gamma^0_{d,\ell}} (z + \epsilon\zeta_1) d\Gamma. \tag{2.30}$$

For its second contribution, which corresponds to hydrodynamic loads, we can add and subtract an integral over the reference waterplane surface Γ^0_w:

$$\int_{\Gamma^0_{d,\ell}} (z + \epsilon\zeta_1) n_z d\Gamma = \int_{\Gamma^0_{d,\ell} \cup \Gamma^0_w} (z + \epsilon\zeta_1) n_z d\Gamma - \int_{\Gamma^0_w} (z + \epsilon\zeta_1) n_z d\Gamma. \tag{2.31}$$

The first integral in the right-hand side can be transformed into a volume integral by a corollary of Gauss' theorem:

$$\int_{\Gamma_{d,\ell} \cup \Gamma^0_w} (z + \epsilon\zeta_1) n_z d\Gamma = \int_{V_0} \frac{\partial}{\partial z} (z + \epsilon\zeta_1) dV = V_0, \tag{2.32}$$

where V_0 is the immersed volume in the reference (hydrostatic) configuration. Since the reference waterplane is an horizontal surface located at $z = 0$ and thus with $n_z = 1$, we have

$$\int_{\Gamma^0_w} (z + \epsilon\zeta_1) n_z d\Gamma = \epsilon A_w \zeta_1, \tag{2.33}$$

so that

$$\int_{\Gamma^0_{d,\ell}} p(\boldsymbol{x} + \zeta \hat{\boldsymbol{z}}) n_z d\Gamma = -\epsilon \int_{\Gamma^0_{d,\ell}} \rho \frac{\partial \phi_1}{\partial t} n_z d\Gamma - \rho g V_0 + \epsilon \rho g A_w \zeta_1. \tag{2.34}$$

Let us now compute the remaining contribution to (2.27). The integral with respect to z is of the form $\int_{a(\epsilon)}^{b(\epsilon)} f(\epsilon, z) dz$. It can be expanded with respect to parameter ϵ:

$$I(\epsilon) = \int_{a(\epsilon)}^{b(\epsilon)} f(\epsilon, z) dz = I(0) + I'(0)\epsilon + o(\epsilon). \tag{2.35}$$

The first order contribution is given by the Leibniz rule:

$$I'(0) = \int_{a(0)}^{b(0)} \frac{\partial f}{\partial \epsilon}(0, z) dz - a'(0) f(0, a(0)) + b'(0) f(0, b(0)) \tag{2.36}$$

Its specialization to our case yields

$$I^*(t) = \int_{\gamma^0_w} \left[\int_{\zeta_0}^{\eta_0} p_0 n_z \frac{dz}{\sqrt{1 - n_z^2}} + (\eta_1 - \zeta_1) p_0(0) \frac{n_z(0)}{\sqrt{1 - n_z^2(0)}} \right] d\gamma + o(\epsilon), \tag{2.37}$$

and this is zero, since in the first integral on the right hand side the integration bounds coincide, and $p_0(0) = 0$. We thus conclude that the vertical component of the force on the device due to the action of the fluid is

$$-\int_{\Gamma_{d,\ell}} p n_z d\Gamma = \epsilon \int_{\Gamma^0_{d,\ell}} \rho \frac{\partial \phi_1}{\partial t} n_z d\Gamma + \rho g V_0 - \epsilon \rho g A_w \zeta_1 + o(\epsilon). \tag{2.38}$$

At order zero, (2.12) reduces to the equilibrium $\kappa\zeta_0 = \rho g V_0 - mg$. At first order, we have a dynamic contribution depending on ϕ_1, and a further hydrostatic contribution proportional to the device's displacement with a negative constant, thus behaving as a restoration force. It is customary to define the hydrostatic stiffness $\kappa_h := \rho g A_w$. Finally, the first order equation of motion can be written as

$$m_\ell \ddot{\zeta}_{\ell,1} + c_\ell \dot{\zeta}_{\ell,1} + (\kappa_\ell + \kappa_{h,\ell})\zeta_{\ell,1} = \rho \int_{\Gamma^0_{d,\ell}} \frac{\partial \phi_1}{\partial t} n_z d\Gamma. \tag{2.39}$$

This equation is coupled to the hydrodynamic problem

$$\begin{cases} \Delta\phi_1 = 0 & \text{in } \Omega^0 \\ \dfrac{\partial \phi_1}{\partial n} = 0 & \text{on } \Gamma_b \\ \dfrac{\partial \phi_1}{\partial n} = \dot{\zeta}_{\ell,1} n_z & \text{on } \Gamma^0_{d,\ell},\ \ell = 1, \dots, N_b \\ \dfrac{\partial \eta_1}{\partial t} = \dfrac{\partial \phi_1}{\partial z} & \text{on } \Gamma^0_s \\ \dfrac{\partial \phi_1}{\partial t} + g\eta_1 = 0 & \text{on } \Gamma^0_s \\ \phi_1 \to \phi_{1,\infty} & \text{for } x^2 + y^2 \to \infty. \end{cases} \tag{2.40}$$

This first order model is commonly referred to as Airy wave theory and it will be further explored in Sec. 2.3.

Higher order expansions still result in Laplace's equation to be solved on the fixed domain Ω^0. In general, the boundary conditions for the problem at a given order are given by combinations of lower order solutions. There have been multiple attempts at defining limits of validity for these models. In [40], a choice is proposed based on the nondimensional error on the dynamic and kinematic boundary conditions. Le Méhauté [116] reports a fairly complete diagram, where the choice is based on wave height H, water depth h and wave period T; it is reproduced in Fig. 2.6. It is acknowledged, however, that the distinction is somewhat arbitrary. In addition to Stokes expansions, it includes the cnoidal wave model, derived for shallow water waves as a power series in the parameter $\epsilon = H/h$. An alternative diagram is introduced by Hedges [83], where crest elevation, total volume flux in the wave direction (zero in the linear case), and matching with experimental data are considered as quality measures.

As a different approach to linearization of the full wave-structure interaction problem, we mention the weak scatterer model [176], in which the free surface boundary condition is expanded around the undisturbed incident wave profile, instead of around the equilibrium free surface. It is valid under the assumption that the presence of a structure produces a small perturbation to the potential field of the ambient waves.

2.3 Airy wave theory

In this section, we discuss some properties of system (2.40) and in particular the possibility of moving to the frequency domain and decoupling the motions of free

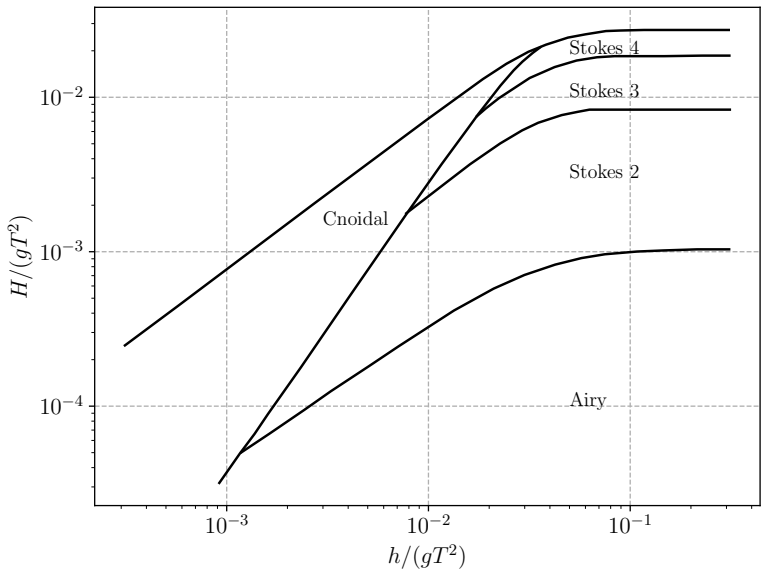

Figure 2.6: *Limits of validity of wave theories proposed by Le Méhauté; reproduced from [116, Fig. 15.7] with conversion to nondimensional units (original diagram in imperial units).*

surface and floating bodies from the hydrodynamic problem. Both possibilities exist thanks to the linearity of the problem. Moreover, in Section 2.3.2, we discuss reciprocity relations, which reveal properties about hydrodynamic interaction matrices, and can save computations in some cases. For convenience, we will drop subscript 1 in the remainder of this thesis. To be more precise and consistent with the expansions (2.28), we mean that we will call simply ϕ the quantity $\epsilon\phi_1$, that is the full first-order contribution to the potential: this is the usual meaning of ϕ in the literature about linear potential flow.

2.3.1 Model formulation

We write the solution as a superposition of time harmonics. Since for progressive waves we expect a space-time dependence of the form $f(kx - \omega t)$, we may write, for a single harmonic component,

$$\phi(\boldsymbol{x}, t) = \mathrm{Re}\left[\hat{\phi}(\boldsymbol{x}) \exp(-i\omega t)\right], \tag{2.41}$$

and similarly for η and ζ. Substitution into (2.40) results in

$$\begin{cases} \Delta\hat{\phi} = 0 & \text{in } \Omega^0 & \text{(2.42a)} \\ \dfrac{\partial\hat{\phi}}{\partial n} = 0 & \text{on } \Gamma_b & \text{(2.42b)} \\ \dfrac{\partial\hat{\phi}}{\partial n} = -i\omega\hat{\zeta}_\ell n_z & \text{on } \Gamma^0_{d,\ell},\ \ell = 1, \ldots, N_b & \text{(2.42c)} \\ -i\omega\hat{\eta} = \dfrac{\partial\hat{\phi}}{\partial z} & \text{on } \Gamma^0_s & \text{(2.42d)} \\ -i\omega\hat{\phi} + g\hat{\eta} = 0 & \text{on } \Gamma^0_s, & \text{(2.42e)} \end{cases}$$

and substitution into (2.39) yields

$$\left[-\omega^2 m_\ell - i\omega c_\ell + (\kappa_\ell + \kappa_{h,\ell})\right] \hat{\zeta}_\ell = \hat{F}_\ell, \quad \hat{F}_\ell = -i\omega\rho \int_{\Gamma^0_{d,\ell}} \hat{\phi} n_z d\Gamma. \tag{2.43}$$

The motion of the free surface can be decoupled from the hydrodynamic problem by eliminating $\hat{\eta}$ in (2.42d) and (2.42e). This leads to the single free surface boundary condition

$$\omega^2 \hat{\phi} - g\frac{\partial \hat{\phi}}{\partial z} = 0, \tag{2.44}$$

which is of the Robin type. The motion of the devices is decoupled by writing the potential as the sum of three contributions:

$$\hat{\phi} = \hat{\phi}_0 + \hat{\phi}_d + \hat{\phi}_r, \tag{2.45}$$

where $\hat{\phi}_0$ is the contribution of ambient waves in the absence of immersed bodies, $\hat{\phi}_d$ is the diffraction contribution due to the presence of bodies, but considering them to be stationary, and $\hat{\phi}_r$ is the radiation contribution, produced by the motion of the bodies in the absence of ambient waves.

The ambient wave potential $\hat{\eta}_0$ can be computed analytically for a monochromatic wave. We consider a harmonic progressive wave of height H propagating in the positive x direction, whose surface elevation is

$$\hat{\eta}_0(x) = \frac{H}{2}\exp(ikx). \tag{2.46}$$

The bottom and free surface boundary conditions need to be enforced. For the free surface, we choose to apply the Dirichlet condition (2.42e), since this choice makes the problem well-posed.[5] Then, substituting (2.46), we obtain

$$\begin{cases} \Delta\hat{\phi}_0 = 0 & \text{in } \Omega^0 \\ \dfrac{\partial\hat{\phi}_0}{\partial n} = 0 & \text{on } \Gamma_b \\ \hat{\phi}_0 = -\dfrac{ig}{\omega}\hat{\eta}_0(x) =: g_D(x) & \text{on } \Gamma^0_s. \end{cases} \tag{2.47}$$

This problem can be solved by separation of variables. We use invariance in the y direction to write $\hat{\phi}_i(x,z) = A(x)B(z)$. Assuming that the bottom is a flat surface at $z = -h$, (2.47) transforms into

$$\begin{cases} \dfrac{A''(x)}{A(x)} = -\dfrac{B''(z)}{B(z)} & \text{in } \mathbb{R}\times(-h,0) \quad (2.48a) \\ A(x) = g_D(x) & (2.48b) \\ B'(-h) = 0 & (2.48c) \\ B(0) = 1. & (2.48d) \end{cases}$$

[5] One could in alternative use the form (2.42d). In this case, the problem would not be well-posed because the solution would not be unique; however, the non-uniqueness only amounts to an additive constant to $\hat{\phi}_0$.

Since (2.48a) must hold for all x and z, quantities on both sides must be everywhere equal to a constant. From (2.48b) and the definition of g_D we recognize that such constant must be $-k^2$. The equation for B can then be written as

$$B''(z) - k^2 B(z) = 0. \tag{2.49}$$

The solution of the problem defined by this equation together with boundary conditions (2.48c) and (2.48d) is

$$B(z) = \frac{\cosh[k(z+h)]}{\cosh(kh)}, \tag{2.50}$$

from which finally

$$\hat{\phi}_0(\boldsymbol{x}) = -\frac{ig}{\omega}\frac{H}{2}\frac{\cosh[k(z+h)]}{\cosh(kh)}\exp(ikx). \tag{2.51}$$

The incident wave potential for waves with a generic direction β can be obtained from this result by a rotation in the horizontal plane, yielding

$$\hat{\phi}_0^{\beta}(\boldsymbol{x}) = -\frac{ig}{\omega}\frac{H}{2}\frac{\cosh[k(z+h)]}{\cosh(kh)}\exp[ik(x\cos\beta + y\sin\beta)]. \tag{2.52}$$

The kinematic boundary condition (2.42d) has not been used to find $\hat{\phi}_0$. It can instead be used to obtain the relationship between the wavenumber and the frequency, that is the dispersion relation. Indeed, substituting the separate variable solution for $\hat{\phi}_0$, it requires

$$-i\omega\hat{\eta} = -\frac{ig}{\omega}\hat{\eta}B'(0), \tag{2.53}$$

where $B'(0)$ can be readily computed, obtaining $B'(0) = k\tanh(kh)$. The dispersion relation is thus

$$\omega^2 = gk\tanh(kh). \tag{2.54}$$

We observe that the phase velocity ω/k is a function of k: linear free surface waves are thus dispersive, meaning that different harmonic components travel at different speeds.

Let us compute the energy density and energy flux of the obtained wave field. Manipulating (2.20), substituting the free surface boundary conditions and averaging over time reveals that for linear waves the mean energy density depends only on the free surface height, and it is

$$E = \rho g \eta_{rms}^2 + \mathcal{O}(H^3), \tag{2.55}$$

where η_{rms} is the root mean square of the free surface elevation. Substituting (2.46) yields the explicit formula for a monochromatic wave:

$$E = \frac{1}{8}\rho g H^2 + \mathcal{O}(H^3). \tag{2.56}$$

For the wave energy flux, substituting (2.51) into (2.25) yields [53, Sec. 4.4]

$$J = \frac{1}{8}\rho g H^2 \frac{\omega}{2k}\left[1 + \frac{2kh}{\sinh(2kh)}\right] + \mathcal{O}(H^3). \tag{2.57}$$

In the deep water (or, equivalently, short wave) limit $kh \to \infty$, the energy flux reduces to

$$J = \frac{1}{16}\frac{\rho g^2 H^2}{\omega} = \frac{1}{32\pi}\rho g^2 H^2 T. \tag{2.58}$$

We now return to the decomposition (2.45) of the potential and discuss the remaining terms. Function $\hat{\phi}_0$ does not satisfy the boundary condition on the surfaces of devices, which the full potential $\hat{\phi}$ must instead do. Recalling (2.42c), we thus have

$$\frac{\partial\hat{\phi}_d}{\partial n} + \frac{\partial\hat{\phi}_r}{\partial n} = -\frac{\partial\hat{\phi}_0}{\partial n} - i\omega\hat{\zeta}_\ell n_z \quad \text{on } \Gamma_{d,\ell}, \quad \ell = 1, \dots, N_b. \tag{2.59}$$

As mentioned above, the radiation contribution is due to the devices' motions, while the diffraction contribution is obtained considering the devices to be fixed. Accordingly, (2.59) is satisfied by the following choice of boundary conditions:

$$\frac{\partial\hat{\phi}_d}{\partial r} = -\frac{\partial\hat{\phi}_0}{\partial n}, \quad \frac{\partial\hat{\phi}_r}{\partial r} = -i\omega\hat{\zeta}_\ell n_z \quad \text{on } \Gamma_{d,\ell}. \tag{2.60}$$

The radiation potential can be further decomposed into the contributions from single devices:

$$\hat{\phi}_r = -i\omega\sum_{\ell=1}^{N_b}\hat{\zeta}_\ell\,\varphi_\ell, \tag{2.61}$$

where each φ_ℓ satisfies a condition of unit velocity amplitude on the surface of the ℓ-th device and an homogeneous condition on all the others.

The diffraction problem is

$$\begin{cases} \Delta\hat{\phi}_d = 0 & \text{in } \Omega^0 \\ \dfrac{\partial\hat{\phi}_d}{\partial n} = 0 & \text{on } \Gamma_b \\ \dfrac{\partial\hat{\phi}_d}{\partial z} - \dfrac{\omega^2}{g}\hat{\phi}_d = 0 & \text{on } \Gamma_s^0 \\ \dfrac{\partial\hat{\phi}_d}{\partial n} = -\dfrac{\partial\hat{\phi}_0}{\partial n} & \text{on } \Gamma_{d,\ell}^0,\ \ell = 1, \dots, N_b, \end{cases} \tag{2.62}$$

while the radiation problem for the ℓ-th device is

$$\begin{cases} \Delta\varphi_\ell = 0 & \text{in } \Omega^0 \\ \dfrac{\partial\varphi_\ell}{\partial n} = 0 & \text{on } \Gamma_b \\ \dfrac{\partial\varphi_\ell}{\partial z} - \dfrac{\omega^2}{g}\varphi_\ell = 0 & \text{on } \Gamma_s^0 \\ \dfrac{\partial\varphi_\ell}{\partial n} = n_z & \text{on } \Gamma_{d,\ell}^0 \\ \dfrac{\partial\varphi_\ell}{\partial n} = 0 & \text{on } \Gamma_{d,m}^0, \quad m = 1, \dots, N_b \wedge m \neq \ell. \end{cases} \tag{2.63}$$

We now observe that boundary value problems (2.62) and (2.63) are still satisfied if a quantity $\phi_0' + \phi_d'$ is added to the solution, where ϕ_0' is an incident wave potential and ϕ_d' is the corresponding diffraction potential [126, Sec. 6.15]. The problems are thus not well posed, since the solution is not unique. This issue is solved by requiring the behavior of the solution for $r = \sqrt{x^2 + y^2}$ to be the one of a purely outgoing wave, ruling out the possibility of an incident wave contribution. The potential should hence be of the form

$$\hat{\phi} \propto A(r) \exp[i(kr - \omega t)] \quad \text{for } r \to \infty, \tag{2.64}$$

where the asymptotic behaviour of function $A(r)$ is determined imposing energy conservation. Indeed, the total energy flux $\mathcal{J}$ across any cylindrical surface of radius r enclosing the bodies and extending through the whole depth must be independent of r. Such quantity can be computed as the integral over a circumference C of the energy flux per unit width J (2.25):

$$\mathcal{J} = \int_C J d\gamma \propto r \frac{\partial \phi}{\partial t} \frac{\partial \phi}{\partial r} \propto r A(r)(A'(r) + kA(r)) = \mathcal{O}(1). \tag{2.65}$$

This yields [126][6]

$$\hat{\phi} \sim r^{-1/2} \exp(ikr). \tag{2.66}$$

An alternative form, which is known as the Sommerfeld radiation condition, is [150, Sec. 5.2]

$$r^{1/2} \left(\frac{\partial \hat{\phi}}{\partial r} - ik\hat{\phi} \right) \to 0 \quad \text{for } r \to \infty. \tag{2.67}$$

In the literature, one may also find the condition as simply $\hat{\phi} \to 0$ [41, Sec. 2.1] or $\partial_r \hat{\phi} \sim ik\hat{\phi}$ [53, Sec. 4.7].

Having discuss hydrodynamics, let us now derive the final form of the dynamic equations describing the devices' motions. The hydrodynamic force on the ℓ-th device is

$$\hat{F}_\ell = \underbrace{-i\omega\rho \int_{\Gamma^0_{d,\ell}} (\hat{\phi}_0 + \hat{\phi}_d) n_z \, d\Gamma}_{\hat{F}_{e,\ell}} - i\omega \sum_{m=1}^{N_b} \hat{\zeta}_m \underbrace{\int_{\Gamma^0_{d,\ell}} \varphi_m n_z \, d\Gamma}_{R_{\ell m}}, \tag{2.68}$$

where $\hat{F}_{e,\ell}$ is the excitation force, due to ambient waves and diffraction, and $R_{\ell m}$ is the radiation impedance. In particular, the contribution to $\hat{F}_{e,\ell}$ due to ϕ_0 is usually called Froude-Krylov force. The radiation impedance can be further split into a term that is in phase with respect to velocity, corresponding to its real part, and one that is out of phase, corresponding to its imaginary part:

$$R_{\ell m} = B_{\ell m} + i\omega A_{\ell m}. \tag{2.69}$$

[6] In [126], a different sign convention is used and thus this equation appears with an opposite sign for the phase. The convention adopted in this thesis is the most common one in the literature.

$A_{\ell m}$ is called added mass and it describes local phenomena, linked to the fact that each device displaces an additional mass of fluid during its motion, thereby increasing its effective inertia. $B_{\ell m}$ is called radiation damping and it is associated with net energy exchange with the environment due to the generation of radiated waves [53, Sec. 5.2.3]. Substituting (2.68) and (2.69) into (2.43) results in the equation of motion

$$\sum_{m=1}^{N_b} Z_{m\ell}\hat{\zeta}_\ell = \hat{F}_\ell, \tag{2.70}$$

where $Z_{\ell m}$ is the generic element of the impedance matrix:

$$Z_{\ell m} = -\omega^2(m_\ell\delta_{\ell m} + A_{\ell m})) - i\omega(c_\ell\delta_{\ell m} + B_{\ell m}) + (\kappa_\ell + \kappa_{h,\ell})\delta_{\ell m}, \tag{2.71}$$

and $\delta_{\ell m}$ is the Kronecker symbol, i.e., the index representation of the identity matrix. The off-diagonal terms of the added mass and radiation damping matrices are the only coupling coefficients between the motions of different devices.

2.3.2 Reciprocity and Haskind relation

Some reciprocity relations satisfied by the linearized hydrodynamic problem, that will be useful in the following, are now mentioned. Reciprocity relations appear in many fields of physics. They are, in a broad sense, symmetry statements, which make it possible to compute an integrated or pointwise quantity related to the solution of a differential problem from the knowledge of the solution of the same problem with a different, and in some sense reciprocal, set of boundary conditions. In some cases, the solution of the reciprocal problem is already known or easily computable, making this approach convenient. An example of reciprocity relation is the Betti-Maxwell theorem of structural mechanics [115, Sec. 5.10]. An extensive review of reciprocity relations for different problems, including the Poisson, Stokes, and Helmholtz equations, is given in [110], highlighting their common origin from Green's second identity.

For the Airy wave problem, reciprocity relations imply that both the added mass matrix A and the radiation damping matrix B (sometimes also called radiation resistance matrix in the literature) are symmetric [126, Sec. 6.17]. Furthermore, the radiation damping matrix B is positive semidefinite, due to energy conservation [53, Sec. 6.5]. There is also the possibility of computing a component of the diffraction force on a body without solving the related diffraction problem, but instead by using the solution of a radiation problem. This is one of the so-called Haskind relations [126, Sec. 6.18], and for our case of an array of devices oscillating in heave it reads

$$\hat{F}^\beta_{e,\ell} = -i\omega\rho \int_{\cup_\ell \Gamma^0_{d,\ell}} \left(\hat{\phi}^\beta_0 \frac{\partial \varphi_\ell}{\partial n} - \varphi_\ell \frac{\partial \hat{\phi}^\beta_0}{\partial n} \right) d\Gamma. \tag{2.72}$$

We have used superscript β to highlight the fact that by using this relation the excitation force can be computed for any wave direction by knowing the radiation potential, which would have been computed anyway in order to form the added mass and radiation matrices, and the incident wave potential, whose analytical

expression is (2.52) and can be directly evaluated. This possibility is leveraged in Sec. 6.2.5.

2.4 Wave climates

The previous sections provided a mathematical description of wave propagation and wave-structure interaction. We now focus on the statistical description of wave trains. This knowledge allows a suitable specification of ambient waves, which in the nonlinear case appear as the farfield limit ϕ_∞ (2.19), and in the linear case as the ambient wave potential $\hat{\phi}_0$ in the boundary data of the diffraction problem (2.62).

As already mentioned, ocean waves are mainly generated by the wind. They can then travel for very long distances, being meanwhile transformed by dispersion, by refraction effects due to variations of the bathymetry [118], and by atmospheric effects. Wave systems that have traveled far from their generation region are referred to as swell waves, while waves generated by the local action of wind are called wind waves. The wave conditions at a specified location may, in general, be a superposition of several wind wave and swell wave systems, and so they can be difficult to predict and widely variable, on time scales ranging from a few wave periods ($\sim 10^2$ s) to years ($\sim 10^8$ s) [52]. For this reason, a statistical approach is adopted. A separation of time scales is possible [12]: it has indeed been observed that the statistical characteristics of the free surface elevation process become stationary after a time of the order of a few minutes, identifying what is usually referred to as an individual sea state, and vary on time scales of the order of hours. It is hence customary to describe the wave conditions at a location as a sequence of sea states. In deep water, a sea state can be characterized with good approximation as Gaussian process, or as a transformation of a Gaussian process [147]. In the following, we adopt the Gaussian hypothesis, recalling that a random process $X(t)$ is Gaussian with mean μ and variance σ^2 if the probability density function of its values through the realizations at any fixed time t is

$$p[X(t)] = \frac{1}{\sqrt{2\pi}\sigma} \exp\left[-\frac{(X(t)-\mu)^2}{2\sigma^2}\right]. \tag{2.73}$$

We will additionally assume ergodicity. A single sea state can be described as a linear superposition of monochromatic waves, with random phase [126]. The energy distribution among the harmonics is expressed in terms of the frequency-directional energy spectrum $\mathcal{S}(f,\beta)$, defined such that the energy per unit area is

$$E = \rho g \int_0^\infty \int_{-\pi}^{\pi} \mathcal{S}(f,\beta) d\beta df. \tag{2.74}$$

In particular, $\rho g \mathcal{S}(f,\beta) d\beta df$ is the energy due to the components with frequency in the interval $[f, f+df]$ and direction in the interval $[\beta, \beta+d\beta]$. The frequency-directional spectrum is often expressed as $\mathcal{S}(f,\beta) = S(f)D(f,\beta)$, where S is the integral of $\mathcal{S}$ with respect to β: then one can also write

$$E = \rho g \int_0^\infty S(f) df. \tag{2.75}$$

Spectra can be computed from wave measurements over time windows of around 20–30 minutes, as detailed in [69, Chap. 10]. Normally, the spectrum is not completely reconstructed, but instead some parameters characterizing it are estimated: the significant wave height H_s, the peak period T_p or the energy period T_e, and the wave direction β. From this data, which is typically recorded as a time series at hourly or half-hourly intervals, the form of the spectrum can be approximately reconstructed by resorting to parametric expressions, some of which will be presented shortly. Furthermore, from the time series of spectrum parameters it is possible to construct a histogram, describing the fraction of time, over a year, for which a certain wave condition has been observed (which can thus be considered an estimation of the probability distribution function of sea states). Such histogram is called scatter diagram of wave statistics [15] or resource characterization matrix [24] in the wave energy literature.

We now discuss parameters H_s, T_p, T_e, and report some specific parametric forms of the energy spectrum. The significant wave height H_s is defined as the mean height of the third of highest waves [69]. Under the assumption that wave heights follow a Rayleigh distribution, this can be approximately computed as $H_s = 4\eta_{rms}$. Comparison with (2.55) reveals that the energy density depends only on H_s:

$$E = \frac{\rho g}{16} H_s^2. \tag{2.76}$$

The peak period T_p is the period corresponding to the maximum value of $S(f)$. The energy period T_e is instead defined as [53, Sec. 4.5.1]

$$T_e = \frac{\int_0^\infty S(f) f^{-1} df}{\int_0^\infty S(f) df}. \tag{2.77}$$

This apparently obscure definition is motivated by the fact that the energy flux can then be written, in the deep water limit, as

$$J = \frac{\rho g^2}{64\pi} T_e H_s^2. \tag{2.78}$$

At least in this limit, the pair (H_s, T_e) fixes unambiguously the values of energy density E and energy flux J. This is not true if the pair (H_s, T_p) is considered, as discussed in [73].

The shape of the energy spectrum $\mathcal{S}(f, \beta)$ can in part be motivated by general physical arguments. Its frequency part $S(f)$ displays a universal asymptotic behavior for $f \to \infty$ in fully developed wind sea. This is the situation in which the wind has blown for a sufficient time over a region of sufficient length (such length being called fetch). In this condition, sharp crests have been observed to appear, corresponding to jump discontinuities in the derivatives of η. This implies that $S(f) \sim f^{-5}$ for $\omega \to \infty$ [138]. Moreover, the directional spreading described by $D(f, \beta)$ is in general larger for short waves than for longer waves.

In this thesis, we will consider the Pierson–Moskowitz spectrum [53]

$$S(f) = \gamma_1 f^{-5} \exp\left(-\gamma_2 f^{-4}\right), \quad \text{with} \quad \gamma_1 = \frac{\gamma_2 H_s^2}{4}, \quad \gamma_2 = \frac{5}{4} f_p^4, \tag{2.79}$$

which displays the mentioned asymptotic behavior. Here, f_p is the peak frequency, $f_p = 1/T_p$. An alternative choice for the case in which waves are not fully developed is the JONSWAP spectrum [69]. For the directional dependence, we will use the simplifying assumption that $D(f, \beta) \approx D(\beta)$ and consider Donelan's spreading function [68]:

$$D(\beta) = \frac{1}{2} k_\beta (\mathrm{sech}[k_\beta(\beta - \beta_0)])^2, \tag{2.80}$$

where β_0 is the dominant direction and k_β is a scale parameter: for increasing k_β, the distribution is more sharply peaked. The two functions are represented in Fig. 2.7.

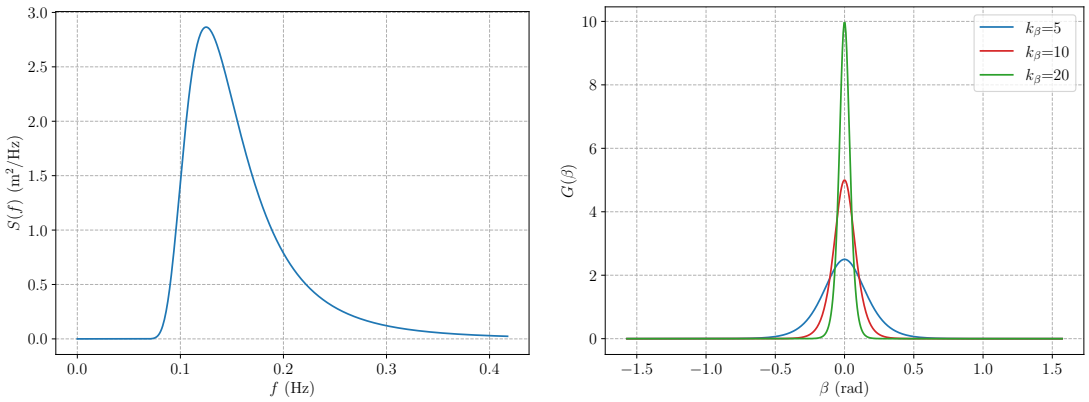

Figure 2.7: *Pierson-Moskowitz spectrum function* (2.79) *for* $H_s = 2$ *m,* $T_p = 8$ *s (left); Donelan spreading function* (2.80) *for different values of* k_β *(right).*

To provide an intuitive picture of the wave spectrum at a specific location, we consider the data recorded at Lampedusa.[7] Scatter plots derived from the annual records of significant wave height and peak period are superimposed on the diagrams of Chakrabarti (see Fig. 2.8), Le Méhauté, and Hedges (see Fig. 2.9). The diagrams are defined in terms of monochromatic waves, while wave climate data is in terms of irregular waves. A detailed description of the representation of irregular waves in terms of monochromatic waves will be provided in Sec. 3.3. For simplicity, since the aim here is to give preliminary, order of magnitude indications (indeed the diagrams are in logarithmic scale), we take $H \sim H_s$. Figure 2.8, drawn for two characteristic sizes that are consistent with wave energy converters, suggests that the potential flow model may be adequate, since quantity H/D is not large enough for drag effects to be relevant (we refer to the discussion in Sec. 2.2). Figure 2.9 suggests that the wave climate for Lampedusa is consistent with the 2nd order Stokes model according to the Méhauté diagram, while the Hedges diagram predicts that the Airy model could be accurate enough. The considered wave climate is representative of the most energetic locations in the Mediterranean Sea, which will be the typical conditions considered in this thesis.

Wave conditions in oceans are generally more energetic than in the Mediterranean Sea. It is then reasonable to expect the validity of a linear model to be questionable in the former case. The accuracy of the linear model has been studied

[7] G. Passoni, personal communication.

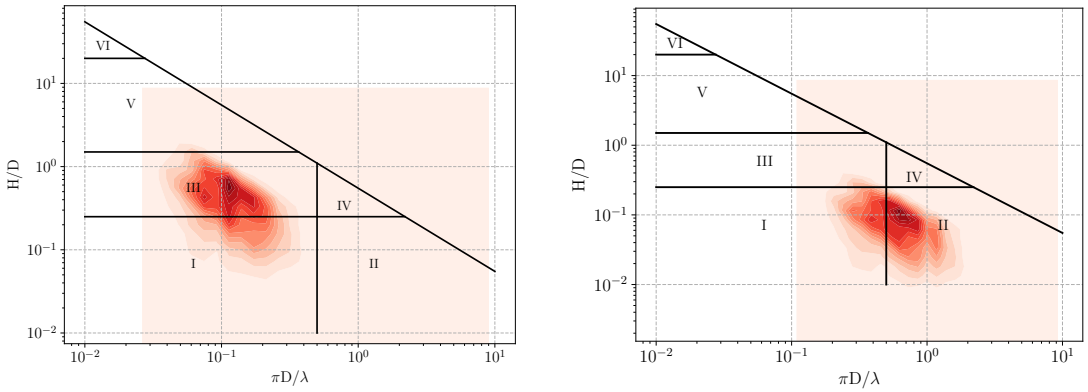

Figure 2.8: *Wave climate of Lampedusa superimposed on the Chakrabarti diagram for a body of characteristic size 2 m (left) and 10 m (right).*

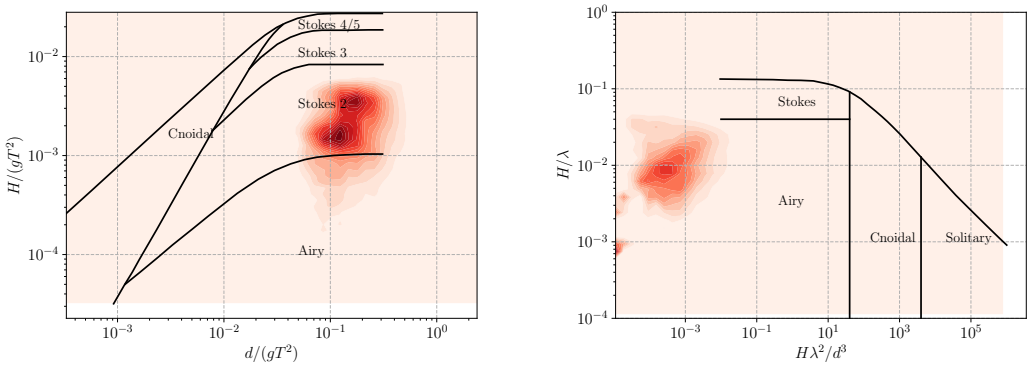

Figure 2.9: *Wave climate of Lampedusa superimposed on the Méhauté diagram (left) and on the Hedges diagram (right).*

in [49], concluding that despite its simplicity and its increasing error for increasing wave height, it can be useful for design purposes. Moreover, the accuracy of the result strongly depends on the control strategy: in particular, higher values of control damping lead to smaller errors. In [66], an error analysis for the nonlinear computation of Froude-Krylov forces for WECs is presented. It is shown that a way to obtain good approximations for the pressure near the surface, and thus for the force, is by applying the Wheeler transformation to the Airy wave solution. This amounts to remapping the vertical coordinate from $[-h, 0]$ to $[-h, \eta]$. Such a transformation is also known in numerical hydrodynamics as the sigma transform (in that case, it is used for a more convenient treatment of the free surface in full 3D models).

Chapter 3

Numerical methods

This chapter presents two different approaches, both used in this thesis, for the solution of the fluid-structure interaction problem introduced in Chapter 2. In Section 3.1 we describe the boundary element method, which is a very versatile solution approach for elliptic problems, and can be applied to both the fully nonlinear problem (2.19) and the linearized problem (2.42). In Section 3.2 we present interaction theory, which is suited for linear problems of the form (2.42), and has many advantages compared to BEM, both in terms of computational efficiency and of applicability to the optimization problems of our interest. Finally, in Section 3.3, the discretization of wave spectra is treated.

3.1 Boundary element method

The boundary element method (BEM) is based on two concepts: the possibility of writing the solution of the Laplace equation as a combination of fundamental solutions (Green functions) and the boundary integral formulation of the problem. Its main advantage over other techniques such as the finite element method is that the number of unknowns can be greatly reduced, since the problem is formulated as an integral equation over the boundary (or even just a subset of the boundary) instead of over the entire domain. Moreover, problems over unbounded domains can be treated naturally. On the other hand, the discrete problem involves a dense matrix instead of a sparse one, and its assembly can be quite computationally expensive because it involves the evaluation of singular integrals. We refer to [25] for a presentation focused on physical meaning and applications, and to [151] for detailed proofs. The basic idea of superimposing fundamental solutions to solve Laplace problems is described extensively in [89], and it is a very common approach in aerodynamics.

Let us consider the Laplace equation $\Delta\phi = 0$ on a bounded domain Ω, with boundary $\Gamma = \partial\Omega$ and normal vector pointing towards the interior, consistently with the convention introduced in section 2.1. Boundary conditions will be specified later. It will also be convenient to define the corresponding exterior domain $\Omega_e := \mathbb{R}^3 \setminus (\Omega \cup \Gamma)$, and we will require $\Delta\phi = 0$ on Ω_e. This is an auxiliary, non-physical problem. Let us call $G(\boldsymbol{x}; \boldsymbol{y})$ the free-space Green function, defined

as the distributional solution of

$$\Delta G(\boldsymbol{x};\boldsymbol{y}) = \delta_{\boldsymbol{y}} \quad \text{in } \mathbb{R}^3, \quad G \to 0 \quad \text{for } \|\boldsymbol{x}-\boldsymbol{y}\| \to \infty, \tag{3.1}$$

where $\delta_{\boldsymbol{y}}$ is the Dirac delta distribution centered in $\boldsymbol{y}$. The solution is [148, Sec. 7.2.2]

$$G(\boldsymbol{x};\boldsymbol{y}) = \frac{1}{4\pi\|\boldsymbol{x}-\boldsymbol{y}\|}. \tag{3.2}$$

In the following, we will call $\boldsymbol{y}$ source point and $\boldsymbol{x}$ field point, in agreement with the nomenclature introduced in [25, Sec. 2.2].

The Green function forms part of a representation of the potential ϕ in the entirety of $\mathbb{R}^3 \setminus \Gamma$ as an integral over Γ, where Dirichlet and Neumann data for both the interior and exterior problems are involved:

$$\phi(\boldsymbol{x}) = \int_\Gamma \left(\left[\!\left[\frac{\partial \phi}{\partial n} \right]\!\right] G(\boldsymbol{x};\boldsymbol{y}) - [\![\phi]\!] \, \nabla_{\boldsymbol{y}} G \cdot \boldsymbol{n} \right) d\Gamma_{\boldsymbol{y}}, \quad \boldsymbol{x} \in \mathbb{R}^3 \setminus \Gamma. \tag{3.3}$$

This is often called the third Green's formula [41, Sec. 2.2]. Here, $[\![v]\!]$ is the jump between external and internal values; more precisely, $[\![v]\!] = v^+ - v^-$, where v^+ is the trace of v from Ω_e and v^- is the trace of v from Ω. The proof of this result is not trivial because of the limited regularity of G; it is presented in [151, Th. 3.1.6]. Starting from (3.3), two different approaches can be adopted: the direct method and the indirect method.

The direct method is based on choosing the potential to be identically zero in Ω_e, and derives its name from the fact that no additional quantities other than ϕ need to be defined. This choice implies setting both the Dirichlet and the Neumann data of the external problem to zero. Substituting this condition in (3.3) and taking the trace on Γ from inside Ω yields

$$\frac{1}{2}\phi(\boldsymbol{x}) = \int_\Gamma \left[-\frac{\partial \phi}{\partial n}(\boldsymbol{y}) G(\boldsymbol{x};\boldsymbol{y}) + \phi(\boldsymbol{y}) \nabla_{\boldsymbol{y}} G \cdot \boldsymbol{n} \right] d\Gamma_{\boldsymbol{y}}, \quad \boldsymbol{x} \in \Gamma. \tag{3.4}$$

If a Dirichlet condition $\phi = g_D$ is imposed on $\Gamma_D \subset \Gamma$ and a Neumann condition $\partial_n \phi = g_N$ is imposed on $\Gamma_N = \Gamma \setminus \Gamma_D$, then, separating known and unknown terms, we have

$$\begin{aligned} &\frac{1}{2}\chi_{\Gamma_N}(\boldsymbol{x})\phi(\boldsymbol{x}) + \int_{\Gamma_D} \frac{\partial \phi}{\partial n}(\boldsymbol{y}) G(\boldsymbol{x};\boldsymbol{y}) d\Gamma_{\boldsymbol{y}} - \int_{\Gamma_N} \phi(\boldsymbol{y}) \nabla_{\boldsymbol{y}} G \cdot \boldsymbol{n} d\Gamma_{\boldsymbol{y}} \\ &= -\frac{1}{2}\chi_{\Gamma_D}(\boldsymbol{x}) g_D(\boldsymbol{x}) - \int_{\Gamma_D} g_D(\boldsymbol{y}) G(\boldsymbol{x};\boldsymbol{y}) d\Gamma_{\boldsymbol{y}} + \int_{\Gamma_N} g_N(\boldsymbol{y}) \nabla_{\boldsymbol{y}} G \cdot \boldsymbol{n} d\Gamma_{\boldsymbol{y}}, \end{aligned} \tag{3.5}$$

where χ_{Γ_i} is the indicator function of Γ_i. The unknowns are the values of ϕ on Γ_N and $\partial_n \phi$ on Γ_D. The problem is then discretized, obtaining a linear system with a block structure. Once the solution has been found, the potential in any point of the domain can be computed by using (3.3). The direct method has been used as a building block for the non-linear hydrodynamic solvers introduced in [67, 123] and in [104].

The indirect method introduces as an additional unknown the value of one of the boundary data jumps in (3.3), and sets the other one to zero. It is also possible

to take a combination of both, but this choice will not be further discussed here. Taking as the auxiliary unknown σ the jump of Neumann data, $\sigma := [\![\partial_n \phi]\!]$, leads to

$$\phi(\boldsymbol{x}) = \int_\Gamma \sigma(\boldsymbol{y}) G(\boldsymbol{x};\boldsymbol{y}) d\Gamma_{\boldsymbol{y}}, \quad \boldsymbol{x} \in \Omega. \tag{3.6}$$

Since $\partial_n \phi$ is the normal velocity, its jump being non-zero corresponds to a net generation of mass at the boundary. σ is accordingly referred to as a source distribution; and indeed, $G(\boldsymbol{x};\boldsymbol{y})$ is the field of a point source located in $\boldsymbol{y}$, so the solution is sought in the form of a superposition of elementary sources. Conversely, taking as auxiliary variable $[\![\phi]\!]$ would correspond to writing the solution as a superposition of doublets. A doublet is formed by two sources of equal magnitude and opposite sign, in the limits of vanishing reciprocal distance and magnitude going to infinity. In the following, we will consider the case of a source distribution. Boundary conditions are enforced by taking appropriate traces of (3.6). After discretization, they lead to a system of equations that needs to be solved to determine σ. The indirect method is implemented in the linear hydrodynamics open source code Capytaine [7, 41], which has been extensively used in this work. For this reason, we now provide more details on the treatment of boundary conditions and the discretization.

We start by noticing that both the diffraction problem (2.62) and the radiation problem (2.63) can be cast in the common form

$$\begin{cases} \Delta\phi = 0 & \text{in } \Omega & \text{(3.7a)} \\ \dfrac{\partial \phi}{\partial n} = 0 & \text{in } \Gamma_{N0} & \text{(3.7b)} \\ \dfrac{\partial \phi}{\partial n} + \alpha\phi = 0 & \text{on } \Gamma_R & \text{(3.7c)} \\ \dfrac{\partial \phi}{\partial n} = g_N & \text{on } \Gamma_N, & \text{(3.7d)} \end{cases}$$

where, referring to Fig. 2.4, $\Omega = \Omega^0$, the homogeneous Neumann boundary is $\Gamma_{N0} = \Gamma_b$, the Robin boundary is $\Gamma_R = \Gamma_s^0 \cup \Gamma_\infty$, the radiation condition being expressed in the equivalent form (2.67), and the non-homogeneous Neumann boundary is $\Gamma_N = \cup_{\ell=1}^{N_b} \Gamma_{d,\ell}^0$. The normal trace of (3.6) is given by [151, Th. 3.3.15]:

$$\frac{\partial \phi}{\partial n}(\boldsymbol{x}) = \frac{1}{2}\sigma(\boldsymbol{x}) + \int_\Gamma \sigma(\boldsymbol{y}) \nabla_{\boldsymbol{x}} G \cdot \boldsymbol{n} d\Gamma_{\boldsymbol{y}}, \quad \boldsymbol{x} \in \Gamma. \tag{3.8}$$

Since a potential of the form (3.6) satisfies (3.7a) for any choice of the source distribution σ, only the boundary conditions need to be explicitly enforced:

$$\frac{1}{2}\sigma(\boldsymbol{x}) + \int_\Gamma \sigma(\boldsymbol{y}) \nabla_{\boldsymbol{x}} G \cdot \boldsymbol{n} d\Gamma_{\boldsymbol{y}} = 0 \quad \boldsymbol{x} \in \Gamma_{N0}, \tag{3.9}$$

$$\frac{1}{2}\sigma(\boldsymbol{x}) + \int_\Gamma \sigma(\boldsymbol{y}) (\nabla_{\boldsymbol{x}} G \cdot \boldsymbol{n} + \alpha G(\boldsymbol{x},\boldsymbol{y})) d\Gamma_{\boldsymbol{y}} = 0 \quad \boldsymbol{x} \in \Gamma_R, \tag{3.10}$$

$$\frac{1}{2}\sigma(\boldsymbol{x}) + \int_\Gamma \sigma(\boldsymbol{y}) \nabla_{\boldsymbol{x}} G \cdot \boldsymbol{n} d\Gamma_{\boldsymbol{y}} = g_N \quad \boldsymbol{x} \in \Gamma_N(\boldsymbol{x}). \tag{3.11}$$

If, moreover, it is possible to define a modified Green function $\mathcal{G}(\boldsymbol{x};\boldsymbol{y})$ satisfying

$$\begin{cases} \Delta\mathcal{G}(\boldsymbol{x},\boldsymbol{y}) = \delta_{\boldsymbol{y}} & \boldsymbol{x}\in\Omega \\ \nabla_{\boldsymbol{x}}\mathcal{G}\cdot\boldsymbol{n} = 0 & \boldsymbol{x}\in\Gamma_{N0} \\ \nabla_{\boldsymbol{x}}\mathcal{G}\cdot\boldsymbol{n} + \alpha\mathcal{G}(\boldsymbol{x},\boldsymbol{y}) = 0 & \boldsymbol{x}\in\Gamma_R \end{cases} \tag{3.12}$$

for any source point $\boldsymbol{y}$, then conditions (3.9), (3.10) are satisfied by setting $\sigma = 0$ on $\Gamma_{N0}\cup\Gamma_R$, and the problem reduces to

$$\frac{1}{2}\sigma(\boldsymbol{x}) + \int_{\Gamma_N}\sigma(\boldsymbol{y})\nabla_{\boldsymbol{x}}\mathcal{G}\cdot\boldsymbol{n}d\Gamma_{\boldsymbol{y}} = g_N(\boldsymbol{x}), \quad \boldsymbol{x}\in\Gamma_N. \tag{3.13}$$

Thus, the only set on which σ needs to be determined is Γ_N; once it has been found, the potential in any point of the domain can be computed using (3.6). The analytical derivation of a modified Green function compatible with (3.12) is detailed in [42].

Equation (3.13) must in principle hold for every field point $\boldsymbol{x}\in\Gamma_N$. To obtain a numerically tractable problem, one must move to a finite-dimensional system of equations. The first step is to discretize Γ_N into a mesh, whose elements $\mathcal{K}_i$, $i = 1,\dots,N_p$ are typically called panels in the context of BEM. It is possible to use either curved panels [151, Sec. 4.1.2], or panels with planar shapes such as quadrilaterals or triangles [67]; in the latter case, an approximation of Γ_N is obtained, while in the former case the exact geometry is retained. The next step is to approximate the source distribution as a finite linear combination of trial functions $\psi_j(\boldsymbol{x})$:

$$\sigma_h(\boldsymbol{x}) = \sum_{j=1}^{N}\sigma_j\psi_j(\boldsymbol{x}). \tag{3.14}$$

The trial functions are typically taken to be piecewise polynomials supported on a patch of panels. Then, two possible approaches can be adopted. The first is to require condition (3.13) to hold only at a finite set of field points $\boldsymbol{x}_i$, $i = 1,\dots,N$, and it is called collocation method. It results in the algebraic system

$$\frac{1}{2}\sum_{j=1}^{N}\sigma_j\psi_j(\boldsymbol{x}_i) + \sum_{j=1}^{N}\sigma_j\underbrace{\int_{\Gamma_N}\psi_j(\boldsymbol{y})\nabla_{\boldsymbol{x}}\mathcal{G}(\boldsymbol{x}_i;\boldsymbol{y})\cdot\boldsymbol{n}d\Gamma_{\boldsymbol{y}}}_{=:V_{ij}} = g_N(\boldsymbol{x}_i), \quad i = 1,\dots,N. \tag{3.15}$$

If the collocation points are chosen such that $\psi_j(\boldsymbol{x}_i) = \delta_{ij}$, then the system can be written as

$$\left(\frac{1}{2}I + V\right)\boldsymbol{\sigma} = \boldsymbol{g}_N. \tag{3.16}$$

The second, which is the Galerkin method, requires to first derive a weak formu-

lation of (3.13):

$$\begin{aligned} &\text{Given } g_N \in H^{-1/2}(\Gamma_N), \text{ find } \sigma \in H^{-1/2}(\Gamma_N) \text{ such that} \\ &\frac{1}{2}(\sigma,\eta)_{L^2(\Gamma_N)} + b(\sigma,\eta) = (g_N,\eta)_{L^2(\Gamma_N)} \quad \forall \eta \in H^{-1/2}(\Gamma_N), \\ &\text{with} \quad b(\sigma,\eta) := \int_{\Gamma_N} \left(\int_{\Gamma_N} \sigma(\boldsymbol{y}) \nabla_{\boldsymbol{x}} \mathcal{G} \cdot \boldsymbol{n} d\Gamma_{\boldsymbol{y}} \right) \eta(\boldsymbol{x}) d\Gamma_{\boldsymbol{x}}, \end{aligned} \tag{3.17}$$

and then to consider a finite dimensional set of test functions $V_h = \text{span}\{\eta_1, \ldots, \eta_N\} \subset H^{-1/2}(\Gamma_N)$ to obtain the discrete weak formulation

$$\frac{1}{2}\sum_{j=1}^{N} \sigma_j (\psi_j, \eta_i)_{L^2(\Gamma_N)} + \sum_{j=1}^{N} \sigma_j b(\psi_j, \eta_i) = (g_N, \eta_i)_{L^2(\Gamma_N)}, \quad i = 1, \ldots, N, \tag{3.18}$$

which can be expressed as

$$\left(\frac{1}{2}M + B\right)\boldsymbol{\sigma} = \boldsymbol{f}. \tag{3.19}$$

Both matrices V and B are in general dense, because while the trial and test functions may be chosen to be compactly supported, the Green function is not. V_{ij} is the contribution to $\partial_n \phi$ evaluated at $(\boldsymbol{x}_i)$ and produced by a source distribution ψ_j. B_{ij} is the weighted average over the support of η_i of the contribution to $\partial_n \phi$ due to the source distribution ψ_j, weighted by η_i. Assembling B requires significantly more computation effort than assembling V, since double integrals need to be computed; for this reason, the collocation approach is currently the most frequently considered for engineering applications. This is also the choice behind Capytaine [6], where in particular quadrilateral panels are considered, each basis function ψ_j is constant on the j-th panel and zero elsewhere, and collocation points are the panels' centers. For convenience, we outline the solution procedure for this particular choice: first, $\boldsymbol{\sigma}$ is found by solving

$$\underbrace{\left(\frac{1}{2}I + V\right)}_{K}\boldsymbol{\sigma} = \boldsymbol{g}_N, \quad V_{ij} = \int_{\mathcal{K}_j} \nabla_{\boldsymbol{x}} \mathcal{G}(\boldsymbol{x}_i; \boldsymbol{y}) \cdot \boldsymbol{n} d\Gamma_{\boldsymbol{y}}. \tag{3.20}$$

Then, the potential at collocation points $\phi_i = \phi(\boldsymbol{x}_i)$ is computed using a discretization of (3.6):

$$\boldsymbol{\phi} = S\boldsymbol{\sigma}, \quad S_{ij} = \int_{\mathcal{K}_j} \mathcal{G}(\boldsymbol{x}_i; \boldsymbol{y}) d\Gamma_{\boldsymbol{y}}. \tag{3.21}$$

A preconditioner for problem (3.20) will be presented in Chapter 4, while Capytaine will be used to compute hydrodynamic quantities for the work described in Chapter 6.

3.2 Interaction theory

Interaction theory is a modeling framework specifically devised for arrays of floating objects. It is built on the idea of using a characterization of the response of each object to incoming waves in isolated conditions, encoded in a so-called diffraction transfer matrix B_ℓ expressed in the local coordinate system of the ℓ-th object. Hydrodynamic coupling between different objects is described through a coordinate transformation matrix $T_{\ell m}$ which allows expressing the wave field emitted by the ℓ-th object in the coordinate system of the m-th object. B_ℓ depends on the object's geometry, but not on its position; conversely, $T_{\ell m}$ depends on positions of the ℓ-th and m-th objects, but not on their geometries. This separation makes the solution of the hydrodynamic problem for large arrays of identical objects very efficient, since matrix B needs to be computed just once and each matrix T is sparse. For the same reason, different spatial configurations involving the same objects can be treated efficiently, too. The method was first introduced in [86] for the diffraction problem and subsequently extended to the combined diffraction-radiation problem for the case of cylindrical objects in [31, 32, 180], to which we refer for the complete derivation of the results reported in the following. A very similar approach is used in the acoustics community to solve the Helmholtz equation; it is known as the equivalent source formulation or source simulation technique [117, 128].

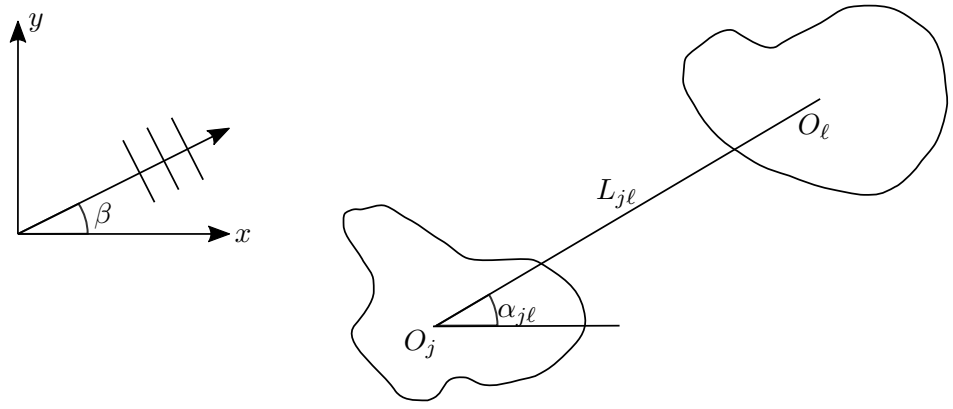

Figure 3.1: *Ambient waves of angle β reaching an array of floating objects (only a pair is shown for simplicity). $O_i = (x_\ell, y_\ell)$ is the center of the ℓ-th object and the origin of its local cylindrical coordinate system.*

In this section, the solution of the fully coupled problem (2.42) is considered. Since diffraction and radiation are not treated separately, the complex potential $\hat{\phi}$ is only decomposed into its ambient contribution $\hat{\phi}_0$, due to undisturbed incident waves, and the contribution due to waves emitted from each object, $\hat{\phi}_\ell^E$:

$$\hat{\phi} = \hat{\phi}_0 + \sum_{\ell=1}^{N_b} \hat{\phi}_\ell^E. \tag{3.22}$$

The unknowns of the problem are then the devices' oscillation amplitudes $\hat{\zeta}_\ell$, $\ell = 1, \ldots, N_b$, and the potentials $\hat{\phi}_\ell^E$. For each body, the emitted wave potential

is expressed in a local cylindrical coordinate system (r_ℓ, θ_ℓ, z), centered in $O_\ell = (x_\ell, y_\ell, -h)$ (see Fig. 3.1) in terms of the following basis of cylindrical outgoing waves:

$$\left(\boldsymbol{\Psi}_\ell^S\right)_m^n = \begin{cases} \dfrac{\cosh(kz)}{\cosh(kh)} \dfrac{H_n(kr_\ell)}{H_n(kR_\ell)} e^{in\theta_\ell}, & m = 0,\ -N_n \le n \le N_n \\ \cos(k_m z) \dfrac{K_n(k_m r_\ell)}{K_n(k_m R_\ell)} e^{in\theta_\ell}, & 1 \le m \le N_m,\ -N_n \le n \le N_n. \end{cases} \tag{3.23}$$

H_n are the Hankel functions of the first kind and K_n are the modified Bessel functions of the second kind. k is the wavenumber, which satisfies the real dispersion relation (2.54), while k_m are the real roots of the imaginary dispersion relation $\omega^2 = -gk_m \tan(k_m h)$. Modes corresponding to $m = 0$ are progressive waves, while modes corresponding to $m > 0$ are evanescent waves, exhibiting an exponential spatial decay and thus related to local interactions. We use the notation $(\boldsymbol{a})_m^n$ to indicate the component of vector $\boldsymbol{a}$ corresponding to the n-th progressive mode and m-th evanescent mode. For matrices, we will use notation $(T)_{ms}^{nl}$ to indicate the element whose row index corresponds to the n-th progressive mode and m-th evanescent mode, and whose column index corresponds to the l-th progressive mode and s-th evanescent mode. Denominators are scaling factors introduced to improve the condition number of the problem [32, Sec. 4.3]. R_ℓ is a characteristic dimension of the ℓ-th device; for a cylinder, the radius is considered. In order to solve the problem exactly, an infinite combination of the basis function would need to be considered. For numerical purposes, the series needs to be truncated. In total, we have $(2N_n + 1)(N_m + 1)$ coefficients to be determined. For implementation purposes, the indices n, m are converted to a single index q and vice versa by transformations

$$\begin{gathered} q = (n + N_n)(N_m + 1) + m, \\ n = \left\lfloor \frac{q - N_n(N_m + 1)}{N_m + 1} \right\rfloor, \quad m = \mathrm{mod}(q - N_n(N_m + 1), N_m + 1). \end{gathered} \tag{3.24}$$

The basis functions satisfy by construction the bottom and free surface boundary conditions (2.42b), (2.44) thanks to their z dependence. Moreover, they satisfy the radiation condition (2.66): indeed, we have the asymptotic behavior [11, Chap. 11]

$$H_n(x) \sim \sqrt{\frac{2}{\pi x}} \exp\left\{ i \left[x - \left(n + \frac{1}{2} \right) \frac{\pi}{2} \right] \right\}, \quad K_n(x) \sim \sqrt{\frac{\pi}{2x}} e^{-x}. \tag{3.25}$$

For $x \to 0$, instead,

$$H_0(x) \sim i \frac{2}{\pi} \ln x, \quad H_n(x) \sim -i \frac{(n-1)!}{\pi} \left(\frac{2}{x} \right)^n, \quad n > 0, \tag{3.26}$$

and analogous behaviors for $K_n(x)$, which means that the basis function are singular on the line $r_\ell = 0$. In particular, H_0 behaves as a line of sources, H_1 as a line of dipoles, and in general H_n as a line of multipoles. Therefore, while in

the formulation of the BEM presented in the previous sections singularities of the source type were distributed on the objects' surfaces, in the present formulation singularities of increasing orders are distributed on lines.[1]

The potential emitted by the ℓ-th object is then written, in the region outside it but not below it, as a combination of the basis functions introduced in (3.23):

$$\hat{\phi}_\ell^E(r_\ell, \theta_\ell, z) = \frac{g}{\omega}\left(\hat{\boldsymbol{\gamma}}_\ell^T + \hat{\zeta}_\ell \boldsymbol{R}_\ell^T\right) \boldsymbol{\Psi}_\ell^s(r_\ell, \theta_\ell, z), \tag{3.27}$$

where the vectors of hydrodynamic coefficients $\hat{\boldsymbol{\gamma}}_\ell \in \mathbb{C}^{(2N_n+1)(N_m+1)}$ and the complex oscillation amplitudes $\hat{\zeta}_\ell$ are the unknowns of the problem, and $\boldsymbol{R}_\ell$ is the solution of the radiation problem for unit oscillation amplitude of an isolated device in terms of the basis.

To determine the values of $\hat{\boldsymbol{\gamma}}_\ell$ and $\hat{\zeta}_\ell$ for each object, the hydrodynamic problem (2.42) and the dynamic problem (2.43) need to be solved. We now concentrate on the former, whose known data is given by the ambient incident waves. Ambient waves are written, in the coordinate system of each object, as a linear combination of a new set of basis functions:

$$\hat{\phi}_0(r_\ell, \theta_\ell, z) = \frac{g}{\omega} \boldsymbol{a}_\ell^T \boldsymbol{\Psi}_\ell^I(r_\ell, \theta_\ell, z), \tag{3.28}$$

where

$$(\boldsymbol{a}_\ell)_m^n = \begin{cases} J_n(kr)e^{in(\pi/2-\beta)}\Theta_\ell, & m = 0, \\ 0, & m \geq 0. \end{cases}, \quad \Theta_\ell = e^{ik(x_\ell \cos\beta + y_\ell \sin\beta)}, \tag{3.29}$$

$$\left(\boldsymbol{\Psi}_\ell^I\right)_m^n = \begin{cases} \dfrac{\cosh(kz)}{\cosh(kh)} \dfrac{J_n(kr_\ell)}{J_n(kR_\ell)} e^{in\theta_\ell}, & m = 0 \\ \cos(k_m z) \dfrac{I_n(k_m r_\ell)}{I_n(k_m R_\ell)} e^{in\theta_\ell}, & m \geq 1. \end{cases} \tag{3.30}$$

Here, J_n are Bessel functions of the first kind, and I_n are modified Bessel functions of the first kind. These, differently from basis functions $\left(\boldsymbol{\Psi}_\ell^S\right)_m^n$ (3.23), have the correct asymptotic behavior for incoming waves, rather than outgoing waves. The resulting potential ϕ_i corresponds to the expression (2.52) up to a phase delay of $\pi/2$. The contribution to the potential due to the j-th object can be evaluated in terms of this basis, too, through the basis transformation matrix $T_{j\ell}$:

$$\hat{\phi}_j^E(r_\ell, \theta_\ell, z) = \frac{g}{\omega}(\hat{\boldsymbol{\gamma}}_j^T + \hat{\zeta}_j \boldsymbol{R}_j^T) T_{j\ell} \boldsymbol{\Psi}_\ell^I(r_\ell, \theta_\ell, z), \tag{3.31}$$

with

$$(T_{j\ell})_{mm}^{nl} = \begin{cases} \dfrac{J_l(kR_\ell)}{H_n(kR_j)} H_{n-l}(kL_{j\ell}) e^{i\alpha_{j\ell}(n-l)}, & m = 0, \\ \dfrac{I_l(k_m R_\ell)}{K_n(k_m R_j)} K_{n-l}(k_m L_{j\ell}) e^{i\alpha_{j\ell}(n-l)}(-1)^l, & m \geq 1, \end{cases} \tag{3.32}$$

[1] This is very similar to the already mentioned equivalent source formulation, in which combinations of singularities are however distributed only in the interiors of objects.

and where we refer to Figure 3.1 for the definitions of $L_{j\ell}$ and $\alpha_{j\ell}$. Notice that matrix T is sparse, since its only nonzero elements are the ones whose column index and row index correspond to the same evanescent mode m. The total potential of waves incident on the ℓ-th object is given by the sum of potential due to ambient waves (3.28), and due to waves emitted by the other objects (3.31):

$$\hat{\phi}^I_\ell(r_\ell, \theta_\ell, z) = \frac{g}{\omega}\Big[\boldsymbol{a}^T_\ell + \sum_{\substack{j=0 \\ j\neq\ell}}^{N_b} \left(\hat{\boldsymbol{\gamma}}^T_j + \hat{\zeta}_j \boldsymbol{R}^T_j\right) T_{j\ell}\Big] \boldsymbol{\Psi}^I_\ell(r_\ell, \theta_\ell, z). \tag{3.33}$$

Since, as already remarked, basis functions (3.23) satisfy the free surface, bottom and radiation conditions, only the boundary conditions on the objects' surfaces need to be explicitly enforced in order to find $\hat{\boldsymbol{\gamma}}_\ell$. The distinctive feature of interaction theory is that these conditions are imposed by solving diffraction problems for each distinct[2] object, in isolated conditions. One problem for each incident wave basis function (3.30) needs to be solved, and the solution must then be written as a combination of scattered wave basis functions (3.23). For each incident wave basis function, the coefficients of the corresponding scattered wave are collected into a column of the diffraction transfer matrix B_ℓ mentioned above, which transforms the coefficients of incident waves into the coefficients of diffracted waves. We can therefore write

$$\hat{\boldsymbol{\gamma}}_\ell = B_\ell\Big[\boldsymbol{a}_\ell + \sum_{\substack{j=0 \\ j\neq\ell}}^{N_b} T^T_{j\ell}\left(\hat{\boldsymbol{\gamma}}_j + \hat{\zeta}_j \boldsymbol{R}_j\right)\Big]. \tag{3.34}$$

Different possibilities exist for computing matrix B, or an approximation of it. The method originally proposed in [86] is a hybrid element method introduced in [181]: it combines finite elements in a near field domain with a series of cylindrical harmonics in the far field. For cylindrical objects, an analytical solution is available [31, 180]; moreover, in this case matrix B is sparse (as is the case for any axisymmetric geometry). In [114], a more general method, not limited to cylindrical geometries, is presented, in which the diffraction problems can be solved using any numerical scheme (BEM is presented as an example); however, evanescent modes are neglected. By separating known terms from unknowns in (3.34), we obtain the interaction theory formulation of the hydrodynamic problem:

$$\sum_{\substack{j=1 \\ j\neq\ell}}^{N_b} \underbrace{B_\ell T^T_{j\ell}}_{M_{\gamma\gamma,\ell j}} \hat{\boldsymbol{\gamma}}_j - \hat{\boldsymbol{\gamma}}_\ell + \sum_{\substack{j=1 \\ j\neq\ell}}^{N_b} \underbrace{B_\ell T^T_{j\ell}\boldsymbol{R}_j}_{M_{\gamma\zeta,\ell j}} \hat{\zeta}_j = \underbrace{-\frac{H}{2} B_\ell \boldsymbol{a}_\ell}_{\boldsymbol{h}_{\gamma,\ell}}, \quad \ell = 1\ldots, N_b. \tag{3.35}$$

If all oscillation amplitude $\hat{\zeta}_\ell$ are set to zero, i.e. if a pure diffraction problem is considered, this block system can be solved for $\hat{\gamma}_\ell$, $\ell = 1, \ldots, N_b$, and the potential in all the fluid domain except for the regions below objects can be obtained. If the fully coupled problem, including radiation, is considered, then the motion of

[2] In the sense that if all objects are identical, diffraction problems for only one object need to be solved.

each object needs to be determined. In order to do this, heave (vertical) forces on objects must be computed; in the case of cylinders, they depend only on the potential in the region below each object, which we now consider.

In this region, which we shall call interior region, an additional set of basis functions $\tilde{\boldsymbol{\Psi}}_\ell^D$ for diffracted waves is defined, and the potential is then written as

$$\begin{aligned}\hat{\phi}_\ell(r_\ell,\theta_\ell,z) = \frac{g}{\omega}\Big\{\Big[\boldsymbol{a}_\ell^T + \sum_{\substack{m=1\\m\neq\ell}}^{N_b}(\hat{\boldsymbol{\gamma}}_m + \hat{\zeta}_m\boldsymbol{R}_m)^T T_{m\ell}\Big]\tilde{B}_\ell^T\tilde{\boldsymbol{\Psi}}_\ell^D(r_\ell,\theta_\ell,z)\\ + \hat{\zeta}_\ell\Big(\tilde{R}_\ell^p(r_\ell,\theta_\ell,z) + \tilde{\boldsymbol{R}}_\ell^T\tilde{\boldsymbol{\Psi}}_\ell^D(r_\ell,\theta_\ell,z)\Big)\Big\}.\end{aligned} \tag{3.36}$$

Matrix $\tilde{B}_\ell$, vector $\tilde{\boldsymbol{R}}_\ell$ and scalar function $\tilde{R}_\ell^p$ are additional hydrodynamic properties of the isolated device, computed from the solution of the diffraction problems and unit amplitude radiation problem mentioned above, and referred to the interior region. Substituting (3.36) into the dynamic equation (2.43) and taking into account that on the bottom surface of each cylinder $n_z = -1$, we have

$$\sum_{\substack{m=1\\m\neq\ell}}^{N_b}\Bigg[\underbrace{\frac{1}{W_\ell}(\widetilde{\boldsymbol{Y}}_\ell^D)^T\widetilde{B}_\ell T_{m\ell}^T}_{M_{\zeta\gamma,\ell m}}\hat{\boldsymbol{\gamma}}_m + \underbrace{\frac{1}{W_\ell}\boldsymbol{R}_m^T T_{m\ell}\widetilde{B}_\ell^T\widetilde{\boldsymbol{Y}}_\ell^D}_{M_{\zeta\zeta,\ell m}}\hat{\zeta}_m\Bigg] + \hat{\zeta}_\ell = \underbrace{-\frac{H}{2W_\ell}\boldsymbol{a}_\ell^T\widetilde{B}_\ell^T\widetilde{\boldsymbol{Y}}_\ell^D}_{\boldsymbol{h}_{\zeta,\ell}}, \tag{3.37}$$

$\ell = 1,\ldots,N_b$. Here, W_ℓ is the mechanical impedance

$$W_\ell = \tilde{Y}_\ell^R - i(\omega^2 m_\ell + i\omega c_\ell - \kappa_{h,\ell} - \kappa_\ell)/(\rho g), \tag{3.38}$$

$\tilde{\boldsymbol{Y}}_\ell^D$ is the vector of integrals of functions $\tilde{\boldsymbol{\Psi}}_\ell^D$, and $\tilde{Y}_\ell^R$ is a radiation quantity containing the integral of function $\tilde{R}_\ell^p$. These integrals are computed on the underside of each device. Equations (3.35) and (3.37) can be solved to find $(\hat{\boldsymbol{\gamma}}_\ell, \hat{\zeta}_\ell)$, $\ell = 1,...,N_b$. They can be written in compact form as the block system

$$\begin{bmatrix} M_{\gamma\gamma} & M_{\gamma\zeta}\\ M_{\zeta\gamma} & M_{\zeta\zeta}\end{bmatrix}\begin{bmatrix}\hat{\boldsymbol{\gamma}}\\ \hat{\boldsymbol{\zeta}}\end{bmatrix} = \begin{bmatrix}\boldsymbol{h}_\gamma\\ \boldsymbol{h}_\zeta\end{bmatrix}. \tag{3.39}$$

Since an implementation of interaction theory in this form was not already available, a code, named floatcyl, was written from scratch; it is available at `https://github.com/marcogambarini/floatcyl`. It was used for the work presented in Chapters 7 and 8. The code is written in Python and it leverages as much as possible the efficient, vectorized operations implemented in libraries Numpy [82] and SciPy [171]. In our implementation, matrix $M_{\gamma\gamma}$ is never explicitly assembled, because this would require a large number of expensive matrix-matrix products of the form $B_\ell T_{j\ell}^T$. Since as discussed above matrices B_ℓ and $T_{j\ell}^T$ are sparse, while their product is not, precomputing and storing $M_{\gamma\gamma}$ would be an easily avoidable waste of memory. Instead, a function computing $M_{\gamma\gamma}\hat{\boldsymbol{\gamma}}$ for any vector $\hat{\boldsymbol{\gamma}}$ is defined based on (3.35) using only matrix-vector products. Matrices B and T are constructed in sparse coordinate format (COO) as a compromise between code readability and efficiency; then, they are converted to compressed sparse

row (CSR) format for computational efficiency [55]. The results of floatcyl are compared with the ones of Capytaine in terms of oscillation amplitude and phase in Figure 3.2 for a test case with 3 cylinders of different dimensions placed irregularly. Very good agreement is observed. The phase oscillations at high frequency are not a matter of concern, since they correspond to negligible amplitude, and since the reference solution has been computed with the boundary element method, which is known to be prone to oscillations at high frequency due to the so-called irregular frequency phenomenon [90, 107].

To conclude this section, we mention that it is possible to combine BEM methods, which can treat complex geometries flexibly, and eigenfunctions methods such as the one presented in this section, which have computational advantages. For instance, this was done in [92], in order to efficiently treat a case with a complex bathymetry in a part of the domain, and a flat bottom in the farfield. By imposing continuity of potential and normal velocity at the interface, a single system is obtained.

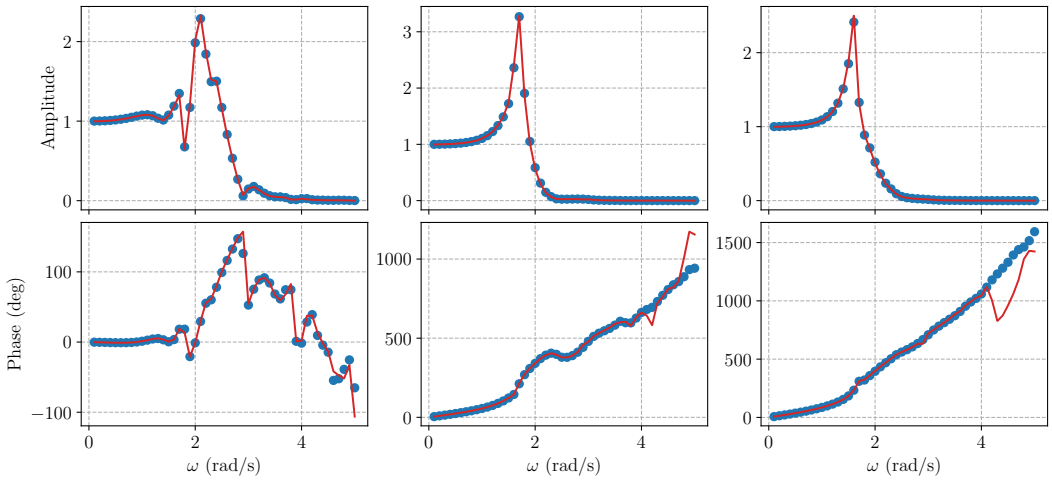

Figure 3.2: *Comparison between Capytaine (red lines) and floatcyl (blue dots) for a test case with 3 devices with* $(x_1, y_1) = (0, 0)$, $R_1 = 2$, $d_1 = 1$; $(x_2, y_2) = (8, -4)$, $R_2 = 3$, $d_2 = 2$; $(x_3, y_3) = (12, 2)$, $R_3 = 3$, $d_3 = 2$; $h = 10$ *(all units are meters).*

3.3 Spectrum discretization

In the previous sections, numerical methods for the solution of the linear hydrodynamic problem for a monochromatic incident wave were described. Here, we detail the discretization of frequency spectra (see Sec. 2.4), which permits the solution of the hydrodynamic problem for any incident wave system by linear superposition. The result of the discretization is an approximation of the free surface elevation field $\eta(x, y, t)$ as a finite sum of regular waves of heights H_q, angular frequencies ω_q, $q = 1, \ldots, N_f$, and phases φ_q. These parameters should be chosen consistently with the power spectral density of the sea state, and with the statistical properties of the signal. We recall that the random process describing the free surface elevation was assumed to be a Gaussian process, i.e., satisfying (2.73). Various ways

to reconstruct the wave signal from the spectrum $S(f)$ are described in [30, 169], and we discuss them in the following: they are the deterministic spectral amplitude method (DSA), the nondeterministic spectral amplitude method (NSA), and filtering of white noise. For simplicity, since only the frequency distribution is of concern here, waves directed along the positive x direction are considered ($\beta = 0$).

In the DSA method, the spectrum $S(f)$ is discretized by first determining an interval $[f_L, f_R]$ representing the effective support of S_f, i.e., capturing most of the total wave energy density. Then, such interval is partitioned into subintervals I_q of center f_q and width Δf_q. The energy density in each subinterval is $E_q = \rho g S(f_q)\Delta f_q + \mathcal{O}(\Delta f_q)^2$. The wave profile is reconstructed as

$$\eta(x, y, t) = \sum_{q=1}^{N_f} \frac{H_q}{2} \cos(k_q x - \omega_q t + \phi_q), \tag{3.40}$$

with $\omega_q = 2\pi f_q$ and k_q satisfying the dispersion relation (2.54). The phases are uniformly distributed random variables $\phi_q \sim \mathcal{U}[0, 2\pi]$, and amplitudes are determined deterministically as follows. The total energy density per unit area of the waves described by (3.40) is

$$E = \rho g \sum_{q=1}^{N_f} \frac{H_q^2}{8}. \tag{3.41}$$

Each monochromatic component is assigned the power of the corresponding frequency interval:

$$H_q = 2\sqrt{2 \int_{I_q} S(f) df}. \tag{3.42}$$

where the integral may be evaluated using a quadrature rule with prescribed accuracy, or approximated as $S(f_q)\Delta f_q$. In the limiting case where only one frequency is considered, one obtains, from (3.42), (2.75) and (2.76),

$$H = 2\sqrt{2 \int_0^\infty S(f) df} = \sqrt{2\frac{E}{\rho g}} = 2\sqrt{2\frac{H_s^2}{16}} = \frac{H_s}{\sqrt{2}}. \tag{3.43}$$

The DSA procedure leads to a Gaussian process only in the limit $N \to \infty$. This can be proved by relying on the Lindeberg-Feller theorem [46, Th. 3.4.10], a generalization of the central limit theorem.

In the NSA approach, amplitudes are instead normally distributed random variables:

$$\eta(x, y, t) = \sum_{q=1}^{N_f} [a_q \cos(k_q x - \omega_q t) + b_q \sin(k_q x - \omega_q t)] \tag{3.44}$$

where $a_q, b_q \sim N(0, S(f_q)\Delta f_q)$, and ω_q, k_q are determined as in the DSA method. Using this approach, the expected value of the power of the monochromatic waves of frequency f_q is equal to the power of the corresponding interval in the spectrum:

$$\mathbb{E}\left[\overline{\eta^2}\right] = \frac{1}{2} \sum_{q=1}^{N_f} \left(\mathbb{E}\left[a_q^2\right] + \mathbb{E}\left[b_q^2\right]\right) = \sum_{q=1}^{N_f} S(f_q)\Delta f_q. \tag{3.45}$$

Thus, power is correctly represented only in a statistical sense. On the other hand, the process is Gaussian for any value of N because, at fixed (x, y, t), η is a linear combination of the Gaussian variables a_q, b_q.

If intervals of constant width Δf are used, leading to $f_q = q\Delta f$, the DSA and NSA methods yield a periodic function. By choosing unequal intervals Δf_q, it is possible to obtain longer periods, as observed in [169], where it is proposed to choose Δf_q such that $S(f_q)\Delta f_q$ is constant, i.e., every frequency component gives approximately the same contribution to the total energy density. The same approach is proposed in [69, Sec. 10.5.2]. We remark that this choice implies that all components produce approximately the same contribution to the energy density E, but not to the energy flux J. In order to have all the components contribute the same energy flux, we start from

$$J = \frac{\rho g^2}{4\pi} \sum_{q=1}^{N_f} \int_{I_q} \frac{S(f)}{f} df = \frac{\rho g^2}{4\pi} \sum_{q=1}^{N_f} \frac{H_q^2}{8 f_q}, \tag{3.46}$$

and require equality term by term in the sums for the computation of the edges of intervals I_q. Then, f_q is chosen as the center of the q-th interval and H_q is computed from (3.42), so that the total energy density is still consistent with the power spectral density $S(f)$.

Finally, we have the method of white noise filtering. A discrete white noise signal of arbitrary duration can be generated by sampling from a normal distribution. Such signal can then be filtered (for example by using a FFT algorithm) so that its power spectral density matches $S(f)$. This approach allows constructing time series of any required duration, but its computational cost is greater [169]. This is sometimes called the shape filter approach [109].

For our purposes, we have adopted the DSA method. This choice is motivated by the facts that we work in the frequency domain, thus ruling out the white noise

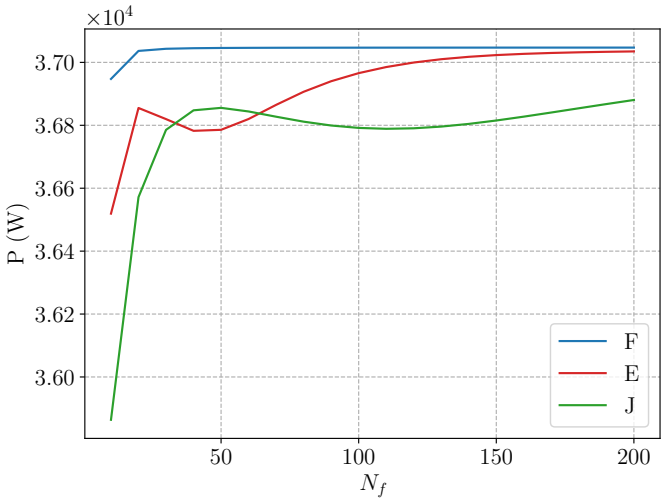

Figure 3.3: *Convergence of the power of a WEC array with respect to the number of harmonics using the DSA method and intervals of constant width in frequency (F), constant energy density (E) and constant energy flux (J).*

filtering approach, and that we are interested in computing and optimizing the power of the wave energy park, so that it is desirable to have the same incident wave power at each realization. In our initial optimization work presented in Chapter 6, we followed the approach suggested in the literature mentioned above of using intervals of constant energy density E. In the later work presented in Chapter 8, we instead used frequency intervals of constant width. This was done because of the observation that the power of a WEC array converged faster, with respect to the number of harmonics, if the latter approach is adopted. In order to test this, we devised a numerical experiment with 4 WEC devices positioned in a square arrangement. The devices have radius $R = 2$ m, draft $d = 0.5$ m, and the edge of the square is $L = 10$ m. A wave climate described by a Pierson-Moskowitz spectrum (2.79) with $T_e = 8$ s, $H_s = 2$ m and $\beta = 0$ forces the array. The devices share the same control parameters $c_\ell = 50000$ N/(m/s), $\kappa_\ell = -20000$ N/m. The linear fluid-structure interaction problem is solved using the floatcyl code (see the previous section 3.2) with truncation parameters $N_n = 4$, $N_m = 25$. The results are shown in Figure 3.3. We can observe that while the approach with constant interval width Δf is the fastest to converge, both other approaches reach values to within 1% of the former when $N_f \gtrapprox 30$.

Chapter 4

A preconditioner for linear free-surface BEM

Hydrodynamic computations on large arrays are needed for wave energy applications because, as already observed in the introduction, wave energy converters are expected to be installed in rather large parks. Moreover, other applications involve problems of this type, such as the design of Very Large Floating Structures (VLFS), especially semisubmersible ones supported by several floating piles [97], and the study of ice floes in the marginal ice zone [157]. The boundary element method, introduced in Section 3.1, is an efficient and versatile method for the simulation of arrays of floating objects, since it only requires a mesh of the objects' wetted surfaces, and it can treat general geometries. However, as the involved matrices are full and in general not symmetric, the solution procedure can become demanding in terms of both memory and time if large arrays need to be simulated. More precisely, building a full matrix and performing matrix-vector products require $\mathcal{O}(N^2)$ operations, while the solution of a system through a direct method such as Gaussian elimination requires $\mathcal{O}(N^3)$ operations, where N is the total number of elements, which can be considered proportional to the number of simulated bodies N_b.

Some techniques are available for reducing such cost, at the expense of introducing a controllable error. The fast multipole method [72, 105] is one of these. It is based on a hierarchical clustering of the elements. Interactions coefficients (i.e., matrix entries) between pairs of elements in the same cluster are computed exactly, while those between elements that are far from each other are computed approximately through Taylor series expansions of the Green function around the clusters' centers. A complexity of $\mathcal{O}(N)$ for matrix-vector multiplication is achieved, and the error can be controlled through the order of truncation of the series. If paired with an iterative method whose convergence rate does not deteriorate as N increases, meaning that the number of iterations required to reach the solution up to some tolerance does not increase, then the global cost of solving the problem is $\mathcal{O}(N)$; this may be achieved through the use of a preconditioner. In the case of our problem of interest, the Green function is not amenable to simple Taylor expansions, since it has a complicated form due to the need of incorporating free surface and bottom boundary conditions. Furthermore, from the

computational point of view, this complexity is tackled in the code we base this work on, Capytaine, by precomputing and storing in tables the values of some intermediate quantities [8]. In this case, hierarchical matrix algorithms [19, 79], which can be considered a generalization of the fast multipole method, can be adopted, leading to an optimal complexity of $\mathcal{O}(N \log N)$ (subquadratic).

In this chapter, we introduce a preconditioner for the solution of problem (3.20). It is based on the coarse-corrected block-Jacobi algorithm [33], and it has been implemented by taking advantage of the hierarchical matrix engine already available in the code Capytaine [8]. The basic algorithm is similar to the multigrid technique presented in [78], in which however the block structure is not explicitly leveraged, and Picard (fixed-point) iterations [36, Sec. 5.2] are used as a smoother. The content of this chapter mostly follows our work [34].[1] In particular, in section 4.1 we present the coarse-corrected block-Jacobi algorithm, together with some numerical tests done on an initial dense-matrix implementation. Then, in section 4.2 we provide details about the hierarchical matrix implementation of the algorithm. Finally, in section 4.3, numerical experiments using the final implementation are presented and discussed.

4.1 The coarse-corrected block-Jacobi algorithm

The matrix K appearing in (3.20) is full, because each element interacts with all others, and non-symmetric. The problem has a natural block structure

$$K = \begin{bmatrix} K_{11} & \cdots & K_{1N_b} \\ \vdots & \ddots & \vdots \\ K_{N_b1} & \cdots & K_{N_bN_b} \end{bmatrix}, \quad \boldsymbol{\sigma} = \begin{bmatrix} \boldsymbol{\sigma}_1 \\ \vdots \\ \boldsymbol{\sigma}_{N_b} \end{bmatrix}, \quad \boldsymbol{b} = \begin{bmatrix} \boldsymbol{b}_1 \\ \vdots \\ \boldsymbol{b}_{N_b} \end{bmatrix}, \tag{4.1}$$

where $\boldsymbol{\sigma}_j$ is a vector containing the unknowns corresponding to the j-th object. The diagonal block K_{ii} represents the interaction of body i with itself. The off-diagonal block K_{ij} represents the effect on body i of waves radiated from body j. The structure of (4.1) suggests the use of a block-Jacobi algorithm, equivalent to the parallel method of reflections. This method, together with a coarse correction, has been presented in [33] for the real Laplace equation in perforated domains. After checking that encouraging scalability results are obtained on relevant test cases, we use the devised stationary iteration as a preconditioner for GMRES. This is guaranteed to obtain at worst the same convergence rate as the initial stationary method in terms of residual reduction per iteration [62].

The block-Jacobi method, in analogy with the basic Jacobi method [140], is based on the splitting $K = D - N$, where D is the block-diagonal part of K. At each iteration, starting from $\boldsymbol{\sigma}^k$, it requires solving for $\boldsymbol{\sigma}^{k+1/2}$ in

$$D\boldsymbol{\sigma}^{k+1/2} = N\boldsymbol{\sigma}^k + \boldsymbol{b}. \tag{4.2}$$

Since D is block-diagonal, each block corresponding to a single object, the system (4.2) corresponds to N_b independent, smaller systems, which can be solved in

[1] Two errors were present in [34] and have been amended here: a sign error was present in line 3 of Algorithm 2, and matrix K was missing in the expression of the inverse preconditioner (4.6).

parallel. After the block-Jacobi step, a coarse correction is performed. This is needed since the Jacobi method is known to only act efficiently on the high-frequency components of the error, so that an additional step is required to reduce the low-frequency components [35]. The coarse correction is performed by solving the correction problem $K\boldsymbol{e} = \boldsymbol{r}^{k+1/2}$ in a low-dimensional (coarse) space $\mathcal{C}$, where $\boldsymbol{r}^{k+1/2} = \boldsymbol{b} - K\boldsymbol{x}^{k+1/2}$ is the residual. Consider, for simplicity, a problem with N_b identical bodies, each one discretized with N_p elements, so that the full system has dimension N_bN_p. Define $\mathcal{C} = \text{span}\{\boldsymbol{c}_1, \boldsymbol{c}_2, \dots, \boldsymbol{c}_m\}$, $m \ll N_bN_p$. Then we can introduce a restriction operator $\mathcal{R} : \mathbb{R}^{N_bN_p} \to \mathcal{C}$ represented by matrix $R = \begin{bmatrix}\boldsymbol{c}_1 & \boldsymbol{c}_2 & \dots & \boldsymbol{c}_m\end{bmatrix}^T$ and a prolongation operator $\mathcal{P} : \mathbb{R}^{N_bN_p} \to \mathcal{C}$ represented by matrix R^T. Let $\boldsymbol{e}_c \in \mathbb{R}^m$ be a vector such that $\hat{\boldsymbol{e}} = R^T\boldsymbol{e}_c$ is an approximation of the error $\boldsymbol{e}$. The coarse problem is

$$RKR^T\boldsymbol{e}_c = R\boldsymbol{r}^{k+1/2}, \tag{4.3}$$

where we define $K_c := RKR^T$. Once the coarse problem (4.3) has been solved, the update

$$\boldsymbol{\sigma}^{k+1} = \boldsymbol{\sigma}^{k+1/2} + R^T\boldsymbol{e}_c \tag{4.4}$$

is performed. The efficiency of the correction step is strongly related to the choice of the coarse space $\mathcal{C}$. This has to be rich enough to well represent the main error components that block-Jacobi cannot deal with, but its dimension m must be relatively small, so that the cost of a single iteration is not increased significantly. A simple choice for the coarse space is taking a constant value of the source distribution σ on each body. This choice is suggested by the one presented in [33] and corresponds to $\boldsymbol{c}_i := \mathbf{1}_i$, $i = 1, \dots, N_b$, $\mathbf{1}_i$ being the discrete indicator function of the i-th object. In this case, the dimension of $\mathcal{C}$ is equal to the number of objects N_b.

Another possible choice is taking approximately constant values of the potential ϕ, instead of the source distribution, on each body. The approximation lies in the fact that, in building the coarse space, we treat the bodies as if they were not interacting: for all i, $\boldsymbol{c}_i$ is defined as a block vector whose elements are all zero except for the i-th block, which is equal to $S_{ii}^{-1}\mathbf{1}$. Since $\boldsymbol{\phi} = S\boldsymbol{\sigma}$, $S_{ii}^{-1}\mathbf{1}$ is the source distribution of an isolated body with constant potential distribution. Here, S is the matrix appearing in (3.21), and S_{ii} is its i-th diagonal block.

Our two-level block-Jacobi method is detailed in Algorithms 1 and 2. The former is a precomputation step, that does not depend on the right-hand side vector. Thus, if multiple systems with the same matrix and different right hand sides need to be solved, Alg. 1 needs to be performed only once. The precomputation of $\widetilde{R}$ is convenient, since it avoids the need of performing an additional, large matrix-vector multiplication for the computation of the residual at each step. However, the computation of $\widetilde{R} = RK$ would in principle require N_b matrix vector products, corresponding to a total of $\mathcal{O}(N_b^3N_p^2)$ operations with dense matrices, and $\mathcal{O}(N_b^2N_p\log(N_bN_p))$ with hierarchical matrices. In order to reduce this cost, in the case of dense matrices one can take advantage of the fact that each row of R is made up of mostly zeros (since the nonzero elements correspond to the elements of just one of the bodies), and neglecting the zeros brings the complexity to $\mathcal{O}(N_b^2N_p^2)$. If instead a hierarchical matrix representation is adopted, then

Algorithm 1 Two-level block-Jacobi algorithm: initialization

1: **for** $i = 1$ to N_b **do**
2: Compute the LU decomposition of A_{ii}.
3: **end for**
4: Compute $\widetilde{R} = RK$, $K_c = \widetilde{R}R^T$.

Algorithm 2 Two-level block-Jacobi algorithm: solution

Require: Initial guess $\boldsymbol{\sigma}^0$, tolerance tol, maximum number of iterations $maxit$.
1: Set $k = 0$.
2: **while** $\|\boldsymbol{b} - K\boldsymbol{\sigma}^k\| > tol$ **and** $k < maxit$ **do**
3: Compute $\boldsymbol{q} = \boldsymbol{b} + N\boldsymbol{\sigma}^k$.
4: **for** $i = 1$ **to** N_b **do**
5: Solve $K_{ii}\boldsymbol{\sigma}_i^{k+1/2} = \boldsymbol{q}_i$ using the LU decomposition of K_{ii}.
6: **end for**
7: Compute the restricted residual $\boldsymbol{r}_c = R\boldsymbol{b} - \widetilde{R}\boldsymbol{\sigma}^{k+1/2}$.
8: Solve for $\boldsymbol{e}_c$ in $K_c\boldsymbol{e}_c = \boldsymbol{r}_c$.
9: Update $\boldsymbol{\sigma}^{k+1} = \boldsymbol{\sigma}^{k+1/2} + R^T\boldsymbol{e}_c$.
10: Update $k = k + 1$.
11: **end while**

the cost can be reduced by using a method that will be presented in Section 4.2. Alg. 2 corresponds to the stationary method

$$\begin{aligned}\boldsymbol{\sigma}^{k+1} &= [I - (P_c + D^{-1} - P_cKD^{-1})K]\boldsymbol{\sigma}^k + (P_c + D^{-1} - P_cKD^{-1})\boldsymbol{b} \\ &= \boldsymbol{\sigma}^k + (P_c + D^{-1} - P_cKD^{-1})\boldsymbol{r}^k,\end{aligned} \tag{4.5}$$

with $P_c = R^T K_c^{-1} R$, and where we can recognize the inverse preconditioner

$$P^{-1} = P_c + D^{-1} - P_cKD^{-1}. \tag{4.6}$$

Such preconditioner can then be used to accelerate a Krylov method. Using P^{-1}, the system is recast as $P^{-1}K\boldsymbol{\sigma} = P^{-1}\boldsymbol{b}$. Since the new system matrix $P^{-1}K$ is not symmetric, a classical choice is GMRES. In our implementation, the preconditioning matrix P^{-1} is not assembled explicitly; instead, GMRES is provided with a function (based on Alg. 2) computing the action of $P^{-1}K$ on an arbitrary vector. To see how this is defined, let us call $\mathcal{S}$ the operator corresponding to a step of the method: $\boldsymbol{\sigma}^{k+1} = \mathcal{S}(\boldsymbol{\sigma}^k, \boldsymbol{b})$. Then, Eq. (4.5) shows that the action of $P^{-1}K$ on a generic vector $\boldsymbol{v}$ is $P^{-1}K\boldsymbol{v} = \boldsymbol{v} - \mathcal{S}(\boldsymbol{v}, \boldsymbol{0})$, while the right hand side can be computed as $P^{-1}\boldsymbol{b} = \mathcal{S}(\boldsymbol{0}, \boldsymbol{b})$.

We now present preliminary tests, performed on a dense matrix implementation, to verify the scalability of the proposed algorithm. Two cases are considered: a regular grid of discs, which we call the WEC test case, and a random, irregular arrangement of discs, which we call the ice floe test case; details are reported in Table 4.1.

The number of iterations required for the solution of the WEC test case using the standard GMRES method without preconditioning, the coarse-corrected

	radius	draft	distance	configuration	panels per body
WEC	3.5	0.5	20	regular	90
Ice floes	1.0	0.5	3 (min); 5 (avg)	random	90

Table 4.1: *Test case parameters; lengths in meters.*

Jacobi algorithm (Jcc), and the GMRES algorithm with the proposed preconditioner (pccGMRES), are presented in Figure 4.1. Results for the ice floe case are instead shown in Fig. 4.2. A comparison between the use of the constant source distribution preconditioner and the approximate constant potential distribution preconditioner is reported. We observe that in all cases, as expected, the preconditioned GMRES method performs better than the coarse-corrected block-Jacobi method used as a standalone stationary iteration. Encouraging scalability results are achieved for the WEC test case using the constant source distribution preconditioner, and for the ice floe test case using the approximate constant potential preconditioner. We also remark that the number of iterations required for the solution of the system using the preconditioned GMRES method is always significantly smaller than N_b. This motivates our effort in reducing the number of operations for the construction of the coarse space, so that this step does not negatively impact the total time required for the solution.

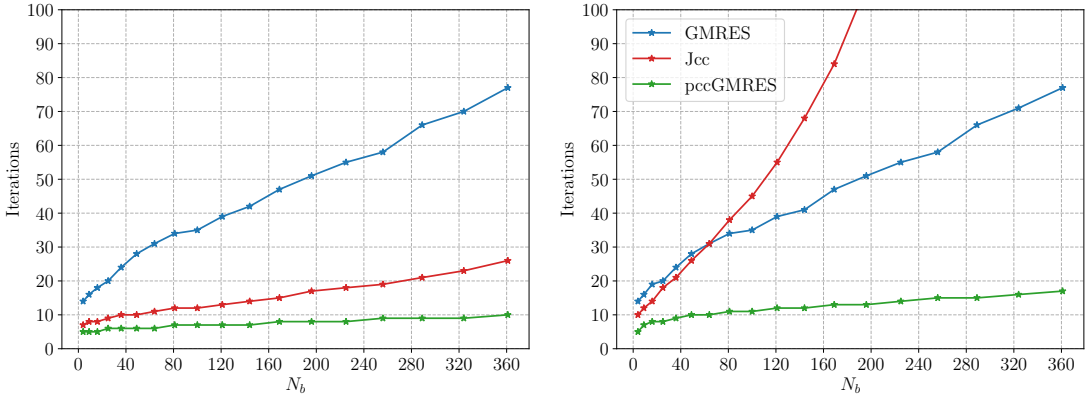

Figure 4.1: *Scalability results for the WEC test case; preconditioner with constant source distribution σ (left) and approximate constant potential distribution ϕ (right).*

4.2 Implementation with $\mathcal{H}$-matrices

Hierarchical matrices, denoted here as $\mathcal{H}$-matrices, are an efficient tool for reducing the storage and computational cost of BEM problems. The method is based on defining a hierarchical cluster tree from the set of mesh elements. The system matrix is then built with a hierarchical block structure accordingly. Each block describes the interaction between two clusters of elements. If the centers of the two clusters are farther than a threshold, then a low-rank approximation of the block is built; otherwise, the block is built in dense form. If the tree is balanced and if we take as leaves of the tree the single objects, discretized with

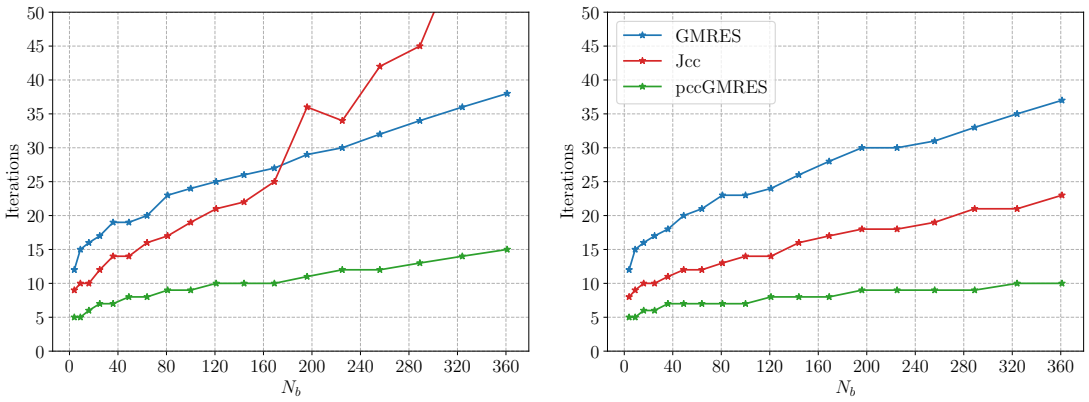

Figure 4.2: *Scalability results for the ice floe test case; preconditioner with constant source distribution σ (left) and approximate constant potential distribution ϕ (right).*

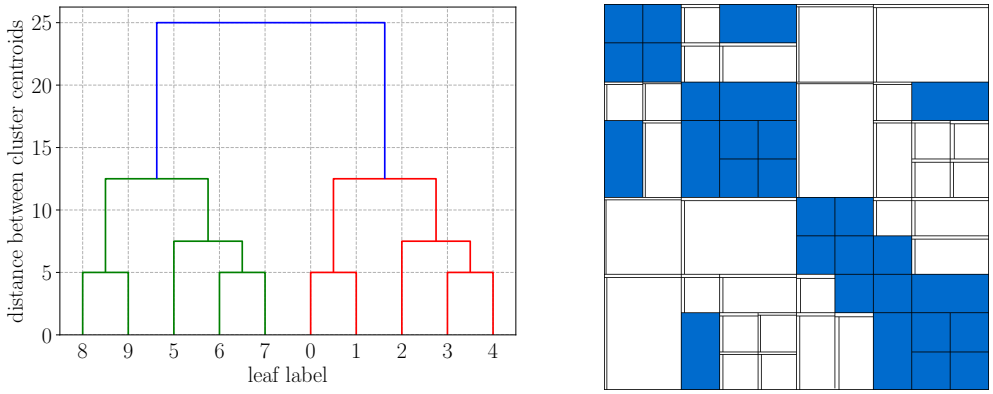

Figure 4.3: *Clustering of positions (left) and hierarchical structure of matrix K (right) for a test with 10 objects.*

N_p elements, then both the costs of storage and of matrix-vector multiplication are $\mathcal{O}(\max(r, N_p)N_bN_p \log(N_bN_p))$ [19, Th. 2.6, 2.8], where r is the maximum rank of matrix blocks.

Fig. 4.3 shows the tree and the hierarchical structure of matrix A for an example with 10 objects on a row, with spacing of 5 m. The ordinate of each node in the tree is the distance between the centers of its sons. In the matrix, blue blocks are dense, while white blocks are low-rank. Notice that dense blocks gather mostly close to the diagonal. Information on the nodes of the tree is stored in the so-called linkage matrix, which is built during the clustering process. The first N_b nodes of the tree are the leaves (the single objects). All other nodes are defined by the rows of the linkage matrix: its i-th row contains the labels of the sons of the $(N_b + i)$-th node. Hierarchical clustering on the positions of the objects is performed using function `linkage` of the SciPy library [171]. It works by aggregation, and builds binary trees, meaning that each node has 2 sons.

Our implementation of Alg. 1 and 2 is done starting from the BEM code Capytaine [7], which includes an $\mathcal{H}$-matrices engine. Matrix-vector multiplication in line 3 of Alg. 2 is performed with the built-in routine. Handling of diagonal blocks and building the coarse space, instead, require special care. Since the

structure of matrix storage is hierarchical, extracting the diagonal blocks of A to build matrices D and N is not immediate. In order to do it, first a list `leaves`, whose i-th element is the list of leaves belonging to node i, is built by sweeping over the rows of the linkage matrix. Then, a list `paths` is constructed. This contains N_b sublists. The i-th sublist has size equal to the level of the i-th leaf. The ℓ-th element of this sublist is equal to 0 or 1, if at the ℓ-th level one has to turn left or right, respectively, to step down toward the i-th leaf. For example, in Fig. 4.3 (left) the path to leaf 5 is `paths`$[5] = [0, 1, 0]$. The lists `leaves` and `paths` are used to compute $\widetilde{R} = RK$ efficiently in Alg. 1. Thanks to the sparsity of the rows of R, that are vectors $\mathbf{c}_i^T$, for dense matrices this operation can be made very efficient by multiplying each of the $\mathbf{c}_i$ only by the rows of K corresponding to its non-zero elements, as already mentioned in Sec. 4.1. Slicing a hierarchical matrix, however, is not as trivial. For this reason, we propose the recursive procedure detailed in Alg. 3 and described graphically in Fig. 4.4. At the beginning, $\widetilde{K} = K$ and $\boldsymbol{v} = \boldsymbol{c}_i$ are set. The algorithm then descends from the root to the level above the i-th leaf following list `path` = `paths`$[i]$. In doing this, because of the binary structure of the tree, 2×2 block matrices are encountered at each level. At level j, the nonzero contributions $\boldsymbol{c}_i K$ come only from the l-th block-row, with $l =$ `path`$[j]$. The off-diagonal part of the l-th block row is directly multiplied by the appropriate slice of $\boldsymbol{v}$; then, the algorithm is applied again to the diagonal block $\widetilde{K}_{ll}$. At the end, only the (dense) diagonal block corresponding to the interaction of the i-th object with itself is left, and this last multiplication is performed. The main advantage of this strategy is that, at each level of the hierarchy except the last, off-diagonal blocks, which are expected to be mostly low-rank, are multiplied.

4.3 Numerical experiments

We simulate two geometries: line arrays and grid arrays. In both cases the objects are half-spheres of radius 2 m and the minimum distance between two bodies is 5 m. The results are reported in Table 4.2. Times for GMRES and preconditioned GMRES refer to the solution of the N_b systems required to build the radiation dataset; thus the number of systems needing to be solved increases with the number of objects. The loops described in Algorithms 2 and 3 are performed serially. We build the radiation dataset only for vertical motion; in the general case of a rigid body, $6N_b$ systems would need to be solved. In some cases, the number of iterations varies depending on the right hand side (i.e., depending on the radiating object).

The presented results indicate that the preconditioned GMRES method has a lower cost than the standard GMRES method for large arrays of floating objects. The advantage becomes larger as the number of bodies increases: speedups of up to a factor of 3.5 are obtained. For the line geometry, the number of iterations of GMRES tends to become constant with respect to the number of objects, while the iterations of preconditioned GMRES remain exactly constant and equal to 7. On the other hand, for the grid geometry the number of iterations of GMRES increases as n grows, while preconditioned GMRES scales well. The use of Alg. 3 for the construction of the coarse space, which needs to be performed only once,

Algorithm 3 Computation of $\widetilde{R} = RK$ for $\mathcal{H}$-matrices

Require: K, $R = [\boldsymbol{c}_1, \cdots, \boldsymbol{c}_n]$ and `paths`.
for $i = 1$ **to** N_b **do**
  Select the path to the i-th leaf: `path` = `paths`$[i]$.
  Set $\widetilde{K} = K$, $\boldsymbol{v} = \boldsymbol{c}_i$, $a = 0$, $b = np$, and initialize a zero array $\boldsymbol{d}$ of size np.
  for $j = 1$ **to** length(`path`) **do**
    Set $l =$ `path`$[j]$ and N_{row} as the number of rows of $\widetilde{K}_{ll}$.
    if $l = 0$ **then**
      Select the first N_{row} rows of $\boldsymbol{v}$: $\boldsymbol{v} = \boldsymbol{v}[0 : N_{row}]$.
      Multiply $\boldsymbol{w} = \boldsymbol{v}\widetilde{K}_{01}$ and set $\boldsymbol{d}[b - \text{length}(\boldsymbol{w}) : b] = \boldsymbol{w}$.
      Update: $b = b - \text{length}(\boldsymbol{w})$.
    else
      Select the last N_{row} rows of $\boldsymbol{v}$: $\boldsymbol{v} = \boldsymbol{v}[\text{end} - N_{row} : \text{end}]$.
      Multiply $\boldsymbol{w} = \boldsymbol{v}\widetilde{K}_{10}$ and set $\boldsymbol{d}[a : a + \text{length}(\boldsymbol{w})] = \boldsymbol{w}$.
      Update: $a = a + \text{length}(\boldsymbol{w})$.
    end if
    Set $\widetilde{K} = \widetilde{K}_{ll}$.
  end for
  Diagonal block multiplication: $\boldsymbol{d}[a : b] = \boldsymbol{v}\tilde{K}$.
  Set $\widetilde{R}[i, :] = \boldsymbol{d}$.
end for

keeps the cost of such operation low. Thus, a substantial speedup can be obtained with respect to standard GMRES even when a small subset of the entire radiation dataset needs to be computed. In the grid test case the percentage of dense blocks is larger, resulting in a larger time for the initialization of Alg. 3 for the largest arrays.

Possible improvements include the parallelization of the loops in Alg. 2 and the use of a preconditioner also for the solution of the coarse problem, whose cost can become relevant for very large arrays. In the case of a single row of bodies, the coarse matrix A_c has a Toeplitz structure, and the natural choice in this case is to use a circulant preconditioner. This strategy has been explored at block level in [6], while some choices of circulant preconditioners are presented in [184].

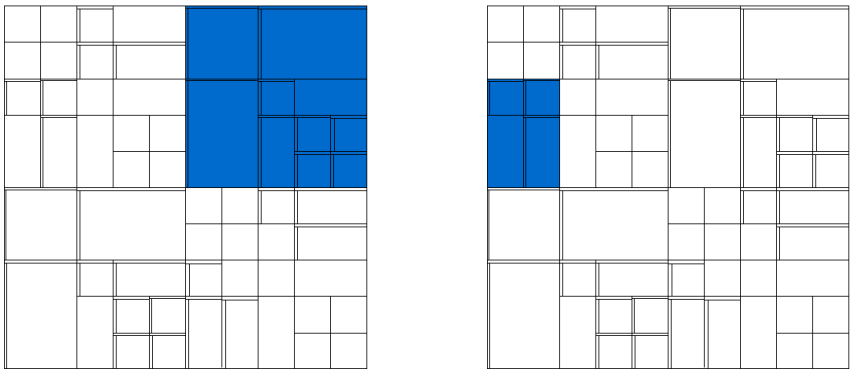

(a) $j = 1$ **(b)** $j = 2$

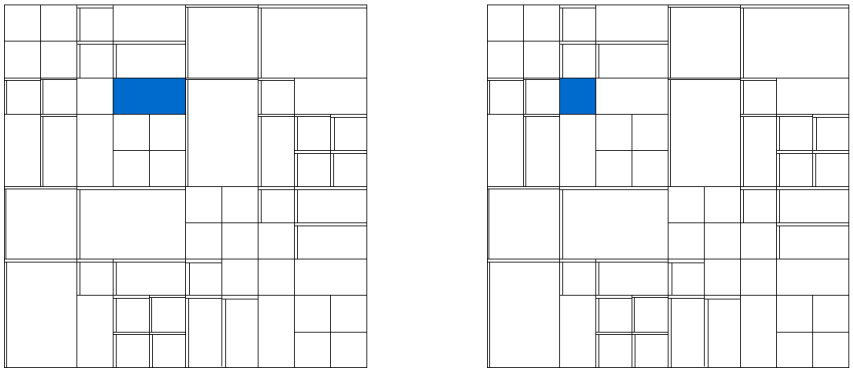

(c) $j = 3$ **(d)** *Diagonal block*

Figure 4.4: *Blocks selected for multiplication in Algorithm 3 for leaf* $i = 5$.

		GMRES			Preconditioned GMRES			
N_b	storage (%)	niter	t (s)	t/N_b (s)	init (s)	niter	t (s)	t/N_b (s)
80	6.19	12	18	0.23	0.47	7	15	0.19
160	3.32	13	107	0.67	1.05	7	68	0.85
240	2.33	14	449	1.87	1.64	7	294	1.23
320	1.75	14-15	831	2.60	2.51	7	487	1.52
400	1.43	15	1182	2.95	3.46	7	698	1.74
480	1.23	15-16	1715	3.57	4.14	7	993	2.07

		GMRES			Preconditioned GMRES			
N_b	storage (%)	niter	t (s)	t/N_b (s)	init (s)	niter	t (s)	t/N_b (s)
16	48.42	10	0.51	0.03	0.07	7	1.03	0.06
64	20.00	13	35	0.55	0.87	8	25	0.40
144	10.82	17	281	1.95	3.40	8-9	157	1.09
256	6.72	24-26	2216	8.66	15.5	9	826	3.23
400	4.82	38-43	7215	18.03	23.5	9-10	2030	5.08

Table 4.2: *Results of the numerical experiment. Top table: line geometry. Bottom table: grid geometry. In both tables, init is the time for initializing the coarse solver (coarse space definition).*

Part II

Optimization of wave energy converter arrays

Chapter 5

Review of control and optimization strategies

As discussed in the introduction (Chapter 1), economically feasible utilization of wave energy requires building arrays of devices. This poses the problem of designing park layouts, i.e. specifying the positions of the devices inside an available sea area, and devising suitable control strategies for the devices' operations. The final aim is in general considered to be the minimization of some suitable measure of the cost of energy, such as the levelized cost of energy (LCOE), which takes into account the entire lifetime of an energy system. In particular, it is the ratio between the sum of capital cost and discounted operational cost, and the amount of energy produced. However, because of the difficulty of estimating costs for such an emerging technology [77], the average power output is often considered as the objective function instead [161]. In particular, hydrodynamic interactions in the optimized, controlled system should be favorable in terms of extracted power. An exception is the work [65], in which the LCOE of a park was minimized by taking into account the cost of cables and electric substations. In Section 5.1, we outline the state of the art about layout optimization, control design, and their combination. Then, in Section 5.2, we discuss the treatment of operational constraints.

5.1 State of the art

The literature on layout design optimization has been examined in the reviews [70, 77, 179]. In some works a parametric layout is considered [63], or requirements that devices are placed on lines or circles are added [112], thus reducing the number of design parameters; most others, instead, consider as unknowns all the coordinates of the devices' centers. Different methods have been proposed for the solution of the optimization problem, adopting diverse points of view. A design method called parabolic intersection, based on a simplified description of hydrodynamics, was introduced in [31]: devices are iteratively placed at points of constructive interference between the ambient waves and the waves emitted by the already placed devices. The method is well suited for regular waves; however, an extension to irregular waves would not be straightforward [32, Chap. 9]. Little

work exists about the use of gradient-based layout optimization methods. An example is [113], where an SQP (sequential quadratic programming) algorithm based on a commercial optimization solver was used, and the point-absorber approximation was adopted; this requires the devices' characteristic dimensions to be significantly smaller than the wavelength. Most of the published research on layout optimization has instead adopted metaheuristic algorithms, such as genetic algorithms, differential evolution, and bio-inspired algorithms [179]. Hybrid algorithms, combining local and global search, have also been considered [125]. Regarding array size, numbers of bodies in the order of the tens, up to about a hundred, have been considered. In rare cases, arrays of hundreds of bodies have been treated, such as in [75]. Here, parameter exploration is performed, by adopting a single-body approximation: mutual hydrodynamic interactions between objects due to diffraction are neglected; interactions due to radiation are instead taken into account.

In order to discuss control strategies, let us start from the general form (2.11) of the dynamic equation and specify some possible forms of the control force $F_u(t)$. We refer to [93, 108] for an extensive review. The simplest choice is damping control, also referred to as passive control, which consists in applying a control force proportional to the device's velocity:

$$F_u(t) = -c_\ell \dot{\zeta}_\ell(t). \tag{5.1}$$

As shown in [49], damping is actually a nonlinear function of the velocity for real electrical generators. However, the linearity assumption greatly simplifies the treatment of optimization problems, and the results can still be a guide for the design process. It will be shown in Chapter 7 that the a water-turbine OWC device can be described, through linearization, as a system with damping control. An evolution of this is reactive control, which introduces an additional stiffness term, resulting in

$$F_u(t) = -c_\ell \dot{\zeta}_\ell(t) - \kappa_\ell \zeta_\ell(t). \tag{5.2}$$

The latter is the expression that was used throughout Chapter 2, and that will be considered in most of this thesis. The damping and stiffness coefficients may be either constant or variable in time. In the former case, modeling and optimization can be performed in the frequency domain, which is convenient for computation since systems of ordinary differential equation reduce to linear algebraic systems. Classical results obtained through frequency domain analysis for regular waves with control parameters kept constant in time are presented in [53]. In an array, the same control parameters may be assigned to all devices, or each device may be assigned its own. The latter approach is referred to as individual optimization and it has been performed in [17] and [156] using SQP, optimizing for a single wave direction and then checking the performance for different directions. For the specific case of a line of identical devices, and adding the mass to the optimization variables in addition to damping and stiffness, an insightful geometric interpretation can be given to the optimization problem [119].

Moving on from reactive control, it is also possible to avoid making specific assumptions on the form of $F_u(t)$, and to instead directly determine its optimal trajectory: we may call this non-parametric control. This may be done either for

each device separately, or by allowing exchange of information between the controllers of different devices. It has been demonstrated in [16] that improvements of the order of 10% can be achieved with inter-device communication. A theoretical analysis about non-parametric optimal control was performed in [185] by using Pontryagin's minimum principle and considering constraints on the maximum and minimum values of F_u. It is found that for a single heaving device, the optimal control is of bang-singular-bang type, meaning that the control alternates between intervals in which it coincides with its upper or lower bound (bang-bang) and intervals in which it assumes an intermediate value. This result can be extended to arrays [106]. The practical implementation of time-domain, non-parametric control can be done in many different ways; we mention here two approaches that have been considered in the literature: model predictive control (MPC) and Q-control. MPC [50, 93] requires the prediction of the wave forces on the controlled device over a time horizon (ideally, the longest possible). Then, the prediction is used to compute the optimal control on all such time horizon. In order to do so, a model of the system needs to be available. The computed control is applied only until the next step; then, the procedure is repeated to obtain a new sequence of optimal controls.[1] Dynamic programming [149] is a possible implementation of MPC; in particular, forward dynamic programming was applied to the WEC control optimization problem in [102]. Q-learning [122], differently from MPC, does not need neither a model of the system, nor a prediction of the forcing term. It is based on the definition of the so-called Q-function, or action-value function, which depends on the current state and control action, and whose value is the maximum sum of the future values of the objective (if maximization is pursued), appropriately discounted. The Q-function is learned and updated dynamically by the controller, and the control is chosen, at each step, with the following logic: with some probability it is chosen randomly; otherwise it is chosen to maximize Q. This is done to seek a balance between exploration, which provides a better estimate of Q, and exploitation, which effectively maximizes the objective. Values of Q can either be stored in a table [9] or learned by a neural network [122, 186]. On the topic of neural networks, we mention that machine learning techniques have recently been considered for control and optimization of wave energy converters: we refer to the review [154]. In particular, they have been applied to the problem of predicting wave loads [103].

Layout optimization can be performed either before or together with control optimization. Although array layout and control strategy are usually optimized separately, it has been recognized that their simultaneous optimization can lead to significantly better results in terms of power [63]. This approach is referred to as control co-design [125, 142].

5.2 Treatment of constraints

Optimization of wave energy parks must be done taking into account geometric and operational constraints. Here, we will discuss operational constraints, and

[1] This is quite intuitive, since it is reasonable to make, and act on, long-time plans based on the best available forecast of the future, but then be ready to change plans if the future outlook changes.

in particular their formulation in the frequency domain, which will be useful in Chapters 6 and 8. Geometric constraints on the array layout will have ad hoc treatments described in Chapters 7 and 8.

Because of physical and design requirements, the devices' motions need to be limited. This leads to the definitions of the slamming and stroke constraints [17, 39]. The slamming constraint requires that devices remain at least partially immersed during their oscillation. A body repeatedly leaving and subsequently re-entering the water would be subjected to significant loads, which could ultimately lead to fatigue damage. Moreover, such a situation would be beyond the limits of validity of the linear model. The constraint can be expressed as

$$\zeta_\ell(t) - \eta_\ell(t) \leq d_\ell, \quad \forall t, \quad \ell = 1, \dots, N_b, \tag{5.3}$$

where $\eta_\ell(t) := \eta(x_\ell, y_\ell, t)$, and where we recall that d_ℓ is the device's draft. A common approximation, that we adopt, is to take the undisturbed free surface elevation η_0 in place of η.

The stroke constraint is instead due to the specific design of the device, which could limit the oscillation amplitude, for example due to the presence of an end-stop, or due to limited length of moorings. Assuming symmetric bounds around the equilibrium elevation, we can write the constraint as

$$-d_{\ell,stroke} \leq \zeta_\ell(t) \leq d_{\ell,stroke}, \quad \forall t, \quad \ell = 1, \dots, N_b. \tag{5.4}$$

In the remainder of this thesis, we will only consider the slamming constraint, since it is a physical constraint that does not depend on the design details of a specific device. The two constraints can be treated in the frequency domain in a statistical sense in analogous ways; in the following, we will focus on slamming.

The linear fluid-structure interaction problem (2.39)-(2.40) can be interpreted as a linear time-invariant (LTI) system, whose input is the ambient incident wave height $\eta_0(x, y, t)$ (or, equivalently, the associated potential), and whose output is the vector of barycenter elevations of devices, $\boldsymbol{\zeta}(t)$. As discussed in Sec. 2.4, we assume η to be a Gaussian random process. If the input of an LTI system is Gaussian, then its output is Gaussian, too [130, Sec. 10.2]. Consequently, $\zeta_\ell - \eta_{0,\ell}$ is also a Gaussian process, and it has zero mean, because both ζ_ℓ and $\eta_{0,\ell}$ are combinations of harmonics of nonzero frequency (the constant, zero frequency component having been removed by linearization around the hydrostatic equilibrium: see Sec. 2.2). In order to compute the probability that the constraint (5.3) is violated, intended as fraction of time, it then suffices to know the variance of $\zeta_\ell - \eta_{0,\ell}$, which can be computed from frequency domain data. This avoids completely the necessity of building an actual time domain realization of the process, thus fitting conveniently in a frequency domain framework.

In the remainder of this section we will concentrate on a single device and drop subscript ℓ for convenience. Let us define the random process

$$W(t) := \zeta(t) - \eta_0(t) = \mathrm{Re}\left[\sum_{q=1}^{N_f} \hat{w}_q \exp(-i\omega_q t)\right], \quad \hat{w}_q := \hat{\zeta}_q - \hat{\eta}_{0,q}, \tag{5.5}$$

where $\hat{\zeta}_q$ is the q-th frequency component of the device's oscillation amplitude. The variance of W is

$$w_{rms}^2 = \frac{1}{2}\sum_{q=1}^{N_f} |\hat{w}_q|^2 \tag{5.6}$$

The probability that $W \geq w$ is then

$$P(W \geq w) = 1 - \Phi\left(\frac{w}{w_{rms}}\right), \tag{5.7}$$

where Φ is the normal cumulative distribution. The probability that $|W| > w$ is instead twice the above result. The probability of constraint violation is thus $P(W \geq d)$, and, in order to guarantee that a prescribed value P_{max} is not exceeded, we must have

$$\Phi\left(\frac{d}{w_{rms}}\right) \geq 1 - P_{max} \tag{5.8}$$

which implies

$$w_{rms} \leq \alpha d, \tag{5.9}$$

with

$$\alpha = \frac{1}{\Phi^{-1}(1 - P_{max})}. \tag{5.10}$$

Equation (5.9) corresponds to the formulation proposed in [17], and the one we adopt. This treatment of the constraint also admits an interpretation in terms of the fraction of peaks exceeding the threshold. Let us call W_p the random variable describing the peaks of $W(t)$. The probability distribution of peaks satisfies [96, Sec. 6.7]

$$P(W_p \geq w) = \frac{1}{2}\mathrm{erfc}\left(\frac{w/w_{rms}}{\sqrt{2(1-r^2)}}\right) + \frac{r}{2}e^{-\frac{w^2}{2w_{rms}^2}}\left[1 + \mathrm{erf}\left(\frac{rw/w_{rms}}{\sqrt{2(1-r^2)}}\right)\right], \tag{5.11}$$

where erf is the error function and erfc the complementary error function. Here, r is called irregularity factor, and it is the ratio between the number of positive zero crossings and the number of positive maxima of $W(t)$ per unit time. It can be computed in terms of the statistical properties of the signal as

$$r = \frac{\dot{w}_{rms}^2}{w_{rms}\ddot{w}_{rms}}. \tag{5.12}$$

If $W(t)$ is narrow banded, than $r = 1$ and the peaks are described by a Rayleigh distribution, obtained as a limit of (5.11). The probability in a generic case in which $0 \leq r \leq 1$ is shown in Figure 5.1: in particular, the case $r = 1$ is associated with the largest exceedance probability, and thus using the Rayleigh distribution provides an upper bound in the general case. If (5.9) is fulfilled, we have

$$P(W_p \geq w) \leq P(W_p \geq w)|_{r=1} = \exp\left(-\frac{d^2}{2w_{rms}^2}\right) \overset{(5.9)}{\leq} \exp\left(-\frac{1}{2\alpha^2}\right). \tag{5.13}$$

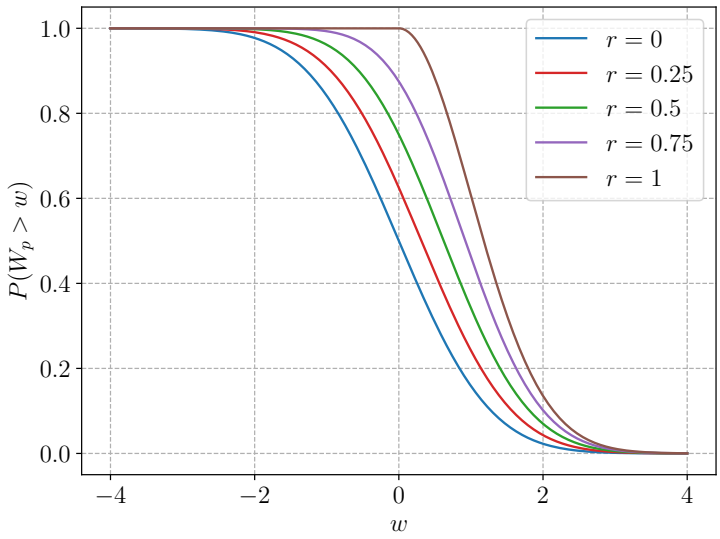

Figure 5.1: *Probability of a peak of $W(t)$ exceeding threshold w for different values of the irregularity factor r (see* (5.11)*).*

Wave spectra have a wide significant bandwidth, so that $W(t)$ cannot be expected to be narrow banded [69], and (5.13) is a cautionary estimate.[2]

We briefly mention that, in alternative to limit the fraction of time above threshold, one could enforce the slamming and stroke constraints by limiting the exceedance frequency. This can be computed using Rice's formula [146]: for a zero-mean Gaussian process, the expected number of positive upcrossings of level w per unit time is

$$\mu^+(w) = \frac{1}{2\pi}\frac{\dot{w}_{rms}}{w_{rms}} \exp\left(-\frac{w^2}{2w_{rms}^2}\right). \tag{5.14}$$

The variance of $\dot{w}$ can be computed as

$$\dot{w}_{rms}^2 = \frac{1}{2}\sum_{q=1}^{N_f} \omega_q^2 |\hat{w}_q|^2. \tag{5.15}$$

[2]We observe, for example, that for a Pierson-Moskowitz spectrum (2.79), $\ddot{\eta}_{rms}$ is not even well defined. Indeed, we have $\ddot{\eta}_{rms}^2 = \int_0^\infty S(f) f^4 df$ [96], and this improper integral does not converge. This is not surprising, because the right tail of the spectrum describes, by construction, the appearance of sharp crests in the wave profile, which correspond to discontinuities of the first derivative, and to Dirac deltas appearing in the second derivative. In fact, in [147] it is suggested to truncate the high frequency components of the spectrum in order to match the observed irregularity factor.

Chapter 6

Robust optimal reactive control of arrays

Starting with this chapter and continuing with the next two, we gradually tackle the problem of optimizing WEC arrays. We start here by presenting a numerical strategy for the robust optimization (maximization) of the power production for arrays of WECs of the WAB type (see Chapter 1) with respect to control parameters. In Chapter 7 we will consider layout optimization, and in Chapter 8 combined layout-control optimization. The content of this chapter is mainly derived from our work [61].[1] We assume that the layout of the array has already been fixed, and concentrate on the control parameters. In particular, we consider reactive control (see Chapter 5): damping and stiffness coefficients of the generators are optimized. We allow each body to have its own control coefficients and assume that the corresponding parameters are constant in time. We also allow control stiffnesses to assume negative values, meaning that the control action must be able to counteract the hydrostatic restoring force, that is the force acting on a floating body when it is displaced from its buoyancy equilibrium position [53, Sec. 5.9]. Even though a negative stiffness could seem counterintuitive or unphysical, such effect, which requires allowing reactive power flow, can indeed be achieved either at the level of the power take-off system [133, Chap. 10], [152] or through specifically designed mechanical systems [165, 182]. For this reason, we do not exclude apriori this case from the set of admissible solutions. Moreover, the optimal solutions must fulfill the slamming constraint (see Sec. 5.2), meaning that devices must not leave the water, and in some test cases we add the constraint of positive stiffness, to assess the benefit of using negative stiffness technologies.

To obtain good performances in real scenarios, the result of optimization needs to be robust against the uncertainty in the incident waves direction. By uncertainty, we mean the fact that the wave spectrum at the location of a WEC array has a directional dependence, as discussed in Sec. 2.4. Hence, at any given time, the array will be subjected to waves coming from a direction that we consider a random parameter. While the sensitivity of WEC array performance to the wave direction is a known fact in the literature [63, 76, 156], to the best of our

[1] © 2023 The Authors. Published by Elsevier Inc. The article is licensed under the CC BY license (http://creativecommons.org/licenses/by/4.0/).

knowledge, the problem of directionally robust control has never been addressed.

In Sec. 6.1.1, we formulate our stochastic (robust) optimal control problem, governed by linear hydrodynamic equations, describing the physics of the system, and characterized by control and state constraints. In Sec. 6.1.2, it will then be proved that the state equation admits a solution, and that the cost function has a minimum. The numerical solution of this optimization problem requires an adequate treatment of different issues: we discuss them, and propose solution strategies, in Sec. 6.2. A reduced approach based on the adjoint equation allows us to work in the space of solutions of the hydrodynamic equations and consider the control as the only optimization variable. Stochasticity is addressed by employing two different approaches suitable for stochastic optimization problems: SAA (Sample Average Approximation) and SA (Stochastic Approximation) [155]. The slamming (state) constraint is treated by using a penalty approach, while the stiffness (control) constraint is enforced by projection. Therefore, our proposed numerical computation framework is obtained by two nested iterative processes. The outer iteration is essentially a quadratic penalty method increasing at each iteration the weight of the penalty term for the slamming constraint. At each penalty iteration a stochastic optimal control problem is solved by a projection method based either on SA or SAA. Results of numerical experiments are reported in Sec. 6.3. The performances obtained by individually optimizing the coefficients of each device are compared with those obtained by setting the coefficients of all devices equal to the tuning parameters of the isolated case. We show that sets of parameters corresponding to feasible solutions for isolated devices can lead to unfeasible (incompatible with the constraints) solutions when the devices are installed in arrays, and that the optimization process leads to sensible increases of the power output in most cases.

6.1 Optimization problem

6.1.1 Problem statement

The cost function that we want to minimize is the expected value with respect to the wave direction β of the time-averaged power of the array, with negative sign. The instantaneous power lost by the ℓ-th device due to the control force $F_u(t)$, and thus available for conversion into electrical energy, can be computed as

$$P_\ell(t) = -F_u(t)\dot{\zeta}_\ell(t). \tag{6.1}$$

In the case of reactive control (5.2), we have

$$P_\ell(t) = \left[c_\ell\dot{\zeta}_\ell(t) + \kappa_\ell\zeta_\ell(t)\right]\dot{\zeta}_\ell(t). \tag{6.2}$$

Now, since Airy wave theory is considered, the elevation of each device can be written as a sum of harmonics. We have

$$\zeta_\ell(t) = \sum_{q=1}^{N_f} \mathrm{Re}\left[\hat{\zeta}_{\ell q}\exp[-i(\omega_q t + \varphi_q)]\right], \tag{6.3}$$

where $\hat{\zeta}_{\ell q} \in \mathbb{C}$ is the q-th frequency component of the ℓ-th device's oscillation amplitude, and φ_q is the phase of the q-th wave component, which we will neglect in the following, as it does not influence the average power. We will call the average power over time simply P_ℓ, without time dependence. It is obtained by substituting (6.3) into (6.2) and averaging:

$$\begin{aligned} P_\ell = \lim_{T\to\infty} \int_0^T \Bigg\{ & c_\ell \sum_{q,r=1}^{N_f} \mathrm{Re}\left[-i\omega_q \hat{\zeta}_{\ell q} \exp(-i\omega_q t)\right] \mathrm{Re}\left[-i\omega_r \hat{\zeta}_{\ell r} \exp(-i\omega_r t)\right] \\ & + \kappa_\ell \sum_{q,r=1}^{N_f} \mathrm{Re}\left[\hat{\zeta}_{\ell q} \exp(-i\omega_q t)\right] \mathrm{Re}\left[-i\omega_r \hat{\zeta}_{\ell r} \exp(-i\omega_r t)\right] \Bigg\} dt. \end{aligned} \tag{6.4}$$

Here, the only contributions with non-zero mean are the ones due to damping, and with $q = r$, this last condition being due to the orthogonality of harmonics. The result, summed over all the devices of the array, is

$$P = \frac{1}{2} \sum_{\ell=1}^{N_b} c_\ell \sum_{q=1}^{N_f} \left(\omega_q |\hat{\zeta}_{\ell q}|\right)^2. \tag{6.5}$$

Up to here, we have not specified a wave direction. To be explicit, and for convenience in the following, we will call $\hat{\boldsymbol{\zeta}}_q^\beta := [\hat{\zeta}_{q1}^\beta, \dots, \hat{\zeta}_{qN_b}^\beta]$ the vector of the q-th frequency component oscillation amplitudes of all devices, and $\hat{\boldsymbol{\zeta}}^\beta \in \mathbb{C}^{N_b N_f}$ the collection of all $\hat{\boldsymbol{\zeta}}_q^\beta$ for $q = 1, \dots, N_f$. The power must be maximized with respect to the damping and stiffness coefficients, which we collect in the control vector $\boldsymbol{u} = [c_1, \dots, c_{N_b}, \kappa_1, \dots, \kappa_{N_b}] \in \mathbb{C}^{2N_b}$. This must be done subject to a state equation of the form (2.70) for each frequency: we thus must have

$$\sum_{m=1}^{N_b} Z_{m\ell,q} \hat{\zeta}_{\ell q} = \hat{F}_{\ell q}, \tag{6.6}$$

with the expression (2.71) of the impedance matrix:

$$Z_{\ell m,q} = -\omega_q^2 (m_\ell \delta_{\ell m} + A_{\ell m,q})) - i\omega (c_\ell \delta_{\ell m} + B_{\ell m,q}) + (\kappa_\ell + \kappa_{h,\ell}) \delta_{\ell m}. \tag{6.7}$$

Moreover, the slamming constraint needs to be imposed, in the form (5.9). We rewrite the latter as the system of inequality constraints

$$g_\ell\left(\hat{\boldsymbol{\zeta}}\right) \le 0, \quad g_\ell(\hat{\boldsymbol{\zeta}}) := \sum_q \left|\hat{\zeta}_{\ell q} - \hat{\eta}_{0,\ell q}\right|^2 - 2\alpha^2 d_\ell^2, \quad \ell = 1, \dots, N_b, \tag{6.8}$$

and then recast it as a differentiable equality constraint $h_\ell\left(\hat{\boldsymbol{\zeta}}\right) = 0$, where

$$h_\ell\left(\hat{\boldsymbol{\zeta}}\right) := \left[g_\ell\left(\hat{\boldsymbol{\zeta}}\right)\right]_+^2, \quad [g]_+ := \max(g, 0). \tag{6.9}$$

The two expressions (6.8) and (6.9) are equivalent in the sense that they define the same active set: $h_\ell\left(\hat{\boldsymbol{\zeta}}\right) = 0 \Leftrightarrow g_\ell\left(\hat{\boldsymbol{\zeta}}\right) \leq 0$. We can now write the expression of our cost function for a fixed wave direction, with its explicit dependencies:

$$J(\boldsymbol{u}, \hat{\boldsymbol{\zeta}}^\beta) = -\frac{1}{2}\sum_{q=1}^{N_f} \omega_q^2 \left(\hat{\boldsymbol{\zeta}}_q^\beta\right)^H C \hat{\boldsymbol{\zeta}}_q^\beta, \tag{6.10}$$

where C is a diagonal matrix with $C_{\ell\ell} = c_\ell$. We require that all bodies have positive generator damping, implying that the mean extracted power is positive for each of them. The admissible set of controls $\mathcal{U}_{ad}$ is then defined by

$$\mathcal{U}_{ad} = \left\{\boldsymbol{u} \in \mathbb{R}^{2N_b} : c_\ell \geq \varepsilon > 0, \kappa_\ell \geq \gamma, \quad \ell = 1, \dots, N_b\right\}, \tag{6.11}$$

where ε is a positive constant, and $\gamma = 0$ if the positive stiffness constraint is applied, $\gamma = -\infty$ otherwise. Finally, our robust optimization problem can be expressed as

$$\min_{\hat{\boldsymbol{\zeta}}^\beta, \boldsymbol{u}\in\mathcal{U}_{ad}} \mathbb{E}_\beta\left[J(\boldsymbol{u}, \hat{\boldsymbol{\zeta}}^\beta)\right] \quad \text{s.t.} \quad \begin{cases} Z_q(\mathbf{u})\hat{\boldsymbol{\zeta}}_q^\beta = \hat{\boldsymbol{F}}_q^\beta & q = 1, \dots, N_f, \ \forall\beta \\ \mathbb{E}_\beta[h_\ell(\hat{\boldsymbol{\zeta}}^\beta)] = 0 & \ell = 1, \dots, N_b, \end{cases} \tag{6.12}$$

where $\mathbb{E}_\beta$ denotes the expected value with respect to β.

6.1.2 Well-posedness of the optimization problem

In the following, we will prove that problem (6.12) is well-posed, in the sense that it admits a solution. We will proceed as follows. First, we will prove that the state equation (6.6) is uniquely solvable for any control vector $\boldsymbol{u}$, any frequency index q and for any wave direction β. Then, we will use this result to pass to the reduced problem, that is, to eliminate the vector of state variables $\hat{\boldsymbol{\zeta}}^\beta$ from the unknowns. The reduced problem will then be proved to be well-posed for a fixed value of β, and finally for the robust case. For a single wave angle, our problem can be stated as

$$\min_{\hat{\boldsymbol{\zeta}}^\beta, \boldsymbol{u}\in\mathcal{U}_{ad}} J(\boldsymbol{u}, \hat{\boldsymbol{\zeta}}^\beta) \quad \text{s.t.} \quad \begin{cases} Z_q(\mathbf{u})\hat{\boldsymbol{\zeta}}_q^\beta = \hat{\boldsymbol{F}}_q^\beta & q = 1, \dots, N_f, \\ h_\ell(\hat{\boldsymbol{\zeta}}^\beta) = 0 & \ell = 1, \dots, N_b. \end{cases} \tag{6.13}$$

Let us start by discussing sufficient conditions for $Z_q(\boldsymbol{u})$ to be invertible.

Lemma 6.1.1. *Let $Z \in \mathbb{C}^{N\times N}$ and call $Z_r = Re(Z)$, $Z_i = Im(Z)$. If Z_r is symmetric and Z_i is symmetric positive (or negative) definite, then Z is invertible.*

Proof. Consider a generic system $(Z_r + iZ_i)(\mathbf{x}_r + i\mathbf{x}_i) = \mathbf{f}_r + i\mathbf{f}_i$. Splitting into real and imaginary parts and solving formally for $\mathbf{x}_r$ and $\mathbf{x}_i$ yields

$$\mathbf{x}_r = \widetilde{Z}^{-1}(Z_r Z_i^{-1}\mathbf{f}_r + \mathbf{f}_i), \quad \mathbf{x}_i = (I + Z_i^{-1}Z_r\widetilde{Z}^{-1}Z_r)Z^{-1}\mathbf{f}_r + Z_i^{-1}Z_r\widetilde{Z}^{-1}\mathbf{f}_i, \tag{6.14}$$

where $\widetilde{Z}$ is the Schur complement $\widetilde{Z} = Z_i + Z_r Z_i^{-1} Z_r$. Suppose Z_i is positive definite, so that its inverse is also positive definite (an analogous argument applies

if Z_i is negative definite). Z_r is real and symmetric, thus $Z_r^H = Z_r$. Then $\widetilde{Z}$ is positive definite:

$$\begin{aligned}\mathbf{v}^H(Z_i + Z_r Z_i^{-1} Z_r)\mathbf{v} &= \mathbf{v}^H Z_i \mathbf{v} + \left(\mathbf{v}^H Z_r^H\right) Z_i^{-1} \left(Z_r \mathbf{v}\right) \\ &= \mathbf{v}^H Z_i \mathbf{v} + \left(Z_r \mathbf{v}\right)^H Z_i^{-1} \left(Z_r \mathbf{v}\right) > 0, \quad \forall \mathbf{v} \neq 0.\end{aligned} \tag{6.15}$$

Since $\widetilde{Z}$ is invertible, the expressions in (6.14) are well defined for any $\mathbf{f}$ and thus Z is invertible. □

Consider now the impedance matrix (6.7), for any given wave frequency ω_q. Matrices A and B are symmetric, and because of energy conservation B is also positive semidefinite (see Sec. 2.3.2). The other involved matrices are diagonal and thus symmetric. Then, the real part of the impedance matrix $Z_r = -\omega^2(M + A) + K$, where K is the diagonal matrix of control and hydrostatic stiffnesses, is symmetric. Regarding the imaginary part $Z_i = -\omega(B + C)$, we have that B is symmetric positive semidefinite. Because of the definition of the admissible set (6.11), C is diagonal with positive values. Thus Z_i is symmetric positive definite and Z_r is symmetric, satisfying the hypotheses of Lemma 6.1.1.

Since the matrix $Z_q(\mathbf{u})$ is invertible for any admissible control vector $\mathbf{u}$, we can formally eliminate the constraint $Z_q(\mathbf{u})\hat{\boldsymbol{\zeta}}^\beta = \hat{\mathbf{F}}^\beta$ and rewrite (6.13) in the reduced form

$$\min_{\boldsymbol{u} \in \mathcal{U}_{ad}} \widetilde{J}(\boldsymbol{u}; \beta) := J(\boldsymbol{u}, \hat{\boldsymbol{\zeta}}^\beta(\boldsymbol{u})) \quad \text{s.t.} \quad h_\ell(\hat{\boldsymbol{\zeta}}^\beta(\boldsymbol{u})) = 0 \quad \ell = 1, \dots, N_b. \tag{6.16}$$

The following properties hold for the case of a single wave direction β. First, we observe that, under our assumptions, the average power produced by the array will be positive (and thus the cost function negative), unless there is no wave forcing.

Lemma 6.1.2. *If there exists an index $\overline{q} \in 1, \dots, N_f$ such that $\hat{\boldsymbol{F}}_{\overline{q}}^\beta \neq 0$, then $\widetilde{J}(\boldsymbol{u}) < 0 \quad \forall \boldsymbol{u} \in \mathcal{U}_{ad}$. Otherwise, $\widetilde{J}(\boldsymbol{u}) = 0 \; \forall \boldsymbol{u} \in \mathcal{U}_{ad}$.*

Proof. Lemma 6.1.1 ensures that $Z_{\overline{q}}(\boldsymbol{u})$ is invertible for all $\boldsymbol{u} \in \mathcal{U}_{ad}$. Then, $\hat{\boldsymbol{F}}_{\overline{q}}^\beta \neq 0$ implies $\hat{\boldsymbol{\zeta}}_{\overline{q}}^\beta \neq 0$. From this and using again the assumption that $\boldsymbol{u} \in \mathcal{U}_{ad}$, so that in particular $c_\ell > 0$ for all values of ℓ, it follows that $\left(\hat{\boldsymbol{\zeta}}_{\overline{q}}^\beta\right)^H C \hat{\boldsymbol{\zeta}}_{\overline{q}}^\beta > 0$. From the definition of J (6.10) we have $\widetilde{J}(\boldsymbol{u}) \leq -\frac{1}{2}\omega_{\overline{q}}^2 \left(\hat{\boldsymbol{\zeta}}_q^\beta\right)^H C \hat{\boldsymbol{\zeta}}_{\overline{q}}^\beta < 0$. □

The following lemma guarantees that the optimal controls cannot be at infinity, because no power would be extracted in this limit.

Lemma 6.1.3. *The following asymptotics hold for $\|\boldsymbol{u}\|_2 \to \infty$ and $\forall q$, $\forall \beta$:*

$$\|Z_q(\boldsymbol{u})\|_2 = \mathcal{O}\left(\|\boldsymbol{u}\|_2\right), \quad \|\hat{\boldsymbol{\zeta}}_q^\beta\|_2 = \mathcal{O}\left(\frac{1}{\|\boldsymbol{u}\|_2}\right).$$

In particular, $\lim_{\|\boldsymbol{u}\|_2 \to \infty} \widetilde{J}(\boldsymbol{u}) = 0$.

Proof. From the expression (6.7) of the impedance matrix, one directly finds $\|Z_q(\boldsymbol{u})\|_F = \mathcal{O}(\|\boldsymbol{u}\|_2)$ for $\|\boldsymbol{u}\| \to \infty$. The equivalence between the Frobenius norm and the 2-norm implies $\|Z_q(\boldsymbol{u})\|_2 = \mathcal{O}(\|\boldsymbol{u}\|_2)$.

For the second statement, consider

$$\|\hat{\boldsymbol{\zeta}}_q^{\beta}(\boldsymbol{u})\|_2 = \|Z_q(\boldsymbol{u})^{-1}\boldsymbol{F}_q\|_2 \leq \|Z_q(\boldsymbol{u})^{-1}\|_2 \|\boldsymbol{F}_q^{\beta}\|_2.$$

Since $\boldsymbol{F}_q$ does not depend on $\boldsymbol{u}$, we have

$$\|\hat{\boldsymbol{\zeta}}_q^{\beta}(\boldsymbol{u})\|_2 = \mathcal{O}\left(\frac{1}{\|Z_q(\boldsymbol{u})^{-1}\|_2}\right) = \mathcal{O}\left(\frac{1}{\|\boldsymbol{u}\|_2}\right).$$

□

Lemma 6.1.4. *There exists a constant $\widetilde{C} > 0$ such that*

$$\min_{\boldsymbol{u}\in\mathcal{U}_{ad}} \widetilde{J}(\boldsymbol{u}) \Leftrightarrow \min_{\boldsymbol{u}\in\mathcal{U}_{ad}\cap\overline{\mathcal{B}_0(\widetilde{C})}} \widetilde{J}(\boldsymbol{u}),$$

where $\mathcal{B}_0(\widetilde{C})$ is a ball of radius $\widetilde{C}$ centered in the origin.

Proof. Lemmas 6.1.2 and 6.1.3 imply that

$$\forall M < 0 \quad \exists \widetilde{C} > 0 \quad \text{s.t.} \quad \widetilde{J}(\boldsymbol{u}) > M \ \forall \boldsymbol{u} \in \mathcal{U}_{ad} \cap \overline{\mathcal{B}_0\left(\widetilde{C}\right)}^{\mathcal{C}}.$$

Consider a control vector $\widetilde{\boldsymbol{u}}$ such that $\widetilde{J}(\widetilde{\boldsymbol{u}}) = M < 0$. Then $\widetilde{J}(\boldsymbol{u}) > \widetilde{J}(\widetilde{\boldsymbol{u}})\ \forall \boldsymbol{u} \in \mathcal{U}_{ad} \cap \overline{\mathcal{B}_0\left(\widetilde{C}\right)}^{\mathcal{C}}$. In particular, if $\widetilde{J}$ has a minimum over such set, then the latter is also a minimum over $\mathcal{U}_{ad}$.

□

Having restricted the problem to a compact set, we can now prove that a minimum exists.

Theorem 6.1.1. *Under the assumptions of Lemma 6.1.2, Problem*

$$\min_{\boldsymbol{u}\in\mathcal{U}_{ad}} \widetilde{J}(\boldsymbol{u};\beta)$$

admits a solution for any β.

Proof. Invertibility of the impedance matrix $Z_q(\boldsymbol{u})$ guarantees that the reduced cost $\widetilde{J}$ is a continuous function of $\boldsymbol{u}$. Lemma 6.1.4 implies that the problem can be equivalently posed on the compact set $\mathcal{U}_{ad}\cap\overline{\mathcal{B}_0\left(\widetilde{C}\right)}$. The existence of a minimum in such set is guaranteed by the Weierstrass theorem. □

The above theorem proved the existence of a minimum without taking into account the slamming constraint: we now include it in our reasoning.

Theorem 6.1.2. *Under the assumptions of Lemma 6.1.2, Problem* (6.16) *admits a solution for any β.*

Proof. Define $h_\ell(\boldsymbol{u}) := h_\ell(\hat{\boldsymbol{\zeta}}^\beta(\boldsymbol{u}))$, $h_\ell : \mathbb{R}^{2N_b} \to \mathbb{R}_+$. We equivalently recast (6.16) as $\min_{\boldsymbol{u}\in\mathcal{U'}_{ad}} \widetilde{J}(\boldsymbol{u};\beta)$, where $\mathcal{U'}_{ad} = \mathcal{U}_{ad} \cap \overline{\mathcal{B}_0\left(\widetilde{C}\right)} \cap \left(\cap_{\ell=1}^{N_b} h_\ell^{-1}(0)\right)$. Since $\{0\}$ is a compact set and h_ℓ is continuous for all ℓ, $h_\ell^{-1}(0)$ is compact. Then, $\mathcal{U'}_{ad}$ is also compact and the same reasonings of Theorem 6.1.1 can be applied. □

Let us go back to the original, robust optimization problem (6.12). Thanks to the solvability of the state problems, it can be recast in reduced form as follows:

$$\begin{aligned} \min_{\boldsymbol{u}\in\mathcal{U}_{ad}} \widetilde{j}(\mathbf{u}) &:= \mathbb{E}_\beta\left(\widetilde{J}(\boldsymbol{u};\beta)\right) \\ \text{s.t.} \quad \mathbb{E}_\beta\left(h_\ell\right) &= 0, \quad \ell = 1,\dots,N_b. \end{aligned} \tag{6.17}$$

We can now prove that it is well posed, using arguments very similar to the ones of the deterministic case.

Theorem 6.1.3. *Problem*

$$\begin{aligned} \min_{\boldsymbol{u}\in\mathcal{U}_{ad}\cap\overline{\mathcal{B}_0\left(\widetilde{C}\right)}} \widetilde{j}(\mathbf{u}) &:= \mathbb{E}_\beta\left(\widetilde{J}(\boldsymbol{u};\beta)\right) \\ s.t. \quad \mathbb{E}_\beta\left(h_\ell\right) &= 0, \quad \ell = 1,\dots,N_b \end{aligned}$$

admits a solution for all $\widetilde{C} > 0$.

Proof. Lemma 6.1.2 guarantees that $\widetilde{J}(\boldsymbol{u},\beta) \le 0\,\forall\beta$, $\forall\boldsymbol{u}\in\mathcal{U}_{ad}$. Then, we have

$$\widetilde{j}(\boldsymbol{u}) = \mathbb{E}_\beta\left(\widetilde{J}(\boldsymbol{u},\beta)\right) \le 0 \quad \forall\boldsymbol{u}\in\mathcal{U}_{ad}.$$

Furthermore, we have

$$\begin{aligned} \lim_{\|\boldsymbol{u}\|_2\to\infty} \left|\widetilde{j}(\boldsymbol{u})\right| &= \lim_{\|\boldsymbol{u}\|_2\to\infty} \left|\int_0^{2\pi} \widetilde{J}(\boldsymbol{u},\beta)D(\beta)\,\mathrm{d}\beta\right| \\ &\le \lim_{\|\boldsymbol{u}\|_2\to\infty} \left|\max_\beta \widetilde{J}(\boldsymbol{u},\beta)\right| \left|\int_0^{2\pi} D(\beta)\,\mathrm{d}\beta\right| = 0, \end{aligned}$$

where the last equality follows from Lemma 6.1.3. Then, the problem can be equivalently recast in a compact set $\mathcal{U}_{ad} \cap \overline{\mathcal{B}_0\left(\widetilde{C}\right)}$, for some suitable positive constant $\widetilde{C}$. Since such set is compact and $\widetilde{J}$ is a continuous function of both its arguments, the Heine-Cantor theorem implies $\widetilde{J}$ is also uniformly continuous. We now use uniform continuity and the fact that $D(\beta)$ is a probability distribution, so that it has unit integral. We have

$$\forall\varepsilon > 0 \quad \exists\delta > 0 \quad \text{s.t.} \quad \|\boldsymbol{u}-\boldsymbol{v}\| < \delta \Rightarrow \left|\widetilde{J}(\boldsymbol{u},\beta) - \widetilde{J}(\boldsymbol{v},\beta)\right| < \varepsilon,$$

where δ does not depend on β. Then, if $\|\boldsymbol{u}-\boldsymbol{v}\| < \delta$, the following inequality

$$\left|\widetilde{j}(\boldsymbol{u}) - \widetilde{j}(\boldsymbol{v})\right| = \left|\int_0^{2\pi} \widetilde{J}(\boldsymbol{u},\beta)D(\beta)\,\mathrm{d}\beta - \int_0^{2\pi} \widetilde{J}(\boldsymbol{v},\beta)D(\beta)\,\mathrm{d}\beta\right|$$

$$= \left| \int_0^{2\pi} \left[\widetilde{J}(\boldsymbol{u}, \beta) - \widetilde{J}(\boldsymbol{v}, \beta) \right] D(\beta) \, \mathrm{d}\beta \right|$$
$$\leq \max_{\beta} \left| \widetilde{J}(\boldsymbol{u}, \beta) - \widetilde{J}(\boldsymbol{v}, \beta) \right| \left| \int_0^{2\pi} D(\beta) \, \mathrm{d}\beta \right| < \varepsilon$$

proves that $\widetilde{j}(\boldsymbol{u})$ is also continuous. Then, existence of a solution for the unconstrained problem follows from the same reasonings applied in the proofs of Lemma 6.1.4 and Theorem 6.1.1.

To include the slamming constraint, we can prove, as done above for $\widetilde{j}$, that $\mathbb{E}_\beta[h_\ell(\boldsymbol{u})]$ is continuous, so its inverse maps $\{0\}$ into a compact set. Then, the remainder of the proof is the same as for Theorem 6.1.2.

□

6.2 Numerical optimization strategy

In this section, we present a computational framework for the solution of the stochastic optimization problem (6.12). It has three different constraints that must be appropriately treated: a system of complex algebraic equations (the state problem), the slamming constraint (a constraint on the state) and the positive stiffness constraint (a constraint on the controls). First, the slamming (state) constraint is treated by using a penalty method, as described in Section 6.2.1. Our framework is based on a reduced approach working in the space of solutions to the state equation and considers the control $\boldsymbol{u}$ as the only optimization variable. To do so, the gradient of the (reduced) cost $\widetilde{j}$ (and its penalized counterpart Q_μ) is obtained by a Lagrangian approach leading to an adjoint problem, as shown in Section 6.2.2. Each iteration of the penalty method requires the solution of a stochastic optimization problem. This is achieved by either an SAA approach (Section 6.2.3), or by a Robust SA (Section 6.2.4). In both cases, if the control constraint of positive stiffness is considered, it is enforced by projection onto the admissible set at each iteration. Moreover, the computation of the diffraction force for given, or random, wave directions, is required: this is discussed in Sec. 6.2.5. Implementation details and a comparison between SAA and Robust SA are given in Section 6.2.6.

6.2.1 Penalty method

The penalized cost function used to enforce the slamming constraint is defined as

$$Q_\mu(\boldsymbol{u}) := \widetilde{j}(\mathbf{u}) + \frac{\mu}{2} \sum_{\ell=1}^{N_b} \mathbb{E}_\beta[h_\ell(\mathbf{u})]$$

and the penalty method consists in solving the sequence of problems

$$\min_{\boldsymbol{u} \in \mathcal{U}_{ad}} Q_\mu(\boldsymbol{u}), \quad \mu \to \infty.$$

The penalized cost function can be rewritten as an expected value thanks to linearity,

$$Q_\mu(\boldsymbol{u}) = \mathbb{E}_\beta \left[\widetilde{J}(\mathbf{u}) + \frac{\mu}{2} \sum_{\ell=1}^{N_b} h_\ell(\mathbf{u}) \right],$$

and, again because of linearity, also the gradient of Q_μ may be computed as the expected value of the quantity in brackets. The optimization procedure is detailed in Algorithm 4.

Algorithm 4 Stochastic quadratic penalty algorithm

1: Set $\boldsymbol{u}_0$, μ_0, $k_\mu > 1$, τ^{out}, $0 < \tau^{out} < 1$, it^{out}_{max}
2: Set $j = 0$
3: **while** $\max_\ell \mathbb{E}_\beta[h_\ell] > \tau^{out}$ **and** $j < it^{out}_{max}$ **do**
4: Compute $\boldsymbol{u}^{j+1} \in \mathcal{U}_{ad}$ by minimizing Q^{j+1}, using either SA or SAA with initial guess $\boldsymbol{u}^j$ and tolerance τ^j
5: $\mu^{j+1} = k_\mu \mu^j$
6: $\tau^{j+1}_{in} = k_\tau \tau^j_{in}$
7: $j \leftarrow j + 1$
8: **end while**

Convergence results for Algorithm 4 can be obtained from [127, Th. 17.1, 17.2]. It is proved that, if at each iteration the exact minimum of Q is found and if $\mu_j \to \infty$, then every limit point of the sequence $\boldsymbol{u}_j$ is a global solution of the original problem. It is further proved that if at each iteration the solution of the optimization problem is computed approximately with vanishing tolerance k_τ, as in Algorithm 4, either a limit point of the sequence $\boldsymbol{u}_j$ is infeasible and corresponds to a stationary point of the penalty term, or it is a KKT point for the original problem. The above results require differentiability of the penalty term, which is satisfied in our case, as $\nabla h_\ell = \nabla [g_\ell]^2_+ = 2[g_\ell]_+ \nabla g_\ell$. Since convergence is only guaranteed in the limit, the method is terminated when constraint violations are below a finite tolerance, that is when the obtained iterate is in, or close enough to, the feasible set.

6.2.2 Gradient computation and first-order optimality condition

Algorithm 4 requires finding the minimum of the penalized cost function Q_μ. In order to do this, the computation of its gradient is needed. The SA method needs a stochastic gradient at each iterate, that is, a gradient computed for a single realization of the wave angle β. The SAA method, instead, needs an estimate of the true gradient, which is the expected value of the stochastic gradient and thus can be computed as a suitable average of stochastic gradients. For a single given angle β, the gradient of the reduced cost can be obtained by using the Lagrangian function defined as

$$\mathcal{L}(\boldsymbol{u}, \hat{\boldsymbol{\zeta}}^\beta, \boldsymbol{y}) = J(\boldsymbol{u}, \hat{\boldsymbol{\zeta}}^\beta) + \frac{\mu}{2} \sum_{\ell=1}^{N_b} [g_\ell(\mathbf{u})]^2_+ + \sum_{q=1}^{N_f} \mathrm{Re} \left[\boldsymbol{y}_q^H \left(Z_q(\boldsymbol{u}) \hat{\boldsymbol{\zeta}}_q^\beta - \hat{\boldsymbol{F}}_q^\beta \right) \right].$$

The problem is set in the space of complex vectors over the field of real numbers, with scalar product $(u, v) = \mathrm{Re}[u^H v]$, thus the presence of the real part in the Lagrangian. The adjoint equation is obtained by differentiation with respect to the state vector,

$$Z_q^H(\boldsymbol{u})\boldsymbol{y}_q = \omega_q^2 C\hat{\boldsymbol{\zeta}}_q^\beta - 2\mu V(\hat{\boldsymbol{\zeta}}_q^\beta - \boldsymbol{\eta}_q), \quad q = 1, \dots, N_f,$$

where V is a diagonal matrix with elements

$$V_{\ell\ell} = [g_\ell(\hat{\boldsymbol{\zeta}})]_+, \quad i = 1, \dots, N_b,$$

that is independent of the frequency. The components of the stochastic gradient are obtained by differentiating with respect to the controls:

$$\frac{\partial \mathcal{L}}{\partial c_\ell}(\boldsymbol{u}, \hat{\boldsymbol{\zeta}}^\beta, \boldsymbol{y}) = -\sum_{q=1}^{N_f} \left(\frac{1}{2}\omega_q^2 |\hat{\zeta}_{\ell,q}|^2 + \mathrm{Re}[j\omega_q y_{\ell,q}^* \hat{\zeta}_{\ell,q}] \right),$$

$$\frac{\partial \mathcal{L}}{\partial \kappa_\ell}(\boldsymbol{u}, \hat{\boldsymbol{\zeta}}^\beta, \boldsymbol{y}) = \sum_{q=1}^{N_f} \mathrm{Re}[y_{\ell,q}^* \hat{\zeta}_{\ell,q}],$$

$$G(\boldsymbol{u}, \beta) = \frac{\partial \mathcal{L}}{\partial \boldsymbol{u}}(\boldsymbol{u}, \hat{\boldsymbol{\zeta}}^\beta, \boldsymbol{y}) = \left[\frac{\partial \mathcal{L}}{\partial c_1}, \dots, \frac{\partial \mathcal{L}}{\partial c_{N_b}}, \frac{\partial \mathcal{L}}{\partial \kappa_1}, \dots, \frac{\partial \mathcal{L}}{\partial \kappa_{N_b}} \right]. \tag{6.18}$$

The first-order optimality condition requires [127]

$$\boldsymbol{u} - \mathcal{P}_{\mathcal{U}_{ad}} \left(\boldsymbol{u} - \mathbb{E}_\beta[G(\boldsymbol{u}, \beta)] \right) = 0,$$

where $\mathcal{P}_{\mathcal{U}_{ad}}$ is the projector onto $\mathcal{U}_{ad}$:

$$\begin{aligned} \mathcal{P}(\boldsymbol{u}) &= \mathcal{P}[c_1, \dots, c_{N_b}, \kappa_1, \dots, \kappa_{N_b}] \\ &= [c_1, \dots, c_{N_b}, [\kappa_1]_+, \dots, [\kappa_{N_b}]_+]. \end{aligned} \tag{6.19}$$

6.2.3 Sample average approximation

The sample average approximation (SAA) method is based on writing the expected value in Problem (6.17) as an integral, and approximating such integral with a suitable quadrature rule:

$$\mathbb{E}_\beta \left[\widetilde{J}(\boldsymbol{u}; \beta) \right] = \int_0^{2\pi} \widetilde{J}(\boldsymbol{u}; \beta)\, D(\beta)\, \mathrm{d}\beta \approx \sum_{i=1}^{N} \widetilde{J}(\boldsymbol{u}; \beta_i)\, w_i.$$

The same approximation is applied to the gradient. One then obtains a deterministic problem that can be solved using standard optimization algorithms. In this work, we use the gradient descent method with step length determined according to the Armijo rule [127, Chap. 3]. The quadrature rule is defined by the choice of nodes β_i and weights w_i. In the following, we consider the Monte Carlo [155] and Gauss-Legendre [140, 168] methods.

For the Monte Carlo method, the nodes β_i are obtained by sampling the wave direction, following the procedure described in Section 6.2.5, and the choice of

weights corresponds to averaging, $w_i = 1/N$. In the case of Gauss-Legendre, instead, nodes are defined as the zeros of Legendre polynomials. Numerical libraries provide nodes and weights $\widehat{\beta}_i$, $\widehat{w}_i$ on the interval $[-1, 1]$, which are then mapped to the desired interval $[a, b]$ using

$$\beta_i = \frac{a+b}{2} + \frac{b-a}{2}\widehat{\beta}_i, \quad w_i = \frac{b-a}{2} D(\beta_i)\widehat{w}_i.$$

In our case, the interval $[a, b]$ is chosen as $[\beta_{min}, \beta_{max}]$. Here, β_{min} and β_{max} define an effective interval of wave angles, which depends on the parameters k_β, β_0, such that the probability is considered negligible outside such interval. Notice that each weight for Gauss-Legendre integration includes the value of the probability distribution function in the corresponding node. This is not the case for Monte Carlo, where the probability distribution is accounted for in the sampling phase.

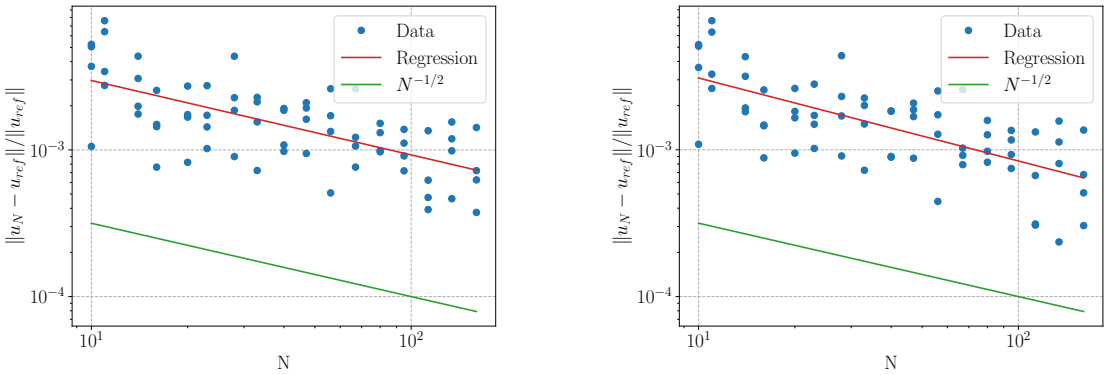

Figure 6.1: *Relative error in the constrained case of the Monte Carlo method with respect to a solution obtained with Gauss-Legendre using* 10 *(left) and* 320 *(right) nodes.*

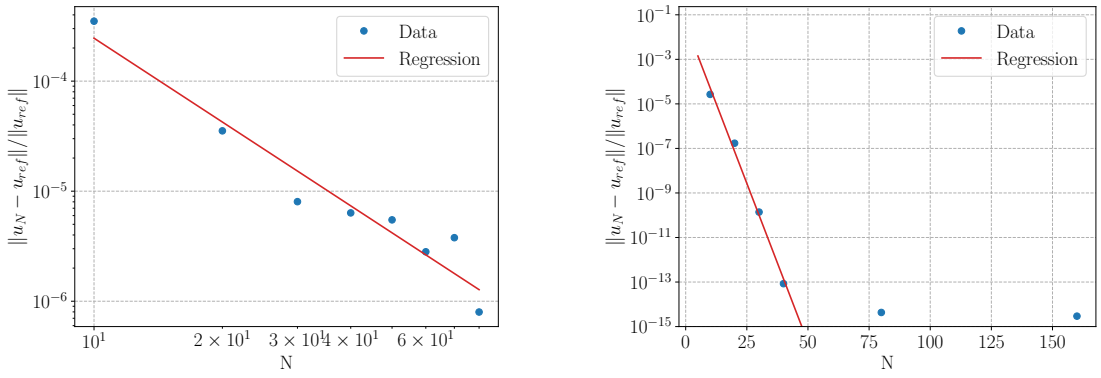

Figure 6.2: *Left: Relative error in the constrained case of Gauss-Legendre method with respect to a reference solution computed with 320 nodes. Right: Relative error in the unconstrained case of the Gauss-Legendre method with respect to a reference solution computed with 320 nodes.*

Convergence of the two methods is studied on a test case with 15 bodies, enforcing the slamming constraint. The results are reported in Figure 6.1 for the Monte Carlo method and in Figure 6.2 (left) for the Gauss-Legendre method.

Since the exact solution of the optimization problem is not known, two reference solutions are computed using Gauss-Legendre, one with 10 nodes, and another with 320 nodes. The convergence rate of Monte Carlo is estimated by computing the slope of the regression line in logarithmic scale. For Monte Carlo, multiple points are available for each value of N, obtained by repeating the computation with different sets of samples. Using the reference solution computed with 10 nodes yields a slope of -0.507 with standard error 0.070, while using the reference solution computed with 320 nodes yields a slope of -0.565 with standard error 0.074. Both values are consistent with the expected convergence rate $-1/2$. This result shows that a Gauss-Legendre solution obtained with a very limited sample size is very accurate compared to a Monte Carlo solution with larger sample size.

The order of convergence of Gauss-Legendre, instead, is estimated at a value of 2.53, while repeating the test for the unconstrained problem leads to a spectral convergence of the Gauss-Legendre method, as shown in Fig. 6.2 (right). In particular, we obtain a behaviour of the type $k\exp(-mN)$, where $m \approx 0.658$. The loss of spectral convergence in the constrained case is explained by the presence of the max operator in the slamming constraint; such operator is present in the right hand side of the adjoint equation.

6.2.4 Robust stochastic approximation

The stochastic approximation method (SA) moves, at each iteration, in the direction of a gradient computed from a single sample of the random variable. We call this vector the stochastic gradient. Since there is no guarantee that the stochastic gradient defines a descent direction, the line-search stepsize strategies suitable for deterministic problems cannot be applied. Instead, the sequence of stepsizes is fixed once the initial step is chosen. A suitable initial step t_0 can be estimated by performing a line search using a single sample of the stochastic gradient.

Some stepsize strategies for SA method are discussed in [124]. We choose the robust variable stepsize strategy, that is, the sequence of steps is

$$t^k = \frac{t^0}{\sqrt{k+1}}, \quad k = 0, 1, \dots \tag{6.20}$$

A convergence estimate is available, based on the assumptions that

$$\exists M > 0 \quad \text{s.t.} \quad \mathbb{E}_\beta[\|G(\boldsymbol{u}, \beta)\|_2^2] \leq M^2 \quad \forall \boldsymbol{u} \in \mathcal{U}_{ad},$$

that Q is convex and that the admissible set $\mathcal{U}_{ad}$ is convex

$$\mathbb{E}\left[Q\left(\tilde{\boldsymbol{u}}_K^N\right) - Q(\boldsymbol{u}_*)\right] \leq \frac{c_Q}{\sqrt{N}},$$

where N is the number of iterations, c_Q is a constant independent on N and $\tilde{\boldsymbol{u}}_K^N$ is a weighted average defined as

$$\tilde{\boldsymbol{u}}_i^j = \sum_{k=i}^{j} \nu^k \boldsymbol{u}^k, \quad \nu^j = \frac{t^j}{\sum_{k=i}^{j} t^k}. \tag{6.21}$$

Such average is taken as the solution of the optimization problem.

As a stopping indicator, we use the norm of an average of the stochastic gradients on the most recent iterations:

$$\text{ind} = \left\| \frac{1}{W} \sum_{k=N-W}^{N} G^k \right\| \leq \tau_{in}, \tag{6.22}$$

where W is the window size. This is a modification of a criterion proposed in [132] and it can be interpreted as an estimate of the gradient of the corresponding deterministic problem.

Algorithm 5 Robust Stochastic Approximation (variable stepsize)

Set initial step t, window size W
while $k \leq it_{max}^{out}$ or $ind > \tau_{in}$ **do**
  Extract β
  for $q = 1 : N_f$ **do**
    Compute $\hat{\mathbf{F}}_q^\beta$
    Find $\hat{\boldsymbol{\zeta}}_q$ by solving the state problem with $(\mathbf{u}_k, \hat{\mathbf{F}}_q^\beta)$
    Find $\mathbf{y}_q$ by solving the adjoint problem with $(\mathbf{u}_k, \hat{\mathbf{F}}_q^\beta)$
  end for
  Compute the stochastic gradient G from (6.18)
  Update $\mathbf{u}^{k+1} = \mathcal{P}(\mathbf{u}^k - t^k G)$, with $\mathcal{P}$ from (6.19) and t^k from (6.20)
  Compute $\tilde{\mathbf{u}}_{k+1-W}^{k+1}$ from (6.21)
  Compute the stopping indicator *ind* from (6.22)
end while

6.2.5 Treatment of stochasticity

We now discuss the computation of a realization of the excitation force, starting from the extraction of a sample from the distribution of wave directions. We consider Donelan's spreading function (2.80), whose cumulative distribution function is

$$\tilde{D}(\beta) = \frac{1}{2} \left[\tanh[k_\beta(\beta - \beta_0)] + 1 \right]. \tag{6.23}$$

To sample a wave direction, we use the inverse transformation technique [81, Sec. 9.2]. First, by using a random number generator, a sample ξ from a uniform distribution $\mathcal{U}(0,1)$ is drawn. The wave direction is then obtained as the angle β corresponding to the value ξ of the cumulative distribution function $\tilde{D}(\beta)$:

$$\beta = \tilde{D}^{-1}(\xi) = \beta_0 + \frac{1}{k_\beta} \text{atanh}(2\xi - 1). \tag{6.24}$$

Once β has been drawn from the distribution as described above, different approaches are possible for computing the force vector $\boldsymbol{F}_q^\beta$: direct diffraction computation, interpolation, and the use of Haskind's relation. We discuss them in the following.

In order to compute the excitation force directly one should, for all wave frequencies, solve a diffraction problem (2.62) with the corresponding incident wave

potential (2.52) as a boundary condition. This requires storing or recomputing N_f dense, and possibly large, matrices, and solving each system once: a rather demanding approach.

Interpolation is potentially cheaper: it requires running a batch of simulations for different values of the wave direction and to construct an interpolating function (e.g., piecewise polynomials) for each frequency, before the optimization process. Then, for each realization, the interpolating functions only need to be evaluated. For the interpolation of a complex function of a real variable, at least two strategies are possible: interpolating real and imaginary parts separately (RI) or amplitude and phase (AP). If the force, here denoted for simplicity as F, is expressed in cartesian and polar form as

$$F(\beta) = R(\beta) + iI(\beta) = A(\beta)\exp[iP(\beta)], \tag{6.25}$$

then RI interpolation is written as

$$\tilde{F}_{RI}(\beta) = \tilde{R}(\beta) + i\tilde{I}(\beta), \tag{6.26}$$

where $\tilde{R}$ is an interpolant of R and $\tilde{I}$ an interpolant of I; AP interpolation is instead written as

$$\tilde{F}_{AP}(\beta) = \tilde{A}(\beta)\exp[i\tilde{P}(\beta)]. \tag{6.27}$$

We remark that the phase needs to be unwrapped before interpolation. It was noticed in [164] that AP interpolation is in general more accurate than RI interpolation for the directional response amplitude (which depends on the direction only through the diffraction force). The same observation was made in [129] in the context of acoustics, where the difference was explained by the presence of an undesirable interference effect in the RI result. In the case of piecewise polynomial interpolation, the two methods achieve the same theoretical order of convergence, as will be shown in the following. If f is a real function, $f \in C^{k+1}[0, 2\pi]$, and $\tilde{f}$ is its piecewise linear interpolant of degree k on a grid with uniform spacing h, then the following asymptotic error estimate holds [140]:

$$\|f - \tilde{f}\|_\infty \leq Ch^{k+1}\|f^{(k+1)}\|_\infty. \tag{6.28}$$

We then have

$$\|F - \tilde{F}_{RI}\|_\infty^2 = \|e_R^2 + e_I^2\|_\infty \leq Ch^{2(k+1)}\left(\|R^{(k+1)}\|_\infty^2 + \|I^{(k+1)}\|_\infty^2\right), \tag{6.29}$$

where e_R and e_I are the separate interpolation errors of $R(\beta)$ and $I(\beta)$. For AP interpolation we obtain, by Taylor expansions,

$$\begin{aligned}\|F - \tilde{F}_{AP}\|_\infty^2 &= \|e_A^2 + Ae_P^2 + o(e_P^2)\|_\infty \\ &\leq Ch^{2(k+1)}\left(\|A^{(k+1)}\|_\infty^2 + \|A\|_\infty^2\|P^{(k+1)}\|_\infty^2\right).\end{aligned} \tag{6.30}$$

The difference in accuracy between the two approaches is thus only in the constants, which depend on the derivatives of the involved functions. However, the relationships between the derivatives of $A(\beta)$ and $P(\beta)$ and those of $R(\beta)$ and $I(\beta)$ do not allow to draw any straightforward conclusion about which of the two methods performs best in a general case.

Another possibility is the use of Haskind's relation (2.72). For its implementation, the integral needs to be computed numerically. As mentioned, we rely on the hydrodynamic code Capytaine, which uses elementwise constant trial functions (see Sec. 3.1). The diffraction force is then computed as

$$\tilde{F}_H(\beta) = -i\omega\rho \sum_{j=1}^{N} \left[\hat{\phi}_0^{\beta}(\boldsymbol{x}_j) \frac{\partial \varphi_\ell}{\partial n}(\boldsymbol{x}_j) - \varphi_\ell(\boldsymbol{x}_j) \frac{\partial \hat{\phi}_0^{\beta}}{\partial n}(\boldsymbol{x}_j) \right] |\mathcal{K}_j|, \tag{6.31}$$

where $\boldsymbol{x}_j$ denotes the center of the j-th panel and $|\mathcal{K}_j|$ its area.

We now consider as a numerical example a square array of 9 floating cylinders of radius 2 m, draft 0.5 m and spacing 15 m, forced by incident waves of frequency $\omega = 1.5$ rad/s and with a sea depth of 50 m. In Figure 6.3, we show the polar and cartesian decompositions of $F(\beta)$ for the object situated at the center of the array and the results of computations performed with the methods described above. We also show the coarse set of points used to construct the interpolation. RI interpolation introduces noticeable error in terms of the amplitude $A(\beta)$, with the appearance of artifacts similar to the ones observed in [129].

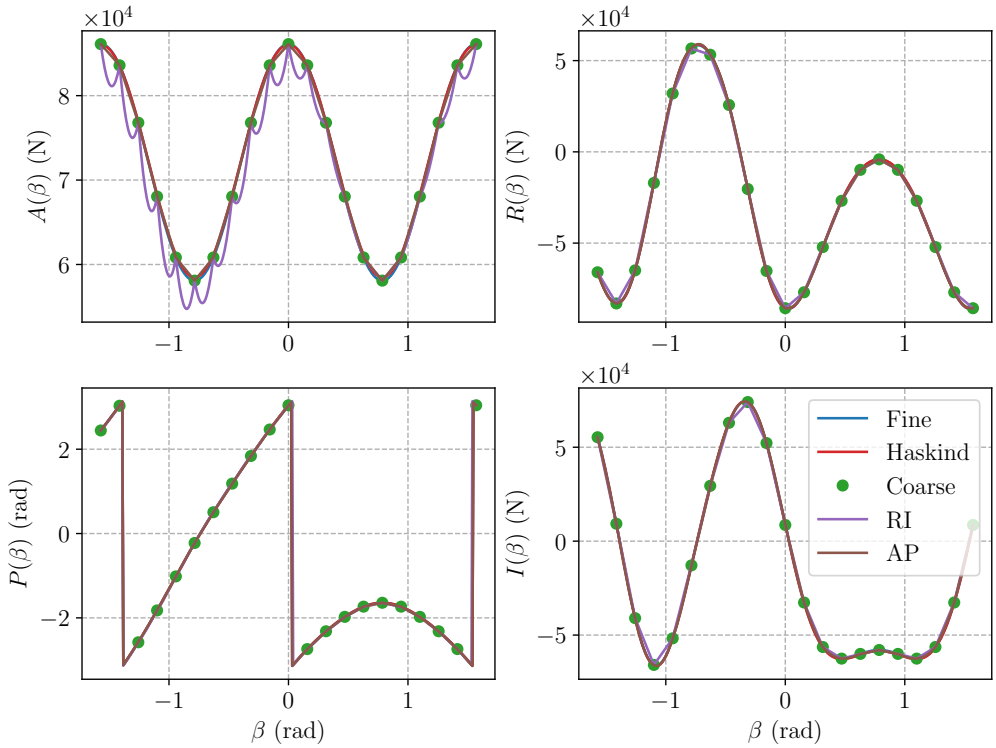

Figure 6.3: *Decompositions of $F(\beta)$: polar (left) and cartesian (right), and comparison between fine data (direct diffraction computations) and reconstruction strategies.*

In Figure 6.4, we show the relative difference between the result of direct diffraction computation F and the reconstruction strategies. It is apparent that Haskind's relation provides the most reliable estimation, while AP interpolation performs slightly worse, and RI interpolation gives the worst results. Moreover, the order of convergence is shown to be 2 for both cases, as expected from (6.29)

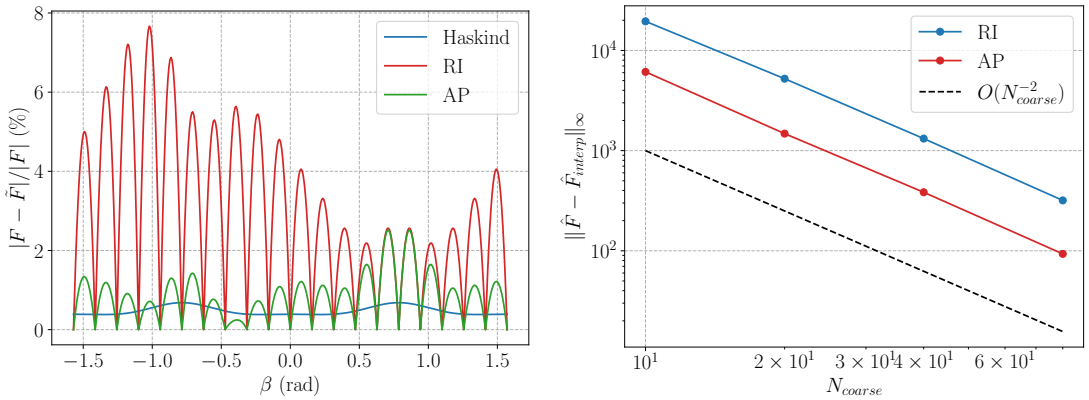

Figure 6.4: *Left: relative difference of Haskind computation and interpolation with respect to the diffraction simulation result. Right: convergence rate plot for the two interpolation strategies.*

and (6.30) for piecewise linear interpolation. We remark that we speak about difference, and not errors, because the results of direct diffraction computations are themselves affected by discretization errors. For a single cylinder forced by waves of direction $\beta = 0$ and variable frequencies, we show in Figure 6.5 the convergence behavior of the difference between direct computation and Haskind's relation with respect to the mesh size parameter n representing the number of angular partitions of the cylinder.

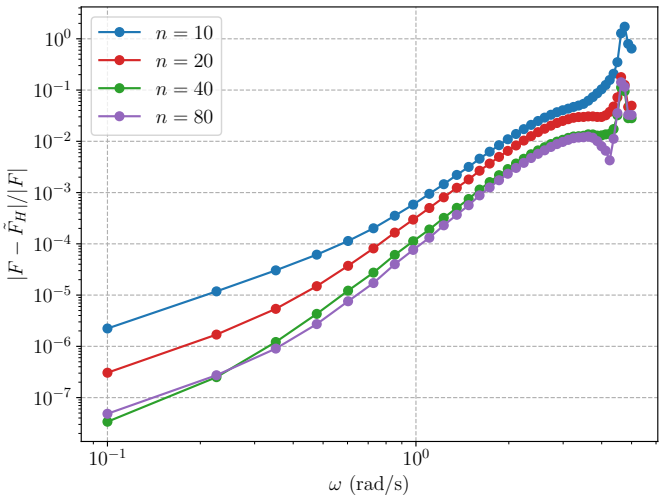

Figure 6.5: *Relative difference between direct computation of the excitation force and use of Haskind's relation for fixed wave direction β, variable wave frequency, and variable discretization parameter n.*

6.2.6 Implementation and comparison between SAA and robust SA

Hydrodynamic data is computed with the boundary element method, introduced in Section 3.1, using the code Capytaine [7], version 1.3. In particular, a radiation problem for each device and for each frequency of the spectrum discretization is

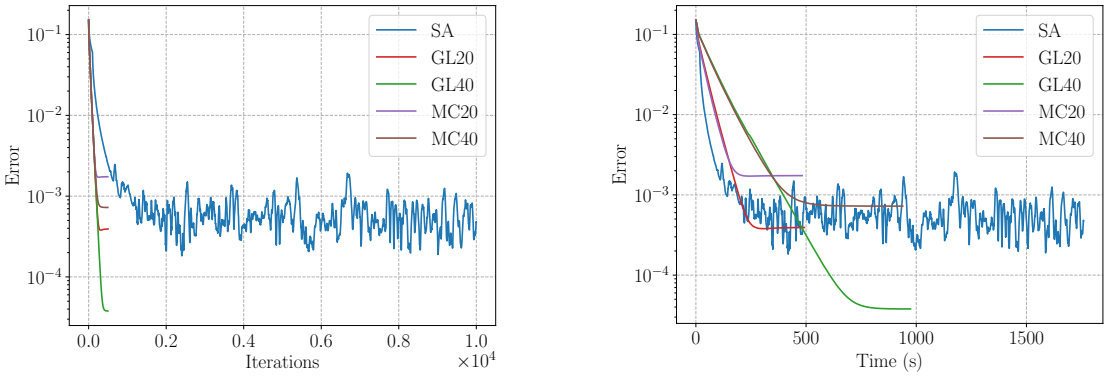

Figure 6.6: *History of relative error on the optimal control with respect to iterations (left) and time (right). Numbers in the labels refer to the number of nodes (Gauss-Legendre) or samples (Monte Carlo).*

solved before starting the optimization. From the resulting radiation potentials, the added mass and radiation damping matrices, which are independent of the wave direction and needed to compute the impedance matrix (2.71), are computed. The radiation potentials are then kept stored, so that they can be used to compute the diffraction forces $\hat{\boldsymbol{F}}_q^\beta$ for any wave direction by applying the Haskind relation. The code is written in Python, using Numba for performance improvement.

The performances of stochastic approximation and sample average approximation using Monte Carlo and Gauss-Legendre integration are compared in Fig. 6.6. A constrained case with 15 bodies and fixed penalization parameter has been considered, using the same initial guess and initial step. The reference solution was obtained by a computation with Gauss-Legendre using 320 nodes. The relative error $\|\mathbf{u} - \mathbf{u}_{ref}\|/\|\mathbf{u}_{ref}\|$ is plotted against execution time and number of iterations. The test is run on an average laptop. We can observe that the SAA methods require a much smaller number of iterations with respect to SA, but, since for the former many problems need to be solved at each iteration, the methods are comparable in terms of computational time. In terms of number of iterations, the histories of Monte Carlo and Gauss-Legendre are almost identical up to a certain value of the error, after which Gauss-Legendre exhibits better accuracy. However, in terms of computational times, the histories of the two methods are similar only when the same number of nodes is used. The error of stochastic approximation, instead, initially decreases at a rate comparable to (in terms of number of iterations) or faster than (in terms of computational time) the other methods, and then starts oscillating, as expected from an SA approach (see, e.g., [124] and references therein). Moreover, the results of Fig. 6.6 provide useful insights into the choice of the method to use in a design phase. If one seeks indicative results in relatively short times, then an SA approach is indeed a reasonable choice: on the one hand, it converges faster in the initial phase when the starting point is far from the optimal solution; on the other hand, it does not require the choice of a number of nodes or of an effective interval of wave angles where the probability distribution is correctly represented. Instead, if one is interested in highly accurate results, then Gauss-Legendre is the method to choose. However, this strategy requires

an appropriate choice of an effective interval of wave angles, which is not needed by a Monte Carlo approach. Moreover, if the number of stochastic parameters becomes very large, then the Gauss-Legendre method could become unfeasible, and an SA strategy is more appropriate.

6.3 Numerical results

The numerical framework presented in the previous sections is used to compute the optimal control parameters of arrays of two different models of WECs (see Table 6.1). In particular, the results presented in this section are obtained by simulations run using SA. The data for the first case is taken from [76]. The second case is derived from the first by rescaling the generator mass proportionally with respect to the volume. In the first case, the resonance frequency of the uncontrolled body is higher than the peak spectrum frequency. The second case is tuned in such a way that the uncontrolled body frequency is lower than the wave spectrum peak frequency.

In both cases, the region of the spectrum containing 99.9% of the power is discretized into 30 bins of equal power as described in Sec. 3.3, so that each realization is obtained as a superposition of 30 harmonics.

To quantify the performance of the obtained configurations, we define the interaction factor q as the ratio between the total average power produced by the array and the sum of the powers of the isolated devices:

$$q = \frac{\sum_{\ell=1}^{N_b} P_\ell}{N_b \, P_{\text{isolated}}}.$$

	radius (m)	draft (m)	generator mass (kg)	generator stiffness (N/m)	depth (m)	H_s (m)	T_p (s)
Case 1	2	0.5	2560	4000	50	1.53	5.83
Case 2	9	1.5	155520	4000	50	1.53	3.49

Table 6.1: *Body parameters and wave climates.*

6.3.1 Single-body optimization

We first consider optimization for a single device. For case 1, if negative stiffnesses are allowed, and using parameters $\mu_0 = 10^6$, $k_\mu = 4$, $\tau^{out} = 10^{-4}$, $it^{out}_{max} = 10$, $\tau^0_{in} = 10^{-4}$, $k_\tau = 0.8$ (see Algorithm 4), an optimal power of 7636 W is obtained, achieved by setting the control parameters to $c = 31820.7$ N·s/m, $s = -27022.2$ N/m. The outer convergence history is shown in Figure 6.7 (left), superimposed on a contour map of the absorbed power. The region above the red dashed line is feasible with respect to the slamming constraint, and the black dot is the constrained optimum obtained by exhaustive search over a rectangular grid. If instead only positive values of stiffness are accepted, the power obtained by optimization using the same parameters mentioned above is 5886 W, and the corresponding controls are

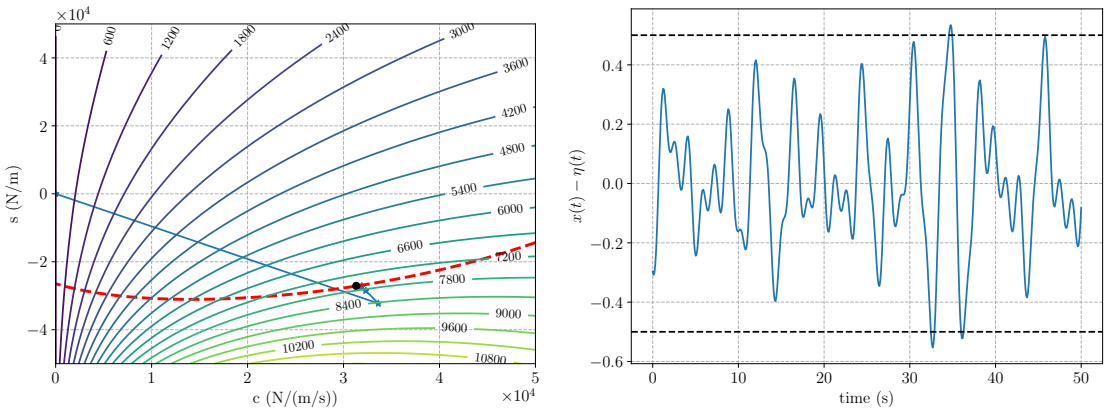

Figure 6.7: *Left: Convergence plot (outer iterations) for the isolated body of case 1 superimposed on power contour map (values in W). Red dashed line: slamming constraint. Right: Time domain realization.*

$c = 61774.8$ N · s/m, $s = 0$. Figure 6.7 (right) shows the statistical meaning of the slamming constraint, which has been formulated in Section 5.2 in the frequency domain. The fraction of peaks exceeding the bound can be controlled by varying α in (6.8).

For case 2, optimization yields a power of 5712 W, obtained with controls $c = 733196$ N · s/m, $s = 1411344$ N/m, without imposing constraints on the sign of s.

The results of this section are used as initial guesses for the multi-body optimization runs: all devices are initially assigned the same control parameters.

6.3.2 Two-body optimization

Table 6.2 shows the results of numerical experiments with 2 bodies of type 1. Configuration $\beta_0 = 0°$ corresponds to bodies aligned along the mean wave vector; $\beta_0 = 90°$ corresponds to bodies aligned perpendicular to the mean wave vector. In both cases, the resulting interaction factor q is larger when the spreading in wave direction is small, that is when k_β is large (see (2.80)). In most cases, the slamming constraint is violated for the initial guess. This results in a reduction of power between the initial guess and the optimized result, the latter being compatible with the constraint up to the tolerance. The results for control parameters in the symmetric case $\beta_0 = 90°$ are not exactly symmetric: this is due to the use of a stochastic optimization method. The asymmetry may be reduced by increasing the window size used for averaging the iterates.

Figure 6.8 reports the convergence history for test 1. The two jumps correspond to a switch to a higher value of the penalization parameter. After a jump, the cost starts decreasing again, but stops at a larger value than the one before the jump, which would now be unattainable because of the stronger enforcement of the constraint.

	k_β	β_0	Initial violation	ΔP (%)	q	c (N·s/m)	κ (N/m)
Test 1	20	0	yes	-2.65	0.949	32095.1 31140.3	-27384.7 -23636.9
Test 2	5	0	yes	-2.59	0.947	32156.5 31188.2	-27379.7 -23701.0
Test 3	1	0	yes	-2.14	0.943	32698.3 32243.6	-27207.6 -23555.7
Test 4	20	90	no	+5.03	1.015	33122.7 33121.3	-29660.8 -29660.6
Test 5	5	90	no	+4.59	1.009	33306.1 33365.8	-29258.7 -29280.5
Test 6	1	90	yes	-2.27	0.940	33353.7 33192.1	-25061.1 -24690.0

Table 6.2: *Tests for 2 bodies, case 1.*

	k_β	β_0	Initial violation	ΔP (%)	q	c (N·s/m)	κ (N/m)
Test 1	20	0	no	+2.41	0.675	689151 728208	1104329 604768
Test 2	5	0	no	+2.63	0.675	671380 716425	1124916 559310
Test 3	1	0	no	+2.20	0.893	659638 783297	1490803 1196127
Test 4	20	90	no	+3.34	0.870	878379 876926	708776 706616
Test 5	5	90	no	+1.01	0.924	869725 869114	1035442 1044426
Test 6	1	90	no	+3.26	1.037	735201 737221	1526562 1528286

Table 6.3: *Tests for 2 bodies, case 2.*

6.3.3 Multi-body optimization: devices on two concentric arcs

We now consider an array of 15 devices in an arrangement with 2 concentric arcs, derived from the ones considered in [76], for case 1. The geometry of the array and the results without constraints on the sign of the stiffness are shown in Fig. 6.9 and 6.10. For all the following tests, the dominant wave direction is zero: the incident wave vector is aligned with the x axis. We observe that the bodies with the smallest stiffnesses are the ones located in the downwave arc, at the center. They are thus the bodies with the lowest tuning frequency, and they receive the largest power increase. Conversely, the devices at the outer edges of the array

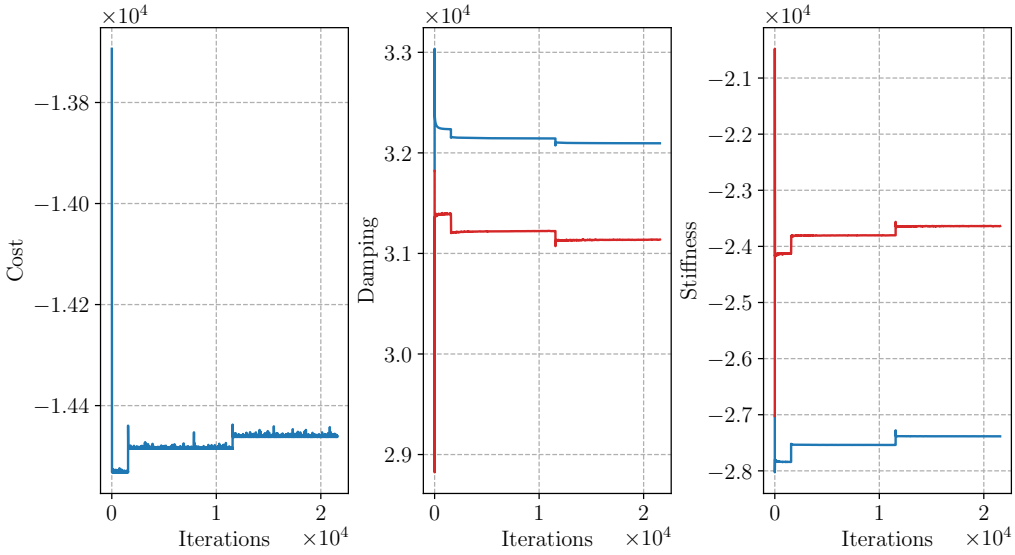

Figure 6.8: *Convergence plot for test 1 (see Table 6.2).*

have the largest stiffnesses and they are subject to a moderate power decrease. Regarding dampings, bodies in the upwave arc have larger values than the ones in the downwave arc, corresponding to wider response peaks: the bodies at the front, roughly speaking, are tuned so that they are able to absorbe power in a wider range of frequencies. The global result is a power increase of 3.44% compared to the initial guess, and an interaction factor of 0.966.

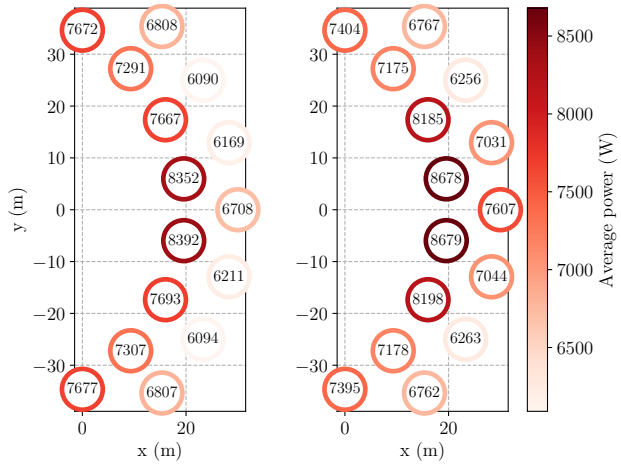

Figure 6.9: *Map of power before (left) and after (right) array optimization; case 1, 15 devices unconstrained stiffness. Bodies not to scale.*

If the constraint of positive stiffnesses is enforced, the results of Fig. 6.11 are obtained. Only a very small power increase of 0.31% is obtained, and an interaction factor of 0.980. Contrary to the previous case, bodies in the downwave arc have larger control dampings than the ones in the upwave arc. All optimal control stiffnesses are zero; this is explained by the large, positive frequency distance between the response peaks of the uncontrolled bodies and the frequencies where

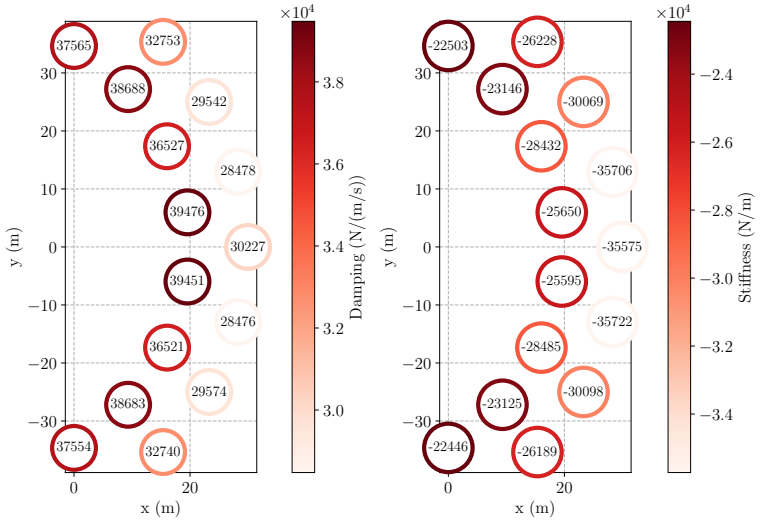

Figure 6.10: *Map of control parameters; case 1, 15 devices, unconstrained stiffness.*

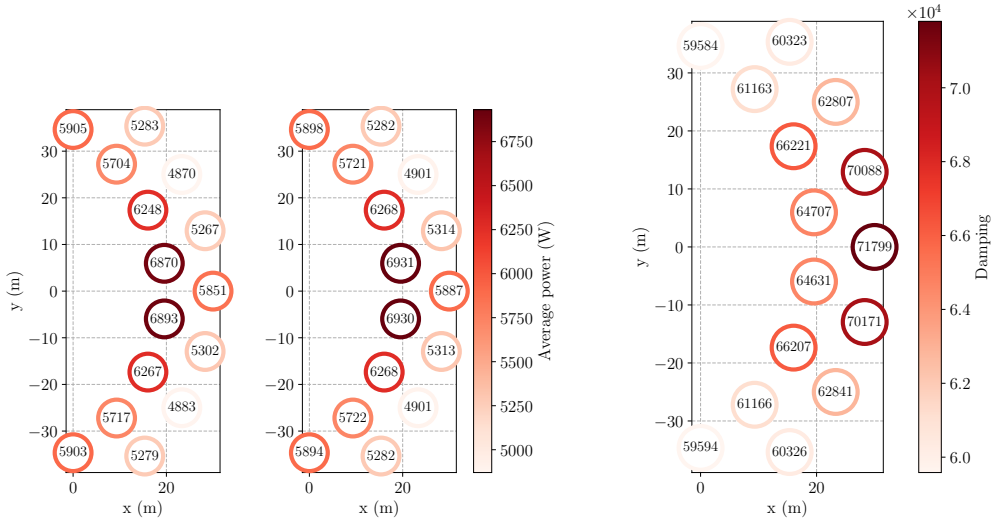

Figure 6.11: *Maps of power (left) and control damping (right); case 1, 15 devices, positive stiffness constraint.*

most of wave power is distributed.

For the same kind of geometry, with bodies of type 2, the results are reported in Figures 6.12 and 6.13. All optimal stiffnesses are positive, without imposing any constraint. As in the corresponding arrangement for case 1, bodies in the upwave arc have generally larger stiffnesses than the ones in the downwave arc, but in this case there is the exception of the body located at $y = 0$ in the downwave row. There is no evident behaviour for dampings between the two arcs. The power increase obtained by optimization is of 3.99%; the interaction factor is 1.144. Notice that the slamming constraint is never active, due to the relatively large draft of the bodies. Due to this, positive interactions in the array are promoted and they are not limited by the constraint.

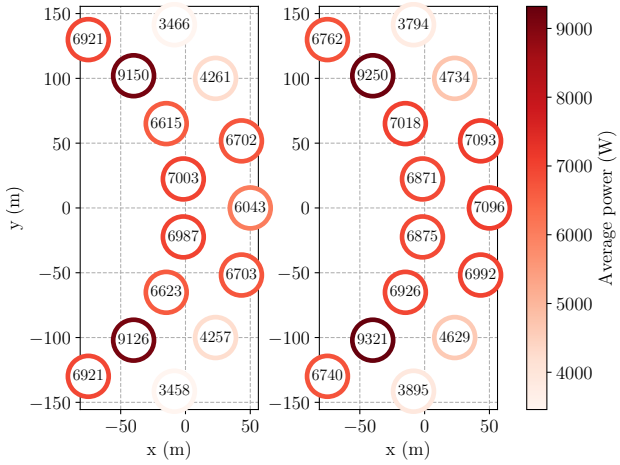

Figure 6.12: *Map of power before (left) and after (right) array optimization; case 2, 15 devices, unconstrained stiffness.*

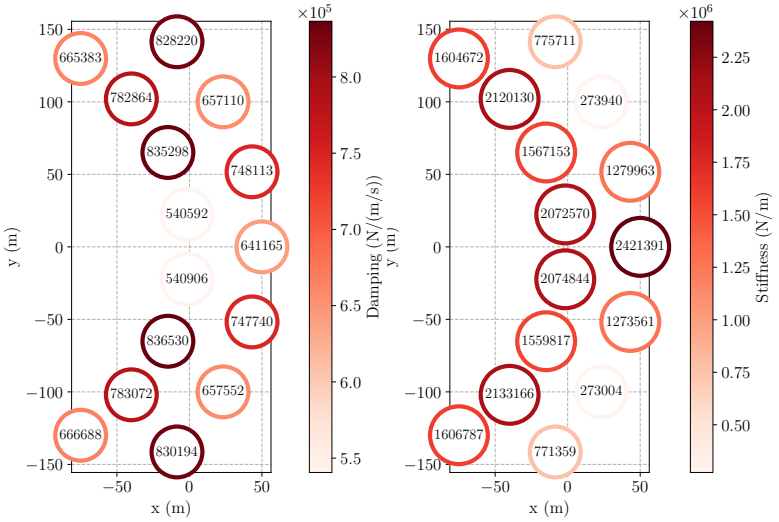

Figure 6.13: *Map of control parameters; case 2, 15 devices, unconstrained stiffness.*

6.3.4 Multi-body optimization: 4×4 square arrangement

Figures 6.14 and 6.15 refer to the case of a square grid of 16 bodies. For case 1, without the constraint of positive stiffnesses, we obtain all negative stiffness, the smallest ones being located in the most downwave rows. Maximum dampings are assigned to the devices at the front and center of the array. Bodies in the upwave rows are subject to a power increase compared to the initial guess; in the downwave rows, devices at the edges see a moderate power increase, while devices at the center see a power decrease, that is particularly intense for the bodies in the last row. The global power increase is of 3.11%, and the interaction factor is 0.766.

If stiffnesses are constrained to positive values, the optimization drives them all to zero. Powers and control dampings are shown in Figure 6.16. This time, the largest power increases are for the devices at the center of the array, which are

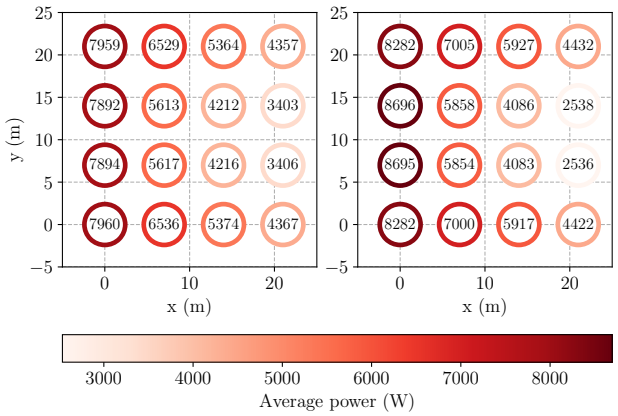

Figure 6.14: *Map of power before (left) and after (right) array optimization; case 1, 16 devices, unconstrained stiffness.*

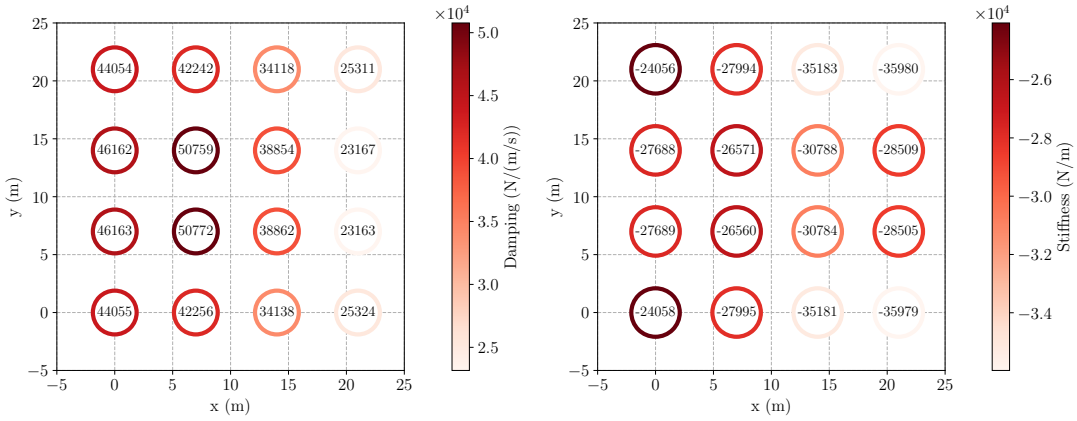

Figure 6.15: *Map of control parameters; case 1, 16 devices, unconstrained stiffness.*

also the ones with the largest control stiffnesses. The power increase is of 0.41%, and the obtained interaction factor is 0.816.

A 4×4 square arrangement has also been simulated for the case 2 considered in the previous section. The results are shown in Figures 6.17 and 6.18. Devices in the most downwave row are subject to a power reduction, while all the others see a power increase. Bodies in the third row are assigned negative stiffnesses. The global power is increased by 9.16% and the interaction factor is 0.835.

The process is repeated with the constraint of positive stiffnesses: see Fig. 6.19, 6.20. In terms of total power, the result is around 76.3 kW in both cases, but in this second one, almost all bodies in the downwave part of the array are assigned stiffnesses close to zero.

6.3.5 Extension to multiple random parameters

The methods presented in the previous sections can be generalized to the case of multiple random variables. We present an application of practical interest involving two random parameters, based on a discussion presented in [23]. This

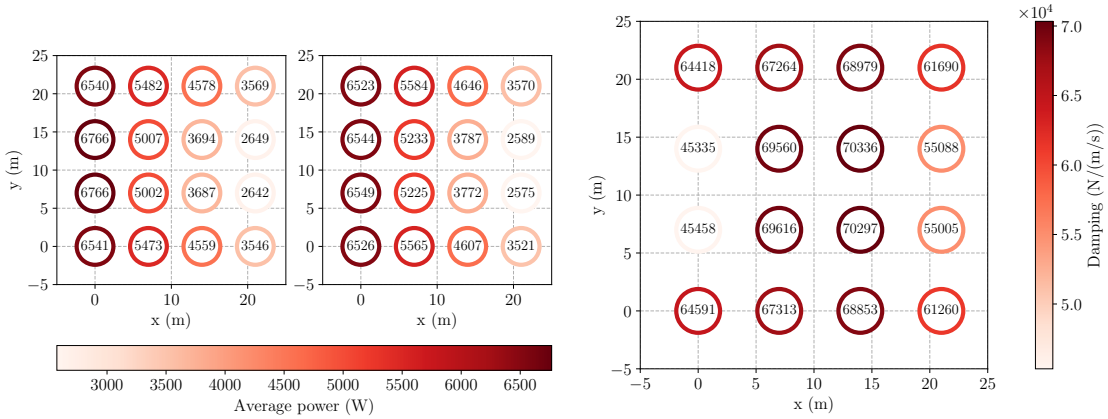

Figure 6.16: *Maps of power (left) and control damping (right); case 1, 16 devices, positive stiffness constraint.*

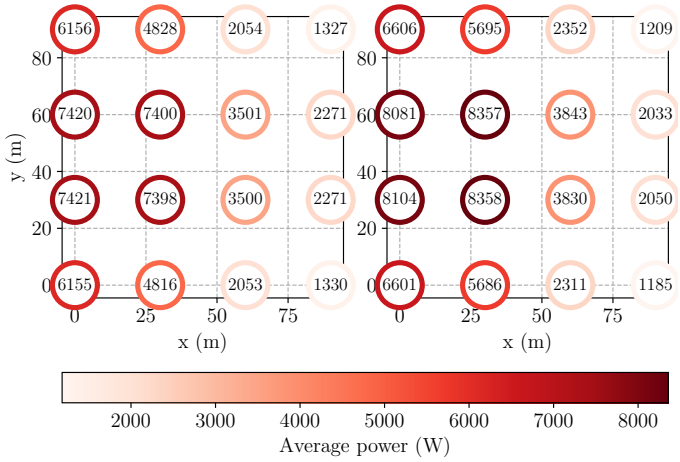

Figure 6.17: *Map of power before (left) and after (right) array optimization; case 2, 16 bodies, unconstrained stiffness.*

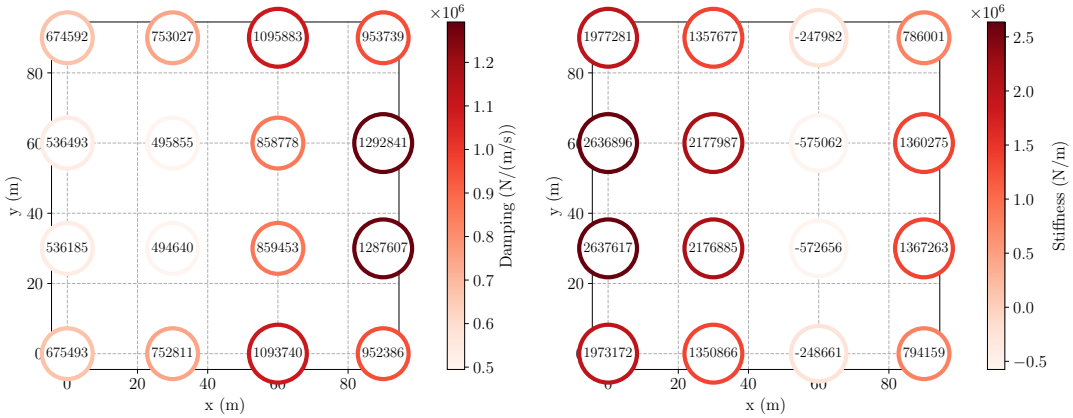

Figure 6.18: *Map of control parameters; case 2, 16 devices, unconstrained stiffness.*

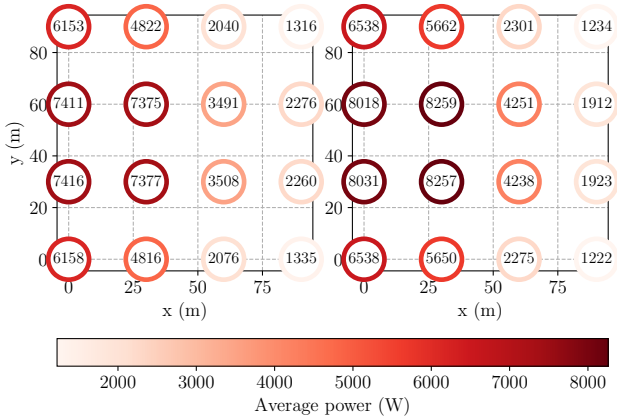

Figure 6.19: *Map of power before (left) and after (right) array optimization; case 2, 16 devices, positive stiffness constraint.*

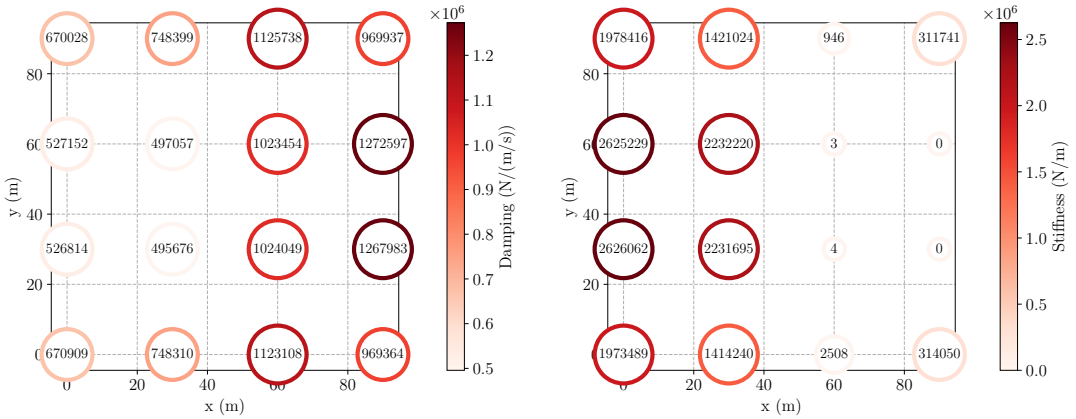

Figure 6.20: *Map of control parameters; case 2, 16 devices, positive stiffness constraint.*

allows us to observe a case where our optimization framework computes an optimal solution that is, from a physical point of view, less intuitive than the ones presented in the previous sections. Consider a sea state formed by a superposition of wind waves and swell waves. Wind waves are generated locally by the action of the wind on the free surface, while swell waves originate from storms occurring far from the measurement point. The frequency spectrum of such sea state typically presents two peaks: a relatively narrow, low-frequency peak corresponding to the swell component, and a relatively wide, high-frequency peak corresponding to the wind component. Assuming linearity of the interaction between the two wave systems, the spectrum can be written as $S(f,\beta) = S_w(f,\beta) + S_s(f,\beta)$, the subscripts $_w$ and $_s$ being referred to the wind contribution and the swell contribution, respectively. Consistently with the approximation adopted for the case of a single random direction, we write $S_w(f,\beta) = S_w(f)D_w(\beta)$, and the analogous expression for swell. The frequency part is given by the Pierson-Moskowitz spectrum (2.79), while the directional part is given by the Donelan distribution function (2.80).

To formulate the robust optimization problem in this case, we assume that

peak frequencies $f_{p,w}$, $f_{p,s}$ and significant wave heights $H_{s,w}$, $H_{s,s}$ are known and fixed values. We define a realization as the sum of two irregular waves, each one unidirectional with directions β_w and β_s, sampled from $D_w(\beta)$ and $D_s(\beta)$, respectively. The excitation force acting on each device is, accordingly, the sum of the excitation forces due to the wind and swell contributions.

We present a case with the 15-device configuration of type 2 (see Tab. 6.1). The parameters of the wind component are $H_s = 2$ m, $T_p = 5$ s, $k_\beta = 5$, $\beta_0 = 30°$. The parameters of the swell component are $H_s = 1$ m, $T_p = 10$ s, $k_\beta = 20$, $\beta_0 = 0°$. The corresponding spectrum is depicted in Fig. 6.21. The results of the optimization run are reported in Fig. 6.22. Let us discuss the obtained results

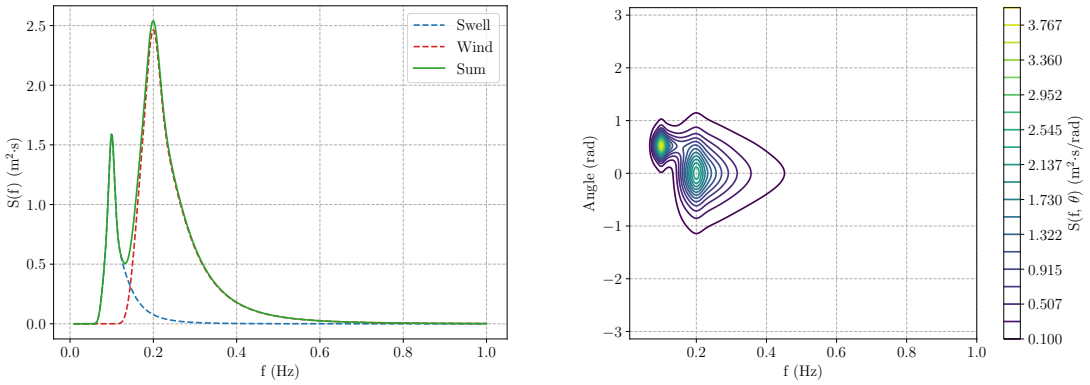

Figure 6.21: *Double-peaked wave spectrum. Left: frequency spectrum; right: frequency-directional spectrum.*

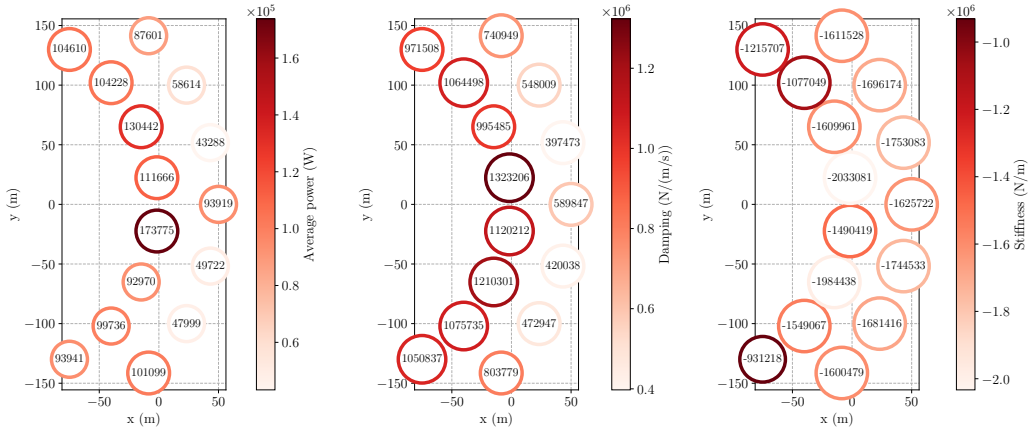

Figure 6.22: *Map of power (left), damping (center) and stiffness (right) for 15 bodies, double-peaked spectrum.*

from a physical point of view. First, it is possible to see that the distributions of damping and stiffness parameters is not symmetric with respect to the x axis. This is due to the asymmetry in the wave directions. More interestingly, one can observe that the parameters are not clearly clustered: even though one may expect to obtain two clusters, dealing with the two peaks in the spectrum independently, the optimal solution presents a more intricate configuration, with a large spread

in the array of the values of stiffness and damping coefficients.

6.4 Discussion and developments

In this chapter, a new computational framework for the robust optimization of arrays of WEC was proposed and tested. In particular, we modelled an optimization problem for the maximization of the power of WEC parks with respect to the individual control damping and stiffness coefficients of each device. The results are robust with respect to the incident wave direction, which is treated as a random variable. The numerical solution to this stochastic optimization problem is obtained as a combination of penalty iterations and stochastic approaches, namely robust SA and SAA based on Monte Carlo or Gauss-Legendre quadrature integration.

The results of our numerical simulations are in agreement with the ones presented (for deterministic problems and unidirectional waves) in classical references in the field of marine engineering, like, e.g., [13], where it was observed that downwave rows are in general less productive than upwave rows. This behaviour is made even more evident by optimization, especially in square arrangements of bodies, where the difference in power between the first and the last row generally increases. Upwave bodies extract more power than they would in isolated conditions, so they benefit from the interactions with downwave bodies. These positive interactions might be impeded or reduced by the slamming constraint. In particular, it is possible that bodies tuned to have admissible oscillations individually (i.e., in isolated conditions) will violate the constraint when installed in an array. In our tests, we observed that when the initial guess is feasible, then the proposed optimization framework leads to performance increases of a few percentage points. When the initial guess is unfeasible, the method leads to a condition that is feasible and that might have a smaller power than the unfeasible initial guess. In most of the explored cases, allowing the stiffness to have negative values provided larger power that enforcing positive stiffness. In this case, technological feasibility considerations should be made about whether such solution is realizable. Finally, by proposing an example with a double-peaked wave spectrum, we showed that our computational framework can be used to control and optimize more complex configurations, so that it is capable to provide useful indications for the preliminary control design of realistic WEC arrays.

The work in this chapter may be extended by considering different stochastic gradient estimators. We mention as examples the adaptive batchsize method proposed in [21] and the biased stochastic gradient estimators reviewed in [45]. Moreover, time-domain control optimization could be pursued. As a research path, we instead opted for remaining in the frequency domain to study the more challenging problems of layout optimization and control co-design, which we treat in the next chapters.

Chapter 7

Optimal layout design of arrays

In this chapter, we present a layout optimization strategy for arrays of WECs. Most of this work has originally appeared as [59][1]. As a test case, we consider a water turbine oscillating water column converter called WaveSAX and developed by the company RSE [22, 134]. Two versions of the device have been designed: the initial design was meant for integration in coastal structures (e.g., harbours and ports), and then a second version was developed for offshore use, possibly in connection with an offshore wind park; in this chapter, we will focus on the latter. It consists of a vertical pipe in which water moves upward and downward, forced by the wave motion. Power is extracted from the flow through a Wells turbine positioned inside the water column. The Wells turbine is of bi-directional type, i.e., the rotor rotates in the same direction during both the ascending and the descending phase of water motion.

We introduce a lumped-parameter mathematical model for the description of a single device, that is simple enough to allow fast computation, but still able to capture the most important features of the apparatus. It is constructed by considering the integral equations of mass and momentum for the dynamics of the water column, linear potential wave theory for the problem of hydrodynamic interaction with the surrounding environment [126], and a description of the Wells turbine through characteristic curves. The resulting nonlinear, time-domain model is used for the determination of the optimal turbine rotational speed for each sea state of interest. The corresponding linearized problem, that can be solved in the frequency domain, is used to build the multibody model adopted for the simulation and optimization of arrays. Layout optimization is then tackled, limiting our scope to cylindrical devices. For such geometry, the semi-analytical model presented in Sec. 3.2 and based on interaction theory can be used. It allows relatively fast computation of oscillation amplitudes and average power for very large arrays of bodies (up to 150 in our test cases), and it does not adopt the single-body often considered in the literature on large arrays [75], taking instead into account the complete linear hydrodynamic problem, including diffraction. Moreover, such formulation allows the computation of the gradient of the cost function through an adjoint approach. Standard gradient descent methods (see, e.g., [127]) can then

[1] © 2024 The Authors. Published by Elsevier Ltd. The article is under the CC BY license (http://creativecommons.org/licenses/by/4.0/)

be used to seek a solution to the minimization problem.

The chapter is structured as follows. In Sec. 7.1, we state our optimization problem. In Sec. 7.2, a mathematical model of the offshore WaveSAX device is presented, together with the results of single-device simulations. Section 7.3 treats the simulation and optimization of arrays of such devices.

7.1 Optimization problem statement

We consider monochromatic waves and the interaction theory model for the fluid-structure interaction problem (see Sec. 3.2). The aim is to maximize the power of a WEC array with respect to the devices' positions, keeping the control parameters fixed. The vector of decision variables consists in the coordinates of the devices' centers:

$$\boldsymbol{u} := [x_1, y_1, \ldots, x_{N_b}, y_{N_b}]. \tag{7.1}$$

We require devices to be inside an admissible domain defined by a convex polygon, which we express as the constraint $\boldsymbol{u} \in \mathcal{U}_{ad}$. Moreover, devices cannot overlap with each other, and this leads to a minimum distance constraint. The problem can be stated as

$$\begin{aligned} \min_{\hat{\boldsymbol{\gamma}}, \hat{\boldsymbol{\zeta}}, \boldsymbol{u} \in \mathcal{U}_{ad}} \quad & J(\hat{\boldsymbol{\zeta}}) := -P(\hat{\boldsymbol{\zeta}}) \\ \text{s.t.} \quad & \hat{\boldsymbol{\gamma}},\ \hat{\boldsymbol{\zeta}} \text{ satisfy the state equation (3.39)}, \\ & \text{the devices' coordinates in } \boldsymbol{u} \text{ satisfy a minimum distance constraint.} \end{aligned} \tag{7.2}$$

7.2 Isolated device

7.2.1 Mathematical model

The operation of the device is described by two coupled mathematical models: an ordinary differential equation (ODE) for the water column and the linear potential model for the external wave problem. The equation for the evolution in time of the water column level ζ with incident waves of frequency ω, to be derived in Sec. 7.2.1, is

$$\begin{aligned} [\rho C(\zeta) S(\zeta) + A(\omega)]\, \ddot{\zeta} + \rho C(\zeta) \frac{dS}{d\zeta} \dot{\zeta}^2 + \frac{1}{2} \rho \dot{\zeta}^2 \left(1 - \frac{S^2(\zeta)}{S^2(z_1)} \right) \\ + \Delta p(v_t, \omega_t) + B(\omega) \dot{\zeta} + \rho g \zeta = p_e(t). \end{aligned} \tag{7.3}$$

Here, ρ is the water density, $C(\zeta)$ and $S(\zeta)$ are geometrical parameters, and g is the gravity field. Frequency-dependent quantities $A(\omega)$, $B(\omega)$ and function $p_e(t)$ are hydrodynamic properties computed by solving the external problem, detailed in Sec. 7.2.1. Δp is the pressure differential due to the turbine, which is obtained from a nondimensional characteristic curve C_a as

$$\Delta p(v_t, \omega_t) = \frac{C_a K_a}{S_t} (v_t^2 + \omega_t r_t^2), \tag{7.4}$$

where v_t is the axial velocity, ω_t is the rotational speed, and K_a, S_t and r_t are geometric parameters. The behavior of the turbine will be detailed in Sec. 7.2.1. Once the coupled problem has been solved, mechanical power is computed as $P = \mathcal{T}\omega_t$, where $\mathcal{T}$ is the torque, obtained from the characteristic curve C_t as

$$\mathcal{T}(v_t, \omega_t) = C_t K_a r_t (v_t^2 + \omega_t^2 r_t^2). \tag{7.5}$$

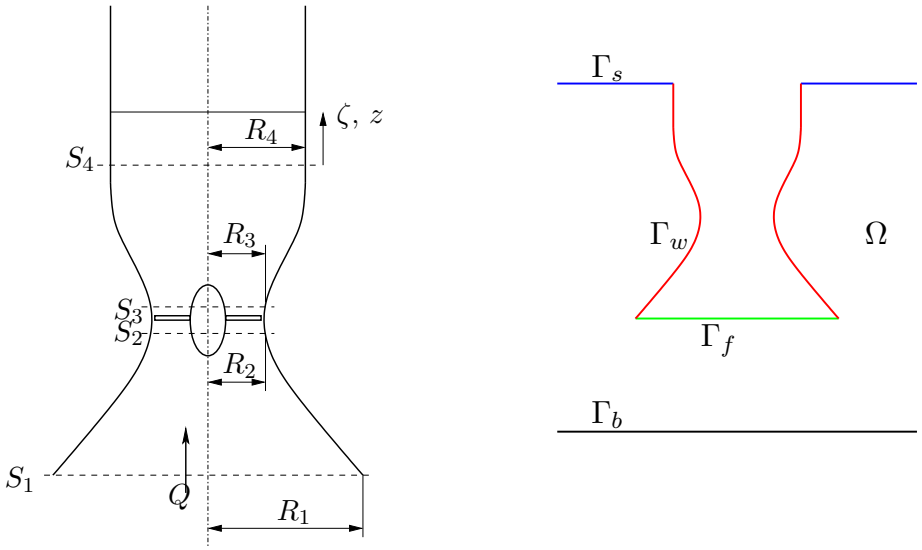

Figure 7.1: *Domain of the internal (left; see Sec. 7.2.1) and external (right; see Sec. 7.2.1) problem.*

The domains of the internal and external models are depicted in Fig. 7.1. The left panel shows the internal domain. Here, S_1 is the inflow section; sections S_2 and S_3 are located immediately below and immediately above the turbine section respectively, while S_4 is located at the equilibrium water level, corresponding to $z = 0$. Finally, Q is the volume flow rate through the inlet section. The right panel shows a 2D slice of the domain Ω of the external wave problem. Its boundaries are the inflow section Γ_f, the external walls of the device Γ_w, the sea bottom Γ_b and the mean free surface Γ_s. The domain Ω is unbounded horizontally.

To make park optimization less computationally demanding, the following linearized form of the equation for the evolution of the water column is used:

$$[\rho C(0) S(0) + A(\omega)]\ddot{\zeta} + [\Lambda S(0) + B(\omega)]\dot{\zeta} + \rho g \zeta = p_e(t). \tag{7.6}$$

Its derivation is shown in Sec. 7.2.1.

Internal model

For the water column, neglecting the effect of viscosity and considering incompressible flow, mass conservation requires

$$Q(t) = S(\zeta)\dot{\zeta}, \tag{7.7}$$

while the momentum balance equation is Euler's equation

$$\rho\frac{\partial \boldsymbol{u}}{\partial t} + \rho(\boldsymbol{u}\cdot\nabla)\boldsymbol{u} = -\nabla p - \rho g\widehat{\boldsymbol{k}}, \tag{7.8}$$

where $\boldsymbol{u}$ is the velocity and $\widehat{\boldsymbol{k}}$ is the upward unit vector. We introduce the quasi-1D approximation

$$\boldsymbol{u}(\boldsymbol{x},t) \approx [0,0,Q(t)/S(z)], \quad p(\boldsymbol{x},t) \approx p(z,t), \tag{7.9}$$

which is valid provided that variations of the device's section are gradual, so that the dominating component of velocity is the longitudinal one. Replacing (7.9) in (7.8) yields

$$\frac{\partial p}{\partial z} = -\frac{\rho\dot{Q}}{S(z)} + \frac{\rho Q^2(t)}{S^3(z)}\frac{\partial S(z)}{\partial z} - \rho g. \tag{7.10}$$

By integration, it is then possible to obtain the pressure difference between the section below the turbine S_2 and the inflow section:

$$p_2 - p_1 = -\rho\dot{Q}\int_{z_1}^{z_2}\frac{dz}{S(z)} + \rho Q^2(t)\int_{z_1}^{z_2}\frac{\partial S(z)}{\partial z}\frac{dz}{S^3(z)} - \rho g(z_2 - z_1), \tag{7.11}$$

and the same can be done for the pressure difference between the atmosphere and the section immediately above the turbine S_3:

$$p_{atm} - p_3 = -\rho\dot{Q}\int_{z_3}^{\zeta}\frac{dz}{S(z)} + \rho Q^2(t)\int_{z_3}^{\zeta}\frac{\partial S(z)}{\partial z}\frac{dz}{S^3(z)} - \rho g(\zeta - z_3). \tag{7.12}$$

For the time being, we generically denote the pressure jump due to the turbine as Δp: then

$$p_3 - p_2 = -\Delta p. \tag{7.13}$$

We also consider negligible the thickness of the turbine section: $z_2 \approx z_3$. The integrals appearing in the above expressions are specified through the definition

$$C(\zeta) = \int_{z_1}^{\zeta}\frac{dz}{S(z)} \tag{7.14}$$

and the computation

$$\int_{z_1}^{\zeta}\frac{\partial S(z)}{\partial z}\frac{dz}{S^3(z)} = \int_{S(z_1)}^{S(\zeta)}\frac{dS}{S^3} = -\frac{1}{2}\left(\frac{1}{S^2(\zeta)} - \frac{1}{S^2(z_1)}\right). \tag{7.15}$$

The time derivative of the flowrate, computed from its expression (7.7), involves the derivative of the section along the axial coordinate:

$$\dot{Q}(t) = S(\zeta)\ddot{\zeta} + \frac{dS}{d\zeta}\dot{\zeta}^2. \tag{7.16}$$

The last contribution is zero if the section is uniform in the upper part of the device. From (7.11), (7.12), and (7.13), we obtain the balance equation

$$\rho C(\zeta)S(\zeta)\ddot{\zeta} + \rho C(\zeta)\frac{dS}{d\zeta}\dot{\zeta}^2 + \frac{1}{2}\rho\dot{\zeta}^2\left(1 - \frac{S^2(\zeta)}{S^2(z_1)}\right) + \Delta p(v_t,\omega_t) + \rho g\zeta = p_1 - p_{atm} + \rho g z_1. \tag{7.17}$$

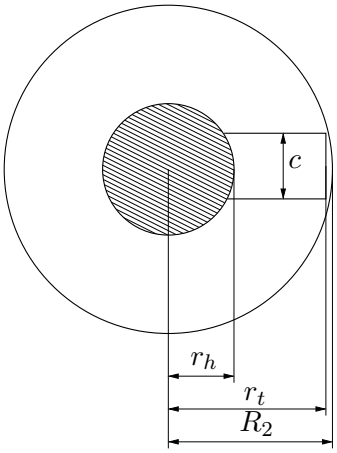

Figure 7.2: *Scheme of the Wells turbine; for simplicity, only one blade is represented.*

We recognize that the forcing term is the pressure deviation from hydrostatic conditions at section 1:

$$p_1' = p_1 - (p_{atm} - \rho g z_1). \tag{7.18}$$

Wells turbine model

The Wells turbine consists of blades generated from the extrusion of a symmetric airfoil and mounted symmetrically on a hub. We shall call ω_t the angular velocity of the turbine, r_t the distance between the axis of the turbine and the blade tips, r_h the hub radius, c the blade chord, n the number of blades and $\mathcal{T}$ the torque exerted on the turbine by the flow (we refer to the diagram in Fig. 7.2). The area of the turbine's flow section, delimited by the hub and the duct walls, is $S_t = \pi(R_2^2 - r_h^2)$, where R_2 is the radius of the section at $z_2 = z_3$. The hydraulic power lost by the flow due to the action of the turbine is $P_{hyd} = Q\Delta p$; the mechanical power available at the shaft is instead $P = \mathcal{T}\omega_t$.

We now recall the definitions of a few common and useful nondimensional variables. The flow coefficient φ is the ratio between the axial velocity $v_t = Q/S_t$ and the tip speed:

$$\varphi := \frac{v_t}{\omega_t r_t}. \tag{7.19}$$

The Reynolds number relative to the chord is

$$\mathrm{Re} := \frac{\sqrt{v_t^2 + r_t^2\,\omega_t^2}\,c}{\nu} = \frac{r_t \omega_t c\sqrt{\varphi^2+1}}{\nu}, \tag{7.20}$$

where ν is the kinematic viscosity. We use the following definition[2] of the nondimensional pressure jump [100]:

$$C_a := \frac{\Delta p S_t}{K_a(v_t^2 + \omega_t^2 r_t^2)}, \tag{7.21}$$

[2]Another common definition in the literature is $\Delta p^* := \Delta p/(\rho\omega_t^2 r_t^2)$ (see [37]).

where $K_a = \rho c(r_t - r_h)n/2$. Likewise, the nondimensional torque is defined[3] as

$$C_t := \frac{\mathcal{T}}{K_a r_t (v_t^2 + \omega_t^2 r_t^2)}. \tag{7.22}$$

In the following, we will consider a formulation based on C_a and C_t, for which literature values are readily available [100]. For clarity, we report the characteristic equations

$$\Delta p(v_t, \omega_t) = \frac{C_a K_a}{S_t}(v_t^2 + \omega_t r_t^2), \tag{7.23}$$

$$\mathcal{T}(v_t, \omega_t) = C_t K_a r_t (v_t^2 + \omega_t^2 r_t^2). \tag{7.24}$$

Finally, the efficiency is

$$\eta = \frac{P}{P_{hyd}}. \tag{7.25}$$

We observe that factor $c(r_t - r_h)n$ in K_a is the total area of the blades, if they are rectangular. Hence, by using the definition of solidity σ as the ratio of blade area to the area of the turbine flow section S_t, we have $K_a = \rho\sigma S_t/2$ and thus the nondimensional pressure coefficient can be written as

$$C_a = \frac{\Delta p}{\sigma q_\infty}, \quad q_\infty := \frac{1}{2}\rho(v_t^2 + \omega_t^2 r_t^2), \tag{7.26}$$

where q_∞ is the dynamic pressure at the blade tips. Analogously,

$$C_t = \frac{\mathcal{T}}{\sigma S_t r_t q_\infty}. \tag{7.27}$$

The pair of functions $C_a(\varphi)$, $C_t(\varphi)$, or alternatively $\Delta p^*(\varphi)$, $\mathcal{T}^*(\varphi)$, represent the characteristic curves of the turbine.

In order to explain the working principle of the turbine and the shape of the characteristic curves, let us consider a single blade. The angle of attack of a blade section at a distance r from the axis of rotation is $\alpha(r) = \arctan(\varphi r_t/r)$: it reaches its maximum value at the hub and its minimum at the blade tips. When the flow coefficient is zero, the blade is at zero incidence. In such conditions, since blades have symmetric airfoils, the lift force is zero, while the drag force is non-zero and produces a negative torque. If a constant angular velocity control strategy is chosen, then such negative torque must be compensated by a motor torque produced by feeding energy to the system. If, instead, the angular velocity is allowed to vary, then mechanical inertia may absorb this effect. As the flow coefficient increases, the lift force on the blades increases. Both the nondimensional pressure jump and the nondimensional torque increase; correspondingly, the efficiency increases, until it reaches a plateau at values typically around 40% to 60%. As the angle of stall is reached, the lift force starts decreasing; this happens more or less abruptly depending on the shape of the airfoil (in particular, on its thickness) and on the turbulence intensity. Thick airfoils typically exhibit a soft stall behavior,

[3] We also report the alternative definition $\mathcal{T}^* := \mathcal{T}/(\rho\omega_t^2 r_t^5)$.

produced by flow separating at the trailing edge; conversely, thin airfoils have a more abrupt stalling behavior, corresponding to leading edge flow separation [10]. Greater turbulence intensities can delay stall and mitigate its effects [158]. Stall causes a reduction in nondimensional torque, while the nondimensional pressure difference keeps increasing. Hence, efficiency decreases until it becomes negligible for values of the flow coefficient around 0.3 to 0.4. We observe that $\varphi = 0.4$ corresponds to an angle of attack of about 21.8° at the blade tip, a very large value for symmetric airfoils.

An additional effect that impacts on the performance of the turbine is due to the value of the distance between the blade tips and the duct walls, called tip clearance or tip gap (TG). In [166], the results of some simulations are reported, showing that the largest efficiencies can be reached for small values of tip clearance, of the order of 1%. Intermediate values of TG lead to worse performance for small values of the flow coefficient, while tip clearances larger than about 10% cause low efficiency in all operating conditions.

Cavitation is another important, and potentially damaging, physical phenomenon for turbines immersed in water. It occurs when the pressure falls below the vapor pressure of the liquid [56]. For water at 20°C, vapor pressure is $p_v = 2.34$ kPa. The minimum pressure on the turbine can be approximately computed by considering the pressure coefficient

$$C_p = \frac{p - p_\infty}{1/2 \rho U_\infty^2}. \tag{7.28}$$

This quantity, for large values of the Reynolds number and small values of the Mach number, does not depend on the freestream velocity U_∞. Thus, for a turbine located at a depth z_t below mean sea level, the minimum absolute pressure can be computed as

$$p_{\min} = p_{\text{atm}} + \rho g(\zeta - z_t) + \frac{1}{2}\rho(v_t^2 + \omega_t^2 r_t^2) C_{p,\min}, \tag{7.29}$$

where $C_{p,\min}$ can be obtained from literature data or from simulations either of the full blade (3D) or of its section (2D). The condition of incipient cavitation is $p_{\min} = p_v$. It is reasonable to expect the minimum pressure to occur on the suction surface, close to the leading edge.[4] In our case, the turbine is not simply located at some depth below sea level: it is immersed in a water column of time-varying depth. Referring to Fig. 7.1, the freestream pressure is p_2 when the flow is ascending, and p_3 when the flow is descending. Using the results from Sec. 7.2.1, we obtain

$$\begin{aligned} p_{\min} = {} & p_{\text{atm}} + \rho g(\zeta - z_t) + \frac{1}{2}\rho(v_t^2 + \omega_t^2 r_t^2) C_{p,\min} \\ & + \rho \left[\frac{dS}{d\zeta} \dot{\zeta}^2 + S(\zeta) \ddot{\zeta} \right] [C(\zeta) - C(z_t)] + \frac{1}{2}\rho \left[1 - \frac{S^2(\zeta)}{S^2(z_t)} \right] \\ & + \begin{cases} \Delta p(v_t, \omega_t) & \text{if } \dot{\zeta} > 0, \\ 0 & \text{otherwise} \end{cases} \end{aligned} \tag{7.30}$$

[4] In this case, talking about upper surface and lower surface could be misleading, since their roles as suction surface and pressure surface are inverted at every half-cycle of oscillation of the water column.

To ensure that the turbine works correctly, it must also always remain immersed. The fact that the constraint of no cavitation is fulfilled does not imply that the constraint of immersed turbine is satisfied, nor vice versa.

In principle, to correctly model the behavior of the turbine, one would have to write a dynamic equation for its rotational motion, including, as forcing terms, the hydrodynamic torque and the electromagnetic torque. At this stage of the design of the device, full-scale data about turbine inertia and about the electrical generator are not known. For this reason, in our simulations we adopted the simplifying assumption of constant rotational speed, which in practice would need to be realized through an appropriate controller.

Torque and pressure difference are computed from the data of [100]. Coefficient $C_{p,\min}$, needed for cavitation computations, has been obtained from simulations of a single blade section performed using Xfoil [44]. We repeated the computation for the NACA0021 airfoil, considered in [136], and the NACA0015 airfoil, considered in [135]. Results are reported in Fig. 7.3. We first notice that the results of inviscid simulations differ greatly from the ones of viscous, turbulent simulations; we will refer to the latter. The minimum pressure coefficient is larger (in absolute value) for the NACA0015 airfoil, due to its smaller thickness, which induces a smaller radius of curvature of the streamlines and thus more intense depressions, being the pressure gradient linked to centripetal acceleration. The results indicate that the NACA0021 airfoil may be less prone to cavitation. We also notice that airfoils become more sensitive to cavitation as the Reynolds number increases. It is reasonable to expect that the data thus obtained yields cautionary estimates of the condition of incipient cavitation. Indeed, the turbine blades have a very small aspect ratio, which may lead to important tip effects. Such effects should reduce the intensity of local suction peaks thanks to the current generated between the pressure side and the suction side.

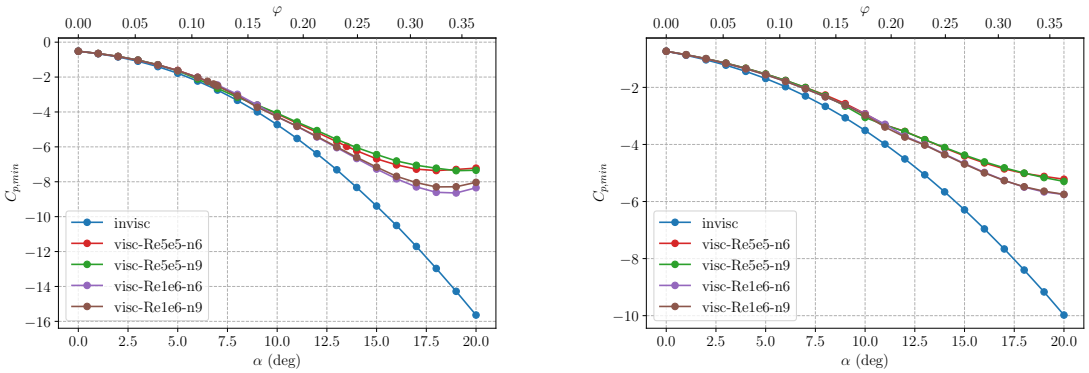

Figure 7.3: *Coefficient $C_{p,min}$ as a function of angle of attack and flux coefficient; NACA0015 (left), NACA0021 (right).*

External model

A decomposition of the potential analogous to (2.45), but adapted to OWC devices, is introduced. The potential is accordingly written as the sum of the potential of ambient incident waves ϕ_0, a diffraction potential ϕ_d, produced by incident

waves with the condition of zero volume flux through the inflow section Γ_f (corresponding to S_1), and radiation potential ϕ_r, obtained, thanks to linearity, by multiplying the average velocity on section S_1 by the potential φ_r corresponding to unit amplitude velocity fluctuations. In the frequency domain, we have

$$\widehat{\phi} = \widehat{\phi}_0 + \widehat{\phi}_d + \frac{\widehat{Q}}{S_1}\varphi_r. \tag{7.31}$$

For any given frequency, (7.31) allows writing the mean pressure on the inflow section as an integral:

$$\begin{aligned}\widehat{p}_1' =& i\omega\rho\frac{1}{S_1}\int_{\Gamma_f}\widehat{\phi}\,d\Gamma \\ =& \underbrace{i\omega\rho\frac{1}{S_1}\int_{\Gamma_f}(\widehat{\phi}_0+\widehat{\phi}_d)\,d\Gamma}_{\text{excitation pressure } \widehat{p}_e(\omega)} + \underbrace{(-i\omega\widehat{\zeta})i\omega\rho\frac{S_4}{S_1}\frac{1}{S_1}\int_{\Gamma_f}\varphi_r\,d\Gamma.}_{\text{radiation pressure } \widehat{p}_r=-R(\omega)(-i\omega\widehat{\zeta})}\end{aligned} \tag{7.32}$$

This quantity depends on the state of the water column through $\widehat{\zeta}(\omega)$, the Fourier transform of $\zeta(t)$. From the potential φ_r, the coefficients of added mass $A(\omega)$ and radiation damping $B(\omega)$ can be computed:

$$R(\omega) = -i\omega A(\omega) + B(\omega) \rightarrow \begin{cases} A(\omega) = \mathrm{Im}\left[i\rho\dfrac{S_4}{S_1}\dfrac{1}{S_1}\displaystyle\int_{\Gamma_f}\varphi_r\,d\Gamma\right] \\ B(\omega) = -\omega\mathrm{Re}\left[i\rho\dfrac{S_4}{S_1}\dfrac{1}{S_1}\displaystyle\int_{\Gamma_f}\varphi_r\,d\Gamma\right]. \end{cases} \tag{7.33}$$

Radiation damping describes the pressure contribution in phase with the flowrate. It corresponds to a net exchange of energy with the environment due to the generation of radiated waves by the device. Added mass describes a pressure contribution with a phase difference of $\pi/2$ with respect to the flowrate; thus, the time-averaged exchange of energy with the environment due to this term is zero. The diffraction potential is obtained from the solution of problem

$$\begin{cases} \Delta\widehat{\phi}_d = 0 & \text{in } \Omega \\ \dfrac{\partial\widehat{\phi}_d}{\partial z} = 0 & \text{on } \Gamma_b \\ \dfrac{\partial\widehat{\phi}_d}{\partial z} - \dfrac{\omega^2}{g}\widehat{\phi}_d = 0 & \text{on } \Gamma_s \\ \dfrac{\partial\widehat{\phi}_d}{\partial n} = -\dfrac{\partial\widehat{\phi}_0}{\partial n} & \text{on } \Gamma_w \cup \Gamma_f, \end{cases} \tag{7.34}$$

where

$$\widehat{\phi}_0 = -i\frac{H}{2}\frac{g}{\omega}\frac{\cosh[k(z+h)]}{\cosh(kh)}\exp[ik(x\cos\beta + y\sin\beta)]. \tag{7.35}$$

Here, H is the wave height, h is the water depth, k is the wavenumber, β is the wave direction and (x, y) are the coordinates in the horizontal plane. We refer to Fig. 7.1 for the nomenclature of the boundaries. The radiation potential satisfies

$$\begin{cases} \Delta\varphi_r = 0 & \text{in } \Omega \\ \dfrac{\partial\varphi_r}{\partial z} = 0 & \text{on } \Gamma_b \\ \dfrac{\partial\varphi_r}{\partial z} - \dfrac{\omega^2}{g}\varphi_r = 0 & \text{on } \Gamma_s \\ \dfrac{\partial\varphi_r}{\partial n} = 0 & \text{on } \Gamma_w \\ \dfrac{\partial\varphi_r}{\partial n} = 1 & \text{on } \Gamma_f. \end{cases} \tag{7.36}$$

It is important to notice that in the radiation problem we have imposed uniform velocity directed upwards on the inflow section. In practice, on the inflow section the radial component of velocity may not be negligible, and the vertical component may not be uniform. The linear potential model would allow to impose a non-uniform vertical velocity on the section. It would instead not be possible to impose a radial component of velocity, because only the component of velocity normal to the boundary (and thus, axial) appears in the boundary condition.

Since the domain is unbounded, a radiation condition needs to be enforced at infinity for both problems; at the numerical level, this is satisfied by the Green functions used. Hydrodynamic simulations have been carried out by employing the open-source code Capytaine [7], which solves the Laplace equation using the boundary element method. The hydrodynamic properties of the considered device,

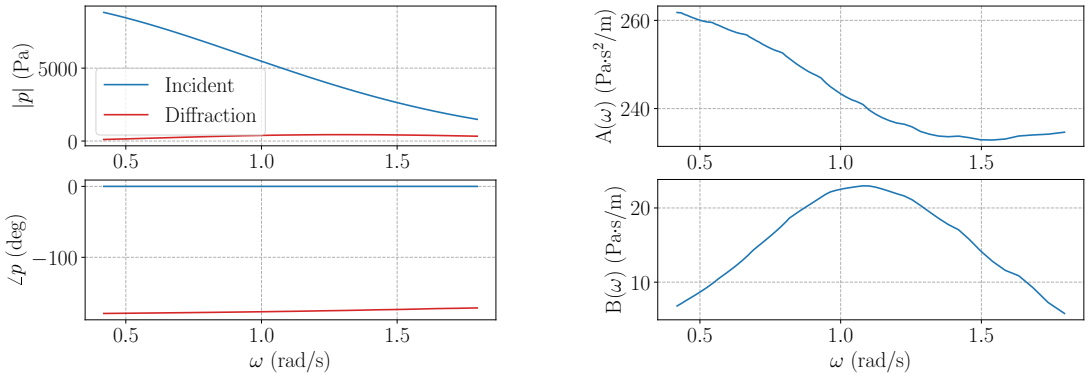

Figure 7.4: *Diffraction (left) and radiation data (right), from the solution of the external problem for an isolated device.*

obtained by solving the external problem, are reported in Fig. 7.4. We notice that especially for low frequencies (long waves), the magnitude of the diffraction pressure is very small compared to the magnitude of the incident wave pressure. This is due to the small size of the device compared to the wavelength. The dominating contribution is thus due to the potential of incident waves (7.35). For $-h < z < 0$, this is an increasing function of z. Hence, the mean pressure on the

inflow section, which is the forcing term of the internal problem, decreases as the draft of the device increases.

Since the internal model is nonlinear, a forcing term due to a purely monochromatic wave would produce a response $\zeta(t)$ that is in general not monochromatic. To correctly represent this effect, one should write a convolution integral (in time) for the radiation term, corresponding to the product $R(\omega)\widehat{\zeta}(\omega)$ in the frequency domain. An accurate computation of such product would require solving the radiation problem for a potentially large number of frequencies, which would significantly increase the computational cost of simulation and optimization. We instead only use the values of added mass $A(\omega)$ and radiation damping $B(\omega)$ corresponding to the frequency ω of the incident monochromatic wave; the same is done for $\widehat{p}_e(\omega)$. Such approximation is reasonable due to the small magnitude of the radiation terms compared to the other terms of the equation. From (7.32) and (7.33), and transforming back to the time domain while treating $A(\omega)$, $B(\omega)$ as constants as discussed above, we obtain $p_1'(t) = p_e(t) - A(\omega)\ddot{\zeta}(t) - B(\omega)\dot{\zeta}(t)$, which, substituted in the dynamic equation (7.17), yields

$$\begin{aligned}[\rho C(\zeta)S(\zeta) + A(\omega)]\,\ddot{\zeta} + \rho C(\zeta)\frac{dS}{d\zeta}\dot{\zeta}^2 + \frac{1}{2}\rho\dot{\zeta}^2\left(1 - \frac{S^2(\zeta)}{S^2(z_1)}\right) \\ +\Delta p(v_t, \omega_t) + B(\omega)\dot{\zeta} + \rho g\zeta = p_e(t),\end{aligned} \tag{7.37}$$

and where the forcing term is reconstructed from its complex coefficient as $p_e(t) = \mathrm{Re}\left[\widehat{p}_e(\omega)\exp(-i\omega t)\right]$. Equation (7.37) is a nonlinear ordinary differential equation in the time domain, where the external forcing is a monochromatic wave of frequency ω.

Linearized model

In this section, a linearization of the model introduced in Sec. 7.2.1 is derived and discussed. The advantages of adopting a linearized model are the possibility of obtaining analytical results that can be useful for an initial understanding of the behavior of the device, the lower computational cost due to the possibility of transforming the problem to the frequency domain and thus to an algebraic problem, and the possibility of coupling with the multi-body, semi-analytical hydrodynamic model presented in Sec. 7.3.1, which is especially suitable for optimization.

Linearization of the equation of motion (7.17) around the equilibrium condition $\zeta(t) = 0$ yields

$$[\rho C(0)S(0) + A(\omega)]\ddot{\zeta} + [\Lambda S(0) + B(\omega)]\dot{\zeta} + \rho g\zeta = p_e(t), \tag{7.38}$$

where $\Lambda = \left.\frac{\partial\Delta p}{\partial Q}\right|_{Q=0}$. To obtain this quantity from (7.23), we compute

$$\left.\frac{\partial\Delta p}{\partial v_t}\right|_{v_t=0} = \left[\frac{\partial C_a}{\partial\varphi}\frac{\partial\varphi}{\partial v_t}\frac{K_a}{S_t}(v_t^2 + \omega_t^2 r_t^2) + \frac{2C_a K_a v_t}{S_t}\right]_{v_t=0} = \left.\frac{\partial C_a}{\partial\varphi}\right|_{\varphi=0}\frac{K_a\omega_t r_t}{S_t}, \tag{7.39}$$

from which, recalling that $Q = v_t S_t$,

$$\Lambda = \left.\frac{\partial\Delta p}{\partial Q}\right|_{Q=0} = \frac{1}{S_t}\left.\frac{\partial\Delta p}{\partial v_t}\right|_{v_t=0} = \left.\frac{\partial C_a}{\partial\varphi}\right|_{\varphi=0}\frac{K_a\omega_t r_t}{S_t^2}. \tag{7.40}$$

This result shows that the turbine has, up to first order, the role of a damping.

We now discuss the limits of validity of the linearized model. In general, the linearization will lead to a good approximation if the oscillation amplitude is small. In addition, the terms multiplying $\dot{\zeta}^2$ in (7.17) will be small regardless of the magnitude of the oscillation amplitude if the variation of the area of the duct sections along z is small close to $z = 0$; under the same conditions, we have $C(\zeta)S(\zeta) \approx C(0)S(0)$. The linearization of the turbine's characteristic equation is acceptable if the flow coefficient is small, if, again, variations of the section are negligible around $z = 0$, and if $C_a(\varphi)$ is well approximated by a straight line. This last requirement is in general fulfilled, as shown in the used characteristic curves [100]. Expanding (7.23) in $\dot{\zeta}$, one obtains

$$\Delta p = \frac{C_a'(0)K_a\omega_t r_t}{S_t^2} S(\zeta)\dot{\zeta} + \frac{C_a'(0)K_a}{\omega_t r_t S_t^5} S^3(\zeta)\dot{\zeta}^3 + o(\dot{\zeta}^3) = \Lambda S(\zeta)\dot{\zeta}(1+\varphi^2) + o(\dot{\zeta}^3), \tag{7.41}$$

which shows that the ratio between the term of order 3 and the term of order 1 is φ^2. Typical values of φ are less than or close to 0.3: the ratio is thus, at most, of order 1/10 for conditions of interest.

Typical values of Λ for the considered converter are of the order of $6 \cdot 10^3$ Pa $\cdot$ s/m^3. Since $S(0)$ is of the order of 1 m^2, and examining the values of radiation damping $B(\omega)$ from Fig. 7.4, we observe that the latter is negligible compared to the contribution from the turbine. Likewise, in the mass term, $\rho C(0)S(0)$ is about an order of magnitude larger than $A(\omega)$. By considering this approximation in the computation of the natural frequency of the linearized system, one obtains

$$\omega_0 = \sqrt{\frac{\rho C(0)S(0) + A}{\rho g}} \approx \sqrt{\frac{C(0)S(0)}{g}} \approx \sqrt{\frac{L}{g}}, \tag{7.42}$$

where the last step is an exact equality in the case of a tube of length L and uniform section. The length of the duct is thus the dimension that influences the natural frequency the most.

In the frequency domain, the linearized dynamic equation reads

$$\left\{-\omega^2[\rho C(0)S(0) + A(\omega)] - i\omega[\Lambda S(0) + B(\omega)] + \rho g\right\} \widehat{\zeta} = \widehat{p}_e. \tag{7.43}$$

The mean hydraulic power is

$$P_{\text{hyd}} = \frac{1}{2}\Lambda\omega^2 S^2(0)|\widehat{\zeta}|^2. \tag{7.44}$$

For the computation of the mean mechanical power, adopting a linearization of the nondimensional torque curve $C_t(\varphi)$ would be too inaccurate, since it would not be possible to describe the presence of the maximum point corresponding to stall. We instead consider an approximation given by an even polynomial

$$C_t(\varphi) = c_0 + c_2(\varphi)\varphi^2 + c_4(\varphi)\varphi^4 + \cdots + c_{2d}(\varphi)\varphi^{2d}, \tag{7.45}$$

whose degree $2d$ can be chosen in order to obtain a prescribed accuracy. This choice leads to the following expression for the instantaneous power:

$$P(t) = \mathcal{T}(t)\omega_t = \left(c_0 + c_2\frac{v_t^2(t)}{\omega_t^2 r_t^2} + c_4\frac{v_t^2(t)}{\omega_t^2 r_t^2} + \dots\right) K_a r_t \left(v_t^2(t) + \omega_t^2 r_t^2\right)\omega_t, \tag{7.46}$$

where the time dependence has been made explicit. Computing the time-average of this quantity involves integrals of the form

$$I_n = \frac{1}{2\pi} \int_{-\pi}^{\pi} [\sin(x)]^{2n} \, dx. \tag{7.47}$$

Integration by parts yields the recursive expression

$$I_n = \begin{cases} 0, & \text{if } n \text{ is odd,} \\ \frac{n-1}{n} I_{n-2}, & \text{if } n \text{ is even,} \end{cases} \tag{7.48}$$

from which we can obtain the explicit expression

$$I_n = \frac{(n-1)(n-3)\dots}{n(n-2)\dots} = \frac{(n-1)!!}{n!!}. \tag{7.49}$$

The mean mechanical power can then be expressed as

$$P = \sum_{n=0}^{d} p_n \left(\omega |\widehat{\zeta}|\right)^{2n}, \tag{7.50}$$

with coefficients p_n given by

$$p_0 = c_0 K_a \omega_t^3 r_t^3, \tag{7.51}$$

$$p_n = I_n (c_{2(n-1)} + c_{2n}) K_a (r_t \omega_t)^{3-2n} \left(\frac{S(0)}{S_t}\right)^{2n}, \quad n = 1, \dots, d-1, \tag{7.52}$$

$$p_d = I_d c_{2(d-1)} K_a (r_t \omega_t)^{3-2d} \left(\frac{S(0)}{S(t)}\right)^{2d}. \tag{7.53}$$

By adopting this approach, passing to the time domain is not required for computing the mean power. The condition of low flux coefficient and thus low angle of attack, in which only the drag component of the hydrodynamic force is acting on the blades and power is negative, is represented by the condition $p_0 < 0$. Higher order terms describe the regimes of positive power and stall.

7.2.2 Simulation and optimization

Figure 7.5 shows the time series of the main quantities of interest obtained from the solution of the dynamic equation (7.37) for a reference wave condition. With reference to Fig. 7.1, the main dimensions of the device are $R_1 = 1.4$ m, $R_2 = 0.5$ m, $R_4 = 0.75$ m, $z_2 = -3.650$ m, $z_4 = -5.650$ m. A phase difference between the levels of the water column and of the free surface outside the device can be observed. The elevation head thus generated makes energy production possible. During each wave period, two maxima and two minima of power and pressure on blades occur. Every power maximum corresponds to a pressure minimum. The latter are observed when the water column is at the reference level ($\zeta = 0$), corresponding to a maximum value of flowrate. The pressure minima that occur when the internal free surface is ascending are less severe than the ones

that occur when the internal free surface is descending. Intervals of negative power are observed around each maximum and each minimum point of the water column level. Power must then be provided to the system in order to keep the turbine in motion at constant speed. Moreover, such maxima and minima occur approximately when the curves of internal and external water levels intersect. The intuitive explanation of this fact is that the tube can fill up only as long as the external level is higher than the internal level, and it can empty only as long as the internal level is higher than the external level. Positive power peaks appear clipped because the condition of maximum efficiency (optimal flow coefficient) is reached and slightly exceeded.

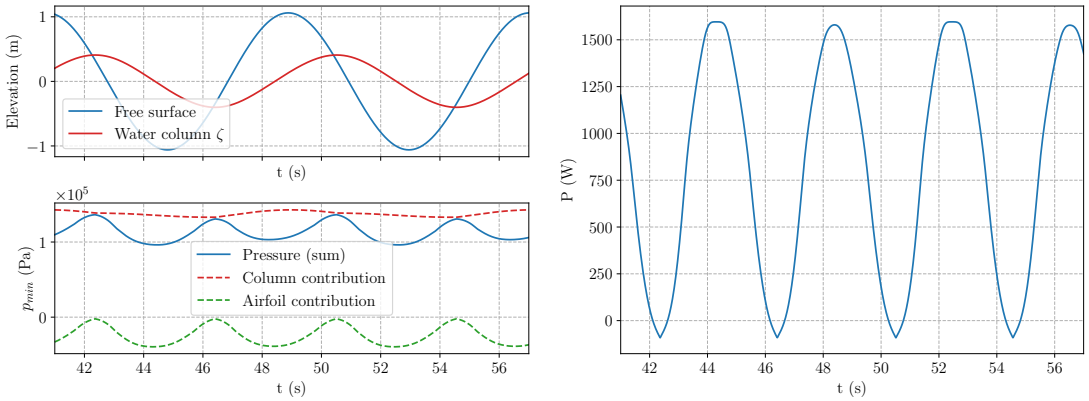

Figure 7.5: *Water level, minimum pressure on blades (left) and extracted power (right) with 7-blade turbine, $H_s = 3$ m, $T = 8.15$ s.*

Control optimization and power matrix estimation

From the linearized model (7.43) it is possible to compute analytically the value of Λ that maximizes the mean hydraulic power (7.44) when a monochromatic wave of angular frequency ω forces the system:

$$\Lambda_{\max P_{hyd}}(\omega) = \frac{1}{S(0)}\sqrt{B^2(\omega) + \frac{\left[-\omega^2(\rho C(0)S(0) + A(\omega)) + \rho g\right]^2}{\omega^2}}. \tag{7.54}$$

The corresponding value of ω_t can be found by inverting (7.40). In practice, however, one does not seek to maximize the mean hydraulic power, but rather the mean mechanical power. For the latter, it is not possible in general to determine the optimal value of ω_t analytically. Nevertheless, the value of ω_t maximizing hydraulic power can be used as the initial guess of an optimization process for mechanical power. The optimization problem was solved using function `minimize_scalar` of `scipy`. A comparison of the two values is shown in Fig. 7.6. We observe that the maximum hydraulic power is reached for a turbine rotational speed that is lower than the one corresponding to maximum mechanical power. Indeed, the maximum flow coefficient reached when the rotational speed is set to the value of maximum hydraulic power corresponds to stall conditions and thus suboptimal efficiency. It can be further noted that while the rotational speed

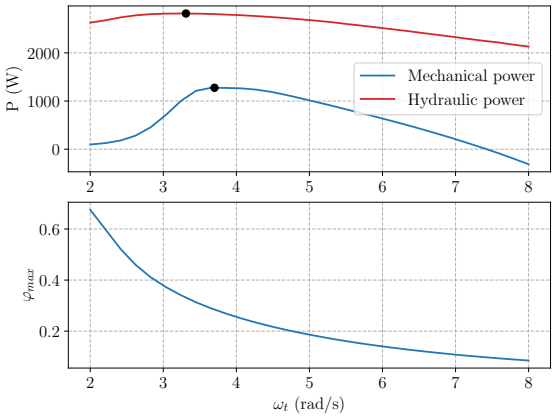

Figure 7.6: *Mechanical power, hydraulic power and maximum flow coefficient as functions of the turbine's rotational speed.*

corresponding to maximum hydraulic power is independent of the height of the incident waves (which can be observed from (7.54) and (7.40)), the rotational speed that maximizes the mechanical power must be chosen based on the flow coefficient, which depends on the oscillation amplitude and thus on the incident wave height.

The computation can be repeated for several sea states, obtaining the maximum power absorbable in each of them under the assumption of constant rotational speed. In this way, we obtain the power matrix of the device. In the literature, power matrices are generally defined in terms of peak period T_p, or energy period T_e, and significant wave height H_s [15]. In the present work, each sea state has been approximated as a single monochromatic wave following the criteria described in 3.3. The results are reported in Appendix A. We have reported, in addition to optimal power and turbine velocity, the maximum and minimum levels of the water column and the minimum pressure on the turbine. The capture width ratio, a performance indicator, is also computed. It is defined as CWR $= P/(2R_1J)$, where P is the mean mechanical power, J is the energy flux of the ambient incident waves, and R_1 is the radius of the duct at the flow section, that is the section of maximum width. It can be observed that the oscillations of the internal free surface are small compared to the vertical scale of the device; in particular, their amplitude is lower for the 7-blade turbine than for the 5-blade turbine, due to the greater hydraulic resistance of the former. The most energetic conditions lead to cavitation for the 5-blade turbine, while this effect is not present in the results for the 7-blade turbine.

As a comparison, a cylindrical device with constant section has been considered. Its radius is 75 cm, equal to the radius of the upper part of the original device, and it is equipped with a 7-blade turbine. Computations on this geometry yield a greater power than the original device. The capture width ratio, in particular, is significantly larger. For this reason, in the following, we will consider only the device with constant section. In all simulated conditions, the minimum pressure is above the vapor pressure.

Finally, the computations for the constant section device have been repeated

using the linearized model introduced in Sec. 7.2.1. The linear model slightly overestimates the power, especially for the most energetic wave conditions, while the results in terms of optimal rotational speed are comparable. The results of this section can be compared to the ones in [135], where the initial design of the WaveSAX device was tested both experimentally and numerically. Qualitative agreement is observed regarding the phase difference between the internal and external water levels reported in Fig. 7.5, and regarding power matrix results. While a full experimental validation of the presented models is out of the scope of the present work, this favorable comparison with previous data suggests that the model choice is appropriate.

Influence of device dimensions on annual power

The mean annual power of a device installed at a specific location can be computed by multiplying term by term the power matrix by resource characterization matrix of such location (see Sec. 2.4), and summing. Given the resource characterization matrix of a location, the mean annual power of a device will depend on the dimensions of the device and on the control strategy. In the following, we present a computationally cheap procedure for parameter exploration on device dimensions. For simplicity, the linear model is used and the control strategy is set to an approximate optimum: we impose that, in each sea state, the maximum magnitude of the flow coefficient (that is the absolute value of its complex amplitude) corresponds to the condition of maximum nondimensional torque. This is equivalent to requiring that at each wave cycle the turbine blades reach the condition of incipient stall without exceeding it. We write such condition as $|\widehat{\varphi}| = \varphi_{\text{opt}}$. Mass conservation requires

$$S\omega|\widehat{\zeta}| = S_t|\widehat{v}_t|. \tag{7.55}$$

The conditions above, together with the definition of the flow coefficient (7.19), yield

$$|\widehat{\zeta}| = \frac{|\widehat{v}_t|S_t}{\omega S} = \frac{\varphi_{\text{opt}} S_t r_t \omega_t}{\omega S}. \tag{7.56}$$

It is possible to determine the value of ω_t by solving the nonlinear equation

$$\left\{[-\omega^2(A(\omega)+\rho L)+\rho g]^2 + \omega^2(B(\omega)+S\Lambda(\omega_t))^2\right\}\frac{\varphi_{\text{opt}} S_t r_t \omega_t}{\omega S} - |\widehat{p}_e|^2 = 0 \tag{7.57}$$

using Newton's method. The results obtained from the wave climates of two locations, Alghero and Civitavecchia, are reported in terms of individual device power, linear power density and surface power density in Fig. 7.7, 7.8.

The presented method has a very low computational cost, but it does not take into account the constraints of immersed turbine and absence of cavitation. For this reason, the obtained results may overestimate the power for some combinations of the parameters. We thus present an alternative method, in which constraints are enforced by penalization.

A generic constraint will be expressed as $c_i \leq 0$. In the frequency domain, the constraint of immersed turbine can be expressed as

$$c_1 = |\widehat{\zeta}| - |z_t|. \tag{7.58}$$

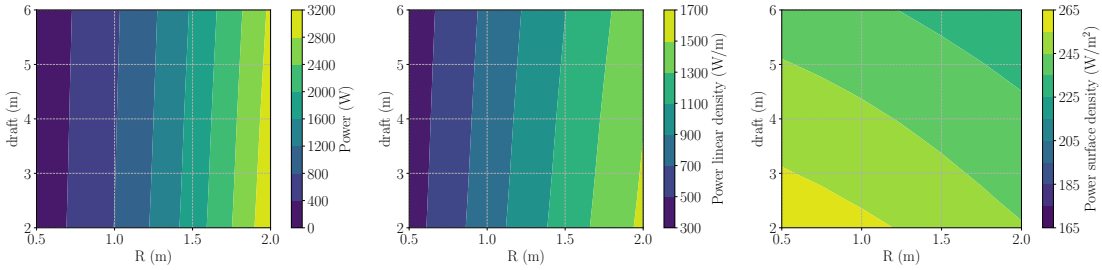

Figure 7.7: *Mean annual power for variable geometric parameters; wave climate of Alghero (unconstrained model).*

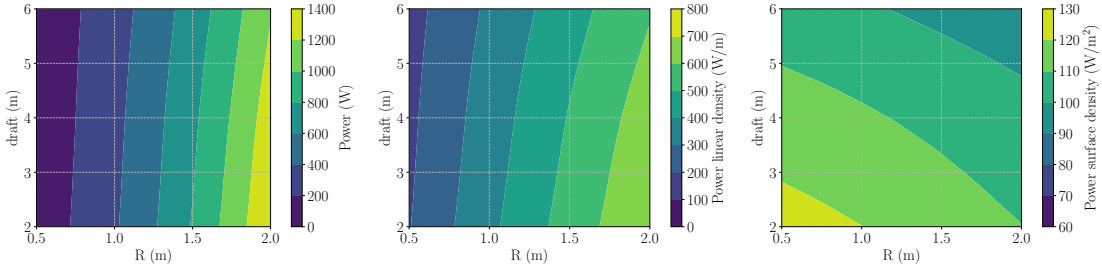

Figure 7.8: *Mean annual power for variable geometric parameters; wave climate of Civitavecchia (unconstrained model).*

The vertical coordinate z_t of the turbine is fixed at 60% of the draft, indicated as d: $z_t = -0.6d$. For the constraint of no cavitation, we introduce a cautionary estimate of the minimum pressure on blades. Starting from (7.29) and defining the minimum over φ of the minimum pressure coefficient

$$\tilde{C}_{p,\min} = \min_{\varphi} C_{p,\min}(\varphi), \tag{7.59}$$

one obtains the lower bound $\tilde{p}_{\min}$:

$$p_{\min}(t) \geq \tilde{p}_{\min}(t) := p_{\text{atm}} + \rho g(\zeta(t) - z_t) + \frac{1}{2}\rho\left(v_t^2(t) + \omega_t^2 r_t^2\right)\tilde{C}_{p,\min}. \tag{7.60}$$

We now express the time evolution of the level of the water column and of the axial velocity from their complex amplitudes (their absolute phases are irrelevant for our purposes):

$$\zeta(t) = |\widehat{\zeta}|\cos(\omega t), \quad v_t(t) = \dot{\zeta}(t)\frac{S}{S_t} = -\frac{\omega|\widehat{\zeta}|S}{S_t}\sin(\omega t). \tag{7.61}$$

It is possible to separate a constant pressure term[5] $\overline{p}$ from fluctuations $\tilde{p}'$:

$$\overline{p} = p_{\text{atm}} - \rho g z_t + \frac{1}{2}\rho\omega_t^2 r_t^2 \tilde{C}_{p,\min}, \tag{7.62}$$

[5]This is not the mean pressure, since the term v_t^2, that is included in the fluctuations, does not have zero mean.

and compute the time derivative of the fluctuations:

$$\tilde{p}'_{min}(t) = \sin(\omega t)\left[-\rho g|\widehat{\zeta}|\omega + \frac{\rho\omega^3|\widehat{\zeta}|^2 S^2}{S_t^2}\tilde{C}_{p,\min}\cos(\omega t)\right]. \tag{7.63}$$

The first pair of stationary points occurs for $\sin(\omega t) = 0$. It corresponds to $\tilde{p}_{\min}(t) = \overline{p} \pm \rho g|\widehat{\zeta}|$, i.e., a local maximum and a local minimum. We take the minimum and introduce the constraint function

$$c_2 = -\overline{p} + \rho g|\widehat{\zeta}| + p_v. \tag{7.64}$$

An additional stationary point exists if the square bracket vanishes in (7.63). Since $\cos(\omega t) \geq -1$ and $\tilde{C}_{p,\min} < 0$, this can happen only if

$$\tilde{C}_{p,\min} \leq -\frac{gS_t^2}{S^2\omega^2|\widehat{\zeta}|}. \tag{7.65}$$

We thus introduce the constraint

$$c_3 = \begin{cases} 0, & \text{(7.65) holds,} \\ -\overline{p} - \dfrac{\rho g^2 S_t^2}{\omega^2 S^2 \tilde{C}_{p,min}} - \dfrac{1}{2}\rho\dfrac{|\widehat{\zeta}|}{S_t^2}\sqrt{(\omega^2|\widehat{\zeta}|S^2\tilde{C}_{p,min})^2 - (gS_t^2)^2} + p_v & \text{otherwise.} \end{cases} \tag{7.66}$$

Finally, for modeling reasons, we impose that the flow coefficient does not exceed the limits of validity of the polynomial approximation of the nondimensional torque curve (7.45). The corresponding constraint function is

$$c_4 = |\widehat{\varphi}| - \varphi_{\text{max, model}}. \tag{7.67}$$

All constraints are enforced by a quadratic penalty function [127]:

$$Q_\mu(\omega_t) = -P(\omega_t) + \mu\sum_{i=1}^{4}[c_i(\omega_t)]_+^2. \tag{7.68}$$

This is the cost function to be minimized; the single variable optimization problem is solved, again, using function `minimize_scalar`. Convergence of the quadratic penalty method to the true constrained minimum is guaranteed in the limit $\mu \to \infty$; thus, optimization is repeated for increasing values of μ until a tolerance on the violation of constraints is satisfied.

Results are shown in Fig. 7.9, 7.10.

The results of the constrained model for the wave climate of Alghero, more energetic than the one of Civitavecchia, are especially different from the ones obtained with the unconstrained model. Indeed, in the unconstrained case, the oscillation amplitude of the water column obtained in the conditions of maximum turbine efficiency corresponds to a violation of the immersion constraint for the geometries with the smallest drafts. Optimal conditions are thus obtained for intermediate values of the draft. The wave climate of Civitavecchia is instead not energetic enough for this effect to be noticeable.

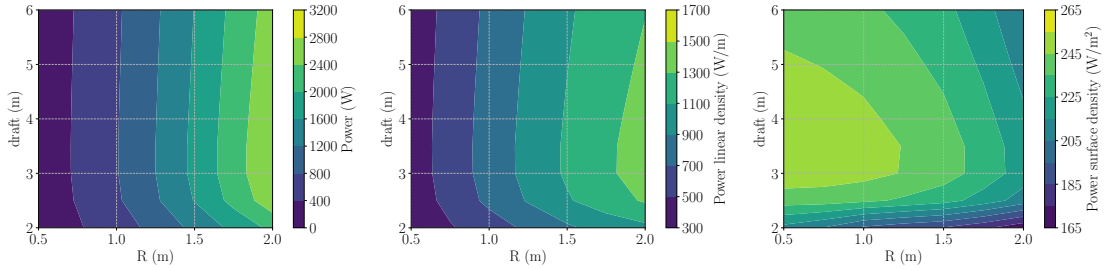

Figure 7.9: *Mean annual power for variable geometric parameters; wave climate of Alghero (constrained model).*

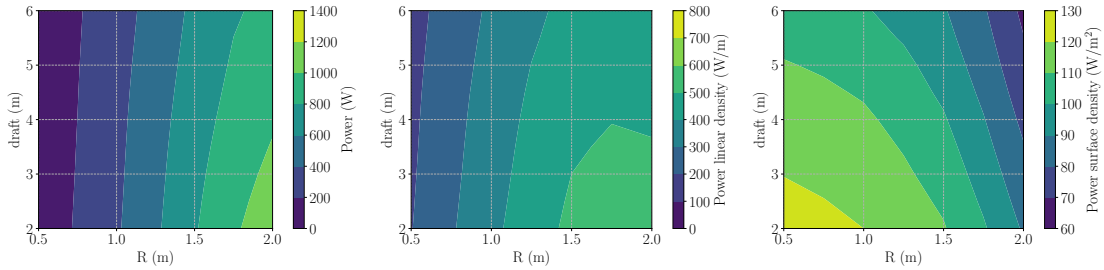

Figure 7.10: *Mean annual power for variable geometric parameters; wave climate of Civitavecchia (constrained model).*

The results presented in this section indicate that a larger device would be more efficient in case of installation in single units or linear arrays, while smaller devices would yield better performance per unit area if, for instance, an installation with multiple rows is devised. The choice of a specific dimension should be based on the location of installation, on mechanical considerations on the feasibility of large turbines, and on economic considerations on the cost of a single device and its scale dependence. Caution needs to be applied in interpreting the results of this section, since diffraction and radiation become important even for very small devices, if they are closely packed.

7.3 Arrays of devices

In this section, we analyze configurations with multiple devices, considering in particular the integration with floating offshore wind energy plants. We consider the mutual hydrodynamic interactions between different devices, and the interactions with the piles of the wind energy platform. Geometry and dimensions are consistent with the ones of the Windfloat project[6].

7.3.1 Mathematical model

Park hydrodynamics are described using the semi-analytical model proposed in [31,180] and based on interaction theory (see Sec. 3.2), valid for cylindrical objects. The hydrodynamic behavior of each cylinder is described by a diffraction transfer

[6] `https://www.boem.gov/sites/default/files/about-boem/BOEM-Regions/Pacific-Region/Renewable-Energy/11-Kevin-Bannister---BOEM-Workshop.pdf`.

matrix, which is independent of the position and can hence be computed once and for all. The interactions between cylinders are described by basis transformation matrices, which instead depend on the positions, and whose analytical expressions can be explicitly differentiated with respect to the coordinates of the center of mass of each device. Truncation of the series leads to the linear, block system (3.39), which we report here for convenience:

$$\begin{bmatrix} M_{\gamma\gamma} & M_{\gamma\zeta} \\ M_{\zeta\gamma} & M_{\zeta\zeta} \end{bmatrix} \begin{bmatrix} \widehat{\boldsymbol{\gamma}} \\ \widehat{\boldsymbol{\zeta}} \end{bmatrix} = \begin{bmatrix} \boldsymbol{h}_1 \\ \boldsymbol{h}_2 \end{bmatrix}. \tag{7.69}$$

The first block-row is the hydrodynamic problem , while the second block-row describes the dynamics of the bodies. $\widehat{\boldsymbol{\gamma}}$ is the vector of coefficients of the series describing the hydrodynamic solution. All blocks of matrix M and of right hand side vector $\boldsymbol{h}$ depend on the coordinates of the devices.

7.3.2 Simulation and optimization

Interaction between a single device and a platform

In the following, the cylindrical device with radius 0.75 m introduced in Sec. 7.2.2 is considered. We first analyze the effect of the presence of the piles of the structure on the performance of a single device. The motion of the piles is assumed to be negligible. In order to realize this effect, the piles are assigned very large values of stiffness. This can be interpreted as the equivalent stiffness of the moorings. A more accurate approach, which has not been explored in the present work, would require taking into account the forces acting on the wind turbine, in order to model the displacement of the floating platform on which it is mounted. Simulations are carried out with a wave condition typical of the Mediterranean as a forcing term, and with the piles located at the vertices of an equilateral triangle. With reference to Fig. 7.11, we consider horizontal wave vectors, in both possible directions.

In the case of waves coming from the left, and considering only the region inside the triangle, an average power of 1470 W is obtained, while considering the whole square the average power is 1364 W. In the case of waves coming from the right, the average power in the internal region is 1312 W, while in the whole square it is 1396 W. The maximum power is 1540 W in both cases. Thus, if only the internal region is available, then the first configuration is more efficient; if, instead, also the external region in the proximity of the piles can be utilized, then the second configuration is better. It has to be taken into account that the choice might be dictated by the necessities of the wind power plant: typically, the turbine is positioned on the downwind vertex of the platform, with respect to the dominant wind direction. In this case, in a location with waves mainly generated by the local wind and thus with a wind vector approximately aligned with the wave vector, the second configuration would be chosen.

Interaction between 2 devices

As a complementary analysis with respect to the one of the previous section, we consider two interacting devices, in the absence of piles. The aim is to quantify the

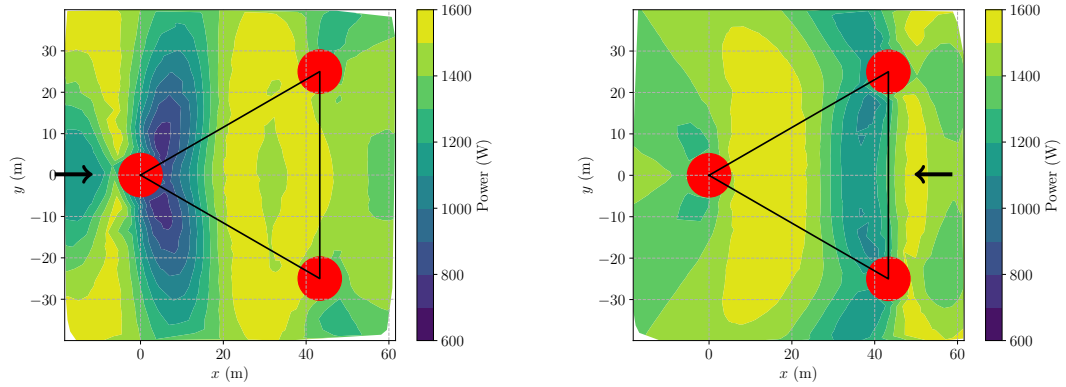

Figure 7.11: *Map of powers for a single device interacting with the piles, for waves coming respectively from the left and from the right, $H_s = 3$ m, $T = 8$ s.*

effect of interaction while varying the distance. The results are shown in Fig. 7.12, with waves coming from the left. It can be observed that the upwave body gains an advantage thanks to the presence of the downwave body. The most unfavorable conditions are the ones with minimum distance between the two devices. The quantitative power variation may seem to indicate that the interaction effect is very small (less than 1%). It has however been observed in the literature that the so-called park effect is relevant only when the number of devices is large enough (indicatively more than 10) [14]. We thus postpone this discussion to Sec. 7.3.2. Some further comparisons with 3D CFD simulations are reported in [5].

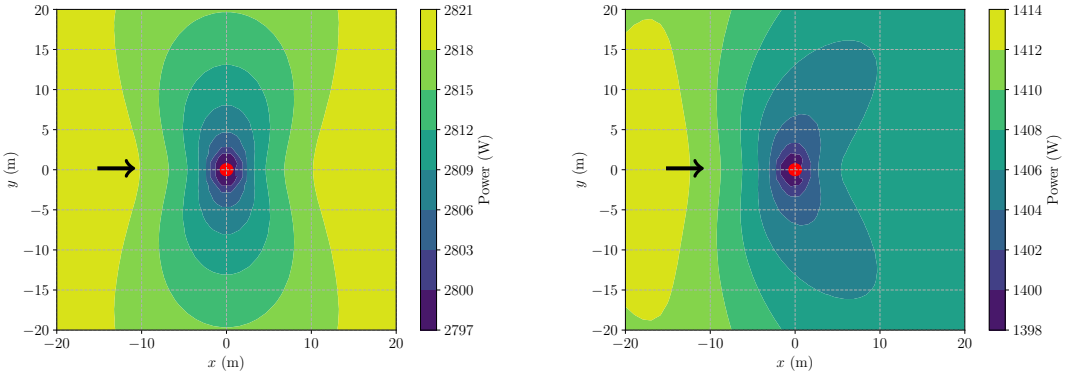

Figure 7.12: *Array of 2 bodies, one in the origin and the other in (x, y). Left: total power; right: power of the device in (x, y).*

Optimization method

We now discuss the solution of the optimization problem (7.2). The cost function is the power, with flipped sign:

$$J(\widehat{\boldsymbol{\zeta}}) = -P(\widehat{\boldsymbol{\zeta}}) = -\sum_{\ell=1}^{N_b}\sum_{n=0}^{d} p_n \left(\omega|\widehat{\zeta}_\ell|\right)^{2n}. \tag{7.70}$$

It must be minimized taking into account the constraints given by the state problem, the available domain and the requirement that devices do not overlap.

We consider as available area the interior of the triangle defined by the centers of the piles supporting the platform (see Fig. 7.13). The devices' centers can be placed anywhere in the light blue region bounded by the dashed line, so that their walls are at most tangent to the boundary defined by the solid line and the piles. Notice that, in addition, the arcs corresponding to the piles are substituted by their tangents in order to make the domain convex, thus allowing the use of a projected gradient algorithm for the enforcement of the constraint.

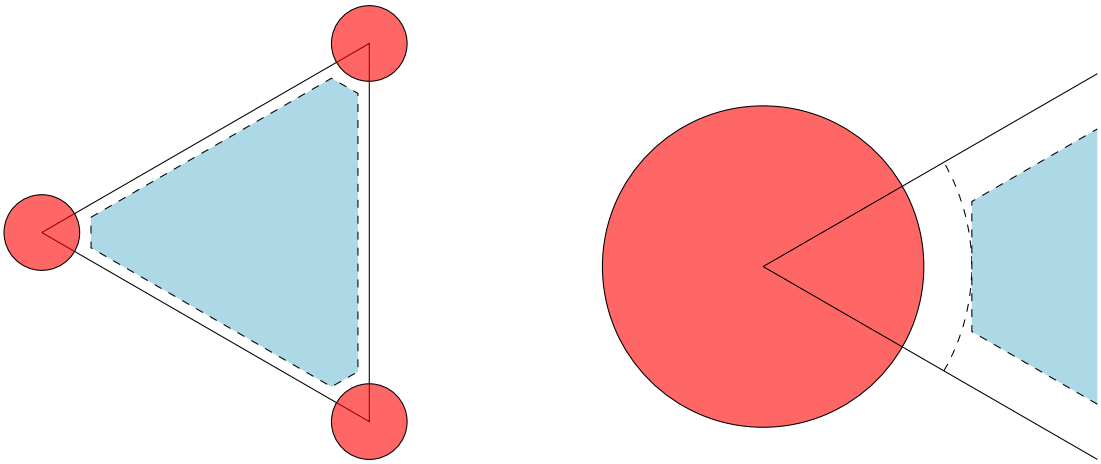

Figure 7.13: *Complete convexified domain (left) and detail of the comparison with the original domain (right).*

For the solutions to be physically meaningful, it is also necessary to impose that devices do not overlap. A minimum distance $d_{\min}$ between the centers of the devices is imposed. This constraint corresponds to a non-convex admissible set. To see this, consider two devices positioned respectively in (x_1, y_1) and (x_2, y_2). The vector of optimization variables is in this case, according to (7.1), $\boldsymbol{u} = (x_1, y_1, x_2, y_2) \in \mathbb{R}^4$. Two admissible configurations are $\boldsymbol{u}_1 = (0, 0, d_{\min}, 0)$ and $\boldsymbol{u}_2 = (0, 0, 0, d_{\min})$. Their convex combination with parameter $1/2$ is $\boldsymbol{u}_3 = (0, 0, d_{\min}/2, d_{\min}/2)$, corresponding to a distance between the centers equal to $d_{\min}\sqrt{2}$. Hence, $\boldsymbol{u}_3$ does not satisfy the constraint of no overlap and the admissible set is not convex.

The state equation is enforced by a Lagrangian approach to find a reduced gradient. Optimization is performed by employing a projected gradient algorithm [127], where projection is onto the convex admissible domain. A modified backtracking line search is executed at each iteration. It is based on the Armijo rule, with the additional requirement that steps are small enough to prevent the devices from colliding.

To find the reduced gradient of the cost function, we introduce multiplier vectors $\boldsymbol{\lambda}$, $\boldsymbol{\mu}$ to enforce the state equation (7.69), and define the Lagrangian function

$$\mathcal{L}(\boldsymbol{x}; \widehat{\boldsymbol{\gamma}}, \widehat{\boldsymbol{\zeta}}; \boldsymbol{\lambda}, \boldsymbol{\mu}) = J(\widehat{\boldsymbol{\zeta}}) + \mathrm{Re}\left[\boldsymbol{\lambda}^H (M_{\gamma\gamma}\widehat{\boldsymbol{\gamma}} + M_{\gamma\zeta}\widehat{\boldsymbol{\zeta}} - \boldsymbol{h}_1) + \boldsymbol{\mu}^H (M_{\zeta\gamma}\widehat{\boldsymbol{\gamma}} + M_{\zeta\zeta}\widehat{\boldsymbol{\zeta}} - \boldsymbol{h}_2)\right]. \tag{7.71}$$

Differentiation with respect to the state variables $\widehat{\boldsymbol{\gamma}}, \widehat{\boldsymbol{\zeta}}$

$$D_\gamma \mathcal{L}(\delta\widehat{\boldsymbol{\gamma}}) = \mathrm{Re}\left[\delta\widehat{\boldsymbol{\gamma}}^H (M_{\gamma\gamma}^H \boldsymbol{\lambda} + M_{\zeta\gamma}^H \boldsymbol{\mu})\right], \tag{7.72}$$

$$D_\zeta \mathcal{L}(\delta\widehat{\boldsymbol{\zeta}}) = -\sum_{\ell=1}^{N_b}\sum_{n=0}^{d} 2np_n \mathrm{Re}[\delta\widehat{\zeta}_\ell^* (\widehat{\zeta}_\ell^*)^{n-1}\widehat{\zeta}_\ell^n] + \mathrm{Re}[\delta\widehat{\boldsymbol{\zeta}}^H (M_{\gamma\zeta}^H \boldsymbol{\lambda} + M_{\zeta\zeta}^H \boldsymbol{\mu})], \tag{7.73}$$

leads to the adjoint equations

$$\begin{bmatrix} M_{\gamma\gamma}^H & M_{\zeta\gamma}^H \\ M_{\gamma\zeta}^H & M_{\zeta\zeta}^H \end{bmatrix} \begin{bmatrix} \boldsymbol{\lambda} \\ \boldsymbol{\mu} \end{bmatrix} = \begin{bmatrix} 0 \\ \widetilde{\boldsymbol{h}}_2 \end{bmatrix}, \quad \widetilde{h}_{2,\ell} = \sum_{n=0}^{d} 2np_n (\widehat{\zeta}_\ell^*)^{n-1}\widehat{\zeta}_\ell^n. \tag{7.74}$$

Differentiation with respect to the positions yields the components of the gradient ∇J with respect to the coordinates of devices:

$$\frac{\partial \mathcal{L}}{\partial x_\ell} = \mathrm{Re}\left[\boldsymbol{\lambda}^H \left(\frac{\partial M_{\gamma\gamma}}{\partial x_\ell}\widehat{\boldsymbol{\gamma}} + \frac{\partial M_{\gamma\zeta}}{\partial x_\ell}\widehat{\boldsymbol{\zeta}} - \frac{\partial \boldsymbol{h}_1}{\partial x_\ell}\right) + \boldsymbol{\mu}^H \left(\frac{\partial M_{\zeta\gamma}}{\partial x_\ell}\widehat{\boldsymbol{\gamma}} + \frac{\partial M_{\zeta\zeta}}{\partial x_\ell}\widehat{\boldsymbol{\zeta}} - \frac{\partial \boldsymbol{h}_2}{\partial x_\ell}\right)\right], \tag{7.75}$$

where derivatives of all blocks in the system can be computed analytically, as detailed in the following (see also [58]). We start from the expression of basis transformation matrices (see (3.32)):

$$(T_{ij})_{mm}^{nl} = \begin{cases} \frac{J_l(kr)}{H_n(kr)} H_{n-l}(kL_{ij}) e^{i\alpha_{ij}(n-l)}, & m = 0, \\ \frac{I_l(k_m r)}{K_n(k_m r)} K_{n-l}(k_m L_{ij}) e^{i\alpha_{ij}(n-l)}(-1)^l, & m \geq 1. \end{cases} \tag{7.76}$$

Differentiating eq. (7.76) and using the expression for the derivative of H_n [11]:

$$\frac{dH_n(x)}{dx} = \frac{H_{n-1}(x) - H_{n+1}(x)}{2},$$

the same holding for K_n, yields

$$\left(\frac{\partial T_{ij}}{\partial x_\ell}\right)_{mm}^{nl} = \begin{cases} \frac{J_l(kr)}{H_n(kr)} \left[k\frac{\partial L_{ij}}{\partial x_\ell}\frac{H_{n-l-1}(kL_{ij}) - H_{n-l+1}(kL_{ij})}{2} \right. \\ \qquad \left. + i\frac{\partial \alpha_{ij}}{\partial x_\ell}(n-l)H_{n-l}(kL_{ij})\right] e^{i\alpha_{ij}(n-l)}, & m = 0, \\ \frac{I_l(k_m r)}{K_n(k_m r)} \left[k_m\frac{\partial L_{ij}}{\partial x_\ell}\frac{K_{n-l-1}(kL_{ij}) - K_{n-l+1}(kL_{ij})}{2} \right. \\ \qquad \left. + i\frac{\alpha_{ij}}{\partial x_\ell}K_{n-l}(k_m L_{ij})\right] e^{i\alpha_{ij}(n-l)}(-1)^l, & m \geq 1. \end{cases}$$

For the derivatives of L_{ij} and α_{ij}, we start from $L_{ij}\cos\alpha_{ij} = x_j - x_i$, $L_{ij}\sin\alpha_{ij} = y_j - y_i$. Differentiation with respect to x_i yields the system

$$\begin{bmatrix} \cos\alpha_{ij} & -L_{ij}\sin\alpha_{ij} \\ \sin\alpha_{ij} & L_{ij}\cos\alpha_{ij} \end{bmatrix} \begin{bmatrix} \frac{\partial L_{ij}}{\partial x_i} \\ \frac{\partial \alpha_{ij}}{\partial x_i} \end{bmatrix} = \begin{bmatrix} -1 \\ 0 \end{bmatrix},$$

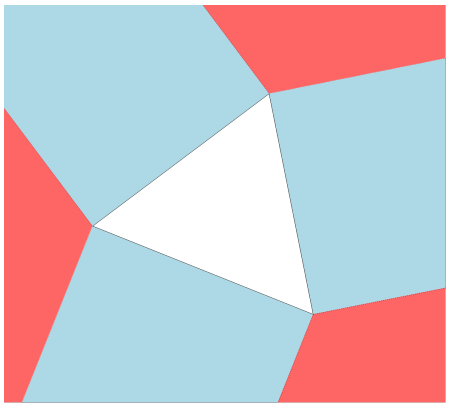

Figure 7.14: *Graphical representation of the projection algorithm.*

whose matrix has determinant L_{ij} and thus is always invertible for distinct points. Analogous systems hold for the other coordinates involved. The expressions of the ambient wave coefficients are [32]

$$(\boldsymbol{a}_\ell)_m^n = \begin{cases} J_n(kr)e^{in(\pi/2-\beta)}\Theta_\ell & m = 0, \\ 0, & m \geq 0, \end{cases} \qquad \Theta_\ell = e^{ik(x_\ell \cos\beta + y_\ell \sin\beta)},$$

and their derivatives are

$$\frac{\partial \boldsymbol{a}_\ell}{\partial x_\ell} = ik\cos\beta \boldsymbol{a}_\ell, \qquad \frac{\partial \boldsymbol{a}_\ell}{\partial y_\ell} = ik\sin\beta \boldsymbol{a}_\ell.$$

The definition of the projector onto the admissible domain is based on the observation of Fig. 7.14. Consider a point $\boldsymbol{x}$ outside the white triangle (in general convex polygon) Ω: the point of Ω at the minimum distance from $\boldsymbol{x}$ is either a vertex (if $\boldsymbol{x}$ is in one of the red regions) or it is on an edge (if $\boldsymbol{x}$ is in one of the light blue regions). To each edge of the polygon we can associate an inequality subconstraint, corresponding to belonging to a half-plane. The constraint of belonging to the polygon will then be given by the system of such subconstraints. If the orthogonal projection of $\boldsymbol{x}$ onto one of the lines corresponding to the violated subconstraints belongs to Ω, then it is the projection of $\boldsymbol{x}$ onto Ω (light blue regions). Otherwise, the projection will be the vertex closest to $\boldsymbol{x}$ (red regions). We will denote with $\mathcal{P}(\boldsymbol{x})$ the projection of a point $\boldsymbol{x}$ onto Ω, computed as described above.

Since the constraint of no overlap is not convex, it needs to be treated differently. It is taken into account during backtracking line search. If the distance between two devices is less than $d_{\min}$, the step is reduced until an admissible condition is obtained. This corresponds to substituting the gradient ∇J with a vector $D\nabla J$, where D is a diagonal matrix with nonnegative elements. A descent direction is obtained, since D is semi-positive definite. An alternative approach could be penalization. In such case, however, it would be required to compute the cost in non-admissible configurations, in which the hydrodynamic problem cannot be solved.

Algorithm 6 summarizes the steps described above. Here, s is the stepsize, α is the Armijo constant and k_d is the backtracking factor.

Algorithm 6 Optimization algorithm

Require: s, tol, maxit, k_d, α
1: Set $k = 0$
2: **while** $k <$ maxit **and** err $>$ tol **do**
3: Compute $\widehat{\boldsymbol{\gamma}}$ and $\widehat{\boldsymbol{\zeta}}$ by solving the state problem (7.69) with device positions $\boldsymbol{x}^k$
4: Compute the cost J^k using (7.70)
5: Compute $\boldsymbol{\lambda}$ and $\boldsymbol{\mu}$ by solving the adjoint problem (7.74)
6: Compute the gradient ∇J^k using (7.75)
7: Set $D = I$
8: Perform the projected gradient step $\widetilde{\boldsymbol{x}} = \mathcal{P}(\boldsymbol{x}^k - sD\nabla J^k)$
9: **while** the set of overlapping pairs of points is not empty **do**
10: Update $d_{\ell\ell} \leftarrow k_d d_{\ell\ell}$ for each point $(\widetilde{x}_\ell, \widetilde{y}_\ell)$ in an overlapping pair
11: Set $\widetilde{\boldsymbol{x}} = \mathcal{P}(\boldsymbol{x}^k - sD\nabla J^k)$
12: Solve the state problem with positions $\widetilde{\boldsymbol{x}}$ and compute the associated cost $\widetilde{J}$
13: **end while**
14: **while** $\widetilde{J} - J^k > -\alpha\|\widetilde{\boldsymbol{x}} - \boldsymbol{x}^k\|^2/(max_\ell d_{\ell\ell} s)$ **do**
15: Update $D \leftarrow k_d D$
16: Repeat lines 8-13
17: **end while**
18: Set $\boldsymbol{x}^{k+1} = \widetilde{\boldsymbol{x}}$
19: Compute err $= |J^k - \widetilde{J}|$ and update $k \leftarrow k + 1$
20: **end while**

Optimization results

The optimization strategy presented in Sec. 7.3.2 was first tested on a triangular domain, without the support structure of the wind turbine, and imposing a minimum distance of 1.6 m between the centers of the devices. For a given number of devices to be installed in the domain, 10 random configurations are obtained by sampling from a uniform distribution with the constraint of minimum distance, and the total power is computed for each of them. Optimization is then carried out starting from the random configuration of maximum power. This process is repeated for increasing values of the number of bodies. A monochromatic wave equivalent, in the sense explained in Section 3.3 (see in particular (3.43)), to the sea state with $H_s = 3$ m and $T_e = 8$ s, and with a wave vector directed as the positive x direction, is considered. The results in terms of total power of the array and average power per device are reported in Fig. 7.15. The total power is monotonically increasing, while the average power per device has a value greater than the one obtained in the isolated case for an array of 10 devices and less than the isolated value for more than 10 devices. The interaction factor, defined as the ratio of the power of an array of N devices to the power of the N devices in isolated conditions [175], is thus greater than 1 for 10 devices, and less than 1 for all other cases considered. The power gain obtained through optimization is significantly larger than the dispersion of power from random tests. This indicates the efficiency of the proposed optimization strategy[7].

[7] In other words, finding a configuration as efficient as the optimum randomly would probably require a very large number of trials.

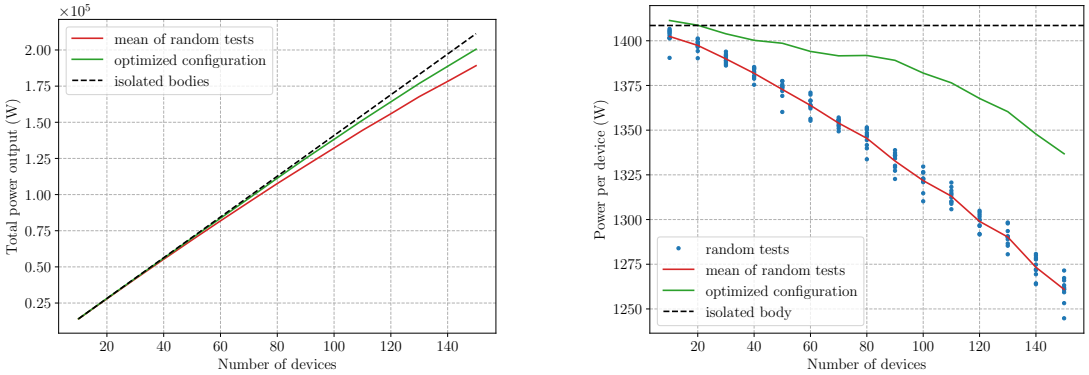

Figure 7.15: *Results for a triangular domain of edge 50 m, $H_s = 3$ m, $T = 8$ s.*

The best and worst configurations from random tests and the optimized configuration are shown in Fig. 7.16 for the case of 100 devices. A common observation from numerical tests is that the best configurations in terms of power have a greater density of devices in the upwave region with respect to the worst performing configurations. In the optimal configurations, we observe the formation of lines of closely packed devices. Histograms of the powers of devices for the same

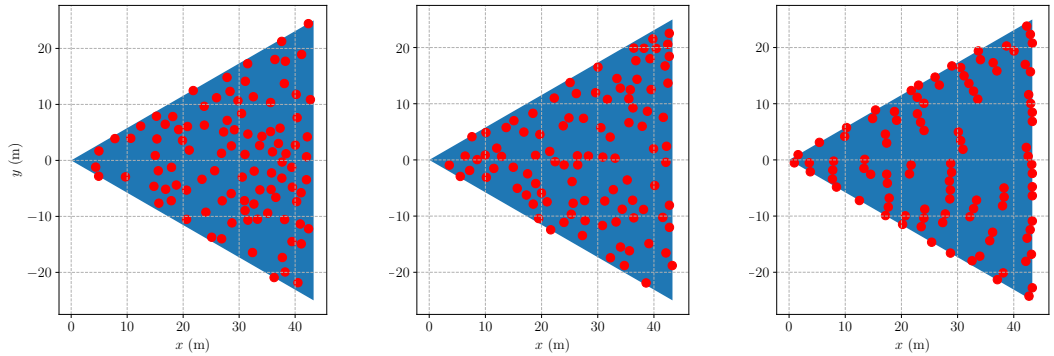

Figure 7.16: *Test with 100 devices, $H_s = 3$ m, $T = 8$ s. From the left: worst (108.5 kW) and best (109.4 kW) configuration from random tests; optimized configuration (112.4 kW).*

test are reported in Fig. 7.17. The most apparent feature of the histograms is the wide variability in the power values. Since no bodies other than the devices are present, such variability is produced by the mutual hydrodynamic interactions. This shows that, as expected, the park effect becomes important when the number of devices is large, even if the hydrodynamic interactions in a single pair of devices appear almost negligible (see Sec. 7.3.2) and even if, as in this case, the characteristic dimension of the devices is much smaller than the wavelength. It can also be observed that the left tail of the distribution in the least favorable condition is absent in the optimized condition. In general, the distribution is shifted to the right by the optimization process.

In the next tests, the truncated triangular domain has been considered, taking into account the interaction with the piles of the structure on which the wind turbine is mounted. A constraint of minimum distance equal to 3 m between the

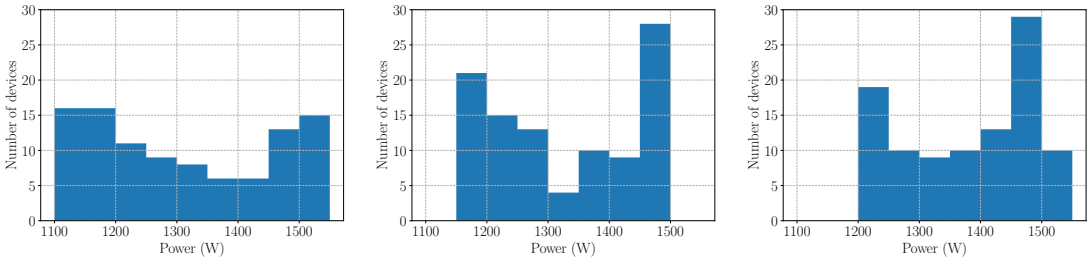

Figure 7.17: *Histograms of the powers of single devices, triangular domain, 100 device test. From the left: worst and best configuration from random tests; optimal configuration.*

centers of the devices has been imposed, and the wave vector is directed along the positive x direction. The results in terms of power are shown in Fig. 7.18. In this case, the mean power of the devices is always greater than the power of an isolated device, thanks to the favorable interaction with the piles. The constraint of minimum distance between the devices significantly reduces the admissible set as the number of devices increases. This, in turn, reduces the dispersion of the results of random tests and the power gain obtained through optimization. We observe that the mean power in the optimized configurations is very close to the maximum power of a single device inside the triangle, that is equal to 1540 W (see Sec. 7.3.2). Optimization runs have been also performed starting from symmetric

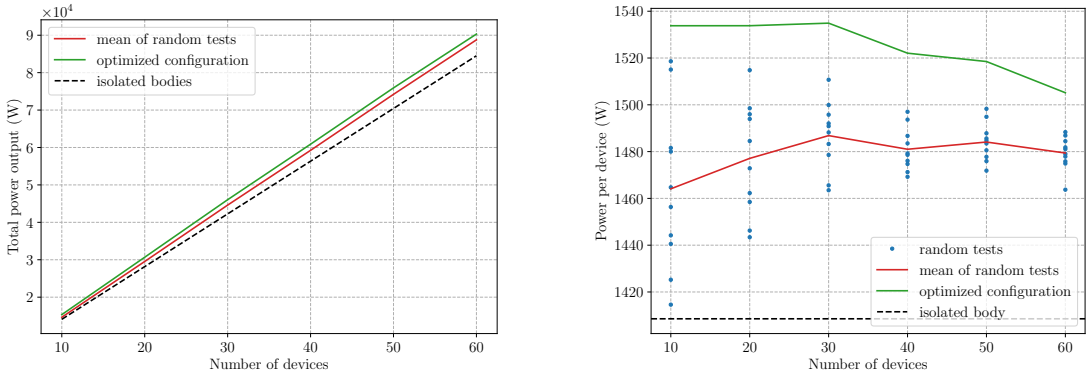

Figure 7.18: *Results for the truncated triangular domain.*

initial conditions, in order to evaluate the difference with respect to random initial conditions. No significant differences are observed in terms of power. An example of a symmetric configuration with 40 devices is shown in Fig. 7.19. In the right panel of the figure, corresponding to the optimal configuration, we have superimposed the optimal configuration over the map of the power of a single device in the domain. The color inside each circle represents, instead, the power absorbed by each device considering the hydrodynamic interactions, with the same color scale as the background. It can be observed that the power output of most of the downwave devices is close to the maximum obtainable by a single device. The most upwave converters achieve a production that is greater than the value expected in the single device case, presumably thanks to favorable interactions with

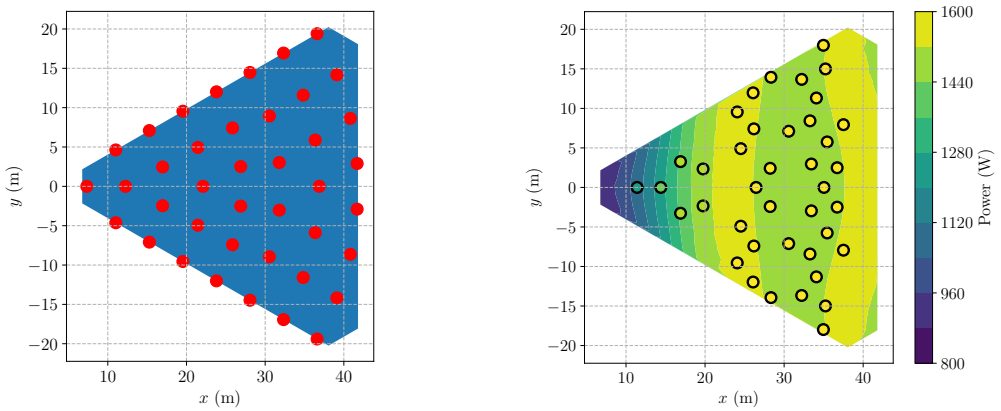

Figure 7.19: *Initial (left) and optimized (right) configuration; truncated triangular domain, 40 devices. In the right panel, the map of the power of a single device in the domain is reported in the background. The color inside each circle represents the actual power of the corresponding device, taking hydrodynamic interactions into account.*

the downwave objects. Power histograms are reported in Fig. 7.20. As in the case of the triangular domain without piles, the effect of optimization is to trim the left tail of the power distribution. As a consequence, the number of devices in the bin of greatest power is increased.

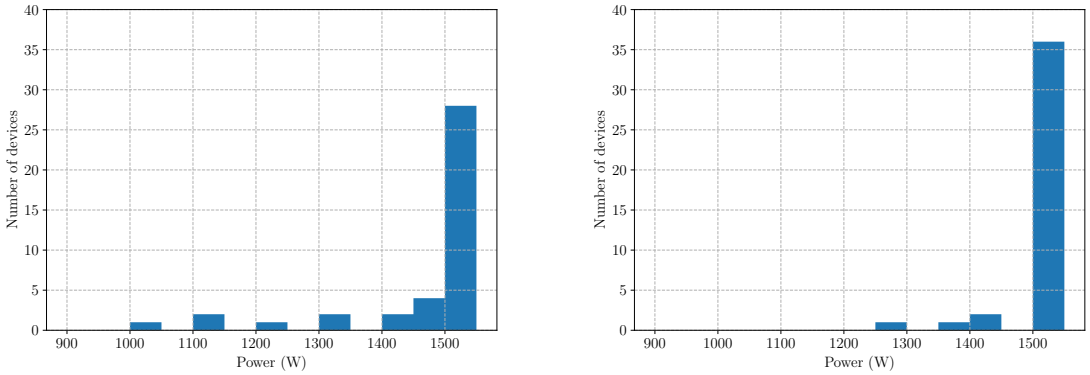

Figure 7.20: *Histograms of the powers of single devices, triangular domain, 100 device test. Initial (left) and optimized (right) configuration.*

The influence of the imposed value of the minimum distance on configurations and power has been studied by performing several optimization runs for an array of 50 devices in the truncated triangular domain. Results in terms of power are shown in Fig. 7.21. As the minimum imposed distance increases, the admissible set is reduced and thus, as expected, the power of the optimized configuration decreases. This happens monotonically. The optimized configurations corresponding to 3 values of minimum distance are reported in Fig. 7.22. When the minimum distance constraint allows it, devices are placed in the region of maximum isolated device power highlighted in Figures 7.11 and 7.19. As the minimum distance increases, the distribution becomes more even.

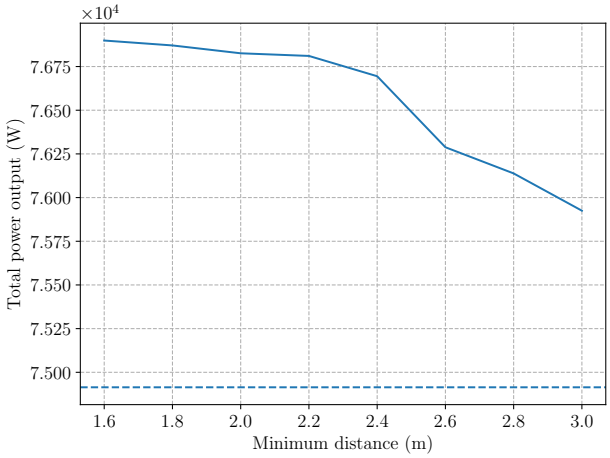

Figure 7.21: *Results for 50 devices on the truncated triangle domain. Solid line: optimal power with variable minimum distance. Dashed line: power of the best random configuration.*

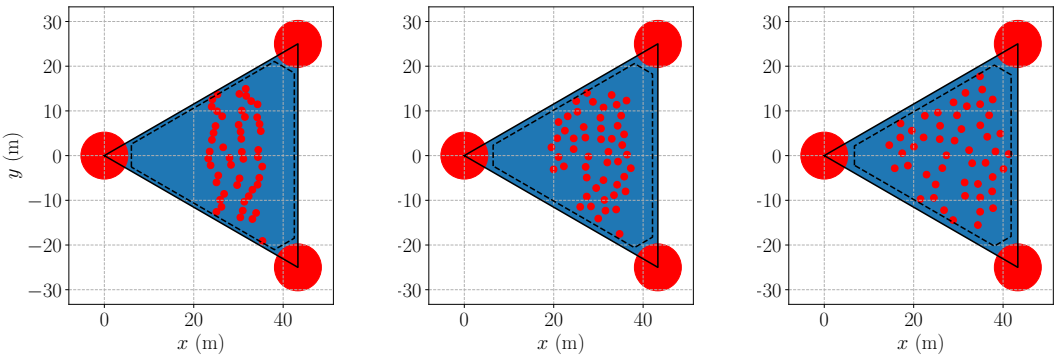

Figure 7.22: *Optimized configurations for minimum distance 1.6 m (left), 2.4 m (center), and 3 m (right).*

Comparison with the nonlinear model

The results of optimization, performed using the linear model described in the previous sections, are now verified by recomputing the powers of all explored configurations with a nonlinear model. We have considered the multibody version of (7.37) for a device of constant section S:

$$\rho C(\zeta_\ell) S \ddot{\zeta}_\ell + \sum_{m=1}^{N_b} A_{\ell m}(\omega) \ddot{\zeta}_m + \Delta p(v_{t,\ell} \omega_t) + \sum_{m=1}^{N_b} B_{\ell m}(\omega) \dot{\zeta}_m + \rho g \zeta_\ell = p_{e,\ell}(t), \quad (7.77)$$

$\ell = 1, \ldots, N_b$, where hydrodynamic interactions between different devices are described by the off-diagonal terms of matrices $\boldsymbol{A}(\omega)$ and $\boldsymbol{B}(\omega)$; moreover, $p_{e,\ell}$ contains diffraction effects. Hydrodynamic properties are obtained by solving the hydrodynamic equations introduced in Sec. 7.2.1 with the methods described therein. Equation (7.77) is solved in the time domain over 8 wave periods, the instantaneous power of the park is computed at each time step and the mean power is obtained by averaging over the last 4 periods.

The recomputed powers for the case of the triangular domain without piles (see Fig. 7.15) are reported in Fig. 7.23. Simulations have been carried out up to 60 devices, since larger test cases would require a significant amount of memory for the hydrodynamic computations. While the absolute values of power differ by about 10%, power in the optimized configuration is confirmed to be significantly greater than powers from random configurations. In particular, as shown in the right panel of Fig. 7.23, the power gained through optimization is comparable between the linear and nonlinear results. Thus, the linear model may be an adequate surrogate of the nonlinear model for purposes of optimization.

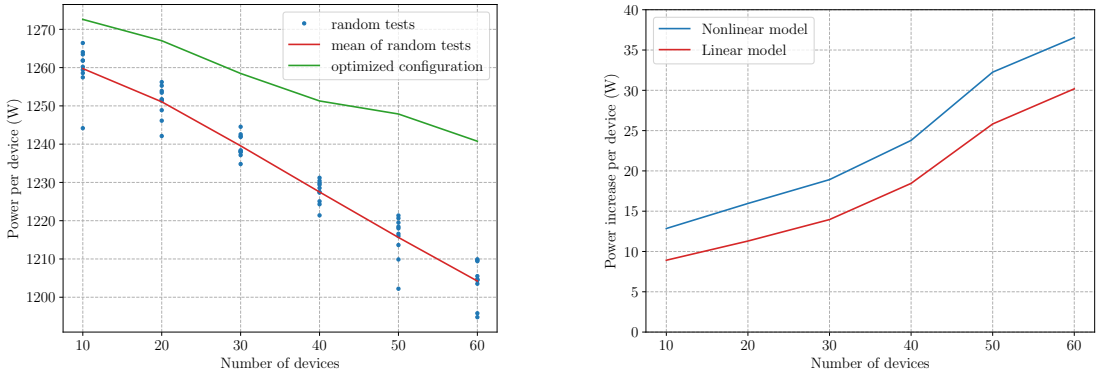

Figure 7.23: *Recomputation of the power per device from the optimization over the triangular domain of edge 50 m using the nonlinear model (left; compare with Fig. 7.15) and power increase per device obtained through optimization and computed with the linear and nonlinear models (right).*

7.4 Discussion and developments

A mathematical model for a water-turbine OWC device has been introduced, incorporating the behavior of the internal water column, of the Wells turbine, and the interaction with the outside environment. The model has enabled the optimization of the turbine's rotational speed for each sea state of interest, and the estimation of the power matrix.

A linearization of the model has been then derived and used to explore the dependence of the annual power production on the dimensions of the device. Then, a generalization to arrays, achieved by limiting the treatment to cylindrical devices, has been introduced. Hydrodynamic simulations show that interactions with the piles of an offshore structure can be beneficial in terms of wave energy production, thanks to the reflections from the piles. Interestingly, even though the diffraction properties of a single device are negligible with respect to mass and stiffness, a large power variability between the devices is observed, showing a significant mutual interaction effect.

Finally, an optimization method has been implemented starting from the linear WEC park model. The results show that optimization improves the power per device significantly by shifting the distribution of power upwards. Moreover, an a-posteriori verification using the nonlinear model corroborates the choice of the

linear model as a cheap surrogate, justifying its use in optimization.

The optimization strategy presented here can be used for more general classes of WEC devices. Furthermore, it can be adapted to perform control co-design, i.e., simultaneous optimization of layout and control variables. Indeed, an extension of the optimization strategy introduced here will be used in Chapter 8 for the optimization of generic parks of WECs. In particular, the simplifying assumptions of monochromatic waves and convex admissible domain will be removed.

Chapter 8

Combined optimization of layout and control parameters

In this chapter, we complete the path started in the previous chapters by treating the problem of simultaneous optimization of layout and control for WEC parks, with the average power as the objective function. In order to do this, we introduce a novel adaptive gradient-flow algorithm. Most of this work has originally appeared in [60]. The problem is formulated as

$$\min_{\boldsymbol{w}} \quad f(\boldsymbol{w}) \quad \text{s.t.} \quad \boldsymbol{e}(\boldsymbol{w}) := \begin{bmatrix} \boldsymbol{e}_\gamma(\boldsymbol{w}) \\ \boldsymbol{e}_\zeta(\boldsymbol{w}) \end{bmatrix} = 0, \quad \boldsymbol{h}(\boldsymbol{w}) := \begin{bmatrix} \boldsymbol{h}_{sl}(\boldsymbol{w}) \\ \boldsymbol{h}_{ad}(\boldsymbol{w}) \\ \boldsymbol{h}_{md}(\boldsymbol{w}) \end{bmatrix} \leq 0. \tag{8.1}$$

Here, the cost function is $f(\boldsymbol{w}) := -P(\boldsymbol{w})$, with $P(\boldsymbol{w})$ the total power absorbed by the park. The vector of decision variables is $\boldsymbol{w}$, corresponding to devices' positions and control parameters, and state variables, given by hydrodynamic coefficients $\hat{\boldsymbol{\gamma}}$ and oscillation amplitudes $\hat{\boldsymbol{\zeta}}$. Vector $\boldsymbol{e}(\boldsymbol{w})$ defines the equality constraints, corresponding to the state problem: in particular, $\boldsymbol{e}_\gamma(\boldsymbol{w})$ is the residual of the hydrodynamic equation and $\boldsymbol{e}_\zeta(\boldsymbol{w})$ is the residual of the dynamic equation. Furthermore, $\boldsymbol{h}(\boldsymbol{w})$ is the vector of inequality constraints: the slamming constraint function $\boldsymbol{h}_{sl}(\boldsymbol{w})$, requiring the devices to remain immersed as they oscillate; the admissible domain constraint function $\boldsymbol{h}_{ad}(\boldsymbol{w})$, describing the sea area available for the park; and finally, the constraint of minimum distance between each pair of devices, expressed by function $\boldsymbol{h}_{md}(\boldsymbol{w})$.

Our optimization algorithm is based on the gradient-flow framework. To the best of our knowledge, the gradient-flow approach has not been considered for wave energy applications before, and more generally gradient-based approaches are rare in the literature on control co-design for WEC arrays. The gradient-flow approach that we consider was originally introduced in [159]. It allows a rather natural treatment of very general constraints, provided that their Jacobian is available. The resulting system of ordinary differential equations (ODE) is solved through an adaptive Runge-Kutta (RK) method [80]. To avoid over-solving while still achieving convergence within a specified threshold, an approach akin to inexact optimization algorithms [27, 28, 178] is adopted: the tolerances of RK stepsize adaptivity and of the conjugate gradient (CG) solver used to compute

the right hand side of the ODE are dynamically determined. For our application, we consider arrays of cylindrical heaving WAB devices with reactive control (see Sec. 5.1), i.e., the control parameters are the equivalent damping and stiffness coefficients of the electric generator, usually referred to as power take-off system (PTO). Hydrodynamics is modeled using linear potential flow theory (see Chapter 2), and irregular waves force the system. The wave spectrum is approximated by a superposition of a finite number of monochromatic waves. As in the layout optimization part of the previous chapter, we consider the frequency domain fluid-structure interaction model based on interaction theory presented in Sec. 3.2. The velocity potential is written as a sum of cylindrical harmonics with unknown coefficients. The latter, together with the devices' oscillation amplitudes, are computed by solving a linear system. The system matrix can be explicitly differentiated with respect to the coordinates of the devices and to the control parameters.

Our optimization algorithm is presented in Sec. 8.1. Its specialization to the WEC array co-design problem is presented in Sec. 8.2. Finally, numerical experiments are reported in Sec. 8.3.

8.1 Optimization algorithm

In this section, we describe the optimization algorithm used. First, in section 8.1.1 we review the gradient-flow approach. Then, in section 8.1.2 we describe the scalings used to improve the conditioning of the problem. In section 8.1.3, we finally discuss the time stepping method used and introduce an inexact solution strategy.

8.1.1 Gradient flow

The gradient-flow method is a continuous version of gradient descent, where the optimal solution is sought by solving a system of ODEs whose forcing term depends on the gradient vector. An advantage of gradient-flow-like algorithms over others, such as penalty methods, is that they generate trajectories that can move along an equality constraint, instead of oscillating around it [57]. For a uniform treatment of the constraints, a quadratic slack variable method [20, Sec. 3.3.2] is used to recast inequality constraints as equality constraints. To do that, vector $\boldsymbol{w}$ is augmented with slack variables $\boldsymbol{s}$, and inequality constraints are replaced by the equality constraint

$$\boldsymbol{g}_{\mathcal{I}}(\boldsymbol{w}) := \boldsymbol{h}(\boldsymbol{w}) + \boldsymbol{s} \odot \boldsymbol{s} = 0,$$

where $\odot$ denotes the element-wise product. Then, a single constraint vector $\boldsymbol{g}$ is introduced, $\boldsymbol{g}(\boldsymbol{w}) = [\boldsymbol{e}(\boldsymbol{w}),\ \boldsymbol{g}_{\mathcal{I}}(\boldsymbol{w})]$, and problem eq. (8.1) is restated as

$$\min_{\boldsymbol{w}} \quad f(\boldsymbol{w}) \quad \text{s.t.} \quad \boldsymbol{g}(\boldsymbol{w}) = 0. \tag{8.2}$$

For problem eq. (8.2), we consider the constrained formulation introduced in [159]:

$$\frac{d\boldsymbol{w}}{dt} = -\underbrace{(D_w \boldsymbol{g}(\boldsymbol{w}))^+ \boldsymbol{g}(\boldsymbol{w})}_{\boldsymbol{\Psi}_g(\boldsymbol{w})} - \underbrace{\left[I - (D_w \boldsymbol{g}(\boldsymbol{w}))^+ D_w \boldsymbol{g}(\boldsymbol{w})\right] \nabla f(\boldsymbol{w})}_{\boldsymbol{\Psi}_f(\boldsymbol{w})} =: \boldsymbol{\Psi}(\boldsymbol{w}), \tag{8.3}$$

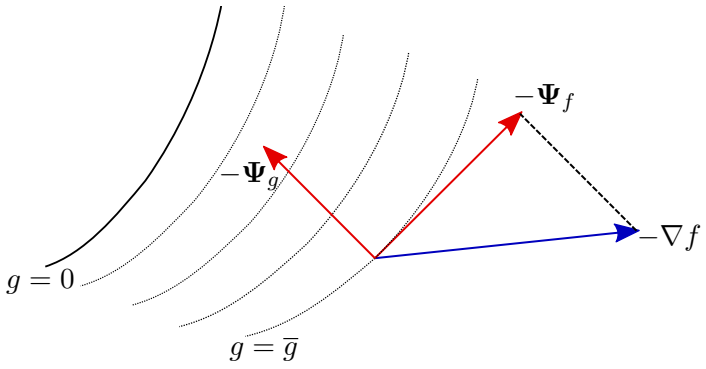

Figure 8.1: *Graphical representation of* (8.3) *for a case with 2 variables and a scalar constraint. Thick solid line: admissible set* $g = 0$*. Thin dotted lines: generic isolines of* g*. Notice that* Ψ_g *is perpendicular to the local isoline.*

where $D_w\boldsymbol{g}(\boldsymbol{w})$ is the differential of the constraint vector, its pseudoinverse operator is

$$(D_w\boldsymbol{g}(\boldsymbol{w}))^+ = (D_w\boldsymbol{g}(\boldsymbol{w}))'[D_w\boldsymbol{g}(\boldsymbol{w})(D_w\boldsymbol{g}(\boldsymbol{w}))']^{-1},$$

and $(D_w\boldsymbol{g}(\boldsymbol{w}))'$ is the adjoint operator of $D_w\boldsymbol{g}(\boldsymbol{w})$. The two contributions to $\boldsymbol{\Psi}$ are represented in Figure 8.1. The first one, $\boldsymbol{\Psi}_g(\boldsymbol{w})$, is orthogonal to the tangent space to the local level set of $\boldsymbol{g}(\boldsymbol{w})$, and it is sometimes referred to as range space step [54], or feasibility step [71]; the second one, $\boldsymbol{\Psi}_f(\boldsymbol{w})$, belongs to the tangent space and is sometimes called null space step, or optimality step. We can rewrite $\boldsymbol{\Psi}(\boldsymbol{w})$ as

$$\boldsymbol{\Psi}(\boldsymbol{w}) = -(D_w\boldsymbol{g}(\boldsymbol{w}))'[D_w\boldsymbol{g}(\boldsymbol{w})(D_w\boldsymbol{g}(\boldsymbol{w}))']^{-1}(\boldsymbol{g}(\boldsymbol{w}) - D_w\boldsymbol{g}(\boldsymbol{w})\nabla f(\boldsymbol{w})) - \nabla f(\boldsymbol{w}).$$

Thus, the term $\boldsymbol{\Psi}(\boldsymbol{w})$ can be computed by either solving the linear system

$$D_w\boldsymbol{g}(\boldsymbol{w})(D_w\boldsymbol{g}(\boldsymbol{w}))'\boldsymbol{\Lambda} = \boldsymbol{g}(\boldsymbol{w}) - D_w\boldsymbol{g}(\boldsymbol{w})\nabla f(\boldsymbol{w}) \tag{8.4}$$

and then substituting $\boldsymbol{\Lambda}$ in $\boldsymbol{\Psi}(\boldsymbol{w}) = -(D_w\boldsymbol{g}(\boldsymbol{w}))'\boldsymbol{\Lambda} - \nabla f(\boldsymbol{w})$, or by solving the saddle point problem

$$\begin{bmatrix} I & (D_w\boldsymbol{g}(\boldsymbol{w}))' \\ D_w\boldsymbol{g}(\boldsymbol{w}) & 0 \end{bmatrix} \begin{bmatrix} \boldsymbol{\Psi}(\boldsymbol{w}) \\ \boldsymbol{\Lambda} \end{bmatrix} = \begin{bmatrix} -\nabla f(\boldsymbol{w}) \\ -\boldsymbol{g}(\boldsymbol{w}) \end{bmatrix}.$$

In the first case, the system matrix is symmetric positive definite, while in the second case, it is symmetric indefinite. In the following, we will consider the first approach, which allows the use of the conjugate gradient method.

For the purpose of checking convergence, we observe that $\boldsymbol{\Psi}(\boldsymbol{w}) = 0$ if and only if there exists a vector $\boldsymbol{\Lambda}$ such that $(D_w\boldsymbol{g}(\boldsymbol{w}))'\boldsymbol{\Lambda} + \nabla f(\boldsymbol{w}) = 0$, which is the statement of the first order optimality condition for problem (8.21) [127, Chap. 12]. Therefore, $\|\boldsymbol{\Psi}(\boldsymbol{w})\|_2$ is taken as a convergence indicator.

8.1.2 Scaling and preconditioning

In our problem, as in most optimization problems of practical interest, the vector $\boldsymbol{w}$ contains quantities of different scales and units. For numerical purposes, they

are divided by reference values to obtain a better scaling of the problem, that is, to prevent a spurious domination of a set of variables over another [127, Sec. 2.2]. We define nondimensional variables $\overline{\boldsymbol{w}}$, $\overline{\boldsymbol{g}}(\overline{\boldsymbol{w}})$ and $\overline{f}(\overline{\boldsymbol{w}})$, positive and diagonal scaling matrices S_w and S_g, and a scaling factor f_0 as

$$\boldsymbol{w} = S_w\overline{\boldsymbol{w}}, \quad \boldsymbol{g}(\boldsymbol{w}) = S_g\overline{\boldsymbol{g}}(\overline{\boldsymbol{w}}), \quad f(\boldsymbol{w}) = f_0\overline{f}(\overline{\boldsymbol{w}}). \tag{8.5}$$

Since the variable t in (8.3) has no physical meaning, we consider it nondimensional. From the chain rule, we obtain

$$\nabla f(\boldsymbol{w}) = \frac{\partial f}{\partial \boldsymbol{w}} = f_0 S_w^{-1}\frac{\partial \overline{f}}{\partial \overline{\boldsymbol{w}}} = f_0 S_w^{-1}\overline{\nabla}\,\overline{f}(\overline{\boldsymbol{w}}) \tag{8.6}$$

$$D_w\boldsymbol{g}(\boldsymbol{w}) = S_g D_{\overline{w}}\overline{\boldsymbol{g}}(\overline{\boldsymbol{w}})S_w^{-1}. \tag{8.7}$$

The right-hand side of the ODE is then written as

$$\overline{\boldsymbol{\Psi}}(\overline{\boldsymbol{w}}) = -(D_{\overline{w}}\overline{\boldsymbol{g}}(\overline{\boldsymbol{w}}))'[D_{\overline{w}}\overline{\boldsymbol{g}}(\overline{\boldsymbol{w}})(D_{\overline{w}}\overline{\boldsymbol{g}}(\overline{\boldsymbol{w}}))']^{-1}(\overline{\boldsymbol{g}}(\overline{\boldsymbol{w}}) - D_{\overline{w}}\overline{\boldsymbol{g}}(\overline{\boldsymbol{w}})\overline{\nabla}\,\overline{f}(\overline{\boldsymbol{w}})) - \overline{\nabla}\,\overline{f}(\overline{\boldsymbol{w}}).$$

Using eq. (8.5), eq. (8.6), and eq. (8.7), we get

$$\begin{aligned}\overline{\boldsymbol{\Psi}}(\overline{\boldsymbol{w}}) = &- S_w(D_w\boldsymbol{g}(\boldsymbol{w}))'[D_w\boldsymbol{g}(\boldsymbol{w})S_w^2(D_w\boldsymbol{g}(\boldsymbol{w}))']^{-1}[\boldsymbol{g}(\boldsymbol{w}) - f_0^{-1}D_w\boldsymbol{g}(\boldsymbol{w})S_w^2\nabla f(\boldsymbol{w})] \\ &- f_0^{-1}S_w\nabla f(\boldsymbol{w}),\end{aligned}$$

which shows that the time evolution $\overline{\boldsymbol{w}}(t)$ is affected S_w, but not by S_g. Thus, S_g can then be chosen to improve the condition number of the linear system (8.4) through row equilibration. Indeed, the involved linear operator is

$$\Sigma = D_{\overline{w}}\overline{\boldsymbol{g}}(\overline{\boldsymbol{w}})(D_{\overline{w}}\overline{\boldsymbol{g}}(\overline{\boldsymbol{w}}))' = S_g^{-1}[D_w\boldsymbol{g}(\boldsymbol{w})S_w^2(D_w\boldsymbol{g}(\boldsymbol{w}))']S_g^{-1}.$$

Hence, S_g can be interpreted as a symmetric diagonal preconditioner for Σ. We choose to perform row equilibration by normalizing the rows of the representative matrix J_g of $D_w\boldsymbol{g}$ with respect to the 2-norm. If the rows of J_g formed an orthogonal set, then our choice would yield $\Sigma = I$. In general, it is only guaranteed that the diagonal terms of $J_gJ_g^T$ will be all ones. It can be proved [170, Thm. 4.1] that the spectral condition number obtained from row equilibration κ_2^{re} and the minimum one obtainable with a symmetric diagonal preconditioner κ_2^{min} satisfy $\kappa_2^{re} \leq n\kappa_2^{min}$, where n is the dimension of all involved matrices. While this result indicates that there may be room for improvement, since the condition number may increase proportionally to n, we have observed that the proposed preconditioner yields reasonable performance in terms of number of iterations and computational time for our purpose.

8.1.3 Adaptive time stepping

We now deal with the time-discretization of eq. (8.3). Since this is a system of ODEs, but it also originates from an optimization problem, a suitable combination of numerical approaches from the two fields can be adopted for an efficient and accurate solution. On the one hand, there is the possibility of using numerical

methods for the discretization of ODEs, possibly adapted to the optimization nature of the original problem. Such a choice was made in [177], where a fourth-order Runge-Kutta scheme with an ad-hoc stepsize choice based on constraint violation was employed. On the other hand, one could rely on constrained optimization concepts, such as merit functions and filters [127, sect. 15.4]. This choice was made in [54], where a merit function was used. Our approach is similar to the former: we start from an adaptive Runge-Kutta method, and introduce criteria for the dynamic update of solver tolerances. In all cases, to avoid the need of subiterating (and the possible need of computing higher order derivatives, if a Newton algorithm is used for subiterations), explicit algorithms are preferable.

When standard methods for ODEs are chosen, a compromise needs to be sought between number of required function evaluations, accuracy and stability. To limit the discussion, we consider single step, multistage methods. The number of stages can be increased with the aim of either improving the accuracy or enlarging the stability region and thus allowing larger steps. Adaptive time stepping can be performed by combining two methods of different orders [80, sect. II.4]. Starting from iterate $\boldsymbol{w}^j$, the solution at the next step is computed using the low-order method, obtaining $\boldsymbol{w}^{j+1}$, and the high-order method, obtaining $\widehat{\boldsymbol{w}}^{j+1}$. Then, the normalized error between the two is computed as [80, eq. 4.11]

$$\epsilon = \sqrt{\frac{1}{N_w}\sum_{\ell=1}^{N_w}\left(\frac{w_\ell^{j+1} - \widehat{w}_\ell^{j+1}}{\varsigma_\ell}\right)^2}, \tag{8.8}$$

where $\varsigma_\ell = \tau_{RK}^{abs} + \max(|w_\ell^j, w_\ell^{j+1}|)\tau_{RK}^{rel}$, τ_{RK}^{abs} being the absolute tolerance and τ_{RK}^{rel} the relative tolerance. The estimated time step is then updated as

$$\Delta t_{\text{est}}^{j+1} = (1/\epsilon)^{1/r}\Delta t^j,$$

where r is the order of the local truncation error of the low-order method (2 for Euler's method). In practice, the variation of the time step between successive iterates is limited by defining safety factors; this leads to the actual updated time step Δt^{j+1}. The cheapest adaptive method built in such a way in terms of stages is the combination of the 1-stage, first-order explicit Euler method and the 2-stage, second-order Heun method. If the solution is updated using the Euler method, a single evaluation of $\boldsymbol{\Psi}(\boldsymbol{w})$ is required at each time step, since the second stage is recycled as the first stage of the next step. The result is algorithm 7.

In the following, we present criteria to select the tolerance of the Runge-Kutta method τ_{RK} and the absolute tolerance on the residual of the CG solver τ_{CG} automatically and adaptively to achieve convergence within a specified tolerance on the final value of $\|\boldsymbol{\Psi}(\boldsymbol{w})\|_2$, τ_Ψ. The first criterion is based on stability, while the second is based on accuracy.

The condition $\Delta t < 2$ was indicated in [54] as a stability requirement, with the following explanation. Consider the expansion

$$\boldsymbol{g}(\boldsymbol{w}^{j+1}) = \boldsymbol{g}(\boldsymbol{w}^j + \Delta t\boldsymbol{\Psi}(\boldsymbol{w}^j)) = \boldsymbol{g}(\boldsymbol{w}^j) + \Delta t J_g(\boldsymbol{w}^j)\boldsymbol{\Psi}(\boldsymbol{u}^j) + \boldsymbol{R}_2,$$

Algorithm 7 First order Euler-Heun method

Set $\boldsymbol{w}^0$, Δt^0, τ_Ψ, t_{max}
Set $t = 0$, $j = 0$
$k_2 = \boldsymbol{\Psi}(\boldsymbol{w}^0)$
while $\|\boldsymbol{\Psi}(\boldsymbol{w}^j)\|_2 > \tau_\Psi$ **and** $t < t_{max}$ **do**
  $k_1 = k_2$
  $k_2 = \boldsymbol{\Psi}(\boldsymbol{w}^j + k_1 \Delta t^j)$
  $\boldsymbol{w}^{j+1} = \boldsymbol{w}^j + k_1 \Delta t^j$
  $\widehat{\boldsymbol{w}}^{j+1} = \boldsymbol{w}^j + \frac{1}{2}(k_1 + k_2)\Delta t^j$
  Compute the relative error between the two updates using (8.8)
  Compute the updated time step Δt^{j+1}
  if $\epsilon \leq 1$ **then**
    Stepsize accepted: $t \leftarrow t + \Delta t^j$
    $j \leftarrow j + 1$
  end if
end while

where $\boldsymbol{R}_2$ is the remainder of the series, $\|\boldsymbol{R}_2\| = \mathcal{O}(\Delta t^2)$. From $J_g \boldsymbol{\Psi} = -\boldsymbol{g}$, which is a consequence of eq. (8.3), and the triangle inequality, we obtain

$$\|\boldsymbol{g}(\boldsymbol{w}^{j+1})\| \leq |1 - \Delta t| \|\boldsymbol{g}(\boldsymbol{w}^j)\| + \|\boldsymbol{R}_2\|,$$

and the condition stems from requiring $|1 - \Delta t| < 1$, which corresponds to a reduction of the constraint vector norm. However, if system (8.4) is solved with finite accuracy, then the maximum time step satisfying the stability requirement is reduced, as seen in the following. Let us call $\widetilde{\Lambda}$ the numerical solution of (8.4) obtained by using an iterative method, and let $\widetilde{\boldsymbol{\Psi}}(\boldsymbol{w}^j)$ be the resulting approximation of $\boldsymbol{\Psi}(\boldsymbol{w}^j)$. Then,

$$\boldsymbol{g}(\boldsymbol{w}^j + \Delta t \widetilde{\boldsymbol{\Psi}}(\boldsymbol{w}^j)) = \boldsymbol{g}(\boldsymbol{w}^j) + \Delta t J_g(\boldsymbol{w}^j) \widetilde{\boldsymbol{\Psi}}(\boldsymbol{w}^j) + \boldsymbol{R}_2. \tag{8.9}$$

From (8.4), and defining $\boldsymbol{e}_\Lambda = \widetilde{\boldsymbol{\Lambda}} - \boldsymbol{\Lambda}$, we have

$$\widetilde{\boldsymbol{\Psi}}(\boldsymbol{w}^j) = -\nabla f(\boldsymbol{w}^j) + J_g^T(\boldsymbol{w}^j)(\boldsymbol{\Lambda} + \boldsymbol{e}_\Lambda) = \boldsymbol{\Psi}(\boldsymbol{w}^j) + J_g^T(\boldsymbol{w}^j)\boldsymbol{e}_\Lambda. \tag{8.10}$$

Now, substituting eq. (8.10) into eq. (8.9) and using again $J_g \boldsymbol{\Psi} = -\boldsymbol{g}$, we get

$$\boldsymbol{g}(\boldsymbol{w}^j + \Delta t \widetilde{\boldsymbol{\Psi}}(\boldsymbol{w}^j)) = (1 - \Delta t)\boldsymbol{g}(\boldsymbol{w}^j) + \Delta t J_g(\boldsymbol{w}^j) J_g^T(\boldsymbol{w}^j)\boldsymbol{e}_\Lambda + \boldsymbol{R}_2.$$

The last expression can be rewritten in terms of the residual of system eq. (8.4) by recalling that, given any system $A\boldsymbol{x} = \boldsymbol{b}$, the relationship between the error $\boldsymbol{e}$ and the residual $\boldsymbol{r}$ is $A\boldsymbol{e} = \boldsymbol{r}$. In our case, we have $J_g(\boldsymbol{w}^j) J_g^T(\boldsymbol{w}^j)\boldsymbol{e}_\Lambda = \boldsymbol{r}$, which leads to

$$\boldsymbol{g}(\boldsymbol{w}^j + \Delta t \widetilde{\boldsymbol{\Psi}}(\boldsymbol{w}^j)) = (1 - \Delta t)\boldsymbol{g}(\boldsymbol{w}^j) + \Delta t \boldsymbol{r} + \boldsymbol{R}_2.$$

If $\Delta t < 2$, using the triangle inequality we obtain

$$\|\boldsymbol{g}(\boldsymbol{w}^j + \Delta t \widetilde{\boldsymbol{\Psi}}(\boldsymbol{w}^j))\| \leq (1 - \Delta t)\|\boldsymbol{g}(\boldsymbol{w}^j)\| + \Delta t \|\boldsymbol{r}\| + \|\boldsymbol{R}_2\|.$$

Rearranging yields the more readily interpretable inequality

$$\|\boldsymbol{g}(\boldsymbol{w}^j)\| - \|\boldsymbol{g}(\boldsymbol{w}^j + \Delta t\widetilde{\boldsymbol{\Psi}}(\boldsymbol{w}^j))\| \geq \Delta t \left(\|\boldsymbol{g}(\boldsymbol{w}^j)\| - \|\boldsymbol{r}\|\right) - \|\boldsymbol{R}_2\|. \tag{8.11}$$

As long as $\|\boldsymbol{r}\| < \|\boldsymbol{g}(\boldsymbol{w}^j)\|$, the first-order term dominates on the second-order term and a reduction of the norm of $\boldsymbol{g}$ is guaranteed for a sufficiently small time step. However, if $\|\boldsymbol{r}\|$ approaches or exceeds $\|\boldsymbol{g}(\boldsymbol{w}^j)\|$, the first order term becomes negligible and eventually negative, and a nonincreasing value of the constraint norm may not be guaranteed for any value of Δt. We thus need to set $\|\boldsymbol{r}\| < \tau_{CG} \ll \|\boldsymbol{g}(\boldsymbol{w}^j)\|$.

Let us now focus on accuracy and assume that the exact gradient-flow trajectory $\boldsymbol{w}(t)$ converges to a constrained optimum, i.e. for any value of tolerance $\tau > 0$ there exists $T > 0$ such that $\|\boldsymbol{\Psi}(\boldsymbol{w}(t))\| < \tau,\ \forall t > T$. We study the effect of the limited accuracy of the ODE and linear system solvers on the possibility of converging to within the prescribed tolerance. We denote as $\hat{\boldsymbol{w}}$ the numerical solution of ODE (8.3). At a certain step $\hat{\boldsymbol{w}}$ along the numerically integrated trajectory, the numerical approximation of the flow map can be split into the following contributions:

$$\widetilde{\boldsymbol{\Psi}}(\hat{\boldsymbol{w}}) = \boldsymbol{\Psi}(\boldsymbol{w}) + \underbrace{(\boldsymbol{\Psi}(\hat{\boldsymbol{w}}) - \boldsymbol{\Psi}(\boldsymbol{w}))}_{\text{ODE solver error}} + \underbrace{\left(\widetilde{\boldsymbol{\Psi}}(\hat{\boldsymbol{w}}) - \boldsymbol{\Psi}(\hat{\boldsymbol{w}})\right)}_{\text{linear solver error}}.$$

The triangle inequality leads to

$$\|\widetilde{\boldsymbol{\Psi}}(\hat{\boldsymbol{w}})\| \leq \|\boldsymbol{\Psi}(\boldsymbol{w})\| + \|\boldsymbol{\Psi}(\hat{\boldsymbol{w}}) - \boldsymbol{\Psi}(\boldsymbol{w})\| + \|\widetilde{\boldsymbol{\Psi}}(\hat{\boldsymbol{w}}) - \boldsymbol{\Psi}(\hat{\boldsymbol{w}})\|.$$

In order to reach and observe convergence up to a tolerance, the two error terms need to be controlled. One may for instance aim to ensure that they are at least an order of magnitude smaller than $\|\boldsymbol{\Psi}(\boldsymbol{w})\|$. For the ODE solver error, we assume Lipschitz continuity of $\boldsymbol{\Psi}$ and write

$$\|\boldsymbol{\Psi}(\hat{\boldsymbol{w}}) - \boldsymbol{\Psi}(\boldsymbol{w})\| \leq L\|\hat{\boldsymbol{w}} - \boldsymbol{w}\|.$$

For the linear solver error, we have

$$\|\widetilde{\boldsymbol{\Psi}}(\hat{\boldsymbol{w}}) - \boldsymbol{\Psi}(\hat{\boldsymbol{w}})\| \leq \|J_g^+(\hat{\boldsymbol{w}})\|\|\boldsymbol{r}\|.$$

The problem is now to find order of magnitude estimates of L and $\|J_g^+(\hat{\boldsymbol{w}})\|$ that are cheaply computable. We adopt the following:

$$L \sim \frac{\|\boldsymbol{\Psi}(\boldsymbol{w}^j) - \boldsymbol{\Psi}(\boldsymbol{w}^{j-1})\|}{\|\boldsymbol{w}^j - \boldsymbol{w}^{j-1}\|}, \quad \|J_g^+(\hat{\boldsymbol{w}})\| \sim \frac{\|J_g^T(\hat{\boldsymbol{w}})\boldsymbol{\Lambda}\|}{\|\boldsymbol{g}(\hat{\boldsymbol{w}}) - J_g(\hat{\boldsymbol{w}})\nabla f(\hat{\boldsymbol{w}})\|}.$$

All the vectors involved are intermediate quantities needed for the solution of the problem; the only additional work required to build the estimates is the computation of the norms. The tolerance of the CG solver can then be set as

$$\tau_{CG}^j = k_\tau \min\left(\frac{\|\boldsymbol{\Psi}(\boldsymbol{w}^{j-1})\|\|\boldsymbol{g}(\boldsymbol{w}^{j-1}) - J_g(\boldsymbol{w}^{j-1})\nabla f(\boldsymbol{w}^{j-1})\|}{\|J_g^T(\boldsymbol{w}^{j-1})\boldsymbol{\Lambda}\|}, \|\boldsymbol{g}(\boldsymbol{w}^j)\|\right),$$

where the stability condition implied by (8.11) is taken into account. The tolerance of the ODE solver can be set as

$$\tau_{RK}^{j} = \min\left(\tau_{RK}^{j-1}, k_\tau \frac{\|\boldsymbol{\Psi}(\boldsymbol{w}^j)\|\|\boldsymbol{w}^j - \boldsymbol{w}^{j-1}\|}{\|\boldsymbol{\Psi}(\boldsymbol{w}^j) - \boldsymbol{\Psi}(\boldsymbol{w}^{j-1})\|}\right),$$

where, for consistency, the error estimate used for stepsize selection needs to be computed in the euclidean norm, that is, (8.8) is replaced with

$$\epsilon = \|\boldsymbol{w}^{j+1} - \hat{\boldsymbol{w}}^{j+1}\|/\tau_{RK}^{j}.$$

Moreover, the previous tolerance τ_{RK}^{j-1} is used as an upper bound for τ_{RK}^{j} in order to avoid large oscillations of the stepsize and frequent stepsize rejections, which may reduce the efficiency of the method. One may set $k_\tau = 0.1$. As an additional measure to prevent over-solving, the time step is halved if conjugate gradient does not converge to the required tolerance within a prescribed maximum number of iterations.

In the following, the presented algorithm is applied to the problem of optimizing positions and control parameters for wave energy converter parks.

8.2 Modeling of the WEC optimal design problem

In this section, we describe in detail the terms of eq. (8.1). Cost function and decision variables are defined in section 8.2.1. The fluid-structure interaction model, whose residual defines the equality constraint, is presented in section 8.2.2. The treatment of the inequality constraints, namely the slamming, available domain, and minimum distance constraints, is described in section 8.2.3. In section 8.2.4, we report the computation of the required differentials.

8.2.1 Cost function and decision variables

We aim to maximize the time-averaged power of an array of N_b WEC devices. The decision variables to be determined through optimization are the projections on the horizontal plane of the devices' centers, collected in vector $\boldsymbol{X} = [\boldsymbol{x}_1, \dots, \boldsymbol{x}_{N_b}] \in \mathbb{R}^{2N_b}$, and the coefficients of the PTO mechanisms: dampings $\boldsymbol{c} = [c_1, \dots, c_{N_b}]$ and stiffnesses $\boldsymbol{\kappa} = [\kappa_1, \dots, \kappa_{N_b}]$. For convenience, we define the vector of decision variables $\boldsymbol{u} = [\boldsymbol{X}, \boldsymbol{c}, \boldsymbol{\kappa}]$. We instead consider fixed the number of devices N_b and their geometries, assumed to be all identical and defined by radius R and draft d. We also fix the sea state, defined by significant wave height H_s, energy period T_e and wave direction β, together with the sea depth, assumed uniform. We use the expression (6.5) of the total power of the array, reported here for convenience:

$$P = \frac{1}{2}\sum_{\ell=1}^{N_b} c_\ell \sum_{q=1}^{N_f} \left(\omega_q |\hat{\zeta}_{\ell q}|\right)^2. \tag{8.12}$$

8.2.2 State problem: dynamic and hydrodynamic equations

The state problem is a linearized fluid-structure interaction problem, which we model using linear potential flow theory (see Chapter 2) and solve through interaction theory (see Sec. 3.2). Thanks to linearity, it can be treated in the frequency domain, with each frequency component evolving independently from all others. For simplicity, we consider unidirectional waves, and discretize the wave spectrum as described in Sect. 3.3, with intervals of constant width in frequency. As before, we consider the Pierson-Moskowitz spectrum (2.79). The result of the discretization is the set of pairs (H_q, ω_q), with the corresponding wavenumbers k_q obtained through the dispersion relation (2.54). The undisturbed free surface elevation at the center of the ℓ-th device is then

$$\eta_\ell(t) = \sum_{q=1}^{N_f} \mathrm{Re}\left[\hat{\eta}_{\ell q} \exp(-i\omega_q t + \varphi_q)\right], \text{ with } \hat{\eta}_{\ell q} = i\frac{H_q}{2}\exp[ik_q(x_\ell \cos\beta + y_\ell \sin\beta)]. \tag{8.13}$$

For each frequency of the spectrum discretization, system (3.39) must hold. Writing the frequency index explicitly for clarity, we have

$$\begin{bmatrix} M_{\gamma\gamma,q}(\boldsymbol{u}) & M_{\gamma\zeta,q}(\boldsymbol{u}) \\ M_{\zeta\gamma,q}(\boldsymbol{u}) & M_{\zeta\zeta,q}(\boldsymbol{u}) \end{bmatrix} \begin{bmatrix} \hat{\boldsymbol{\gamma}}_q \\ \hat{\boldsymbol{\zeta}}_q \end{bmatrix} = \begin{bmatrix} \boldsymbol{h}_{\gamma,q}(\boldsymbol{u}) \\ \boldsymbol{h}_{\zeta,q}(\boldsymbol{u}) \end{bmatrix}. \tag{8.14}$$

The residuals of all such systems, for $q = 1, \ldots, N_f$, form the equality constraint vector of our optimization problem:

$$\boldsymbol{e}_q(\boldsymbol{u}, \hat{\boldsymbol{\gamma}}_q, \hat{\boldsymbol{\zeta}}_q) = \begin{bmatrix} \boldsymbol{e}_{\gamma,q} \\ \boldsymbol{e}_{\zeta,q} \end{bmatrix} = \begin{bmatrix} M_{\gamma\gamma,q}(\boldsymbol{u})\hat{\boldsymbol{\gamma}}_q + M_{\gamma\zeta,q}(\boldsymbol{u})\hat{\boldsymbol{\zeta}}_q - \boldsymbol{h}_{\gamma,q}(\boldsymbol{u}) \\ M_{\zeta\gamma,q}(\boldsymbol{u})\hat{\boldsymbol{\gamma}}_q + M_{\zeta\zeta,q}(\boldsymbol{u})\hat{\boldsymbol{\zeta}}_q - \boldsymbol{h}_{\zeta,q}(\boldsymbol{u}) \end{bmatrix}. \tag{8.15}$$

For our purposes, the most important features of this formulation are the following. Firstly, the residual of the state problem can be differentiated analytically with respect to the decision variables, as detailed in section 8.2.4. In particular, the dependence on the devices' coordinates is only contained in coordinate transformation matrices $T_{m\ell}$ and ambient wave vectors $\boldsymbol{a}_\ell$, the dependence on stiffness and damping is only contained in the mechanical impedances W_ℓ, and both have differentiable analytic expressions. Secondly, all other quantities are independent of the decision variables and can be precomputed, so that, as vector $\boldsymbol{u}$ is updated at each optimization iteration, the residual of the state problem and its differential can be computed efficiently. This is in contrast with other popular modelling approaches such as the boundary element method, in which grids and interaction matrices would need to be completely reassembled as the devices' positions change.

8.2.3 Inequality constraints

In this section, we first detail the slamming, available domain and minimal distance inequality constraints, and then convert them into equality constraints through a slack variable formulation, as explained for a generic optimization problem in section 8.1.1.

Slamming constraint

The model presented in the previous section is linear; hence, it poses no limits on the magnitude of the oscillation amplitudes of devices. To ensure that the latter remain physically meaningful, in the sense that the devices do not leave the water, the slamming constraint can be enforced [17]. As explained in Sec. 5.2, if a frequency domain approach is adopted, the constraint can be approximately enforced by limiting the root mean square value of $\zeta_\ell(t) - \eta_\ell(t)$:

$$h_{sl,\ell} = \sum_{q=1}^{N_f} |\hat{\zeta}_{\ell q} - \hat{\eta}_{\ell q}|^2 - 2\alpha^2 d^2 \leq 0, \quad \ell = 1, \dots, N_b, \tag{8.16}$$

where $\hat{\eta}_{\ell q}$ is the complex amplitude of the q-th wave component evaluated at the center of the ℓ-th device. Here, α is the parameter controlling the admissible exceedance probability, and d is the draft.

Layout constraints

In this section, the treatment of the constraints on the devices' layout is described: they are the available domain constraint and the minimum distance constraint.

We assume the available sea area to be a simply connected set Ω_{ad}, which we do not require to be convex. On the one hand, this allows to consider a larger class of domains of practical interest; on the other hand, it makes the numerical treatment more delicate.[1] To impose the domain constraint as an equality, we would need a function with value zero inside Ω_{ad} and positive outside. However, such a function would also have zero gradient inside Ω_{ad}, thus making the constraint Jacobian matrix singular and requiring the adoption of a different framework. We instead opt for defining the constraint as an inequality, and requiring the corresponding function h to be negative inside Ω_{ad}. This is achieved by solving two Poisson problems (see fig. 8.2): one on the admissible domain,

$$-\Delta h = \sigma_{int} \text{ in } \Omega_{ad}, \quad h = 0 \text{ on } \Gamma_{ad}, \tag{8.17}$$

and one on an exterior domain Ω_{ext},

$$-\Delta h = \sigma_{out} \text{ in } \Omega_{ext}, \quad h = 0 \text{ on } \Gamma_{ad}, \quad \frac{\partial h}{\partial n} = \nu_N \text{ on } \Gamma_{ext}. \tag{8.18}$$

We set $\sigma_{int} = -1$, $\sigma_{out} = 1$ and $\nu_N = 0$. We now remark on some desirable properties of the solutions, whose proofs are reported in Appendix B. The maximum principle for both the classical and the weak form of the problems guarantees that h can have no global maxima in the interior of Ω_{ad} and no global minima in the interior of Ω_{ext} [26]. Moreover, for classical solutions it is possible to prove using a modification of the mean value property [148] that neither local maxima can exist in Ω_{ad} (resp. minima in Ω_{ext}). It is also possible to prove, both for the classical and weak formulation, that ∇h can be zero on at most a set of zero

[1] For example, a convex polygonal set can be described as a system of linear inequalities; this is instead not possible for a concave polygon.

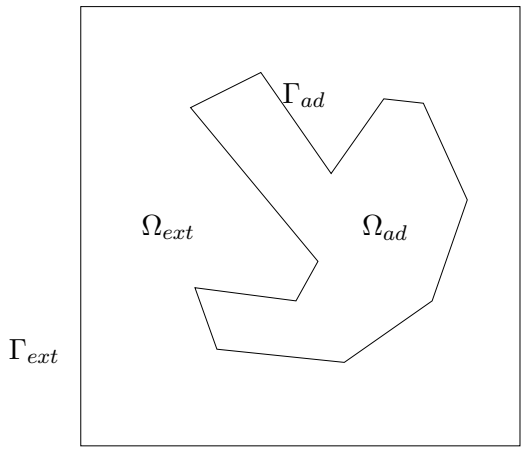

Figure 8.2: *Poisson equation domain.*

measure. To compute h, the problem needs to be discretized. If the finite element method is used, with $\mathbb{P}^1$ elements on a Delaunay triangulation, then the numerical solution satisfies local and global discrete maximum properties [18].

The gradient of h needs to be computed to build the differential of constraint functions. If $\mathbb{P}^1$ elements are used, then the exact gradient is discontinuous, potentially making the gradient-flow ODE system stiff. To avoid this possible issue, we can compute a more regular approximation G_h of ∇h through projection, i.e. by solving the following problem:

$$(G_h, v) + \eta(\nabla G_h, \nabla v) = (\nabla h, v) \quad \forall v \in H^1(\Omega),\ \Omega = \Omega_{ad} \cup \Omega_{ext}.$$

The constraint of admissible domain is then imposed as

$$h_{\mathrm{ad},\ell} = h(\boldsymbol{x}_\ell) \neq 0, \quad \ell = 1, \dots, N_b.$$

The constraint of minimum distance between devices is written as

$$h_{md,\ell m} = d_{min}^2 - \|\boldsymbol{x}_\ell - \boldsymbol{x}_m\|^2 \leq 0, \quad \ell, m = 1, \dots, N_b,\ l \neq m. \tag{8.19}$$

It can be verified that it corresponds to a non-convex admissible set [59].

Slack variable formulation

In order to write the final form of our optimal design problem, we first collect all inequality constraints into a single vector $\boldsymbol{h} = [\boldsymbol{h}_{sl}, \boldsymbol{h}_{ad}, \boldsymbol{h}_{md}]$ and define a corresponding vector of slack variables $\boldsymbol{s} = [\boldsymbol{s}_{sl}, \boldsymbol{s}_{ad}, \boldsymbol{s}_{md}]$. The constraints of slamming, admissible domain and minimum distance are then rewritten as

$$\boldsymbol{g}_{\mathcal{I}}(\boldsymbol{u}, \hat{\boldsymbol{\gamma}}, \hat{\boldsymbol{\zeta}}, \boldsymbol{s}) := \boldsymbol{h}(\boldsymbol{u}, \hat{\boldsymbol{\gamma}}, \hat{\boldsymbol{\zeta}}) + \boldsymbol{s} \odot \boldsymbol{s} = 0.$$

By defining a single constraint vector

$$\boldsymbol{g}(\boldsymbol{u}, \hat{\boldsymbol{\gamma}}, \hat{\boldsymbol{\zeta}}, \boldsymbol{s}) = [\boldsymbol{e}_1(\boldsymbol{u}, \hat{\boldsymbol{\gamma}}, \hat{\boldsymbol{\zeta}}), \dots, \boldsymbol{e}_{N_q}(\boldsymbol{u}, \hat{\boldsymbol{\gamma}}, \hat{\boldsymbol{\zeta}}), \boldsymbol{g}_{\mathcal{I}}(\boldsymbol{u}, \hat{\boldsymbol{\gamma}}, \hat{\boldsymbol{\zeta}}, \boldsymbol{s})], \tag{8.20}$$

our optimization problem can be restated as an equality-constrained minimization of the opposite of the power eq. (8.12):

$$\min_{\boldsymbol{u}} \quad f(\boldsymbol{u}, \hat{\boldsymbol{\gamma}}, \hat{\boldsymbol{\zeta}}) = -\frac{1}{2} \sum_{\ell=1}^{N_b} c_\ell \sum_{q=1}^{N_f} \left(\omega_q |\hat{\zeta}_{\ell q}| \right)^2 \quad \text{s.t.} \quad \boldsymbol{g}(\boldsymbol{u}, \hat{\boldsymbol{\gamma}}, \hat{\boldsymbol{\zeta}}, \boldsymbol{s}) = 0. \tag{8.21}$$

For convenience, we finally define $\boldsymbol{w} = [\boldsymbol{u}, \hat{\boldsymbol{\gamma}}, \hat{\boldsymbol{\zeta}}, \boldsymbol{s}] \in \mathbb{C}^{N_w}$, so that the generic formulation eq. (8.2) is recovered.

8.2.4 Algebraic setting and differentials

In this section, we derive the gradient of the cost function and the differential of the constraint vector for our specific application. We call $D_w f(\boldsymbol{v})$ the Fréchet differential of f at $\boldsymbol{w}$ with increment $\boldsymbol{v} = [\boldsymbol{v}_u, \boldsymbol{v}_\gamma, \boldsymbol{v}_\zeta, \boldsymbol{v}_s]$. A description based on the differential operator, instead of a matrix representation, is convenient for computational purposes. Indeed, assembling the matrices of the state problem (see eq. (3.35), eq. (3.37)) would require a large number of inefficient matrix-matrix multiplications, and moreover matrices B_ℓ, $T_{m\ell}$ are sparse, while their product is dense. In our implementation we instead only perform matrix-vector multiplications, by carefully choosing the order of operations: so, the matrices of the state problem are actually treated as abstract linear operators.

The cost function (8.21) depends explicitly only on the damping coefficients $\boldsymbol{c}$ and on the oscillation amplitudes $\hat{\boldsymbol{\zeta}}$. We have

$$\frac{\partial f}{\partial c_\ell} = -\frac{1}{2} \sum_{q=1}^{N_f} \left(\omega_q |\hat{\zeta}_{\ell q}| \right)^2, \quad D_\zeta f(\boldsymbol{v}_\zeta) = -\sum_{\ell_1}^{N_b} c_\ell \sum_{q=1}^{N_f} \omega_q^2 \mathrm{Re}\left[v^*_{\zeta_{\ell q}} \hat{\zeta}_{\ell q} \right],$$

where * denotes the complex conjugate. The computed differential is $\mathbb{R}$-linear, but not $\mathbb{C}$-linear (in the nomenclature of [99, sect. III.2]), because of the presence of the real part operator. A suitable setting for our problem is thus the space of complex vectors over the field of real scalars $(\mathbb{C}^{N_w}, \mathbb{R})$, with inner product $(\boldsymbol{u}, \boldsymbol{v}) = \mathrm{Re}[\boldsymbol{u}^H \boldsymbol{v}]$, where ^{H} denotes the hermitian (transpose conjugate), and the gradient with respect to oscillation amplitudes is the corresponding Riesz representative of the differential:

$$\frac{\partial f}{\partial \hat{\zeta}_{\ell q}} = -\omega_q^2 c_\ell \hat{\zeta}_{\ell q}.$$

The differential of the constraint vector $\boldsymbol{g}$ is split as

$$D_w \boldsymbol{g} = [D_w \boldsymbol{e}_1, \ldots, D_w \boldsymbol{e}_{N_q}, D_w \boldsymbol{h}_{sl}, D_w \boldsymbol{h}_{ad}, D_w \boldsymbol{h}_{md}].$$

Let us start from the residual of the state problem eq. (8.15), focusing on a single frequency and thus disregarding subscript q:

$$D_w \boldsymbol{e}(\boldsymbol{v}) = \begin{bmatrix} M_{\gamma\gamma}(\boldsymbol{u})\boldsymbol{v}_\gamma + M_{\gamma\zeta}(\boldsymbol{u})\boldsymbol{v}_\zeta + D_u \boldsymbol{e}_\gamma(\boldsymbol{v}_u) \\ M_{\zeta\gamma}(\boldsymbol{u})\boldsymbol{v}_\gamma + M_{\zeta\zeta}(\boldsymbol{u})\boldsymbol{v}_\zeta + D_u \boldsymbol{e}_\zeta(\boldsymbol{v}_u) \end{bmatrix}.$$

As already mentioned, the blocks of system eq. (8.14) depend on the decision variables through coordinate transformation matrices, ambient wave vectors and mechanical impedance: in particular, from the ℓ-th block-row of eq. (3.35) we obtain

$$D_u \boldsymbol{e}_{\gamma,\ell}(\boldsymbol{v}_u) = \sum_{\substack{m=1 \\ m\neq\ell}}^{N_b} B_\ell \left(D_u T_{m\ell}(\boldsymbol{v}_u)\right)^T \left(\hat{\boldsymbol{\gamma}}_m + \boldsymbol{R}_m \hat{\zeta}_m\right) + \frac{H}{2} B_\ell \left(\frac{\partial \boldsymbol{a}_\ell}{\partial x_\ell} v_{x_\ell} + \frac{\partial \boldsymbol{a}_\ell}{\partial y_\ell} v_{y_\ell}\right),$$

and from the ℓ-th row of eq. (3.37)

$$\begin{aligned} D_u e_{\zeta,\ell}(\boldsymbol{v}_u) = &\sum_{\substack{m=1 \\ m\neq\ell}}^{N_b} \frac{1}{W_\ell} \left[(\widetilde{\boldsymbol{Y}}_\ell^D)^T \widetilde{B}_\ell \left(D_u T_{m\ell}(\boldsymbol{v}_u)\right)^T \hat{\boldsymbol{\gamma}}_m + \boldsymbol{R}_m^T D_u T_{m\ell}(\boldsymbol{v}_u) \widetilde{B}_\ell^T \widetilde{\boldsymbol{Y}}_\ell^D \hat{\zeta}_m\right] \\ &+ \frac{H}{2W_\ell} \left(\frac{\partial \boldsymbol{a}_\ell^T}{\partial x_\ell} v_{x_\ell} + \frac{\partial \boldsymbol{a}_\ell^T}{\partial y_\ell} v_{y_\ell}\right) \tilde{B}_\ell^T \tilde{\boldsymbol{Y}}_\ell^D - \frac{1}{W_\ell} (e_{\zeta,\ell} - \hat{\zeta}_\ell) D_u W_\ell(\boldsymbol{v}_u). \end{aligned}$$

The differential of the basis transformation matrix reads

$$D_u T_{m\ell}(\boldsymbol{v}_u) = \frac{\partial T_{m\ell}}{\partial x_\ell} v_{x_\ell} + \frac{\partial T_{m\ell}}{\partial y_\ell} v_{y_\ell} + \frac{\partial T_{m\ell}}{\partial x_m} v_{x_m} + \frac{\partial T_{m\ell}}{\partial y_m} v_{y_m},$$

while the differential of the mechanical impedance eq. (3.38) is

$$D_u W_\ell(\boldsymbol{v}_u) = \frac{\omega}{\rho g} v_{c_\ell} + \frac{i}{\rho g} v_{\kappa_\ell}.$$

The expressions of the derivatives of matrices $T_{m\ell}$ and vectors $\boldsymbol{a}_\ell$ have been derived in Sec. 7.3.2.

The slamming constraint vector $\boldsymbol{h}_{sl}$ depends on the oscillation amplitudes $\hat{\boldsymbol{\zeta}}$ explicitly, and on the devices' positions through the phase of incident waves. Its derivatives with respect to positions can be directly evaluated (see eq. (8.13)):

$$\begin{aligned} \frac{\partial h_{sl,\ell}}{\partial x_\ell} &= -2 \sum_{q=1}^{N_f} \mathrm{Re}\left[(\hat{\zeta}_{q\ell} - \hat{\eta}_{q\ell})^* \frac{\partial \hat{\eta}_{q\ell}}{\partial x_\ell}\right], \\ \frac{\partial \hat{\eta}_{q\ell}}{\partial x_\ell} &= \frac{\partial}{\partial x_\ell}\left[i\frac{H_q}{2} \exp[ik(x_\ell \cos\beta + y_\ell \sin\beta)]\right] = ik\cos\beta \hat{\eta}_{q\ell}. \end{aligned}$$

We observe that

$$\mathrm{Re}\left[\hat{\eta}_{q\ell}^* \frac{\partial \hat{\eta}_{q\ell}}{\partial x_\ell}\right] = \frac{1}{2} \frac{\partial}{\partial x_\ell} |\hat{\eta}_{q\ell}|^2 = 0,$$

since coordinate x_ℓ has an effect on the phase of $\hat{\eta}_{q\ell}$, but not on its magnitude. Hence,

$$\frac{\partial \hat{\eta}_{q\ell}}{\partial x_\ell} = -2\cos\beta \sum_{q=1}^{N_f} k_q \mathrm{Re}\left(i\hat{\zeta}_{q\ell}^* \hat{\eta}_{q\ell}\right) = 2\cos\beta \sum_{q=1}^{N_f} k_q \mathrm{Re}\left(i\hat{\zeta}_{q\ell} \hat{\eta}_{q\ell}^*\right).$$

An analogous result holds for y_ℓ, with $\sin\beta$ in place of $\cos\beta$. Differentiation with respect to oscillation amplitudes yields

$$D_\zeta h_{sl,\ell}(\boldsymbol{v}_\zeta) = \sum_{q=1}^{N_f} 2\mathrm{Re}\left[v^*_{\zeta_{q\ell}}\left(\hat{\zeta}_{q\ell} - \hat{\eta}_{q\ell}\right)\right].$$

The full differential of the ℓ-th component of the slamming constraint reads

$$D_w h_{sl,\ell}(\boldsymbol{v}) = \frac{\partial h_{sl,\ell}}{\partial x_\ell} v_{x_\ell} + \frac{\partial h_{sl,\ell}}{\partial y_\ell} v_{y_\ell} + \sum_{q=1}^{N_f} 2\mathrm{Re}\left[v^*_{\zeta_{q\ell}}\left(\hat{\zeta}_{q\ell} - \hat{\eta}_{q\ell}\right)\right] + 2s_{sl,\ell} v_{s_{sl,\ell}}.$$

The computation of the gradient of the admissible domain constraint has been discussed in section 8.2.3, and the corresponding differential is

$$D_w h_{ad,\ell}(\boldsymbol{v}) = G_h(\boldsymbol{x}_\ell)\cdot \boldsymbol{v}_{x_\ell} + 2s_{ad,\ell} v_{s_{ad,\ell}}.$$

The derivatives of the minimum distance constraint function eq. (8.19) with respect to the coordinates can be readily computed, yielding the differential

$$D_w h_{md,\ell m}(\boldsymbol{v}) = -2(\boldsymbol{x}_\ell - \boldsymbol{x}_m)\cdot(\boldsymbol{v}_{x_\ell} - \boldsymbol{v}_{x_m}) + 2s_{md,\ell m} v_{s_{md,\ell m}}.$$

The computation of the adjoint of the differential, $(D_w \boldsymbol{g})'$, appearing in eq. (8.3), can be done directly using the definition of adjoint operator: $(\boldsymbol{p}, D_w\boldsymbol{g}(\boldsymbol{v})) = (\boldsymbol{v}, (D_w\boldsymbol{g})'(\boldsymbol{p}))$. We define $\boldsymbol{p} = [\boldsymbol{p}_e, \boldsymbol{p}_{sl}, \boldsymbol{p}_{ad}, \boldsymbol{p}_{md}]$, and hence the computation amounts to writing $\mathrm{Re}[\boldsymbol{p}^H D_w\boldsymbol{g}(\boldsymbol{v})]$, taking the hermitian inside the real part operator and collecting terms. As for $D_w\boldsymbol{g}$, we split the computation of the adjoint operator into block-rows, corresponding to the decision, state and slack variables.

$$\begin{aligned}
(D_w\boldsymbol{g})'_{x_\ell}(\boldsymbol{p}) = \sum_{q=1}^{N_f} \mathrm{Re}\Bigg\{ & \left[\sum_{\substack{m=1\\m\neq\ell}}^{N_b}\left(\hat{\boldsymbol{\gamma}}_m^H + \hat{\zeta}_m^* \boldsymbol{R}_m^H\right)\frac{\partial T^*_{m\ell}}{\partial x_\ell} B_\ell^H + \frac{H}{2}\frac{\partial \boldsymbol{a}_\ell^H}{\partial x_\ell} B_\ell^H\right]\boldsymbol{p}_{e_{\gamma,\ell}} \\
& + \left[\sum_{\substack{m=1\\m\neq\ell}}^{N_b}\left(\hat{\boldsymbol{\gamma}}_\ell^H + \hat{\zeta}_\ell^* \boldsymbol{R}_\ell^H\right)\frac{\partial T^*_{\ell m}}{\partial x_\ell} B_m^H\right]\boldsymbol{p}_{e_{\gamma,m}} + \frac{1}{W_\ell}\left[\sum_{\substack{m=1\\m\neq\ell}}^{N_b}\hat{\boldsymbol{\gamma}}_m^H \frac{\partial T^*_{m\ell}}{\partial x_\ell}\tilde{B}_\ell^H(\tilde{\boldsymbol{Y}}_\ell^D)^*\right. \\
& \left. + \sum_{\substack{m=1\\m\neq\ell}}^{N_b}\hat{\zeta}_m^*(\boldsymbol{Y}_\ell^D)^H\tilde{B}_\ell^*\frac{\partial T^H_{m\ell}}{\partial x_\ell}\boldsymbol{R}_m^*\right]p_{e_{\zeta,\ell}} + \frac{H}{2W_\ell}(\tilde{\boldsymbol{Y}}_\ell^D)^H\tilde{B}_\ell^*\frac{\partial \boldsymbol{a}_\ell^*}{\partial x_\ell}p_{e_{\zeta,\ell}} \\
& + \frac{1}{W_m}\left[\sum_{\substack{m=1\\m\neq\ell}}^{N_b}\hat{\boldsymbol{\gamma}}_\ell^H\frac{\partial T^*_{\ell m}}{\partial x_\ell}\tilde{B}_m^H(\tilde{\boldsymbol{Y}}_m^D)^* + \sum_{\substack{m=1\\m\neq\ell}}^{N_b}\hat{\zeta}_\ell^*(\boldsymbol{Y}_m^D)^H\tilde{B}_m^*\frac{\partial T^H_{\ell m}}{\partial x_\ell}\boldsymbol{R}_\ell^*\right]p_{e_{\zeta,m}}\Bigg\}_q \\
& + \frac{\partial h_{sl,\ell}}{\partial x_\ell}p_{sl,\ell} + G_h(\boldsymbol{x}_\ell)\cdot\hat{\boldsymbol{x}}\,p_{ad,\ell} - 2\sum_{\substack{m=1\\m\neq\ell}}^{N_b}(x_\ell - x_m)p_{md,\ell m},
\end{aligned}$$

where $\hat{\boldsymbol{x}}$ denotes the unit vector in the x direction, and where all the quantities inside curly brackets are related to the q-th frequency component, as indicated by

the subscript at the end. The same relation holds for $(D_u \boldsymbol{g})'_{y_\ell}$, replacing x with y. The component related to damping is

$$(D_w \boldsymbol{g})'_{c_\ell}(\boldsymbol{p}) = \sum_{q=1}^{N_f} \mathrm{Re}\left[-\frac{1}{W_\ell}(e_{\zeta,\ell} - \hat{\zeta}_\ell)^* \frac{\partial W_\ell^*}{\partial c_\ell} p_{e\zeta,\ell} \right]_q ,$$

and the one related to stiffness is analogous, with κ_ℓ in place of c_ℓ. The rows corresponding to state variables $\hat{\boldsymbol{\gamma}}$, $\hat{\boldsymbol{\zeta}}$ are

$$(D_w \boldsymbol{g})'_{\gamma}(\boldsymbol{p}) = \sum_{q=1}^{N_f} \left[M^H_{\gamma\gamma} \boldsymbol{p}_{e\gamma} + M^H_{\zeta\gamma} \boldsymbol{p}_{e\zeta} \right]_q$$

$$(D_w \boldsymbol{g})'_{\zeta}(\boldsymbol{p}) = \sum_{q=1}^{N_f} \left[M^H_{\gamma\zeta} \boldsymbol{p}_{e\gamma} + M^H_{\zeta\zeta} \boldsymbol{p}_{e\zeta} \right]_q + 2 \sum_{\ell=1}^{N_b} \sum_{q=1}^{N_f} (\hat{\zeta}_{q\ell} - \hat{\eta}_{q\ell}) p_{sl,\ell},$$

and finally the ones corresponding to slack variables are

$$(D_w \boldsymbol{g})'_{s_{sl}} = 2\boldsymbol{s}_{sl} \odot \boldsymbol{p}_{sl}, \quad (D_w \boldsymbol{g})'_{s_{ad}} = 2\boldsymbol{s}_{ad} \odot \boldsymbol{p}_{ad}, \quad (D_w \boldsymbol{g})'_{s_{md}} = 2\boldsymbol{s}_{md} \odot \boldsymbol{p}_{md}.$$

Some remarks are in order regarding the scaling described in section 8.1.2. Rows of J_g corresponding to inequality constraints are normalized with their 2-norm, while block-rows corresponding to the state problem are left unchanged for two reasons. The first is that the state problem is already fairly well conditioned [32, Sec. 4.3]; the second is that, as mentioned in section 8.2.4, the blocks of the state system are implemented as linear operators instead of matrices for computational efficiency, so that the rows of their representatives should be recovered by computing their action on all vectors of the canonical basis, an expensive step.

8.3 Numerical experiments

In this section, we present numerical experiments based on two admissible domains, represented in fig. 8.3. The first is a simple square, while the second is a square with a triangular cut. The latter represents an available sea area in which a floating wind turbine platform, whose typical shape is a triangle (we mention as an example the Windfloat project [144]), needs to be installed, thus reducing the space available for the wave energy park. The resulting domain is not convex.

To compare different possible strategies for the numerical solution of the optimization problem, four simulations were performed for each domain geometry, using the following settings:

S1: Explicit Euler, $\Delta t = 1$, $\tau_{CG} = 10^{-6}$;

S2: Explicit Euler, $\Delta t = 1.5$, $\tau_{CG} = 10^{-6}$;

S3: RK12, adaptive Δt: $\tau_{RK}^{rel} = 10^{-3}$, $\tau_{RK}^{abs} = 10^{-6}$, $\tau_{CG} = 10^{-6}$;

S4: RK12, adaptive tolerances for RK and CG.

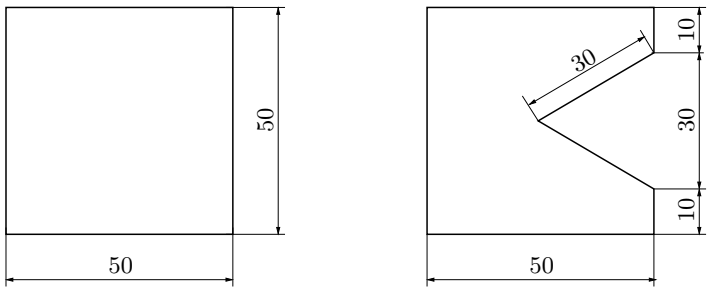

Figure 8.3: *Available sea area for the square (left) and cut square (right) test cases; all lengths in meters.*

	f_{end}	$\|g\|_{end}$	$\|\boldsymbol{\Psi}\|_{end}$	ncalls	tot Tcalls (s)
run1	-1.388	1.851×10^{-6}	0.0010	406	11 251
run2	-1.388	1.685×10^{-6}	0.0010	269	7673
run3	-1.388	2.611×10^{-6}	0.0010	252	7273
run4	-1.388	1.640×10^{-6}	0.0010	242	6162

Table 8.1: *Results for the square admissible domain.*

In all computations we consider devices of radius $R = 2$ m and draft $d = 0.5$ m, and a sea depth $D = 30$ m. The sea state is represented by a Pierson-Moskowitz wave spectrum [53] with $T_e = 8$ s, $H_s = 2.12$ m and waves directed along the positive x coordinate ($\beta = 0$). The spectrum is discretized with 30 harmonics. For the solution of the state problem, $N_n = 4$, $N_m = 25$ are chosen. The stopping tolerance is set to $\tau_\Psi = 10^{-3}$.

Numerical simulations have been performed on a laptop with a 4-core, 8-thread Intel Core i5-10210U CPU and 8 GB of RAM. The presented test cases require about 2 GB of RAM for execution. The code has been implemented in Python and has been made available for reproducibility of the results at `https://github.com/marcogambarini/floatcyl`.

The results of the test cases are reported in table 8.1 and table 8.2: we show the final values of cost, f_{end}, constraint vector norm, $\|\boldsymbol{g}\|_{end}$, and stopping indicator, $\|\boldsymbol{\Psi}\|_{end}$. Values of $\|\boldsymbol{\Psi}\|_{end}$ in red signify that the stopping criterion has not been met within the maximal fictitious time interval. We further report the total number of calls to the function computing $\boldsymbol{\Psi}$ and the total time required by such calls. For both cases, using the explicit Euler method (S1 and S2) leads to convergence. The Runge-Kutta method with adaptive tolerance (S4) also reaches convergence, requiring a significantly smaller computational time. The Runge-

	f_{end}	$\|g\|_{end}$	$\|\boldsymbol{\Psi}\|_{end}$	ncalls	tot Tcalls (s)
run1	-1.396	2.716×10^{-6}	0.0010	968	25 155
run2	-1.395	4.034×10^{-6}	0.0010	673	18 307
run3	-1.395	0.001	0.0038	1112	31 499
run4	-1.395	4.499×10^{-5}	0.0010	763	15 020

Table 8.2: *Results for the cut square test case.*

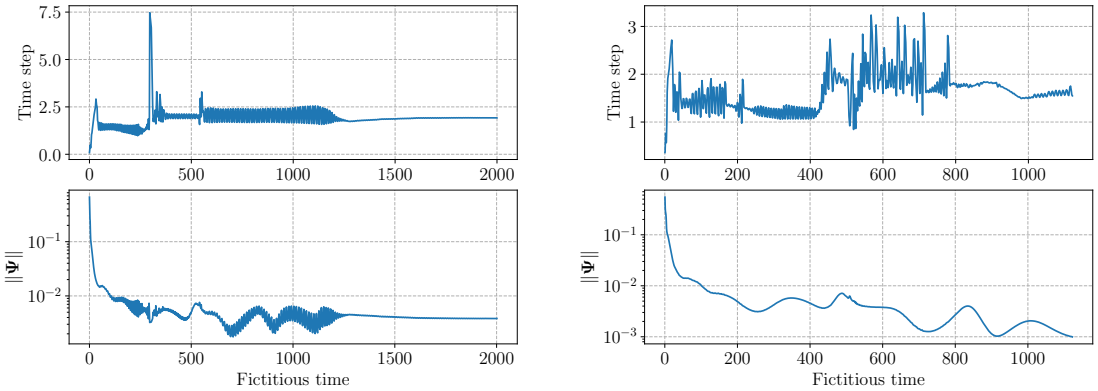

Figure 8.4: *Cut square geometry, history of adaptive time step and stopping indicator, settings S3 (left) and S4 (right).*

Kutta method without adaptive tolerances (S3), instead, is only able to fulfill the stopping criterion in the square case. Regarding the cost function, we observe that the result reached for the cut square geometry is more favorable than the one on the square. This may appear counterintuitive; for this reason, a test using the result on the cut square geometry as initial guess for an optimization on the whole square was performed. The resulting optimal solution has a negligible difference in terms of cost from the initial guess, suggesting that the solution obtained in the cut square case is also close to a local minimum over the entire square.

We now focus on the Runge-Kutta method applied to the cut square test case. fig. 8.4 shows the evolution of adaptive time step and stopping indicator. For both settings S3 and S4, the selected time step oscillates around 2 for most of the time, with more pronounced reductions for S4 in the first half of the simulation. The value of $\|\boldsymbol{\Psi}\|$ is not monotonically decreasing, nor is it expected to be. However, the adaptive tolerance criteria adopted in S4 enable converging to the prescribed stopping tolerance, while in the case of S3 the stopping indicator, after an oscillatory phase, decreases very slowly and seems to stagnate. We further show, in fig. 8.5, that using the adaptive tolerance strategy (settings S4) significantly reduces the number of iterations of the conjugate gradient method compared to using fixed tolerances (settings S3). The time required for computing $\boldsymbol{\Psi}$ at each time step is also reduced, as expected.

The results of optimization in terms of positions are reported in fig. 8.6, while results for controls are shown in fig. 8.7 for the square case, and in fig. 8.8 for the cut square test case. The results show that the treatment of the domain constraint is effective even when the initial guess is not feasible. Moreover, upwave devices are assigned greater values of both stiffness and damping than downwave devices. A physical interpretation of this fact is that upwave devices should be tuned to higher frequencies than downwave devices. The same qualitative result was obtained in [61].

From the point of view of robustness with respect to changes in the constraint parameters, we show in fig. 8.9 the results obtained by varying the minimum distance between devices, d_{min}. The initial layouts are compliant with the constraint, so that they are all different. Correspondingly, different results in terms of layout

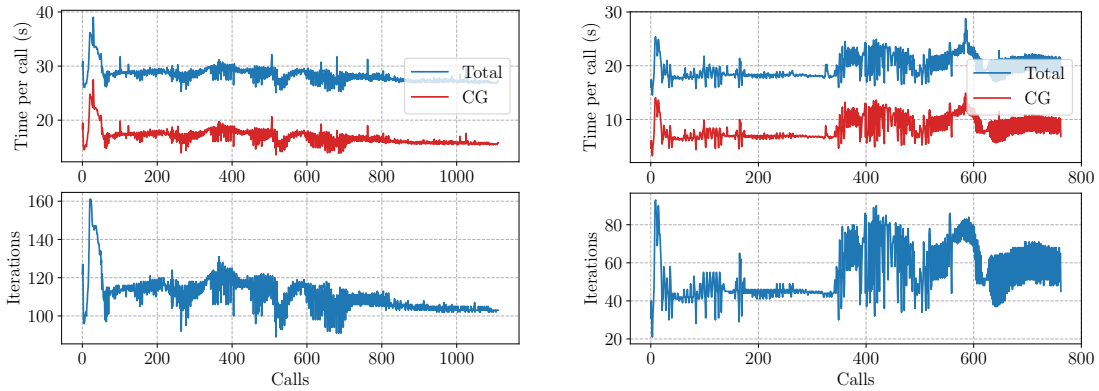

Figure 8.5: *Cut square geometry, history of walltime per call and CG iterations, settings S3 (left) and S4 (right).*

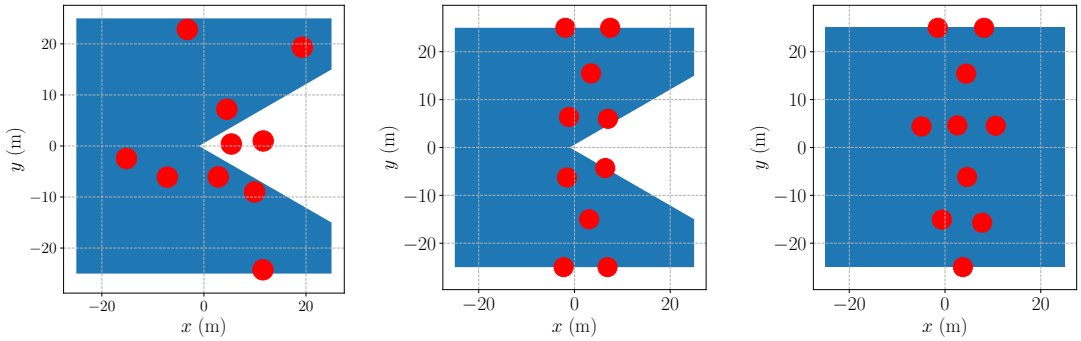

Figure 8.6: *Initial layout guess (left), final layout for the cut square geometry (center), and for the square geometry (right), with settings S4.*

and controls are obtained; however, as the figure shows, the variation in optimal power is very small. In terms of computational cost, the number of calls to the computation of $\boldsymbol{\Psi}$ increases as the constraint is tightened, and the computational time grows approximately proportionally, but the proposed method is still able to reach convergence up to the required tolerance.

8.4 Discussion and developments

In this work, a gradient-flow framework with a suitable time-stepping scheme and automatic tolerance adaptation for the solution of optimization problems with rather general constraints has been presented. Such a framework has then been applied to the problem of preliminary optimal design of a wave energy park.

From the point of view of numerical algorithms, the presented framework could be used as the local optimization step in a hybrid local-global method (see e.g. [47, 141, 172] and the application to wave energy [125]). Moreover, we have considered the simplest adaptive Runge-Kutta scheme. Other promising choices are multistep methods, of which Nesterov's optimization algorithm can be considered a particular case [153], and Runge-Kutta-Chebyshev methods [48], which introduce additional stages to improve stability and thus allow the use of very

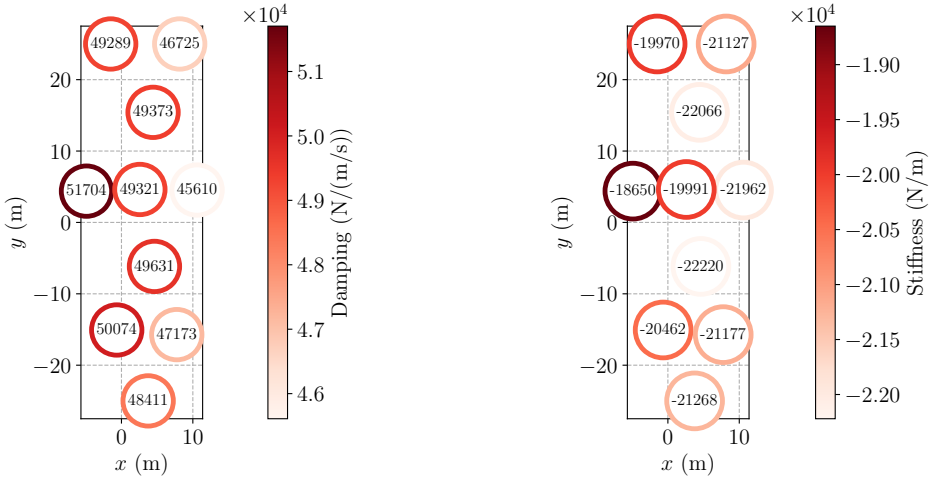

Figure 8.7: *Square geometry, settings S4, optimal damping (left) and stiffness (right).*

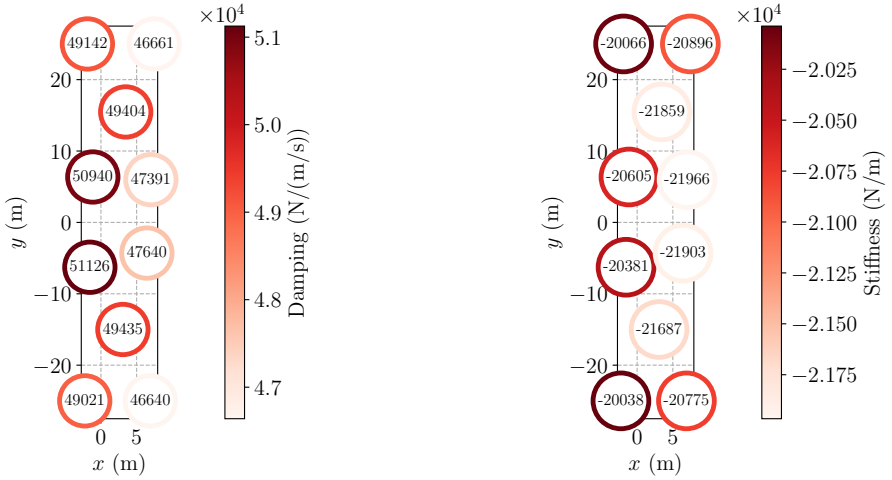

Figure 8.8: *Cut square geometry, settings S4, optimal damping (left) and stiffness (right).*

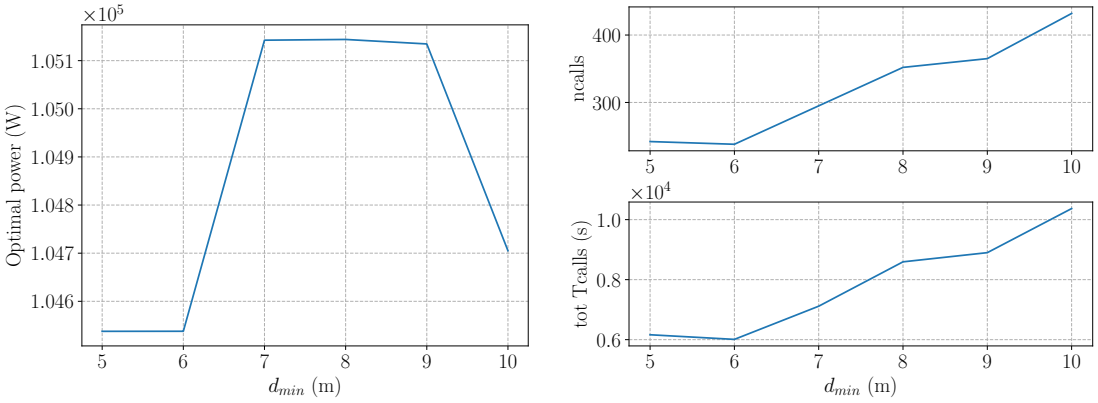

Figure 8.9: *Square geometry, 10 devices, variable value of d_{min}.*

large time steps.

Concerning the application, the main limitation of this work is the restriction to cylindrical devices, which allows the analytic computation of derivatives. The presented framework is based on interaction theory and may be extended to more general shapes through the strategy introduced in [114]. More advanced control strategies could additionally be taken into account.

Chapter 9

Conclusions and developments

This thesis introduced mathematical models and numerical methods for the simulation and optimization of parks of wave energy converters.

In Part I, we reviewed models (Chap. 2) and methods (Chap. 3) for the description of free surface wave-body interaction. Then, in Chapter 4, we proposed a novel preconditioner for the solution of the linearized hydrodynamic problem using the boundary element method [34]. The resulting algorithm is effective in terms of computational cost, and it is available for use, having been added to the Capytaine library [7]. While the linear model is adequate for describing the behavior of WEC devices in design conditions, off-design and survivability analyses involve large wave amplitudes and body motions and thus require the adoption of nonlinear models. To this end, we are currently working on a solver for the nonlinear potential problem, building on the work presented in [123]. A critical part of the solution process, which makes it significantly different from the linearized case, is the need to take into account the motion of the free surface. In order to avoid mesh degeneracies in the case of large waves, and thus large motion of the free surface nodes, a mesh smoothing technique based on the solution of a mixed-dimensional Laplace-Beltrami problem is being developed.[1]

In Part II, we treated WEC array control and layout optimization. We considered robust control optimization in Chapter 6 [61], then layout optimization in Chapter 7 [59], and finally the combined problem of control co-design in Chapter 8 [60]. An application of the robust control methods of Chap. 6 to control co-design has been explored in the thesis [167]. These contributions are based on a frequency-domain description of the linear hydrodynamic problem, and produce constant control coefficients, which may be implemented on a real controller by using, for example, look-up tables. A different approach, based on a time-domain description, could be adopted, as described in the review provided in Chap. 5: extending the methods presented in this thesis to such case could be the starting point for future work. Moreover, the optimization methods introduced here are gradient-based, thus leading to convergence to local minima. It would be possible to use them as building blocks for combined local-global optimization algorithms, possibly after a landscape analysis on the cost function, using techniques such as the ones of [120].

[1] This work is being done jointly with prof. Andrea Mola of Scuola IMT Alti Studi Lucca.

Appendix A

Power matrices and related results

This section contains the main results of the simulation and control optimization of a single device, both in the original configuration shown in Fig. 7.1 and in the constant section configuration. For the latter, a comparison with the linearized model is included. We refer to Sec. 7.2.2 for the discussion of the results.

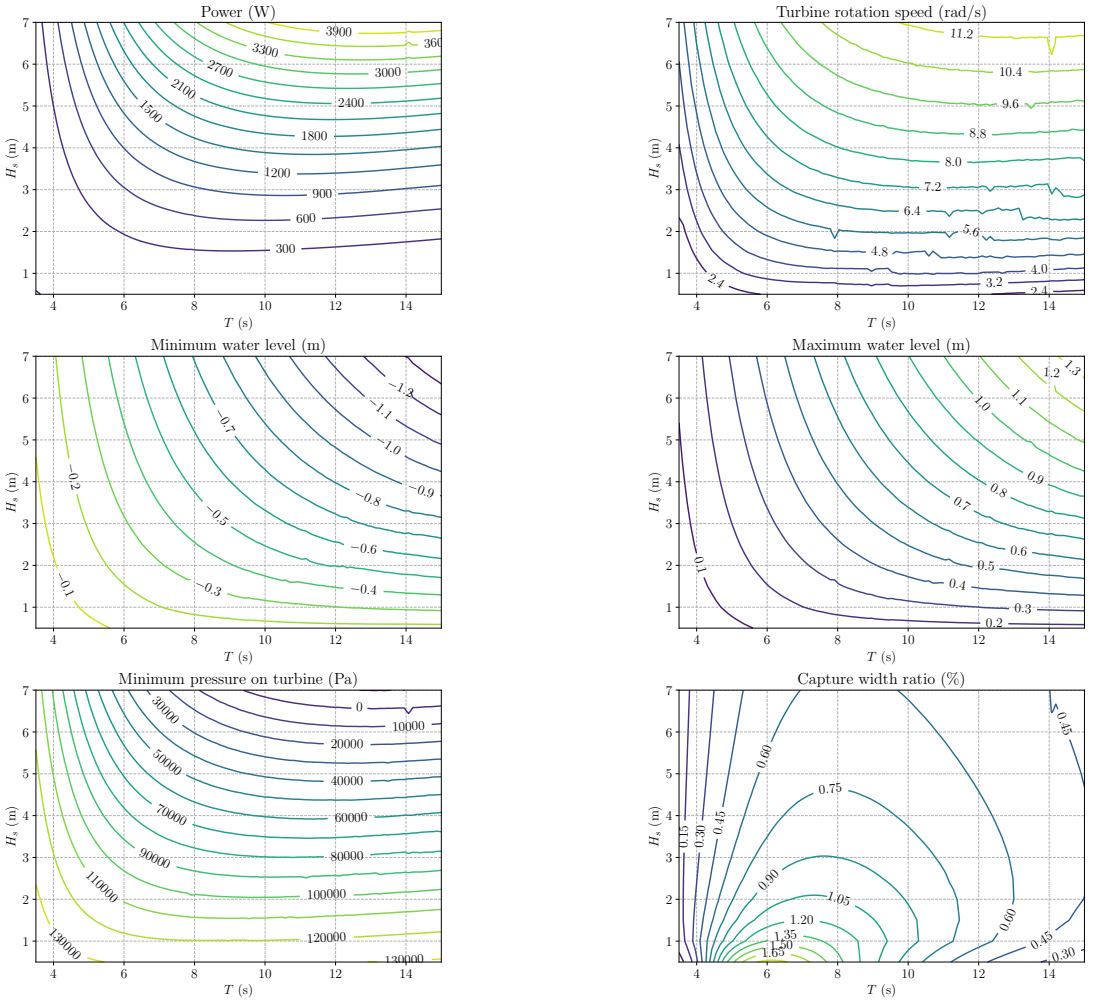

Figure A.1: *Isolated device results, original device, 5-blade turbine.*

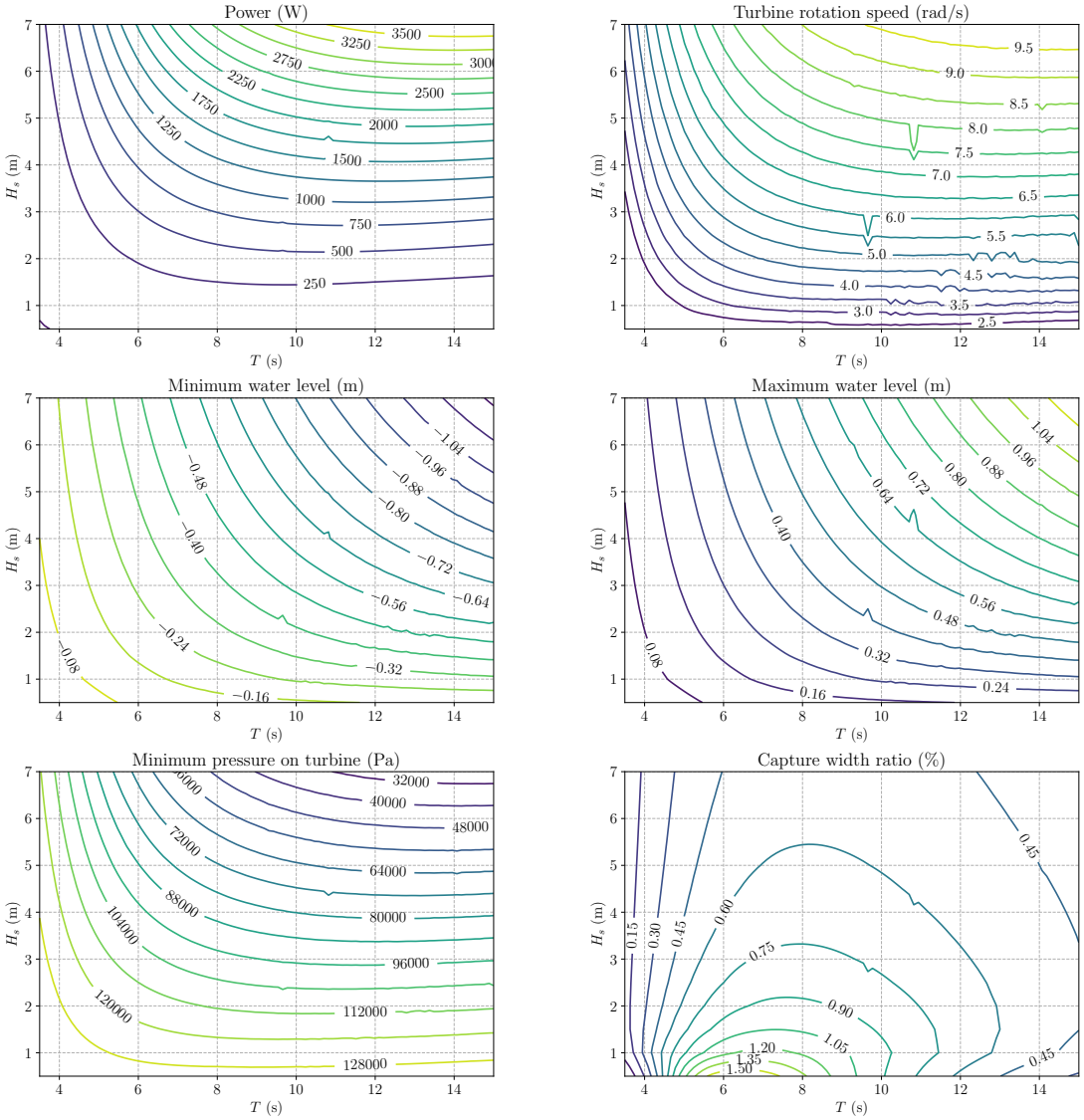

Figure A.2: *Isolated device results, original device, 7-blade turbine.*

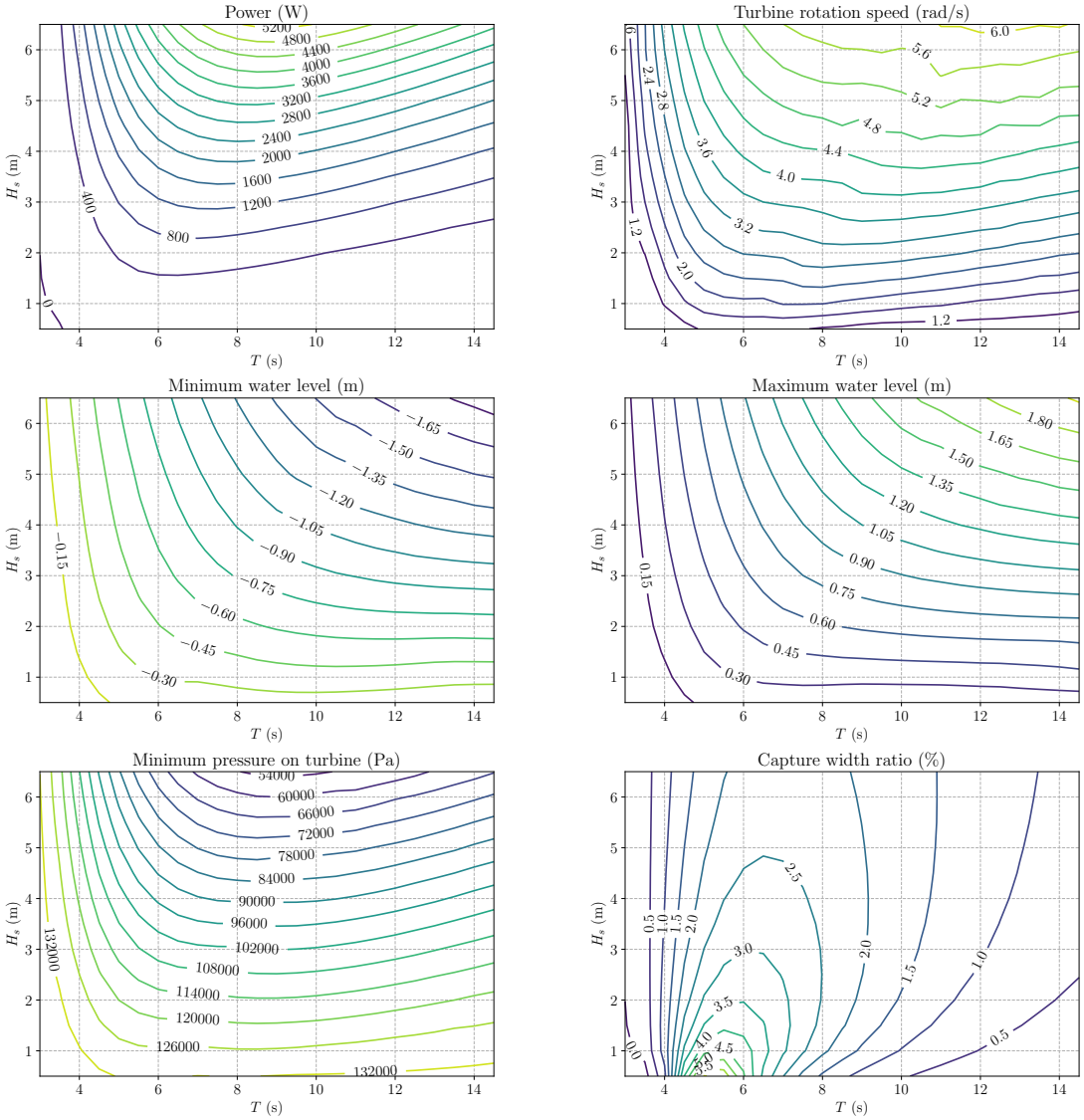

Figure A.3: *Isolated device results, constant duct section, 7-blade turbine.*

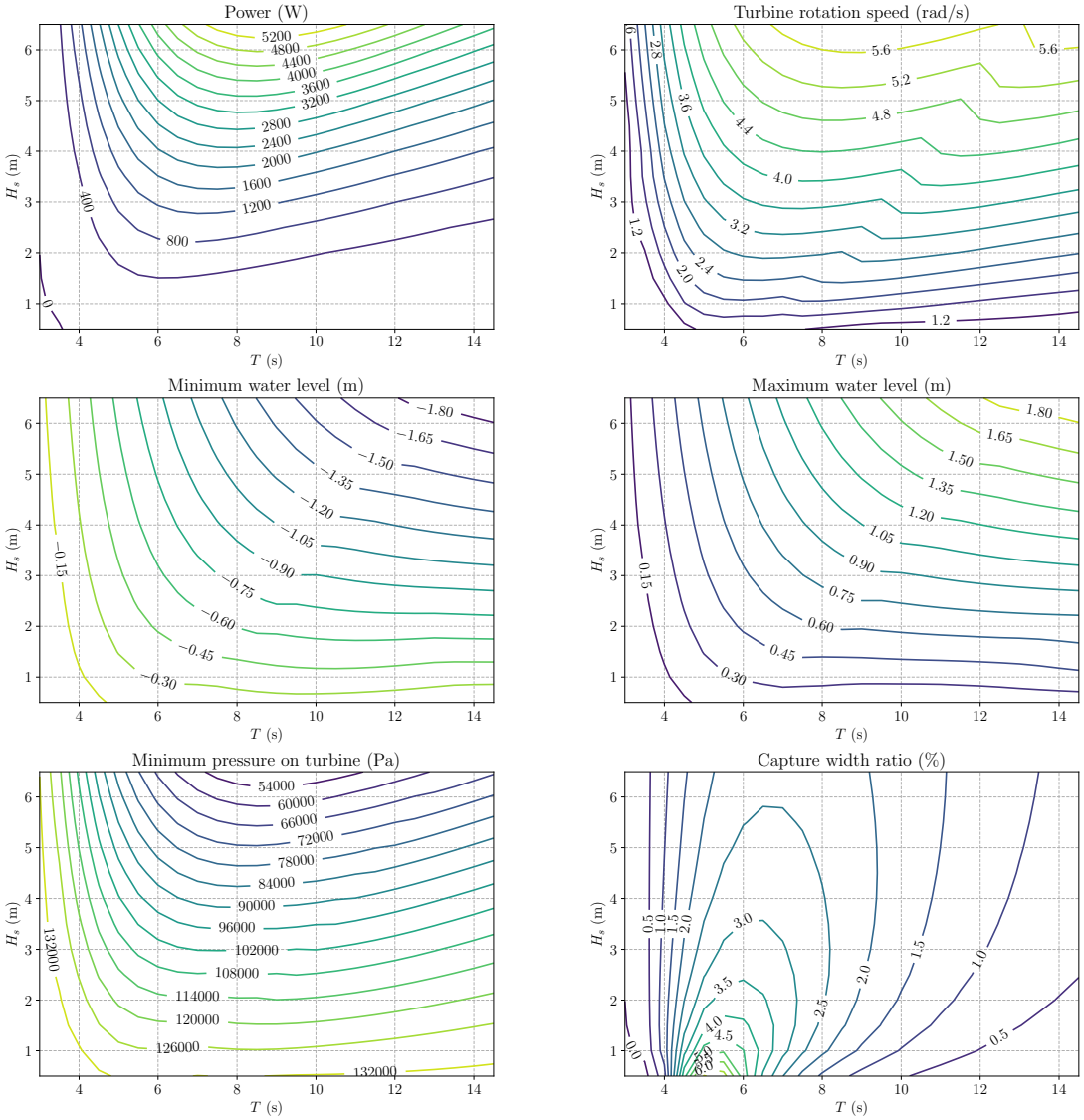

Figure A.4: *Isolated device results, constant duct section, 7-blade turbine; linear model.*

Appendix B

Results about the domain constraint

In this section, we recall and derive some properties that justify the treatment of the domain constraint proposed in section 8.2.3. First, we prove that the classical solution of a suitable Poisson problem has no local minima.

Theorem B.0.1. *Let $h \in C^2(\Omega)$ satisfy*

$$-\Delta h = \sigma \quad \text{in } \Omega,$$

with $\sigma \in C(\Omega)$, $\sigma > \sigma_{min} > 0$. Then, for all $\boldsymbol{x} \in \Omega$ and for all $B_r(\boldsymbol{x})$ such that $\overline{B_r(\boldsymbol{x})} \subset \Omega$,

$$h(\boldsymbol{x}) > \frac{1}{|\partial B_r(\boldsymbol{x})|} \int_{\partial B_r(\boldsymbol{x})} h(\boldsymbol{y}') d\boldsymbol{y}' + \frac{r^2}{2d} \sigma_{min}. \tag{B.1}$$

In particular, there can be no local minima of h in Ω.

Proof. The proof is similar to the one of [148, Th. 3.2, Chap. 3]. Define a function

$$g(r; \boldsymbol{x}) := \frac{1}{|\partial B_r(\boldsymbol{x})|} \int_{\partial B_r(\boldsymbol{x})} h(\boldsymbol{y}') d\boldsymbol{y}' = \frac{1}{|\partial B_1(\boldsymbol{0})|} \int_{\partial B_1(\boldsymbol{0})} h(\boldsymbol{x} + r\boldsymbol{y}) d\boldsymbol{y}.$$

Its derivative with respect to r is

$$\frac{\partial g}{\partial r}(r; \boldsymbol{x}) = \frac{1}{|\partial B_1(\boldsymbol{0})|} \int_{\partial B_1(\boldsymbol{0})} \boldsymbol{y} \cdot \nabla h(\boldsymbol{x} + r\boldsymbol{y}) d\boldsymbol{y}.$$

Since the domain of integration is the surface of the unit ball, $\boldsymbol{y}$ is the unit normal vector and $\boldsymbol{y} \cdot \nabla h = \partial_n h$. The divergence theorem can then be applied, where the divergence must be computed with respect to the integration variable $\boldsymbol{y}$, that is,

$$\frac{\partial}{\partial y_i} \left(\frac{\partial h}{\partial y_i}(x_i + r y_i) \right) = r \Delta h.$$

This implies

$$\begin{aligned} \frac{\partial g}{\partial r}(r; \boldsymbol{x}) &= \frac{r}{|\partial B_1(\boldsymbol{0})|} \int_{B_1(\boldsymbol{0})} \Delta h(\boldsymbol{x} + r\boldsymbol{y}) d\boldsymbol{y} \\ &= -\frac{r}{|\partial B_1(\boldsymbol{0})|} \int_{B_1(\boldsymbol{0})} \sigma(\boldsymbol{x} + r\boldsymbol{y}) d\boldsymbol{y} < -\frac{r |B_1(\boldsymbol{0})| \sigma_{min}}{|\partial B_1(\boldsymbol{0})|} = \frac{r \sigma_{min}}{d}, \end{aligned}$$

where d is the number of space dimensions. Using the result above and $g(0, \boldsymbol{x}) = h(\boldsymbol{x})$, eq. (B.1) is obtained by integration.

Now suppose by contradiction that $\boldsymbol{x}$ is a local minimum point of h. Then $\exists r : h(\boldsymbol{y}) \geq h(\boldsymbol{x})$ for all $\boldsymbol{y} \in \partial B_r(\boldsymbol{x})$. But since $\sigma_{min} > 0$, this contradicts eq. (B.1). □

With a suitable discretization, the numerical solution of the problem preserves this property.

Theorem B.0.2 (Properties of the stiffness matrix [18])**.** *Let $\Omega \subset \mathbb{R}^2$ and consider a finite element discretization of the Poisson problem with $\mathbb{P}_1$ elements. If a Delaunay triangulation of the domain is employed, then the stiffness matrix A satisfies the conditions*

$$\sum_j a_{ij} = 0, \quad i = 1, \ldots, N, \tag{B.2}$$

$$a_{ij} \leq 0, \quad i = 1, \ldots, N, \ j \neq i. \tag{B.3}$$

Corollary B.0.1. *The numerical solution of the Poisson equation has no local minima under the above assumptions and with homogeneous boundary conditions.*

Proof. The finite element discretization of the Poisson problem leads to the algebraic system

$$a_{ii} h_i + \sum_{j \neq i, j \in \mathcal{N}(i)} a_{ij} h_j = b_j, \quad j = 1, \ldots, N,$$

where $\mathcal{N}(i)$ denotes the set of neighbours of node i and the right hand side is

$$b_j = \int_\Omega \sigma v_j d\boldsymbol{x} + \int_{\Gamma_N \subset \partial\Omega} g_N v_j d\boldsymbol{x} > 0 \quad \forall j,$$

v_j being the test function related to the j-th node. The inequality is due to the fact that $\mathbb{P}_1$ test functions are positive on their support, and that homogeneous boundary conditions are assumed. Hence,

$$a_{ii} h_i > - \sum_{j \neq i, j \in \mathcal{N}(i)} a_{ij} h_j = \sum_{j \neq i, j \in \mathcal{N}(i)} |a_{ij}| h_j.$$

theorem B.0.2 guarantees that $a_{ii} = \sum_{j \neq i} |a_{ij}|$. As a consequence, h_i is greater than the weighted average of the solution on the neighbouring nodes, and thus it is not possible that $h_j > h_i$ for all $j \in \mathcal{N}(i)$. Since values of h in all points of the domain other than nodes are obtained from linear interpolation of the nodal values, there can be no local minima. □

Remark. *In this work, we have used the Delaunay triangulation algorithm implemented in* `gmsh`[1]*.*

Our final result says that the classical and weak solution may have zero gradient only at most on a set of zero measure.

[1] `https://gmsh.info/doc/texinfo/gmsh.html#Choosing-the-right-unstructured-algorithm`

Proposition B.0.1. *The gradients of both the classical solution h and the weak solution h_w of the Poisson problem*

$$-\Delta h = \sigma \text{ in } \Omega, \quad h = 0 \text{ on } \Gamma_D, \quad \partial_n h = 0 \text{ on } \Gamma_N,$$

with $\Gamma_D \cup \Gamma_N = \partial\Omega$, $\Gamma_D \neq \emptyset$, can be zero at most on a set of zero measure.

Proof. For the classical solution, suppose that $\nabla h = 0$ on a set $S \subset \Omega$. Then

$$0 = \int_S -\nabla \cdot (\nabla h) d\boldsymbol{x} = \int_S \sigma d\boldsymbol{x} > \sigma_{min}|S|,$$

implying $|S| = 0$ since $\sigma_{min} > 0$. The weak solution $h_w \in H^1_{0,\Gamma_D}(\Omega)$ satisfies

$$\int_\Omega \nabla h_w \cdot \nabla v d\boldsymbol{x} = \int_\Omega \sigma v d\boldsymbol{x} \quad \forall v \in H^1_{0,\Gamma_D}(\Omega).$$

Consider a test function $\tilde{v} \in C^\infty(\overline{\Omega})$, with $\text{supp}\tilde{v} = S \subset \Omega$, $\tilde{v} > 0$ inside S. Suppose by contradiction that $\nabla u = 0$ in S and that $|S| > 0$. Then

$$\begin{aligned} 0 &= \int_\Omega \nabla h_w \cdot \nabla \tilde{v} d\boldsymbol{x} = \int_S \nabla h_w \cdot \nabla \tilde{v} d\boldsymbol{x} = \int_S \nabla h_w \cdot \nabla \tilde{v} d\boldsymbol{x} \\ &= \int_S \sigma \tilde{v} d\boldsymbol{x} > \sigma_{min} \int_S \tilde{v} d\boldsymbol{x} > 0, \end{aligned}$$

which is a contradiction. □

Even though this property has no straightforward discrete counterpart, it indicates that it is unlikely that rows of the Jacobian matrix corresponding to domain constraints become zero.

Bibliography

[1] 2030 ocean energy vision: Industry analysis of future deployments, costs and supply chains. Technical report, Ocean Energy Europe, 2020.

[2] An EU Strategy to harness the potential of offshore renewable energy for a climate neutral future. Technical report, European Commission, 2020.

[3] Progress of clean energy competitiveness (SWD (2020) 953 final). Technical report, European Commission, 2020.

[4] Wind energy in Europe 2021. Statistics and the outlook for 2022-2026. Technical report, Wind Europe, 2022.

[5] G. Agate, M. Gambarini, S. Maran, and G. Quinteri. Ottimizzazione dell'installazione offshore di dispositivi di generazione di energia elettrica da moto ondoso (WaveSAX). Technical Report 23013058, RSE S.p.A., 2023. URL: https://www.rse-web.it/rapporti/ottimizzazione-dellinstallazione-offshore-di-dispositivi-di-generazione-di-energia-elettrica-da-moto-ondoso-wavesax/.

[6] M. Ancellin and F. Dias. Using the floating body symmetries to speed up the numerical computation of hydrodynamics coefficients with Nemoh. volume 9: Offshore Geotechnics; Honoring Symposium for Professor Bernard Molin on Marine and Offshore Hydrodynamics of *International Conference on Offshore Mechanics and Arctic Engineering*, 06 2018. doi:10.1115/OMAE2018-77924.

[7] M. Ancellin and F. Dias. Capytaine: a Python-based linear potential flow solver. *Journal of Open Source Software*, 4(36):1341, apr 2019. doi:10.21105/joss.01341.

[8] M. Ancellin, P. Marchand, and F. Dias. Towards high-performance linear potential flow BEM solver with low-rank compressions. *Energies*, 17(2):372, Jan. 2024. doi:10.3390/en17020372.

[9] E. Anderlini, D. I. M. Forehand, P. Stansell, Q. Xiao, and M. Abusara. Control of a point absorber using reinforcement learning. *IEEE Transactions on Sustainable Energy*, 7(4):1681–1690, Oct. 2016. doi:10.1109/tste.2016.2568754.

[10] J. D. Anderson. *Fundamentals of Aerodynamics*. McGraw-Hill, 1991.

[11] G. G. Arfken and H. J. Weber. *Mathematical Methods for Physicists*. Elsevier Academic Press, 2005.

[12] G. A. Athanassoulis, P. B. Vranas, and T. H. Soukissian. A new model for long-term stochastic analysis and prediction—part I: Theoretical background. *Journal of Ship Research*, 36(01):1–16, Mar. 1992. doi:10.5957/jsr.1992.36.1.1.

[13] A. Babarit. On the park effect in arrays of oscillating wave energy converters. *Renewable Energy*, 58:68–78, 2013. doi:https://doi.org/10.1016/j.renene.2013.03.008.

[14] A. Babarit. A database of capture width ratio of wave energy converters. *Renewable Energy*, 80:610–628, 2015. doi:https://doi.org/10.1016/j.renene.2015.02.049.

[15] A. Babarit, J. Hals, M. Muliawan, A. Kurniawan, T. Moan, and J. Krokstad. Numerical benchmarking study of a selection of wave energy converters. *Renewable Energy*, 41:44–63, may 2012. doi:10.1016/j.renene.2011.10.002.

[16] G. Bacelli, P. Balitsky, and J. V. Ringwood. Coordinated control of arrays of wave energy devices—benefits over independent control. *IEEE Transactions on Sustainable Energy*, 4(4):1091–1099, oct 2013. doi:10.1109/tste.2013.2267961.

[17] G. D. Backer, M. Vantorre, C. Beels, J. D. Rouck, and P. Frigaard. Power absorption by closely spaced point absorbers in constrained conditions. *IET Renewable Power Generation*, 4(6):579, 2010. doi:10.1049/iet-rpg.2009.0188.

[18] G. R. Barrenechea, V. John, and P. Knobloch. Finite element methods respecting the discrete maximum principle for convection-diffusion equations. *SIAM Review*, 66(1):3–88, Feb. 2024. doi:10.1137/22m1488934.

[19] M. Bebendorf. *Hierarchical Matrices*. Lecture Notes in Computational Science and Engineering. Springer Berlin, Heidelberg, 2008. doi:https://doi.org/10.1007/978-3-540-77147-0.

[20] D. P. Bertsekas. *Nonlinear Programming*. Athena Scientific, 1999.

[21] R. Bollapragada, R. Byrd, and J. Nocedal. Adaptive sampling strategies for stochastic optimization, 2017. doi:10.48550/ARXIV.1710.11258.

[22] S. Bonamano, M. A. Peviani, G. Agate, C. G. Burgio, G. Fersini, and M. Marcelli. The evaluation of WaveSAX power generation to support port energy self-sufficiency. *Journal of Marine Science and Engineering*, 11(11):2097, Nov. 2023. doi:10.3390/jmse11112097.

[23] A. Boukhanovsky and C. G. Soares. Modelling of multipeaked directional wave spectra. *Applied Ocean Research*, 31(2):132–141, apr 2009. doi:10.1016/j.apor.2009.06.001.

[24] S. Bozzi, G. Besio, and G. Passoni. Wave power technologies for the Mediterranean offshore: scaling and performance analysis. *Coastal Engineering*, 136:130–146, 2018. doi:10.1016/j.coastaleng.2018.03.001.

[25] C. A. Brebbia, J. C. F. Telles, and L. C. Wrobel. *Boundary Element Techniques*. Springer Berlin Heidelberg, 1984. doi:10.1007/978-3-642-48860-3.

[26] H. Brezis. *Functional Analysis, Sobolev Spaces and Partial Differential Equations*. Springer New York, 2011. doi:10.1007/978-0-387-70914-7.

[27] D. A. Brown and S. Nadarajah. Effect of inexact adjoint solutions on the discrete-adjoint approach to gradient-based optimization. *Optimization and Engineering*, 23(3):1643–1676, Sept. 2021. doi:10.1007/s11081-021-09681-5.

[28] R. H. Byrd, F. E. Curtis, and J. Nocedal. An inexact SQP method for equality constrained optimization. *SIAM Journal on Optimization*, 19(1):351–369, Jan. 2008. doi:10.1137/060674004.

[29] F. Cao, M. Yu, M. Han, B. Liu, Z. Wei, J. Jiang, H. Tian, H. Shi, and Y. Li. WECs microarray effect on the coupled dynamic response and power performance of a floating combined wind and wave energy system. *Renewable Energy*, 219:119476, Dec. 2023. doi:10.1016/j.renene.2023.119476.

[30] S. K. Chakrabarti. *Hydrodynamics of Offshore Structures*. Computational Mechanics Publications. Springer-Verlag, 1987.

[31] B. Child and V. Venugopal. Optimal configurations of wave energy device arrays. *Ocean Engineering*, 37(16):1402–1417, nov 2010. doi:10.1016/j.oceaneng.2010.06.010.

[32] B. F. M. Child. *On the configuration of arrays of floating wave energy converters*. PhD thesis, The University of Edinburgh, 2011.

[33] G. Ciaramella et al. Methods of Reflections: relations with Schwarz methods and classical stationary iterations, scalability and preconditioning. *SMAI J. Comput. Math*, 5:161–193, 2019. URL: https://smai-jcm.centre-mersenne.org/articles/10.5802/smai-jcm.46/, doi:10.5802/smai-jcm.46.

[34] G. Ciaramella, M. Gambarini, and E. Miglio. A preconditioner for free-surface hydrodynamics BEM. In *Domain Decomposition Methods in Science and Engineering XXVII*, pages 125–132. Springer Nature Switzerland, 2024. doi:10.1007/978-3-031-50769-4_14.

[35] G. Ciaramella and M. J. Gander. *Iterative Methods and Preconditioners for Systems of Linear Equations*. Society for Industrial and Applied Mathematics, Jan. 2022. doi:10.1137/1.9781611976908.

[36] V. Comincioli. *Metodi Numerici e Statistici per le Scienze Applicate*. Università degli Studi di Pavia, 2004.

[37] R. Curran and L. M. C. Gato. The energy conversion performance of several types of Wells turbine designs. *Proceedings of the Institution of Mechanical Engineers, Part A: Journal of Power and Energy*, 211(2):133–145, mar 1997. doi:10.1243/0957650971537051.

[38] B. Czech and P. Bauer. Wave energy converter concepts: Design challenges and classification. *IEEE Industrial Electronics Magazine*, 6(2):4–16, June 2012. doi:10.1109/mie.2012.2193290.

[39] G. De Backer. *Hydrodynamic Design Optimization of Wave Energy Converters Consisting of Heaving Point Absorbers*. PhD thesis, Ghent University. Faculty of Engineering, 2009.

[40] R. G. Dean. Relative validities of water wave theories. *Journal of the Waterways, Harbors and Coastal Engineering Division*, 96(1):105–119, 1970. doi:10.1061/AWHCAR.0000003.

[41] G. Delhommeau. *Les problemes de diffraction-radiation et de resistance de vagues: etude theorique et resolution numerique par le methode des singularites*. PhD thesis, Ecole Nationale Supérieure de Mécanique de Nantes, 1987.

[42] G. Delhommeau. Amélioration des performances des codes de calcul de diffraction-radiation au premier ordre. In *2émes Journées de l'Hydrodynamique*, 1989.

[43] V. Do, H. McBrien, N. M. Flores, A. J. Northrop, J. Schlegelmilch, M. V. Kiang, and J. A. Casey. Spatiotemporal distribution of power outages with climate events and social vulnerability in the USA. *Nature Communications*, 14(1), Apr. 2023. doi:10.1038/s41467-023-38084-6.

[44] M. Drela. XFOIL: An analysis and design system for low Reynolds number airfoils. In *Lecture Notes in Engineering*, pages 1–12. Springer Berlin Heidelberg, 1989. doi:10.1007/978-3-642-84010-4_1.

[45] D. Driggs, J. Liang, and C.-B. Schönlieb. On biased stochastic gradient estimation. *J. Mach. Learn. Res.*, 23(1), jan 2022.

[46] R. Durrett. *Probability: Theory and Examples*. Cambridge Series in Statistical and Probabilistic Mathematics. Cambridge University Press, 5 edition, 2019.

[47] G. D'Angelo and F. Palmieri. GGA: A modified genetic algorithm with gradient-based local search for solving constrained optimization problems. *Information Sciences*, 547:136–162, 2021. doi:https://doi.org/10.1016/j.ins.2020.08.040.

[48] A. Eftekhari, B. Vandereycken, G. Vilmart, and K. C. Zygalakis. Explicit stabilised gradient descent for faster strongly convex optimisation. *BIT Numerical Mathematics*, 61(1):119–139, July 2020. doi:10.1007/s10543-020-00819-y.

[49] M. Eriksson, R. Waters, O. Svensson, J. Isberg, and M. Leijon. Wave power absorption: Experiments in open sea and simulation. *Journal of Applied Physics*, 102(8):084910, oct 2007. doi:10.1063/1.2801002.

[50] N. Faedo, S. Olaya, and J. V. Ringwood. Optimal control, MPC and MPC-like algorithms for wave energy systems: An overview. *IFAC Journal of Systems and Control*, 1:37–56, sep 2017. doi:10.1016/j.ifacsc.2017.07.001.

[51] A. Falcão. *Comprehensive Renewable Energy*, volume 8, chapter Historical Aspects of Wave Energy Conversion, pages 7–9. Oxford: Elsevier, 2012.

[52] J. Falnes. A review of wave-energy extraction. *Marine Structures*, 20(4):185–201, Oct. 2007. doi:10.1016/j.marstruc.2007.09.001.

[53] J. Falnes and A. Kurniawan. *Ocean Waves and Oscillating Systems: Linear Interactions Including Wave-Energy Extraction*. Cambridge University Press, 2 edition, 2020. doi:10.1017/9781108674812.010.

[54] F. Feppon, G. Allaire, and C. Dapogny. Null space gradient flows for constrained optimization with applications to shape optimization. *ESAIM: Control, Optimisation and Calculus of Variations*, 26:90, 2020. doi:10.1051/cocv/2020015.

[55] L. Formaggia, F. Saleri, and A. Veneziani. *Solving Numerical PDEs: Problems, Applications, Exercises*. Springer Milan, 2012. doi:10.1007/978-88-470-2412-0.

[56] J.-P. Franc and J.-M. Michel. *Fundamentals of Cavitation*. Springer Dordrecht, 2005. doi:10.1007/1-4020-2233-6.

[57] G. A. Gabriele and K. M. Ragsdell. The generalized reduced gradient method: A reliable tool for optimal design. *Journal of Engineering for Industry*, 99(2):394–400, May 1977. doi:10.1115/1.3439249.

[58] J. Gallizioli. Optimization of WEC arrays: A new approach for the combined optimization of positions and damping coefficients. Master's thesis, Politecnico di Milano, 2022.

[59] M. Gambarini, G. Agate, G. Ciaramella, E. Miglio, and S. Maran. Modeling and optimization for arrays of water turbine OWC devices. *Ocean Engineering*, 312:119132, 2024. doi:https://doi.org/10.1016/j.oceaneng.2024.119132.

[60] M. Gambarini, G. Ciaramella, and E. Miglio. A gradient flow approach for combined layout-control design of wave energy parks. 2024. Submitted; arXiv preprint available. doi:10.48550/ARXIV.2409.10200.

[61] M. Gambarini, G. Ciaramella, E. Miglio, and T. Vanzan. Robust optimization of control parameters for WEC arrays using stochastic methods. *Journal of Computational Physics*, 493:112478, nov 2023. doi:10.1016/j.jcp.2023.112478.

[62] M. J. Gander. On the origins of linear and non-linear preconditioning. In *Lecture Notes in Computational Science and Engineering*, pages 153–161. Springer International Publishing, 2017. doi:10.1007/978-3-319-52389-7_14.

[63] P. B. Garcia-Rosa, G. Bacelli, and J. V. Ringwood. Control-informed optimal array layout for wave farms. *IEEE Transactions on Sustainable Energy*, 6(2):575–582, apr 2015. doi:10.1109/tste.2015.2394750.

[64] C. J. Garrison. The consistent second-order theory of wave/structure interaction. Technical report, Naval Postgraduate School, Monterey, California, 1979.

[65] M. Giassi, V. Castellucci, and M. Göteman. Economical layout optimization of wave energy parks clustered in electrical subsystems. *Applied Ocean Research*, 101:102274, 2020. URL: https://www.sciencedirect.com/science/article/pii/S0141118720300869, doi:https://doi.org/10.1016/j.apor.2020.102274.

[66] G. Giorgi and J. Ringwood. Relevance of pressure field accuracy for nonlinear Froude-Krylov force calculations for wave energy devices. *Journal of Ocean Engineering and Marine Energy*, 02 2018. doi:10.1007/s40722-017-0107-5.

[67] N. Giuliani, A. Mola, and L. Heltai. pi-BEM: A flexible parallel implementation for adaptive, geometry aware, and high order boundary element methods. *Advances in Engineering Software*, 121:39–58, July 2018. doi:10.1016/j.advengsoft.2018.03.008.

[68] Y. Goda. A comparative review on the functional forms of directional wave spectrum. *Coastal Engineering Journal*, 41(1):1–20, mar 1999. doi:10.1142/s0578563499000024.

[69] Y. Goda. *Random Seas and Design of Maritime Structures*. World Scientific, 2000.

[70] D. Golbaz, R. Asadi, E. Amini, H. Mehdipour, M. Nasiri, B. Etaati, S. T. O. Naeeni, M. Neshat, S. Mirjalili, and A. H. Gandomi. Layout and design optimization of ocean wave energy converters: A scoping review of state-of-the-art canonical, hybrid, cooperative, and combinatorial optimization methods. *Energy Reports*, 8:15446–15479, Nov. 2022. doi:10.1016/j.egyr.2022.10.403.

[71] C. C. Gonzaga, E. Karas, and M. Vanti. A globally convergent filter method for nonlinear programming. *SIAM Journal on Optimization*, 14(3):646–669, Jan. 2004. doi:10.1137/s1052623401399320.

[72] L. Greengard and V. Rokhlin. A fast algorithm for particle simulations. *Journal of Computational Physics*, 73(2):325–348, Dec. 1987. doi:10.1016/0021-9991(87)90140-9.

[73] N. Guillou. Estimating wave energy flux from significant wave height and peak period. *Renewable Energy*, 155:1383–1393, aug 2020. doi:10.1016/j.renene.2020.03.124.

[74] K. Gunn and C. Stock-Williams. Quantifying the global wave power resource. *Renewable Energy*, 44:296–304, Aug. 2012. doi:10.1016/j.renene.2012.01.101.

[75] M. Göteman, J. Engström, M. Eriksson, and J. Isberg. Optimizing wave energy parks with over 1000 interacting point-absorbers using an approximate analytical method. *International Journal of Marine Energy*, 10:113–126, jun 2015. doi:10.1016/j.ijome.2015.02.001.

[76] M. Göteman, J. Engström, M. Eriksson, J. Isberg, and M. Leijon. Methods of reducing power fluctuations in wave energy parks. *Journal of Renewable and Sustainable Energy*, 6:043103, 07 2014. doi:10.1063/1.4889880.

[77] M. Göteman, M. Giassi, J. Engström, and J. Isberg. Advances and challenges in wave energy park optimization—a review. *Frontiers in Energy Research*, 8:26, 2020. doi:10.3389/fenrg.2020.00026.

[78] W. Hackbusch. The solution of large systems of BEM equations by the multi-grid and panel clustering technique. *Rendiconti del Seminario Matematico*, special issue 'Numerical Methods in Applied Science and Industry':163–187, 06 1991.

[79] W. Hackbusch. *Hierarchical Matrices: Algorithms and Analysis*. Springer Berlin Heidelberg, 2015. doi:10.1007/978-3-662-47324-5.

[80] E. Hairer, G. Wanner, and S. P. Nørsett. *Solving Ordinary Differential Equations I: Nonstiff Problems*. Springer Series in Computational Mathematics 8. Springer-Verlag Berlin Heidelberg, 2 edition, 1993.

[81] A. Haldar and S. Mahadevan. *Probability, Reliability and Statistical Methods in Engineering Design*. John Wiley & S., 2000.

[82] C. R. Harris et al. Array programming with NumPy. *Nature*, 585(7825):357–362, Sept. 2020. doi:10.1038/s41586-020-2649-2.

[83] T. Hedges. Regions of validity of analytical wave theories. *Proceedings of the Institution of Civil Engineers - Water Maritime and Energy*, 112:111–114, 01 1995. doi:10.1680/iwtme.1995.27656.

[84] IEA. Electricity 2024. Technical report, IEA, Paris, 2024. https://www.iea.org/reports/electricity-2024, Licence: CC BY 4.0.

[85] S. Jin and D. Greaves. Wave energy in the UK: Status review and future perspectives. *Renewable and Sustainable Energy Reviews*, 143:110932, June 2021. doi:10.1016/j.rser.2021.110932.

[86] H. Kagemoto and D. K. P. Yue. Interactions among multiple three-dimensional bodies in water waves: an exact algebraic method. *Journal of Fluid Mechanics*, 166(1):189, May 1986. doi:10.1017/s0022112086000101.

[87] C. Kalogeri, G. Galanis, C. Spyrou, D. Diamantis, F. Baladima, M. Koukoula, and G. Kallos. Assessing the European offshore wind and wave energy resource for combined exploitation. *Renewable Energy*, 101:244–264, Feb. 2017. doi:10.1016/j.renene.2016.08.010.

[88] J. Kapica, J. Jurasz, F. A. Canales, H. Bloomfield, M. Guezgouz, M. De Felice, and Z. Kobus. The potential impact of climate change on European renewable energy droughts. *Renewable and Sustainable Energy Reviews*, 189:114011, Jan. 2024. doi:10.1016/j.rser.2023.114011.

[89] J. Katz and A. Plotkin. *Low-Speed Aerodynamics*. McGraw-Hill, 1991.

[90] T. Kelly, I. Zabala, Y. Peña-Sanchez, M. Penalba, J. V. Ringwood, J. C. Henriques, and J. M. Blanco. A post-processing technique for removing 'irregular frequencies' and other issues in the results from BEM solvers. *International Marine Energy Journal*, 5(1):123–131, June 2022. doi:10.36688/imej.5.123-131.

[91] J. Kemper, C. Windt, K. Graf, and J. Ringwood. Development towards a nested hydrodynamic model for the numerical analysis of ocean wave energy systems. 08 2019.

[92] S. Koley and K. Trivedi. Mathematical modeling of oscillating water column wave energy converter devices over the undulated sea bed. *Engineering Analysis with Boundary Elements*, 117:26–40, Aug. 2020. doi:10.1016/j.enganabound.2020.03.017.

[93] U. A. Korde and J. Ringwood. *Hydrodynamic Control of Wave Energy Devices*. Cambridge University Press, sep 2016. doi:10.1017/cbo9781139942072.

[94] G. S. Krishnaswami and S. Phatak. The added mass effect and the Higgs mechanism: How accelerated bodies and elementary particles can gain inertia. *Resonance*, 25(2):191–213, Feb. 2020. doi:10.1007/s12045-020-0936-8.

[95] P. Kundu, I. Cohen, and D. Dowling. *Fluid Mechanics*. Elsevier Science, 2012.

[96] C. Lalanne. *Random Vibration*. CRC Press, feb 1999. doi:10.1201/9780367812096.

[97] M. Lamas-Pardo, G. Iglesias, and L. Carral. A review of Very Large Floating Structures (VLFS) for coastal and offshore uses. *Ocean Engineering*, 109:677–690, Nov. 2015. doi:10.1016/j.oceaneng.2015.09.012.

[98] H. Lamb. *Hydrodynamics*. Dover publications, 1945.

[99] S. Lang. *Linear Algebra*. Springer New York, 1987. doi:10.1007/978-1-4757-1949-9.

[100] J. Lekube, A. Garrido, I. Garrido, E. Otaola, and J. Maseda. Flow control in Wells turbines for harnessing maximum wave power. *Sensors*, 18(2):535, feb 2018. doi:10.3390/s18020535.

[101] B. Li, S. Basu, S. J. Watson, and H. W. J. Russchenberg. Mesoscale modeling of a "Dunkelflaute" event. *Wind Energy*, 24(1):5–23, Aug. 2020. doi:10.1002/we.2554.

[102] G. Li, G. Weiss, M. Mueller, S. Townley, and M. R. Belmont. Wave energy converter control by wave prediction and dynamic programming. *Renewable Energy*, 48:392–403, dec 2012. doi:10.1016/j.renene.2012.05.003.

[103] L. Li, Y. Gao, D. Ning, and Z. Yuan. Development of a constraint non-causal wave energy control algorithm based on artificial intelligence. *Renewable and Sustainable Energy Reviews*, 138:110519, Mar. 2021. doi:10.1016/j.rser.2020.110519.

[104] X. Liu and S. Sakai. Time domain analysis on the dynamic response of a flexible floating structure to waves. *Journal of Engineering Mechanics*, 128(1):48–56, jan 2002. doi:10.1061/(asce)0733-9399(2002)128:1(48).

[105] Y. Liu and N. Nishimura. The fast multipole boundary element method for potential problems: A tutorial. *Engineering Analysis with Boundary Elements*, 30(5):371–381, May 2006. doi:10.1016/j.enganabound.2005.11.006.

[106] J. Lyu. *Optimization and control of arrays of wave energy converters*. PhD thesis, Michigan Technological University, 2019. doi:10.37099/mtu.dc.etdr/946.

[107] S. Marburg and S. Amini. Cat's eye radiation with boundary elements: comparative study on treatment of irregular frequencies. *Journal of Computational Acoustics*, 13(01):21–45, Mar. 2005. doi:10.1142/s0218396x05002566.

[108] A. Maria-Arenas, A. J. Garrido, E. Rusu, and I. Garrido. Control strategies applied to wave energy converters: State of the art. *Energies*, 12(16):3115, aug 2019. doi:10.3390/en12163115.

[109] P. Masarati. Dynamics and control of flexible aircraft. Lecture notes, 2019.

[110] H. Masoud and H. A. Stone. The reciprocal theorem in fluid dynamics and transport phenomena. *Journal of Fluid Mechanics*, 879, Sept. 2019. doi:10.1017/jfm.2019.553.

[111] Y. Masuda. An experience of wave power generator through tests and improvement. In *Hydrodynamics of Ocean Wave-Energy Utilization*, pages 445–452. Springer Berlin Heidelberg, 1986. doi:10.1007/978-3-642-82666-5_36.

[112] J. McGuinness and G. Thomas. Hydrodynamic optimisation of small arrays of heaving point absorbers. *Journal of Ocean Engineering and Marine Energy*, 2(4):439–457, July 2016. doi:10.1007/s40722-016-0064-4.

[113] J. McGuinness and G. Thomas. Optimisation of wave-power arrays without prescribed geometry over incident wave angle. *International Marine Energy Journal*, 4(1):1–10, Mar. 2021. doi:10.36688/imej.4.1-10.

[114] J. C. McNatt, V. Venugopal, and D. Forehand. A novel method for deriving the diffraction transfer matrix and its application to multi-body interactions in water waves. *Ocean Engineering*, 94:173–185, jan 2015. doi:10.1016/j.oceaneng.2014.11.029.

[115] T. Megson. *Aircraft Structures for Engineering Students*. Elsevier aerospace engineering series. Elsevier Science, 2007.

[116] B. Méhauté. *An Introduction to Hydrodynamics and Water Waves*. Springer-Verlag, 1976.

[117] R. Mehra, N. Raghuvanshi, L. Antani, A. Chandak, S. Curtis, and D. Manocha. Wave-based sound propagation in large open scenes using an equivalent source formulation. *ACM Transactions on Graphics*, 32(2):1–13, Apr. 2013. doi:10.1145/2451236.2451245.

[118] C. C. Mei, M. Stiassnie, and D. K.-P. Yue. *Theory and Applications of Ocean Surface Waves*. World Scientific, 2005. doi:10.1142/5566.

[119] A. Mérigaud, B. Thiria, and R. Godoy-Diana. Geometrical framework for hydrodynamics and control of wave energy converters. *PRX Energy*, 2(2):023003, may 2023. doi:10.1103/prxenergy.2.023003.

[120] O. Mersmann, B. Bischl, H. Trautmann, M. Preuss, C. Weihs, and G. Rudolph. Exploratory landscape analysis. In *Proceedings of the 13th annual conference on Genetic and evolutionary computation*, GECCO '11. ACM, July 2011. doi:10.1145/2001576.2001690.

[121] H. V. J. L. Meur. Derivation of a viscous Boussinesq system for surface water waves. *Asymptotic Analysis*, 94(3-4):309–345, 2015.

[122] V. Mnih et al. Human-level control through deep reinforcement learning. *Nature*, 518(7540):529–533, Feb. 2015.

[123] A. Mola, N. Giuliani, O. Crego, and G. Rozza. A unified steady and unsteady formulation for hydrodynamic potential flow simulations with fully nonlinear free surface boundary conditions. *Applied Mathematical Modelling*, 122:322–349, Oct. 2023. doi:10.1016/j.apm.2023.06.001.

[124] A. Nemirovski, A. Juditsky, G. Lan, and A. Shapiro. Robust stochastic approximation approach to stochastic programming. *SIAM Journal on Optimization*, 19(4):1574–1609, jan 2009. doi:10.1137/070704277.

[125] M. Neshat, B. Alexander, and M. Wagner. A hybrid cooperative co-evolution algorithm framework for optimising power take off and placements of wave energy converters. *Information Sciences*, 534:218–244, Sept. 2020. doi:10.1016/j.ins.2020.03.112.

[126] J. N. Newman. *Marine Hydrodynamics*. The MIT Press, 2018.

[127] J. Nocedal and S. J. Wright. *Numerical Optimization*. Springer New York, 2006. doi:10.1007/978-0-387-40065-5.

[128] M. Ochmann. The source simulation technique for acoustic radiation problems. *Acustica*, 81(6):512–527, 1995.

[129] J. Panzer and L. Ferekidis. The use of continuous phase for interpolation, smoothing and forming mean values of complex frequency response curves. In *Audio Engineering Society Convention 116*. Audio Engineering Society, 2004.

[130] A. Papoulis. *Probability, Random Variables, and Stochastic Processes*. McGraw-Hill, New York, 1965.

[131] M. Parhamfar, I. Sadeghkhani, and A. M. Adeli. Towards the application of renewable energy technologies in green ports: Technical and economic perspectives. *IET Renewable Power Generation*, 17(12):3120–3132, July 2023. doi:10.1049/rpg2.12811.

[132] V. Patel. Stopping criteria for, and strong convergence of, stochastic gradient descent on Bottou-Curtis-Nocedal functions. *Mathematical Programming*, oct 2021. doi:10.1007/s10107-021-01710-6.

[133] A. Pecher and J. Kofoed. *Handbook of Ocean Wave Energy*. Ocean Engineering & Oceanography. Springer International Publishing, 2017. URL: https://books.google.it/books?id=IuTxjwEACAAJ.

[134] M. Peviani, G. Agate, S. Bonamano, M. Marcelli, and C. Burgio. WaveSAX design and PTO optimization: modelling and sea tests at the port of Civitavecchia. https://www.ocean-energy-systems.org/publications/icoe-conference/icoe-2022/document/wavesax-design-and-pto-optimization-modelling-and-sea-tests-at-the-port-of-civitavecchia/. Presentation at ICOE-OEE, San Sebastian, Spain, 18–20 October 2022.

[135] M. Peviani, G. Agate, S. Bonamano, and S. Scanu. Ottimizzazione degli aspetti costruttivi del dispositivo WaveSAX. Technical report, RSE S.p.A., 2021.

[136] M. A. Peviani, G. Agate, A. Danelli, G. Quinteri, S. Bonamano, and F. Lauria. Ottimizzazione della producibilità del dispositivo WaveSAX. Technical report, RSE S.p.A., 2020.

[137] O. M. Phillips. On the generation of waves by turbulent wind. *Journal of Fluid Mechanics*, 2(05):417, July 1957. doi:10.1017/s0022112057000233.

[138] O. M. Phillips. The equilibrium range in the spectrum of wind-generated waves. *Journal of Fluid Mechanics*, 4(04):426, aug 1958. doi:10.1017/s0022112058000550.

[139] J. Pinkster. *Low frequency second order wave exciting forces on floating structures*. PhD thesis, TUDelft, 1980.

[140] A. Quarteroni, R. Sacco, and F. Saleri. *Numerical Mathematics (Texts in Applied Mathematics)*. Springer-Verlag, Berlin, Heidelberg, 2006.

[141] M. Requena-Perez, A. Albero-Ortiz, J. Monzo-Cabrera, and A. Diaz-Morcillo. Combined use of genetic algorithms and gradient descent optmization methods for accurate inverse permittivity measurement. *IEEE Transactions on Microwave Theory and Techniques*, 54(2):615–624, 2006. doi:10.1109/TMTT.2005.862671.

[142] J. V. Ringwood, S. Zhan, and N. Faedo. Empowering wave energy with control technology: Possibilities and pitfalls. *Annual Reviews in Control*, 55:18–44, 2023. doi:10.1016/j.arcontrol.2023.04.004.

[143] H. Ritchie, P. Rosado, and M. Roser. Breakdown of carbon dioxide, methane and nitrous oxide emissions by sector. *Our World in Data*, 2020. https://ourworldindata.org/emissions-by-sector.

[144] D. Roddier, C. Cermelli, A. Aubault, and A. Weinstein. Windfloat: A floating foundation for offshore wind turbines. *Journal of Renewable and Sustainable Energy*, 2(3), May 2010. doi:10.1063/1.3435339.

[145] L. Rusu and E. Rusu. Evaluation of the worldwide wave energy distribution based on ERA5 data and altimeter measurements. *Energies*, 14(2):394, jan 2021. doi:10.3390/en14020394.

[146] I. Rychlik. Five lectures on reliability applications of Rice's formula for the intensity of level crossings. In S. Jendo and K. Dolinski, editors, *Reliability-Based Design and Optimisation*, pages 241–323. Centre of Excellence for Advanced Materials and Structures, 2003.

[147] I. Rychlik, P. Johannesson, and M. Leadbetter. Modelling and statistical analysis of ocean-wave data using transformed Gaussian processes. *Marine Structures*, 10(1):13–47, jan 1997. doi:10.1016/s0951-8339(96)00017-2.

[148] S. Salsa. *Equazioni a Derivate Parziali*. Springer-Verlag Italia, 3rd edition, 2016.

[149] S. Salsa and A. Squellati. *Dynamical Systems and Optimal Control*. Bocconi University Press, 2018.

[150] T. Sarpkaya. *Wave Forces on Offshore Structures*. Cambridge University Press, Feb. 2010. doi:10.1017/cbo9781139195898.

[151] S. A. Sauter and C. Schwab. *Boundary Element Methods*. Springer Berlin Heidelberg, 2011. doi:10.1007/978-3-540-68093-2.

[152] B. W. Schubert. *Performance Enhancement of Submerged Ocean Wave Energy Converter using Nonlinear Stiffness*. PhD thesis, School of Mechanical Engineering, University of Adelaide, 2021.

[153] D. Scieur, V. Roulet, F. Bach, and A. d'Aspremont. Integration methods and optimization algorithms. In I. Guyon, U. V. Luxburg, S. Bengio, H. Wallach, R. Fergus, S. Vishwanathan, and R. Garnett, editors, *Advances in Neural Information Processing Systems*, volume 30. Curran Associates, Inc., 2017. URL: https://proceedings.neurips.cc/paper_files/paper/2017/file/bf62768ca46b6c3b5bea9515d1a1fc45-Paper.pdf.

[154] A. Shadmani, M. R. Nikoo, A. H. Gandomi, R.-Q. Wang, and B. Golparvar. A review of machine learning and deep learning applications in wave energy forecasting and WEC optimization. *Energy Strategy Reviews*, 49:101180, Sept. 2023. doi:10.1016/j.esr.2023.101180.

[155] A. Shapiro, D. Dentcheva, and A. Ruszczyński. *Lectures on Stochastic Programming: Modeling and Theory, Second Edition*. Society for Industrial and Applied Mathematics, jan 2014. doi:10.1137/1.9781611973433.

[156] A. Sinha, D. Karmakar, and C. G. Soares. Performance of optimally tuned arrays of heaving point absorbers. *Renewable Energy*, 92:517–531, jul 2016. doi:10.1016/j.renene.2016.02.043.

[157] V. A. Squire. Ocean wave interactions with sea ice: A reappraisal. *Annual Review of Fluid Mechanics*, 52(1):37–60, jan 2020. doi:10.1146/annurev-fluid-010719-060301.

[158] K. E. Swalwell, J. Sheridan, and W. H. Melbourne. The effect of turbulence intensity on stall of the NACA 0021 aerofoil. *14th Australasian Fluid Mechanics Conference*, 2001.

[159] K. Tanabe. A geometric method in nonlinear programming. *Journal of Optimization Theory and Applications*, 30(2):181–210, feb 1980. doi:10.1007/bf00934495.

[160] E. Tapoglou, A. Georgakaki, S. Letout, A. Kuokkanen, A. Mountraki, E. Ince, D. Shtjefni, G. Joanny Ordonez, O. Eulaerts, and M. Grabowska. Clean Energy Technology Observatory: Ocean Energy in the European Union – 2022 Status Report on Technology Development, Trends, Value Chains and Markets. Technical report, Publications Office of the European Union, 2022.

[161] F. Teixeira-Duarte, D. Clemente, G. Giannini, P. Rosa-Santos, and F. Taveira-Pinto. Review on layout optimization strategies of offshore parks for wave energy converters. *Renewable and Sustainable Energy Reviews*, 163:112513, July 2022. doi:10.1016/j.rser.2022.112513.

[162] P. Thompson. *Compressible-fluid Dynamics*. Advanced engineering series. McGraw-Hill, 1972.

[163] K. Thorne and R. Blandford. *Modern Classical Physics: Optics, Fluids, Plasmas, Elasticity, Relativity, and Statistical Physics*. Princeton University Press, 2017.

[164] E. Thornhill. Interpolation of complex-valued response amplitude operators. Technical report, DRDC – Atlantic Research Centre, Nov. 2019.

[165] J. H. Todalshaug, G. S. Ásgeirsson, E. Hjálmarsson, J. Maillet, P. Möller, P. Pires, M. Guérinel, and M. Lopes. Tank testing of an inherently phase-controlled wave energy converter. *International Journal of Marine Energy*, 15:68–84, sep 2016. doi:10.1016/j.ijome.2016.04.007.

[166] M. Torresi, S. Camporeale, P. Strippoli, and G. Pascazio. Accurate numerical simulation of a high solidity Wells turbine. *Renewable Energy*, 33(4):735–747, apr 2008. doi:10.1016/j.renene.2007.04.006.

[167] G. Travaglini. Stochastic optimization of a WEC array. Master's thesis, Politecnico di Milano, 2024.

[168] L. N. Trefethen. *Approximation Theory and Approximation Practice, Extended Edition*. Society for Industrial and Applied Mathematics, jan 2019. doi:10.1137/1.9781611975949.

[169] M. Tucker, P. Challenor, and D. Carter. Numerical simulation of a random sea: a common error and its effect upon wave group statistics. *Applied Ocean Research*, 6(2):118–122, apr 1984. doi:10.1016/0141-1187(84)90050-6.

[170] A. van der Sluis. Condition numbers and equilibration of matrices. *Numerische Mathematik*, 14(1):14–23, dec 1969. doi:10.1007/bf02165096.

[171] P. Virtanen et al. SciPy 1.0: Fundamental Algorithms for Scientific Computing in Python. *Nature Methods*, 17:261–272, 2020. doi:10.1038/s41592-019-0686-2.

[172] D. J. Wales and J. P. K. Doye. Global optimization by basin-hopping and the lowest energy structures of Lennard-Jones clusters containing up to 110 atoms. *The Journal of Physical Chemistry A*, 101(28):5111–5116, July 1997. doi:10.1021/jp970984n.

[173] W. Wang, C. Pákozdi, A. Kamath, T. Martin, and H. Bihs. Hydrodynamic coupling of viscous and nonviscous numerical wave solutions within the open-source hydrodynamics framework REEF3D. *Journal of Offshore Mechanics and Arctic Engineering*, 144(4), mar 2022. doi:10.1115/1.4053848.

[174] J. V. Wehausen and E. V. Laitone. Surface waves. In *Fluid Dynamics / Strömungsmechanik*, pages 446–778. Springer Berlin Heidelberg, 1960. doi:10.1007/978-3-642-45944-3_6.

[175] H. Wolgamot, P. Taylor, and R. E. Taylor. The interaction factor and directionality in wave energy arrays. *Ocean Engineering*, 47:65–73, jun 2012. doi:10.1016/j.oceaneng.2012.03.017.

[176] P.-Y. Wuillaume. *Simulation numérique des opérations d'installation pour les fermes d'éoliennes offshore*. PhD thesis, École Centrale de Nantes, 2019.

[177] H. Yamashita. A differential equation approach to nonlinear programming. *Mathematical Programming*, 18(1):155–168, 1980.

[178] X. Yan and V. Quintana. Improving an interior-point-based OPF by dynamic adjustments of step sizes and tolerances. *IEEE Transactions on Power Systems*, 14(2):709–717, May 1999. doi:10.1109/59.761902.

[179] B. Yang, S. Wu, H. Zhang, B. Liu, H. Shu, J. Shan, Y. Ren, and W. Yao. Wave energy converter array layout optimization: A critical and comprehensive overview. *Renewable and Sustainable Energy Reviews*, 167:112668, oct 2022. doi:10.1016/j.rser.2022.112668.

[180] O. Yilmaz. Hydrodynamic interactions of waves with group of truncated vertical cylinders. *Journal of Waterway, Port, Coastal, and Ocean Engineering*, 124(5):272–279, sep 1998. doi:10.1061/(asce)0733-950x(1998)124:5(272).

[181] D. K. P. Yue, H. S. Chen, and C. C. Mei. A hybrid element method for diffraction of water waves by three-dimensional bodies. *International Journal for Numerical Methods in Engineering*, 12(2):245–266, Jan. 1978. doi:10.1002/nme.1620120207.

[182] H. Zhang, R. Xi, D. Xu, K. Wang, Q. Shi, H. Zhao, and B. Wu. Efficiency enhancement of a point wave energy converter with a magnetic bistable mechanism. *Energy*, 181:1152–1165, aug 2019. doi:10.1016/j.energy.2019.06.008.

[183] K. Zhu, H. Shi, S. Michele, M. Han, and F. Cao. Analytical study on dynamic performance of a hybrid system in real sea states. *Energy*, 290:130259, Mar. 2024. doi:10.1016/j.energy.2024.130259.

[184] Z. Zhu and M. B. Wakin. On the asymptotic equivalence of circulant and Toeplitz matrices. *IEEE Transactions on Information Theory*, 63(5):2975–2992, 2017. doi:10.1109/TIT.2017.2676808.

[185] S. Zou, O. Abdelkhalik, R. Robinett, G. Bacelli, and D. Wilson. Optimal control of wave energy converters. *Renewable Energy*, 103:217–225, apr 2017. doi:10.1016/j.renene.2016.11.036.

[186] S. Zou, X. Zhou, I. Khan, W. W. Weaver, and S. Rahman. Optimization of the electricity generation of a wave energy converter using deep reinforcement learning. *Ocean Engineering*, 244:110363, Jan. 2022. doi:10.1016/j.oceaneng.2021.110363.